Interactions between a Colour Centre, Optical, and Mechanical Resonator Modes in a Diamond Structure

Dissertation

zur Erlangung des Grades
des Doktors der Naturwissenschaften
der Naturwissenschaftlich-Technischen Fakultät
der Universität des Saarlandes

von

Laura Kreiner

Saarbrücken

2017

Tag des Kolloquiums: 17. November 2017

Dekan: Univ.-Prof. Dr. rer. nat. Guido Kickelbick

Mitglieder des Prüfungsausschusses: Univ.-Prof. Dr. rer. nat. Rolf Pelster
Univ.-Prof. Dr. rer. nat. Christoph Becher
Univ.-Prof. Dr. rer. nat. Giovanna Morigi
Dr.-Ing. Sebastian Suarez

Abstract

This work shows a route towards the implementation of diamond-based platforms as highly integrated system for quantum information processing. To this end, a structure where three degrees of freedom mutually couple at the single particle level is investigated based on numerical modelling. A practical implementation is tested and challenges towards an experimental demonstration are identified.

The structure considered in this work is a photonic and phononic crystal that confines an optical and a mechanical resonator mode and that hosts a colour centre. Besides the well-explored Purcell coupling, optomechanical interaction and strain coupling to both the ground and excited state levels of a single nitrogen vacancy colour centre determine the dynamics in this structure. In addition, a hybrid interaction involving all three degrees of freedom is explored to demonstrate the unique possibilities in this highly integrated system.

With regard to an experimental implementation, established fabrication techniques are improved and a novel dry etching technique is developed with the aim to achieve a better mode confinement. The practical feasibility of measurements in vacuum, required for detecting the mechanical oscillation via optomechanical or strain coupling, is assessed. Unexpected features in the optical mode spectrum are detected and systematically investigated so that a future experimental demonstration is within reach.

Zusammenfassung

In dieser Arbeit wird eine Diamantplattform als hochintegriertes System im Bereich der Quanteninformationsverarbeitung vorgestellt. Dazu wird eine Struktur simuliert, in der drei Freiheitsgrade auf der Ebene einzelner Quanten in Wechselwirkung treten. Eine praktische Umsetzung wird getestet wobei Hindernisse auf dem Weg zu einer experimentellen Demonstration identifiziert werden.

In dieser Arbeit wird ein photonischer und phononischer Kristall untersucht, der eine optische und eine mechanische Resonatormode lokalisiert und in dessen Mitte ein Farbzentrum eingebracht ist. Neben der bekannten Purcell-Kopplung bestimmen optomechanische Kopplung und die Wechselwirkung zwischen mechanischer Schwingung und den Grund- und angeregten Zuständen eines einzelnen Stickstoff-Fehlstellen-Zentrums die Dynamik des Systems. Darüber hinaus wird eine gleichzeitige Wechselwirkung aller drei Freiheitsgrade untersucht um die einzigartigen Möglichkeiten dieses hochintegrierten Systems aufzuzeigen.

Im Hinblick auf eine experimentelle Umsetzung werden bekannte Herstellungstechniken verbessert und ein neues Trockenätzverfahren entwickelt um eine bessere Lokalisation der Moden zu erzielen. Messungen im Vakuum, die für den indirekten Nachweis der mechanischen Schwingung über optomechanische Kopplung nötig sind, werden getestet. Dabei wird ein unerwartetes Verhalten der optischen Eigenschaften beobachtet und systematisch untersucht sodass eine experimentelle Umsetzung in greifbare Nähe rückt.

Contents

Chapter 1

Introduction

Hybrid Quantum Systems in Diamond

As the field of quantum technologies is advancing more and more, applications that could only be imagined for a long time are within reach for a practical implementation. A number of seminal experiments showed that an application of quantum systems as extremely sensitive detectors [1], and as building block for quantum computing [2,3] or quantum communication [4] is indeed possible. A drastic improvement, however, is required to transfer the results of these proof-of-principle experiments to quantum technologies of practical use. The properties of individual components need to be optimised to fulfil their tasks like storage, processing, readout or transfer of information. While there is a variety of different physical systems that are investigated with the aim to implement quantum technologies, there is no platform known to date that is equally suitable for all aspects of an integrated quantum network. It became thus obvious that a combination of different components is required to implement quantum technologies [5,6]. The use of such hybrid systems assembled from different building blocks allows to use the best platform for each function and combine them such that the strengths of the individual parts can be exploited and the weaknesses are mitigated by complementary subsystems.

The individual building blocks of hybrid architectures vary according to the application and there is no consensus about the question which degrees of freedom are most suitable for what function. Many hybrid quantum systems comprise an internal degree of freedom in the form of a two-level system for functions like memory or computational quantum bits, or as single photon sources. Non-classical radiation of a single trapped ion has been detected decades ago [7] and since then a broad variety of single photon sources like quantum dots, superconducting qubits, molecules, or defect centres in semiconductors has been studied [8–10]. While quantum dots have been studied as electrically driven single photon sources [11], most two-level systems require an optical or microwave control field to generate single photon emission and to store, retrieve, or process quantum information. Therefore, nearly all proposals for hybrid quantum networks also include an optical degree of freedom and Lasers are a standard and convenient tool to control two-level systems. Optical resonators strongly confine their light field and allow to enhance the optical field strength in defined resonator modes to increase control over the two-level system. Besides this application as technical tool, an optical degree of freedom is also studied in the form of single photons. As "flying qubits", they can be the centrepiece in applications like quantum repeaters [12] or quantum information processing [13] and especially the combination of stationary and flying qubits can be exploited for quantum computation [14]. A third degree of freedom that is more and more discussed for the integration in quantum hybrid systems are mechanical resonators on the nanoscale [15,16]. Their ability to interconnect systems of disparate energy scales make them an interesting component in more complex hybrid architectures where very different building blocks need to be assembled. On the level of fundamental experiments, their still nearly macroscopic dimensions allow to observe signatures of quantum mechanics on a scale far above the single particle level and make mechanical resonators an interesting system to test quantum effects. Mechanical resonators have been investigated for an application as memory [17] and very sensitive detectors for mass [18–21],

position [22], or biological and chemical components [23, 24]. The mechanical degree of freedom has also been investigated at the single particle level and phononic applications play an increasing role in quantum technologies. Phononic networks and switchable phonon routers [25] have been investigated, analogous setups to optical cavity quantum electrodynamics based on phononic two-level systems and their corresponding networks have been studied [26], and the processing of information with phononic computing is within reach with current technologies [27].

All these individual degrees of freedom show properties rendering them suitable for different tasks in hybrid quantum networks. The crucial factor, however, is the interconnection of these different components as the dynamics of a hybrid system is determined by the interactions between the individual degrees of freedom. The coupling between different physical systems even opens for new applications based on the interaction as such and allows the use of novel protocols based on the interaction profiles. In the recent years, more and more attention was drawn to diamond-based systems for quantum applications [28–33]. Diamond has the advantage to provide a flexible platform where various degrees of freedom can be integrated in a monolithic architecture. This allows for the co-localisation of an optical, a mechanical and an internal degree of freedom in a single device. These different building blocks of hybrid architectures have been investigated in diamond-based structures and the investigation of their interactions as well as a practical implementation are subject to on-going research.

Individual Building Blocks in the Diamond Structure: Optical, Mechanical and Internal Degree of Freedom

Many simulations on optical resonators in diamond have been performed. Waveguide heterostructure designs [34–36], two-dimensional photonic crystal cavities [34, 37–39], and one-dimensional photonic crystal cavities [40–42] have been investigated. However, the nanofabrication of diamond structures remains a challenge due to the chemical inertness and mechanical resistance of the material as well as the lack of established standard fabrication procedures. In nanocrystalline diamond, microdisk structures [43], photonic crystal cavities [44] and waveguide heterostructures [45] have been fabricated for optical wavelengths at 637 nm and the telecom band at 1550 nm. The optical quality factors Q_{opt} reach values of around hundred for the ring resonators, up to 500 for the photonic crystal cavities and up to 2800 for the waveguide heterostructures. In single crystal diamond, ring resonators have been fabricated for optical and telecom wavelengths with quality factors of a few thousand [46–48]. The first one- and two-dimensional photonic crystal cavities in single crystal diamond have been fabricated in our group with quality factors up to 700 [42]. Higher quality factors of few thousands have been reached in subsequent work with two- [49] and one-dimensional [50] photonic crystal cavity structures. With an angled etching technique leading to a triangular cross-section, quality factors up to 5000 could be reached with one-dimensional structures designed for the visible range and up to 150000 with ring resonators at telecom wavelengths [51, 52]. Very recently, photonic crystal structures designed for optical wavelengths could be fabricated using an under-etching technique and showed quality factors exceeding 14000 [53].

Also mechanical resonators have been fabricated from diamond. Doubly clamped paddles with dimensions of $2\,\mu$m have been fabricated in nanocrystalline diamond [54]. The flexural modes showed resonance frequencies in the range $6-30\,$MHz with mechanical quality factors Q_{m} ranging up to 3500. Also in nanocrystalline diamond doubly clamped beam with dimensions $40\,$nm $\times\,180\,$nm $\times\,2,5-8\,\mu$m showed quality factors up to 10^4 for resonance frequencies in the order of $10-160\,$MHz [55]. Various structures like square or round paddle arrays and tuning forks with resonance frequencies in the range $10-40\,$MHz and quality factors of $1000-8000$ have been fabricated in polycrystalline diamond [56]. With specific "antenna structures" resembling a fish-bone (dimensions approximately $600\,$nm $\times\,400\,$nm $\times\,10\,\mu$m), mechanical frequencies up to $1.44\,$GHz and quality factors up to 20000 could be reached [57]. The first single crystal diamond resonators were nanodome resonators with frequencies of $50-600\,$MHz and mechanical quality factors up to 20000 (at room temperature $Q_{\mathrm{m}} \approx 1000$) [58]. Also, cantilevers in single crystal diamond with dimensions of $60-80\,\mu$m $\times\,15-20\,\mu$m $\times\,0.8-1.8\,\mu$m with resonance frequencies in the range $600-1400\,$kHz and quality factors at room temperature up to 338000 have been fabricated [59]. Single crystal diamond cantilevers and doubly clamped beams in the micron range achieved high mechanical frequencies up to $10\,$MHz and quality factors of 10^4 (where cantilevers and larger structures show higher quality factors than doubly clamped beams and smaller structures) [60, 61]. Quality factors of 1 million at room temperature could be shown with cantilevers and allowed for a systematic study on how the diamond quality and surface termination affects the mechanical quality factors [62]. Microdisk resonators in single crystal diamond reached quality factors of 9000 for mechanical frequencies of $2\,$GHz [63]. Phononic crystals in single crystal diamond were fabricated and showed mechanical modes arising from the X-band with quality factors of 10^3 at frequencies around $5\,$GHz [52].

While there is a large variety of different resonator types, only whispering gallery mode resonators and selected photonic and phononic crystal cavities are suitable to co-localise both an optical and mechanical resonator mode in a single structure. Whispering gallery mode resonators confine light through total internal reflection in spherical geometries and toroid structures support different types of mechanical oscillations including breathing and flexural modes. They typically show high quality factors and moderate spatial confinement of optical and mechanical resonator modes. In order to maximise the interaction strength between the individual degrees of freedom, photonic and phononic crystal modes are better suited due to their extremely strong mode confinement and the resulting very high peak intensities of the cavity fields. These structures have first been investigated with respect to their optical properties as photonic crystals [64–66]. A periodic pattern of varying refractive index can be engineered such that a bandgap or modegap effect gives rise to a localised optical cavity mode in its centre. Also for the localisation of mechanical resonator modes, structures with periodically patterned materials have been investigated [67]. In that case, the modulation of the elastic properties gives rise to phononic modes. The combination of both approaches can be achieved by carefully engineering a structure with respect to both its optical and mechanical properties to co-localise photons and phonons in a single device [68]. The functionality of the structure is predominantly defined by the design of the device, but the properties of the host material set the general framework. Diamond is transparent from the ultraviolet

to the far infrared and allows for confined optical modes in a wide range of wavelengths including the visible spectrum, while its very high Young's modulus allows for reaching record mechanical frequencies that are not accessible with other materials.

In addition to optical and mechanical resonator modes, also two-level systems can be incorporated in diamond architectures. Various different colour centres can be formed by the incorporation of impurity atoms and the creation of vacant lattice positions [10,69]. Among the most-studied colour centres is the negatively charged nitrogen vacancy colour centre consisting of a nitrogen impurity and an adjacent vacant lattice position [70]. It has been studied as single photon source [71], for applications like quantum repeaters [72] or quantum key distribution [73], and for fundamental tests of quantum mechanical concepts like the violation of a temporal Bell inequality [74] and a loophole-free violation of a spatial Bell inequality [75], entanglement between the spin state of a nitrogen vacancy colour centre and an optical photon [76], or the entanglement between remote colour centres [77]. It has been demonstrated that strong driving of the spin [78] and all-optical control of the spin state with continuous [79] or pulsed [80] protocols are possible. The integration of nitrogen vacancy colour centres into various photonic structures has been demonstrated [81]. It is possible to create nitrogen vacancy colour centres with defined localisation in vertical [33,82] or lateral [83–85] dimensions and very small target volumes of $450\,\text{nm} \times 450\,\text{nm} \times 4\,\text{nm}$ can be achieved when combining both approaches [86]. High-resolution spectroscopy then allows the localisation of single emitters with a precision down to few nanometres [87]. Also the orientation of nitrogen vacancy colour centres with respect to the crystal lattice can be controlled during sample growth [88–90].

Interactions Between the Different Components

A photonic and phononic crystal cavity in single crystal diamond is thus a suitable platform to integrate different degrees of freedom in a monolithic structure. The interactions that occur between these components are the coupling between the nitrogen vacancy colour centre and the mechanical as well as the optical resonator mode, and the optomechanical coupling inside the diamond structure. The interaction between a two-level-system and an optical resonator is a standard tool in quantum electrodynamics and is typically exploited to enhance the interaction between light and the two-level system. It has also been studied in the context of nitrogen vacancy colour centres coupling to monolithic diamond optical resonators. The coupling between diamond optical resonators and single nitrogen vacancy colour centres could be demonstrated with ring-shaped whispering gallery mode resonators [46, 47] as well as with two-dimensional [49, 91] and one-dimensional [50] photonic crystal resonators. With these proof-of-principle demonstrations, significant improvements of the fabrication technologies are the next step to establish this interaction profile as standard technology and also an even more detailed investigation will not contribute much to this aim. Therefore, this work will focus more on the interactions between the optical and mechanical degree of freedom as well as between the colour centre and the mechanical cavity mode.

Radiation pressure effects have already been discussed centuries ago by Johannes Kepler and could be demonstrated experimentally in the early 20th century [92,93]. They

are exploited in applications like optical tweezers [94] and laser cooling of atoms [95,96] that became powerful tools for a broad range of experiments at the single particle level. Optomechanical interaction has also been studied in the context of gravitational wave detectors under the term "ponderomotive effect" [97,98] and the investigation of radiation pressure effects in optical resonators was adding a new perspective to the field. An entire field of research investigating cavity optomechanics down to the quantum scale developed [99–103] and there is a number of ideas for applications [104]. It has been discussed very early that optomechanical devices allow for quantum non-demolition measurements [105–107], the generation of squeezed states [108–110], or Schrödinger cat states [111,112] and detailed proposals for the preparation of entangled states between optics and mechanics have been specified later on [113–115]. Also, the possibilities for optomechanical cooling [116,117] and heating [117] have been assessed shortly after. The early experiments in cavity optomechanics investigated static effects like optical bistability [118] and dynamic effects like the optical spring effect [119–122] and the parametric instability [121–124]. Microstructures that co-localise optical and mechanical modes in a monolithic device have been fabricated [123,124] and dispersive coupling has been demonstrated where the interaction is proportional to the square of the displacement [125,126].

The most studied application of the optomechanical interaction is cooling of mechanical motion. While it was mediated by photo-thermal forces in an initial experiment [127], various different cooling protocols have been studied later on. From a theoretical perspective, the required condition for cooling to phonon numbers below one has been found to be the regime of resolved sidebands [128] and two fundamentally different cooling protocols have been studied and compared [129]. Experimentally, both cold damping [130–132] and back-action cooling have been demonstrated [121,122,133,134]. Later, also optomechanical cooling in the limit of resolved sidebands has been demonstrated [135–137]. Finally, the ground state of motion could be reached through optomechanical cooling with photons in the microwave [138] and the telecom range [139]. Clear signatures of the quantum regime could be detected in the form of asymmetric phononic sidebands of the optical resonator [140].

The regime of strong optomechanical coupling could be demonstrated [125,141] and quantum-coherent optomechanical coupling could be demonstrated with microwave [142] and optical photons [143]. Applications like optomechanically induced or mediated transparency [144–146], optomechanical frequency conversion [147,148], or precision measurements of position [137,142], force [149], and mass [150] have been studied. On the level of fundamental quantum mechanical experiments, phonon shot noise has been measured [151], and the heralded single phonon generation, storage, and readout corresponding to the manipulation of mechanical Fock states has been explored in an optomechanical system [152]. Also, the use of pulsed protocols for optomechanical applications has been investigated that could allow for several possibilities like observing quantum features despite the preparation from a thermal state or surpassing the cooling limit imposed by classical sideband cooling [102,153,154].

The extreme confinement of both optical and mechanical resonator modes to a very small volume in photonic and phononic crystal resonators is advantageous for reaching high optomechanical coupling strengths. This has been exploited in various experiments

with both two- [155] and one-dimensional structures [139, 140, 144, 145, 156]. Also, diamond structures have been exploited and optomechanical interaction could be demonstrated in doubly-clamped beams [157] and paddles [158] fabricated from polycrystalline diamond. Recently, also single crystal diamond has been used as platform to demonstrate optomechanical coupling in whispering gallery mode resonators [63] and photonic and phononic crystal resonators [52].

The interaction between a two-level system and a mechanical oscillation is frequently termed strain coupling. While it is inherent to solid state emitters that can directly couple to phononic modes supported by the host material, there is a variety of implementations to couple two-level systems and mechanical motion via an additional degree of freedom that mediates the interaction. Non-solid state emitters like ultracold atoms, ions, or molecules can only indirectly couple to a localised mechanical resonator mode, for example via radiation pressure forces in an optical resonator. The interaction between superconducting qubits and a mechanical resonator mode is typically mediated by capacitive or magnetomotive coupling. There are proposals [159, 160] and experimental demonstrations [161] for coupling quantum dots to mechanical displacement fields and a mechanical resonator mode could be cooled to its ground state of motion through strain coupling to a superconductive quantum bit [162]. However, many contributions to the growing field of strain coupling focus on the interaction between a mechanical oscillation and the electronic ground or excited state levels of the nitrogen vacancy colour centre in diamond [163]. Many implementations are based on magnetically mediated strain coupling [164–168]. In these setups, a magnetic field gradient is exploited such that a mechanical oscillation results in an oscillation of the magnetic field intensity at the location of the colour centre. The varying magnetic field then interacts with the ground state spin states of the nitrogen vacancy colour centre and causes a shifting, splitting, or mixing of the different levels. Magnetically mediated strain coupling has been used for coherent control of the spin state [167], and the generation of a phononic Mollow triplet [168]. These indirect access routes can open the possibility for strain coupling in two-level systems that could not undergo this interaction otherwise or facilitates the experimental setup in some cases. However, in the case of the nitrogen vacancy colour centre in diamond, the magnetically mediated coupling scheme cannot give access to the transition between the ground state levels with $m_\mathrm{s} = +1$ and $m_s = -1$. In addition, the interaction strength is inherently limited by the magnetic field gradients that can be generated at the location of the colour centre.

A direct interaction between a mechanical resonator mode and a nitrogen vacancy colour centre is thus the more promising approach for opening up new experimental possibilities and to facilitate the integration into hybrid systems. This direct interaction requires a two-level system embedded in or attached to a mechanical oscillator such that the strain field directly affects the electronic states of the emitter. The coupling is based on the deformation of electronic orbitals upon interaction with a strain field. The effect is orders of magnitude larger for the excited state levels with considerably larger orbitals than for the ground state levels with smaller orbitals. Two fundamentally different architectures are commonly used for the demonstration of strain coupling. Standing acoustic waves in the bulk of the diamond material generated by high overtone bulk acoustic resonators or interdigitated transducers at the surface have been coupled to

the ground [169–171] and excited [172] state levels of the nitrogen vacancy colour centre and also actuated mechanical cantilevers showed strain coupling to the ground [173–175] and excited state levels [176]. With direct strain coupling, the generation of phononic dressed states could be shown [175], the spin coherence times could be increased with the help of a continuous dynamical decoupling technique [170,175], and strong mechanical driving [175] as well as coherent control [171] of the spin could be demonstrated. Strain coupling to the excited state levels even entered the regime of resolved sidebands [172].

Scope and Content of this Thesis

The scope of this thesis is to investigate a hybrid quantum system based on a photonic and phononic crystal structure in diamond that also hosts a single nitrogen vacancy colour centre. The properties of all individual building blocks are investigated and the couplings occurring between all individual degrees of freedom are studied including a hybrid interaction between all three subsystems. The practical feasibility of such a hybrid diamond architecture is tested and possible applications are critically assessed.

The following chapter gives the theoretical background for this work starting with the relevant material properties of diamond. All individual degrees of freedom are described, namely a photonic crystal as optical resonator, a phononic crystal as mechanical resonator and a nitrogen vacancy colour centre as two-level system. All interactions occurring between these building blocks are presented. These are the Jaynes-Cummings interaction between optical and internal degree of freedom, optomechanical interaction in the photonic and phononic crystal structure, strain coupling between the nitrogen vacancy colour centre and the mechanical resonator mode, and a hybrid interaction including all degrees of freedom.

Then, the numerical modelling of this structure is shown. The methods to model both optical and mechanical resonator modes are introduced and the properties of a photonic and phononic crystal resonator in single crystal diamond are described. The method to quantify optomechanical interaction is shown and the coupling in the diamond structure is analysed. Strain coupling between a single nitrogen vacancy colour centre and the mechanical resonator mode is investigated including the interaction with both the ground and excited state levels. Finally, an integrated system hosting all three degrees of freedom is considered and the hybrid interaction in this structure is studied.

Another chapter shows the fabrication and testing of such a structure. All processing steps are described including fabrication and characterisation of single crystal diamond membranes as well as patterning of photonic and phononic crystal structures with focused ion beam milling and reactive ion etching. The optical characterisation of the resulting structures is shown and challenges with respect to an experimental application are identified.

The practical implications of the results of this work are evaluated in a detailed discussion. The performance of the integrated diamond structure is analysed based on results from numerical modelling and from the fabricated samples. This allows to assess the feasibility of hybrid quantum systems in diamond architectures based on the structure presented in this work.

Chapter 2

Theoretical Background

This chapter introduces the concepts that form the basis of this work. First, the material properties of diamond are briefly shown along with an overview of different sample types and their suitability for the fabrication of photonic and phononic crystal structures. Then, all individual degrees of freedom are presented. This includes the particular features of photonic and phononic crystal structures and relevant figures of merit in the case of the optical and mechanical resonator modes. To introduce the nitrogen vacancy colour centre in diamond, its electronic properties are described and and possibilities for a targeted creation are evaluated. Then, the mutual interactions between the individual degrees of freedom are shown. The coupling between emitter and optical resonator mode is described with a focus on the Purcell regime of weak coupling. Optomechanical coupling is presented by introducing the corresponding physical formalism. In addition, the linearised description of the interaction, different coupling regimes, the sideband resolution, experimental possibilities with optically driven systems, and the nature of the interaction in the particular case of photonic and phononic crystal structures are shown. Strain coupling is described with a separate description of the interaction between the mechanical resonator mode the ground and excited state levels of the nitrogen vacancy colour centre, respectively. This includes the relevant coupling regimes and possible applications of driven strain coupled systems. To illustrate the unique possibilities the integrated structure investigated in this work offers, a hybrid interaction between all three degrees of freedom is investigated based on a theoretical model. The threefold coupling is evaluated based on a specific cooling application where energy is dissipated based on the interaction between a single nitrogen vacancy colour centre, a mechanical, and an optical resonator mode co-localised in a photonic and phononic crystal structure.

2.1 Diamond Material Properties

Diamond is among the hardest materials found in nature and its favourable optical and thermal properties make it a widely used material for technical applications. Diamond is formed by carbon atoms arranged in a tetrahedral crystal lattice. This configuration is based on an sp^3-hybridisation of carbon where each atom directly binds to its four closest neighbours. This crystal lattice provides an extraordinarily strong bond between the individual carbon atoms and determines the special material properties of diamond.

Young's modulus for single crystal diamond is as high as $E = 1050\,\mathrm{GPa}$. This makes diamond a very attractive material for applications as mechanical resonator due to the extremely high resonance frequencies that can be reached already with rather simple geometries and comparably large devices. The highly symmetric tetrahedral structure also provides isotropy for the mechanical material properties of diamond.

Single crystal diamond is a linear elastic material and the stress tensor σ is directly proportional to the strain tensor ϵ.

$$\sigma = E \cdot \epsilon \tag{2.1}$$

Diamond has a density of mass $\rho = 3515\,\mathrm{kg/m^3}$ and Poisson's ratio is $\nu = 0.1$. The longitudinal and transversal velocities of sound are $v_\mathrm{l} = 17520\,\mathrm{m/s}$ and $v_\mathrm{t} = 12820\,\mathrm{m/s}$, respectively [177].

Also the optical properties of single crystal diamond are outstanding. The strong sp^3 bonds forming the diamond structure create an indirect bandgap of 5.5 eV [178]. Due to this large bandgap, diamond is transparent from ultraviolet to infrared wavelengths with a high refractive index of $n = 2.4$ in the visible range. The large bandgap is also determining the electrical properties of diamond as semiconductor and allows the creation of colour centres, optically active defects with electronic states located in the bandgap and transitions in the visible or near infrared range [10, 69].

With respect to colour centres hosted in diamond, also other material properties are interesting. The large Debye temperature of diamond of $T_\mathrm{D} = 2200$ K leads to a comparatively small thermal phonon population even at room temperature what limits unwanted relaxation processes between defect centre spins and the surrounding diamond material [163]. In addition, due to the small spin-orbit coupling of diamond, almost no undesired spin flips occur in electronic transitions of colour centres [163].

Besides the advantageous optical and mechanical characteristics, diamond is a chemically inert material due to the strong carbon bonds. This property helps with establishing cleaning procedures and corrosion is a negligible factor for diamond samples. However, the strong resistance against chemical reactions is also a drawback as it makes nanofabrication of diamond structures very challenging.

Diamond shows good heat conductivity and low thermal expansion what is advantageous for experiments involving high optical pump powers. Experimental setups with a strong pump laser often suffer from local thermal expansion. This leads to a slight change of the geometrical shape of the structure that will persist if the heat transfer away from the beam spot is poor due to low thermal conductivity. Even very small variations of the geometric parameters can drastically shift optical and mechanical resonance frequencies of the devices investigated in this work (see sections 3.2 and 3.3). Although this effect can be exploited to switch cavities on and off resonance as demonstrated for example in reference [179], it is an unwelcome problem for most measurements.

To calculate optomechanical coupling, the photoelastic constants of diamond are relevant. This is a measure of how much the refractive index is changed when a material is strained. For single crystal diamond, the photoelastic constants are $p_{11} = -0.277$, $p_{12} = 0.058$, and $p_{44} = -0.171$ according to literature [180, 181]. The expected photoelastic effect in diamond is large as high photoelastic constants also allow for a strong interaction as can be seen based on the formulas shown in section 2.6.6. The values for diamond are considerably higher than those of other commonly used materials like silicon, gallium phosphide, gallium arsenide or aluminium nitride [180, 182, 183].

Not only single crystal diamond is used for the implementation of quantum systems, but there are many applications that employ polycrystalline diamond. Due to better optical and mechanical properties, single crystal diamond is preferred over polycrystalline samples. Polycrystalline diamond partly contains graphite-like sp^2-hybridised carbon at grain boundaries, a significantly weaker bond type. This can reduce Young's modulus down to half of the value for single crystal diamond [178, 184]. In addition, most polycrystalline samples suffer from very high optical losses at the grain boundaries as the black graphite-like material strongly absorbs light in the visible spectrum and colour centres often do not show fluorescence as the luminescent charge state is not stable in that case. Therefore, this work is only based on single crystal diamond.

Besides the crystal quality, also the orientation of a single crystal diamond sample is important. Currently, single crystal diamond samples with polished surfaces corresponding to a (100), a (110) or a (111) plane in terms of crystallographic orientation are available [88, 185, 186]. The most common (100) type samples stem from standard chemical vapour deposition (CVD) growth process and profit from a very smooth surface as polishing is easier for this surface orientation. However, a (111) surface orientation is favourable for some applications. Colour centres incorporated in the diamond material can then be oriented perpendicular to the surface and the corresponding dipole orientation allows for very efficient collection of the emitted radiation. However, this sample type is very rare as it is more challenging to polish and the resulting surface roughness remains poor compared to (100) oriented samples.

2.2 Optical Resonator: Photonic Crystal Cavity

Optical resonators consist of a structure where light can circulate so that an optical excitation is maintained longer than in free space. The principle of an optical resonator can best be described by a so-called Fabry-Pérot resonator, a set of two parallel mirrors in between which light is reflected. This leads to the formation of standing waves inside the resonator and thus a restriction to confined optical modes. This simple example of an optical resonator is shown in figure 2.1. The characterising parameters of optical
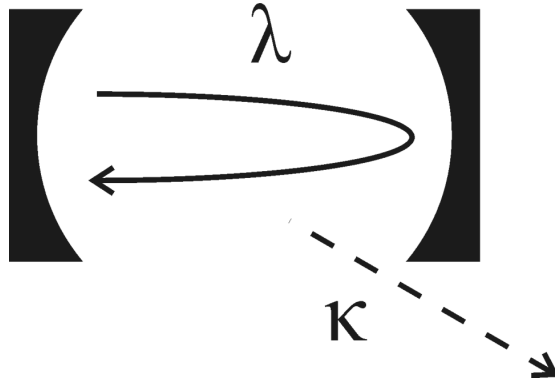
Figure 2.1: Principle of an optical resonator. A cavity mode with optical wavelength λ circulates inside the resonator and is subject to losses described by the decay rate κ.

resonators are the resonance frequency ω_{opt} or as alternative the optical wavelength λ, the mode volume V_{opt} describing the spatial confinement, as well as the quality factor Q_{opt} or the decay rate κ describing the temporal confinement of the optical mode. In the case of a Fabry-Pérot resonator, ω_{opt} corresponds to the constructive interference condition, V_{opt} to the resonator size mainly determined by its length, and Q_{opt} is a measure for the storage time in the system. For most experiments, the desired wavelength has to be adjusted to the application of the optical resonator like for example coupling to the specific transition of an emitter (see section 2.5). For most experiments,

the quality factor should be rather high so that losses are minimised and the optical excitation is stored in the resonator for a longer time. This increases interaction possibilities and gives a clear signature in the measurement spectrum. In general, small modal volumes are desirable so that stronger local field intensities can be reached. A strong spatial localisation increases the interaction cross-sections for various couplings like for example Purcell enhancement or optomechanical interaction. However, a strong mode confinement can often only be reached at the price of significantly lower quality factors and a compromise needs to be found.

2.2.1   Optical Resonator Types

There are various different systems functioning as optical resonators [187]. Classical Fabry-Pérot resonators are typically used to increase optical emission from atoms or ions in traps [188]. These resonators are very flexible as the resonance frequency can be adapted by varying the resonator length, but at the same time mode volumes are by orders of magnitude larger than a cubic wavelength. Fabry-Pérot resonators are not based on a resonator material what is an advantage for the interaction with trapped atoms or ions. However, it can be a drawback for the assembly of integrated systems where a monolithic approach is more promising. This problem can be overcome by inserting a small amount of the desired medium, for example nanodiamonds containing colour centres, into a Fabry-Pérot resonator. However, the large modal volumes imply very small interaction cross-sections. While Fabry-Pérot resonators are not suited for on-chip-devices, they can still be integrated with other systems when using fibre-based resonators [189]. Here, the end facets of optical fibres are curved and coated with mirror layers so that small mode volumes in the range of few ten cubic wavelengths can be reached [190]. Thus, Fabry-Pérot resonators are very flexible but less suited when a monolithic approach is favored or when a strong spatial confinement of the optical mode is required.

Another resonator type are spherical dielectric objects where light is confined to a circular trajectory by total internal reflection on the material surface. The resulting mode shape is also named whispering gallery mode and resembles a bended waveguide mode. Depending on the overall size of the device, a considerable fraction of the confined light is guided outside the resonator material in so-called leaky modes. There are different geometries like spheres [191], toroids [192], disks [193], or rings [194] that have been fabricated on the nanoscale level in order to achieve a strong spatial confinement of the optical resonator field. Also more specialised approaches have been tested like manufacturing so-called bottle resonators from optical fibres that are designed such that cavity modes can travel along the fibre circumference perpendicular to the fibre axis [195]. The resonance wavelength of all whispering gallery modes is determined by the dielectric constant of the resonator material, the circumference of the resonator, and the particular shape. In experiments, relatively high quality factors can be obtained. Losses are mainly caused by surface roughness and the radiation of leaky modes. The modal volumes are moderate by design and typically reach few ten cubic wavelengths. The fact that whispering gallery modes are confined in the dielectric material can be exploited for the interaction with other degrees of freedom like coupling to incorpo-

rated colour centres [46] or optomechanical interaction with vibrational modes of the resonator [196].

A very different approach is the use of photonic crystal cavities where the resonator is created by a photonic band structure that is engineered by a patterned dielectric medium. The confined light is restricted to allowed photonic states what gives rise to highly symmetric cavity modes. The resonance frequency can be scaled both by the refractive index of the dielectric material, and the overall size of the structure. The optical mode volume typically is in the range of the cubic wavelength and the spatial confinement in photonic crystal cavities surpasses that of all other resonator types. As in the case of whispering gallery mode resonators, the optical mode is confined in the dielectric material. This allows for interaction with incorporated colour centres [42] or phononic modes co-localised in the same structure [156]. Photonic crystal cavities can be designed with very high quality factors. However, a precise patterning of the designed structure is absolutely crucial for minimising losses and high experimental quality factors could only be reached with common semiconductor materials where sophisticated fabrication techniques are available [197]. As technical improvements on this field are to expect for diamond as well, photonic crystal cavities have the potential to provide optical resonator modes with a very strong confinement in space and time.

When cavity modes are propagating inside the resonator as it is the case for whispering gallery and photonic crystal modes, possible cavity materials have to be transparent in the desired wavelength range. Commonly used semiconductor materials like silicon, gallium arsenide, and silicon nitride are transparent only in the infrared domain. They show very good results when exploited for telecom wavelengths around $1310\,\mathrm{nm}$ or $1550\,\mathrm{nm}$, but for application in the visible or near infrared range only few materials like silicon dioxide, silicon carbide, and diamond are available. For the interaction with two-level systems, diamond is particularly well-suited as colour centres can directly be created inside the structure.

2.2.2 Photonic Crystal Cavities

Photonic crystal resonators are based on the principle of band structure engineering. The periodic arrangement of materials, here diamond and air, with different refractive index n creates a periodic potential for photons. Maxwell's equations can then be expressed as an eigenfunction of the electric field $\mathbf{E}$ in a source-free linear dielectric.

$$\nabla \times \nabla \times \mathbf{E} = \left(\frac{\omega_{\mathrm{opt}}}{c}\right)^2 \varepsilon \mathbf{E} \tag{2.2}$$

Here, ω_{opt} is the optical frequency, c is the speed of light, and $\varepsilon = n^2$ is the dielectric constant of the material. This equation can be fulfilled by Bloch modes that establish a photonic band structure inside the periodically patterned material. These are guided modes with a characteristic mode shape where only the first two photonic bands are relevant for the design of photonic crystal cavities. The lowest order photonic band is called dielectric band as the maximum of the electric field is located in the dielectric material. In the second band, the air band, the maximum of the electric field is concentrated in the air holes.

Often, photonic crystal cavities are not fully three-dimensional structures and the periodic pattern is only extending in one or two directions of space. The Bloch modes are then confined in the other directions by total internal reflection at the material borders, so-called index-guiding. Typical geometries based on this principle are slab structures where a diamond membrane is patterned with a two-dimensional photonic crystal or where airbridge structures containing a line of regularly spaces holes are designed. The radiation losses perpendicular to the photonic crystal plane attributed to non-perfect index guiding can be described by the light cone, an area in the first Brillouin zone. This area is defined as the space above the light line, a line through the origin whose steepness corresponds to the index contrast between air and the cavity material. All contributions within the light cone correspond to radiation losses. Although the choice of a high index material is in general favourable for keeping out-of-plane losses small, this cannot always be respected when other material properties are strictly required for a particular experiment. This is the case for the hybrid structure studied in this work as high photoelastic constants, the presence of colour centres, and transparency in the visible wavelength range make diamond the only possible material for the desired architecture.

To localise an optical cavity mode, the perfect periodicity of the photonic crystal structure has to be disturbed by introducing a defect. This can be done by two fundamentally different approaches: air defects are created when less material is present in the centre of the cavity than in the surrounding photonic crystal structure, whereas dielectric defects are created when excess dielectric material is used in order to localise the photonic mode. Dielectric defects create modes arising from the air band while air defects create modes arising from the dielectric band. The lower resonance frequencies of localised modes arising from the dielectric band result in a smaller overlap with the light cone compared to modes arising from the air band. Therefore, optical cavity modes based on the dielectric band should be preferred when high quality factors are to achieve as they usually show a better mode confinement by design as will also be discussed in section 3.2.2.

Two-dimensional photonic crystal resonators have widely been studied and various different ways to introduce a defect have been proposed. In the most basic structures, a defect can be based on simply leaving out one or more holes [198, 199]. Alternatively, a gentle confinement approach can be chosen where the size or position of selected holes is varied [39, 200–202]. In the most common designs, a combination of missing and altered holes forms the photonic crystal cavity [37, 38, 203–207]. Most of these studies focus on the purely phenomenological reduction of out-of-plane losses that can be achieved by adapting the innermost holes. However, there are some more theoretical studies revealing that other effects like the phase matching with the reflected wave, an optimal penetration depth into the mirror cladding, and a decrease in the group velocity of the mode can significantly improve the confinement of a photonic crystal mode [208–211]. These aspects are merged in an inverse approach where the desired cavity field is the basis for establishing the precise structure of the resonator [212, 213]. In order to minimise losses, the envelope of the optical resonator mode's electrical field should have a Gaussian shape and with a Fourier transform, relevant design criteria that define the optimal resonator structure can be identified.

In another design approach, a complete row of holes is left out in order to form a waveguide and a defect is introduced by locally varying the photonic crystal pattern. This can either be done by varying the lattice constant in steps, ranging from simple designs with only two areas to more sophisticated designs where the lattice parameters are varied gradually [34,36,199,214–217], or by changing the position or diameter of few holes in the centre of the waveguide [35,203,218–220]. There is also a special application of this principle where the holes of a completely homogeneous photonic crystal forming a waveguide are locally filled with liquid such that the resonator can be tuned by the refractive index of the liquid and the area in which it is dispensed [221].

Also one-dimensional photonic crystal resonators can be formed in a variety of ways. What they all have in common is that they are based on an airbridge structure where index guiding is confining the resonator mode in two dimensions and the photonic crystal pattern only consists of a single line of holes. The most simple design is a row of holes with a slightly increased so-called defect spacing between the innermost holes of the structure [222, 223], possibly also combined with an additional width modulation of the airbridge [50]. A resonator mode can alternatively be localised when the spacing between the innermost holes is reduced and thus an air defect is created [41]. As in the case of two-dimensional structures, a taper section is frequently introduced where the hole diameters and spacings are adapted in a gentle confinement design [224–228].

However, in the case of one-dimensional photonic crystal structures, the inverse design approach is the most commonly used method. Some geometries maintain a constant ratio of hole diameter to spacing and introduce a modulation by varying their absolute values, either with larger holes diameter and spacing in the centre [229], or the opposite [40, 230]. Alternatively, the lattice spacing can be kept constant and a modulation of the hole size creates a resonator, again either with smaller holes in the centre forming a dielectric defect [220] or the opposite with larger holes in the centre creating an air defect [231–233]. The latter option is more advantageous as the resulting mode arises from the dielectric band what helps with reducing losses from poor index guiding. Therefore, this type of photonic crystal structure is investigated in this work. Alternatively, a defect can be created using a modulation in the hole spacing rather than in the hole size [234], elliptical holes whose width decreases linearly from the centre [235], or even a geometry where both the lattice constant and the hole size and shape are varied gradually [236].

Depending on the type of defect introduced, cavity modes can either be localised inside the band gap of the surrounding photonic crystal (band gap effect) or at a band edge where propagation is only allowed within the defect region (mode gap effect). This distinction is mostly relevant for theoretical considerations as both principles can be exploited to design well-localised optical modes with good spatial and temporal confinement. Utilising designs based on the mode gap effect has the advantage that only cavity modes with the well-defined symmetry condition imposed by the corresponding guided mode can be localised inside the photonic crystal structure. More interesting for the properties of the resulting cavity modes is whether the defect is arising from the dielectric band or from the air band. Cavity modes arising from the dielectric band have the maximum of the electric field located inside the dielectric material. This is not only advantageous for reducing radiation losses to the light cone, but also interactions like

optomechanical or the coupling to colour centres are stronger when the field intensities are maximal in the bulk of the material as discussed in sections 2.6 and 2.5, respectively. Other types of interaction which are not subject to this work, like for example the coupling to single atoms in vacuum brought close to photonic crystal cavities, would profit from modes arising from the air band.

2.2.3   Figures of Merit for the Optical Resonator

The spatial confinement of an optical cavity mode can be expressed in terms of the effective mode volume V_{opt}. This is a measure for the spatial extent of a particular cavity mode localised by an arbitrary optical resonator structure.

$$V_{\text{opt}} = \int \frac{\varepsilon |\mathbf{E}|^2}{\max\left(\varepsilon |\mathbf{E}|^2\right)} dV \tag{2.3}$$

A smaller mode volume indicates a stronger spatial confinement of the cavity mode. This is particularly important for interactions with other degrees of freedom as it can be translated in a maximal confined field intensity. This is relevant for both the Purcell enhancement of a single emitter where a large overlap between the optical mode and a dipole is required, and optomechanical coupling where the interaction strength is determined by the overlap integral of the optical and the mechanical cavity mode.

The quality factor Q_{opt} defines the temporal confinement of the mode and can be expressed in terms of the fraction of energy that is dissipated per optical cycle.

$$Q_{\text{opt}} = 2\pi \times \frac{W_{\text{opt,tot}}}{\Delta W_{\text{opt}}} \tag{2.4}$$

Here, $W_{\text{opt,tot}}$ is the total energy stored in the optical cavity mode and ΔW_{opt} the radiation energy lost per oscillation cycle. Alternatively, losses can directly be derived from equation 2.2 by considering that the frequency ω_{opt} is a complex number whose real part defines the optical mode frequency and whose imaginary part indicates losses. The optical quality factor Q_{opt} can then be found by comparing the real and imaginary parts of the optical mode frequency ω_{opt}.

$$Q_{\text{opt}} = \left| \frac{\text{Re}\left(\omega_{\text{opt}}\right)}{2 \cdot \text{Im}\left(\omega_{\text{opt}}\right)} \right| \tag{2.5}$$

In a more practical approach, the quality factor also defines the spectral width $\Delta\lambda_{\text{opt}}$ of a cavity mode with optical wavelength λ_{opt}.

$$Q_{\text{opt}} = \frac{\lambda_{\text{opt}}}{\Delta\lambda_{\text{opt}}} \tag{2.6}$$

Optical modes with high quality factors do not only show a better temporal confinement but are also advantageous with respect to practical considerations. As their spectral signal is narrower, good filtering can help to select the resonator mode from a background what allows to eliminate some noise from the measurement.

While the quality factor is a very intuitive measure, the decay rate of photons from the optical resonator is the more commonly used parameter to describe the temporal confinement of the cavity mode. The decay rate κ is the inverse of the cavity lifetime τ_{opt}, the average time photons spend in the cavity mode before they decay from the resonator.

$$\kappa = \frac{1}{\tau_{\mathrm{opt}}} \equiv \Delta\omega_{\mathrm{opt}} = \frac{2\pi c}{\lambda Q_{\mathrm{opt}}} \tag{2.7}$$

The cavity field decay rate κ is directly linked to its spectral width $\Delta\omega_{\mathrm{opt}}$. An additional contribution can be the external decay rate κ_{ext} that originates from losses at the in- and out-coupling of the cavity as for example shown in section 3.2.3 for a grating coupler structure. The external decay rate of an optical resonator determines its performance in experimental schemes where the cavity mode is populated by a pump laser.

The average steady state photon population inside a resonator pumped with an excitation laser denoted $\overline{n}_{\mathrm{opt}}$ is given by the following relation.

$$\overline{n}_{\mathrm{opt}} = \frac{\kappa_{\mathrm{ext}}}{\Delta^2 + (\kappa/2)^2} \frac{P_{\mathrm{L}}}{\hbar\omega_{\mathrm{L}}} \tag{2.8}$$

Here, ω_{L} is the laser frequency, $\Delta_{\mathrm{L}} = \omega_{\mathrm{L}} - \omega_{\mathrm{opt}}$ is the detuning between the laser and the resonator mode, and P_{L} is the laser power. The photon population of the cavity is highest for a strong pump laser that is efficiently coupled to a high-quality cavity and exactly matches the resonator frequency. In reality, however, the in- and out-coupling is the weak link in the excitation and detection path. In that case, the resonator is considered over-coupled as the external decay rate κ_{ext} associated with coupling losses is large compared to the intrinsic decay rate of the optical resonator κ. Exploiting the relation between the effective photon population of the optical resonator and the Laser input power[1], the photon occupation number of the optical resonator mode can then be expressed as

$$\overline{n}_{\mathrm{opt}} = \frac{\kappa_{\mathrm{ext}}}{\Delta^2} \frac{P_{\mathrm{L}}}{\hbar\omega_{\mathrm{L}}} \tag{2.9}$$

Overcompensating the losses associated with in-coupling of light into the optical resonator with an even stronger pump power potentially gives rise to new unwanted effects as for example a bistability of the mechanical resonator in the Doppler regime of optomechancial coupling (see section 2.6.5). Thermal population does not play a role in the case of optical cavity modes as the required photon energies are clearly surpassing the thermal energy provided by a realistic bath temperature.

---

[1]Without loss of generality a single-sided cavity is considered in order to simplify the expression.

2.3   Mechanical Resonator: Phononic Crystal Cavity

Mechanical resonators consist of a structure susceptible to mechanical excitation that can perform an oscillating movement. The most simple case is a spring where a mass attached to one of its ends performs an oscillating movement as shown in figure 2.2. Any mechanical resonator can be characterised by the same set of parameters: the os-
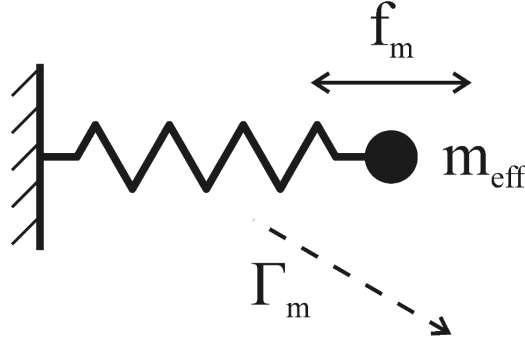
Figure 2.2: Principle of a mechanical resonator. A mass m_{eff} oscillates at frequency f_{m} and is subject to losses described by the damping rate Γ_{m}.

cillation frequency ω_{m}, typically also expressed as $f_{\mathrm{m}} = \omega_{\mathrm{m}}/2\pi$, the effective mass m_{eff} contributing to the movement, and the quality factor Q_{m} or as alternative the damping rate Γ_{m} describing the temporal confinement of the mechanical resonator mode. The most basic physical system to describe a mechanical resonator is an elastic spring, but there is a broad variety of mechanical resonator types. Different materials and geometries are used in order to meet the requirements for numerous applications ranging from standard sensing techniques [18–21, 23, 24], over mechanical memories [17], to fundamental quantum science [133, 139, 140, 142, 162]. Downscaling the entire system is desirable for many applications in order to access quantum effects or reaching higher resonance frequencies [100, 103, 237]. The most interesting property as compared to other degrees of freedom is, that in the case of mechanical resonators even the quantum regime can be reached with relatively large and massive objects in the size range of several microns [133, 162].

2.3.1   Mechanical Resonator Types

For micro-mechanical applications, the most commonly used resonator geometries are suspended cantilevers [59, 62], doubly-clamped beams [60, 133], and membranes or mirrors moving as a whole [125, 141]. These systems are relatively easy to fabricate and their mechanical motion can be described analytically. Downscaling is important with regard to the aims of reaching higher frequencies, developing extremely sensitive detectors, and observing quantum effects. Therefore, more sophisticated fabrication techniques have been developed and even unconventional approaches like using single carbon nanotubes as oscillators are pursued [237].

Other than by downscaling, higher resonance frequencies can also be achieved when using materials with a higher Young's modulus. Many approaches use common semiconductor materials like silicon [17–19, 135, 139, 140, 238–240] or silica [150, 196, 241] in order to profit from standard processing techniques that are available from chip fabrication. Few work exists on structures fabricated from other semiconductor materials like aluminium nitride [145, 242, 243] or indium phosphite [155, 244]. Aluminium nitride has the advantage of showing high piezoelectric constants that allow for direct actuation with the help of electric fields. The mechanical mode can then be addressed by applying electrical voltages resulting in a linear response of the device instead of relying on other more indirect methods like magneto-motive, capacitive, or optical excitation [242]. Very often silicon nitride is used in order to achieve higher resonance frequencies due to its high Young's modulus of $300\,\mathrm{GPa}$ and the possibility to further increase the resonance frequency of mechanical oscillators by using pre-strained samples [133, 245, 246]. Also diamond, the material with the highest known Young's modulus, is used with the intention to create mechanical resonators at even higher frequencies. Due to the better availability of polycrystalline diamond samples, this material is widely used [54, 56, 57, 157, 158] although its Young's modulus is significantly lower compared to monocrystalline samples [184]. Many different mechanical resonators with rather simple geometries have been fabricated from single crystal diamond in the last years [52, 58–60, 62, 63, 173, 174, 247]. However, fabricating tiny structures in diamond remains a challenging task and thus diamond nanomechanical resonators are still far from being available as standard devices ready for application.

A different strategy to achieve high resonance frequencies up to the gigahertz regime is to design completely different resonator types. Innovative geometries allow for a very strong spatial confinement of a mechanical resonator mode at high frequencies. However, this improvement can only be realised at the price of considerable modelling efforts and more advanced fabrication techniques. Nanodome resonators [58], fish-bone structures [57], and two-dimensional arrays of circular or square paddles [56] have been fabricated from diamond. Resonators with rotational geometry that show various radial and flexural modes can achieve even smaller effective masses than classical and the above-mentioned geometries. Different appearances including microtoroids [196], microrings [243], microdisks [63, 146, 248], and microspheres [241] exploit this principle.

The highest resonance frequencies, up to the GHz range, and an even stronger spatial confinement of the mechanical oscillation can be achieved with phononic crystal cavities. In complete analogy to the photonic crystal structures presented in the previous section, these structures follow the same principle based on the mechanical instead of the optical properties. The esulting mechanical resonators are based on a so-called phononic band gap material consisting of a periodically patterned material that does not allow for the propagation of mechanical modes [249, 250]. Localised modes can be confined when a defect region is surrounded by such a periodic lattice structure [67, 68]. Alternatively, the geometric parameters can be varied gradually to achieve an equally strong mode confinement through mechanical band structure engineering [251]. As these structures follow a meta-material approach where the shape of a device determines its properties, they can be scaled to match any desired frequency. This allows for various different applications ranging from sonar to thermal resonators [252]. The very small mode

volumes and the resulting strongly localised mechanical oscillations reached in these structures allow for entering the quantum regime of mechanical motion [139,140]. They also increase interaction cross-sections for optomechanical coupling, strain coupling, and electromechanical interaction due to very strong localised strain fields [234].

2.3.2   Phononic Crystal Cavities

A phononic crystal is based on a periodic arrangement of materials with different elastic properties. This regular pattern creates a phononic or acoustic band gap in a very similar way as an electronic band gap is formed in solids or an optical bandgap in photonic crystals. Also here, the regular pattern is on the order of the wavelength of the quasi-particle phonon. This periodic variation of the elastic properties can, for example, be achieved with regularly spaced air holes in a material slab, or a layered system consisting of different materials. The equation of motion inside a phononic crystal structure can be written as an eigenfunction of the mechanical displacement $\mathbf{u}$.

$$\nabla\left(\underline{\mathbf{C}} : \nabla_\mathrm{s}\mathbf{u}\right) = -4\pi^2\rho f_\mathrm{m}^2\mathbf{u} \tag{2.10}$$

Here, $\underline{\mathbf{C}}$ is the fourth order elasticity tensor only being dependent on Young's modulus E and Poisson's ratio ν in an isotropic medium. An alternative complete description can be based on the longitudinal and transversal velocities of sound in a medium v_l and v_t, respectively. ρ is the density of mass for the diamond material, f_m the phonon frequency, the colon denotes a double scalar product, and $\nabla_\mathrm{s} = \left(\nabla + \nabla^\mathrm{T}\right)/2$ is the symmetric gradient operator with ∇^T being the transposed differential operator. An acoustic or phononic band structure is created confining phonons to specific modes with defined frequencies and distinct mode profiles and the solution to equation 2.10 is a Bloch mode type for the mechanical displacement field $\mathbf{u}$. If the band structure is engineered by adapting the geometric parameters of the phononic crystal in a suitable way, acoustic band gaps can be formed.

Complete phononic band gaps can only be reached in two- or three-dimensional phononic crystals as the propagation of the mechanical resonator mode is strongly suppressed in these structures. In one-dimensional phononic crystals, as considered in this work, band gaps can only be established for selected symmetries of the mechanical modes. The phononic crystal pattern inhibiting the propagation of a mechanical excitation in only one direction of space does not allow for a complete suppression of acoustic wave propagation for several symmetry conditions in a single structure. The symmetry of the mode with respect to the phononic crystal structure characterises the oscillation pattern and possible interactions with other degrees of freedom. For the confinement of high quality mechanical modes with a given symmetry, a band gap for one symmetry condition is sufficient. As in the case of optical resonator modes, one-dimensional photonic and phononic crystal structures cannot create full bandgaps for modes of arbitrary symmetry conditions. For one-dimensional structures, the symmetry along the periodicity axis cannot clearly be determined to even or odd. However, modes can be distinguished into arising from the Γ-point or from the X-point in the first Brillouin zone of the phononic crystal, corresponding to even and odd symmetry, respectively (see sec-

tion 3.3.2). Here, fully symmetric modes are chosen as they allow strong optomechanical interaction with a photonic crystal mode co-localised in the same structure.

To strongly localise phonons and thus create a confined mechanical cavity mode, the perfect periodicity of a bandgap material needs to be modulated. To this end, a geometrical defect has to be introduced to the otherwise perfectly regular pattern. In layer structures, the dimensions or materials of selected slices can be varied in order to localise a mechanical oscillation [67, 253]. In a material slab, a defect is commonly introduced by leaving away holes [68, 155, 238, 254–257], by changing the hole spacing [156, 234, 245, 251], or by a combination of a variation in hole spacing, size, and shape [140, 236, 246]. The localised mode can then only exist in a very small region of space and a propagation outside the defect region is suppressed by the surrounding bandgap material. Each localised mode has a characteristic spatial field distribution corresponding to the oscillation pattern of the propagating mode it arises from. In addition to this qualitative information, the spatial and temporal confinement of the vibration are important characteristics of a resonator mode and can be used to quantify a mechanical resonator's performance. A trade-off between the localisation of mechanical excitation in space and in time as well as a consideration of its mode shape determines the choice of a specific cavity structure.

2.3.3 Figures of Merit for the Mechanical Resonator

The spatial confinement of the localised mechanical mode can be described in terms of the effective mass m_{eff}.

$$m_{\text{eff}} = \rho \int \left(\frac{|\mathbf{u}|}{\max(|\mathbf{u}|)} \right)^2 dV \qquad (2.11)$$

The effective mass is large when a big part of material is contributing to the mechanical movement like, for example, in suspended cantilevers and small when only a very little portion of cavity material is oscillating like in the case of phononic crystal cavities. For implementing optomechanical or strain coupling, strongly localised modes are very advantageous and the effective mass should ideally be as small as possible.

As in the case of the optical resonator mode, the analogously defined mechanical quality factor Q_{m} is giving a measure for the temporal confinement of the mechanical motion. In this case, it determines the temporal confinement of the mechanical oscillation and is defined as

$$Q_{\text{m}} = 2\pi \times \frac{W_{\text{m,tot}}}{\Delta W_{\text{m}}} \qquad (2.12)$$

Here, $W_{\text{m,tot}}$ is the total energy stored in the mechanical movement and ΔW_{m} the mechanical energy lost per oscillation cycle. Alternatively, losses of the mechanical oscillator can be described by an imaginary part of the resonator frequency. The ratio between the real and the imaginary part of the oscillator frequency gives an alternative expression for the mechanical quality factor.

$$Q_{\text{m}} = \left| \frac{\text{Re}(\omega_{\text{m}})}{2 \cdot \text{Im}(\omega_{\text{m}})} \right| \qquad (2.13)$$

In a more phenomenological approach, the energy stored in the mechanical oscillation can be evaluated as a function of the excitation frequency. This generates a Lorentzian peak whose centre frequency corresponds to the resonance frequency ω_m of the mode. Losses lead to a broadening of a resonator's spectral signal with $\Delta\omega_\mathrm{m}$, the full width at half maximum of the mechanical mode's response.

$$Q_\mathrm{m} = \frac{\omega_\mathrm{m}}{\Delta\omega_\mathrm{m}} \tag{2.14}$$

A high quality factor characterises a resonator with few losses and a narrow spectral bandwidth.

The main loss channels occurring in phononic crystal cavities are clamping losses and radiation into the substrate, viscous damping due to friction at the surface, thermoelastic damping, and losses associated with less than perfect material properties attributed to two-level defects or surface termination [62, 103, 258]. Clamping losses and radiation into the substrate can be reduced through a more advanced design by adding a two-dimensional phononic structure with a complete band gap as described for example in [236]. Friction at the surface can be avoided when performing measurements in vacuum and there is evidence in literature that losses associated with two-level defects can be reduced when using samples of high crystalline quality and that losses arising from non-optimal surface termination can be mitigated just as thermoelastic damping by measuring at low temperatures [62]. The different processes are due to different physical effects and are thus independent of each other. The overall quality factor $Q_\mathrm{m,tot}$ can in this case be expressed in terms of $Q_\mathrm{m,i}$, the individual mechanical quality factors only limited by one of the above-mentioned loss mechanisms.

$$Q_\mathrm{m,tot}^{-1} = \sum Q_\mathrm{m,i}^{-1} \tag{2.15}$$

The dependence on inverse numbers indicates that a considerable suppression of the most relevant loss mechanism results in a much more significant contribution to the overall performance than a slight reduction of all losses simultaneously. The mechanical decay rate of the resonator Γ_m can be calculated on the basis of the mechanical frequency ω_m and the mechanical quality factor Q_m.

$$\Gamma_\mathrm{m} = \frac{\omega_\mathrm{m}}{Q_\mathrm{m}} \tag{2.16}$$

The inverse relation between the decay rate and the mechanical quality factor shows that devices with very high mechanical quality factors are required for experiments where the excitation should be conserved for a reasonable amount of time.

Mechanical oscillator modes can be populated thermally because the phonon energies required for this process are small compared to the energy provided by the thermal bath. The average phonon number of a mechanical resonator populated by its thermal environment $\overline{n}_\mathrm{th}$ is given as

$$\overline{n}_\mathrm{th} = \left(e^{\frac{\hbar\omega_\mathrm{m}}{k_\mathrm{B}T}} - 1\right)^{-1} \tag{2.17}$$

with $\hbar$ being the reduced Planck constant, k_B the Boltzmann constant, and T the absolute temperature of the thermal bath. In the high temperature limit, this expression simplifies to

$$\overline{n}_{th} \approx \frac{k_B T}{\hbar \omega_m} \tag{2.18}$$

A high thermal occupation number is more challenging to achieve for modes of high mechanical frequency as the per-phonon energy increases along with the oscillation frequency. This allows for cryogenic cooling close to the quantum ground state of resonators with mechanical frequencies in the range of GHz.

The rate at which the mechanical resonator undergoes an exchange with phonons from the thermal bath is also called thermal decoherence rate of the mechanical cavity mode Γ_{th}.

$$\Gamma_{th} = \overline{n}_{th} \cdot \Gamma_m \approx \frac{k_B T}{\hbar Q_m} \tag{2.19}$$

Here, the high temperature limit for the thermal phonon population number has been exploited. This means that in addition to the mechanical decay rate of the resonator Γ_m caused by damping losses, the coupling to the thermal bath induces a further source of decoherence. This formula also confirms that although the coupling to the thermal environment can help with reaching high phonon occupation numbers, it is at the same time a source of decoherence. Measurements should thus be performed at very low temperatures if decoherence is an issue for the particular experiment or alternative measurement techniques should be used like for example pulsed optomechanical interaction that still allows the detection of quantum effects from a thermal state [153].

High quality factors help with keeping the thermal decoherence low even if a thermal population of the mode is needed. Therefore, the product $Q_m \times f_m$ can be considered a figure of merit for the decoupling of the mechanical oscillator mode from the thermal bath. The number of coherent oscillations N_{osc} in the presence of thermal decoherence is given as

$$N_{osc} = \frac{\omega_m}{\overline{n}_{th} \Gamma_m} = Q_m \times f_m \cdot \frac{h}{k_B T} \tag{2.20}$$

The product $Q_m \times f_m$ should thus be considerably larger than $k_B T / h$ so that coherent oscillations can take place before thermal effects dominate the dynamics.

With the increasing interest in exploiting a mechanical degree of freedom, a large variety of resonator types, materials and dimensions is being investigated. To allow for a meaningful comparison between the individual devices and their corresponding figures of merit, a universal scaling is necessary. The zero point fluctuation x_{ZPF} corresponds to the mechanical displacement of the resonator upon excitation of a single phonon.

$$x_{ZPF} = \frac{1}{2\pi} \sqrt{\frac{h}{2 m_{eff} f_m}} \tag{2.21}$$

All kinds of mechanical resonators including differently sized phononic crystal cavities can be scaled to a movement per single phonon based on the zero point fluctuation. Their performance can then be compared without overrating large cavities due to macroscopic displacements that are impossible to achieve in smaller cavities. In the case of phononic

crystal resonators, the zero point fluctuation corresponds to the maximal local elonga-
tion of the structure for a single phonon excitation. A higher population of the phonon
states would increase the elongation of the resonator. The opposite is also true and me-
chanical driving of the resonator increases the phonon population. The phonon number
in the mechanical mode is then increased accordingly and the maximal local elonga-
tion of the structure $\max\left(|\mathbf{u}|\right)$ determines the phonon number inside the mechanical
resonator.

$$\overline{n}_{\mathrm{m}} = \frac{\max\left(|\mathbf{u}|\right)}{x_{\mathrm{ZPF}}} \tag{2.22}$$

In the case of a passive mechanical resonator that is only subject to thermal effects,
the phonon population of the mechanical resonator mode $\overline{n}_{\mathrm{m}}$ coincides with the thermal
population number $\overline{n}_{\mathrm{th}}$.

2.4   Nitrogen Vacancy Colour Centre in Diamond

Electronic transitions in two-level systems are commonly used as internal degree of free-
dom for quantum applications and there is a large variety of different systems available
for this purpose [8]. Both the ability to generate single photons and a function as
quantum bit make two-level-systems the centre piece in most proposals for quantum
networks. In the following, different systems are presented and their suitability for both
an application as single photon source and as quantum bit is discussed.

The most obvious choice for this internal degree of freedom is an isolated atom or
ion where the discrete electronic levels are linked via optical or microwave transitions.
This interaction with photons can be used for storage, control and read-out of informa-
tion what has been exploited for the demonstration of quantum information processing
like quantum cryptography and qubit operations. In contrast to most other systems
exploited as internal degree of freedom, they interact only weakly with the environment
what assures very long coherence time but makes them less suitable for applications
where the interaction with other degrees of freedom is required. Trapped atoms and
ions are not ideal for the use in practical applications as the required traps are very com-
plex setups. In addition, many experiments cannot be performed with these systems as
their electronic properties cannot be engineered. While the well-defined level structure
of individual atoms or ions offers many advantages for proof-of-principle demonstra-
tions, different types of solid state two-level-systems are investigated for an application
as single photon source or quantum bit [10, 31].

Superconducting Josephson junctions are very interesting candidates for the applica-
tion as quantum bit [259]. Very low dissipation assures reasonably long coherence times
and also complex circuits can be microfabricated with standard techniques providing
good scalability. Josephson junctions show a highly non-linear response what allows for
single microwave photon operation and provides non-degenerate energetic states with
transitions in the microwave spectrum. Superconducting circuits are a very promis-
ing platform for the application as computational qubit due to their fast processing
capabilities. However, moderate coherence times and the required cooling to very low
temperatures limits their field of application.

Quantum dots are engineered semiconductor structures where a spatial confinement in the order of the desired wavelength gives rise to a discrete energy states for electrons [10]. They typically show emission in the near infrared spectrum that can further be fine-tuned through charge control. As their properties can be engineered by adopting the choice of materials, the size, and shape of the structures to the desired application and because electrical pumping is possible, quantum dots are very suitable for practical applications. However, their complex electronic level structure is far from a pure two-level system and higher excitations cannot be ignored.

Another type of two-level systems are defect centres in crystals. They can be considered as artificial atoms trapped in the crystal lattice with a discrete electronic level structure within the bandgap of the host material. As diamond has a very large optical bandgap of $5.5\,\text{eV}$ it is an ideal carrier for defect centres [33]. There is a broad variety of colour centres in diamond with emission in the visible and near infrared spectrum [260]. Their outstanding property with respect to practical application is that their spin states can be controlled at ambient conditions without need for vacuum or cooling. For optical interfacing, however, strong cooling is still required to achieve good properties. As colour centres are embedded in the bulk of the material, an integration to circuits is possible. While the interaction with the surrounding crystal lattice can facilitate the interaction with other degrees of freedom like for example strain coupling to a mechanical oscillation, it can also be a source of noise when for example charge fluctuations or thermal effects degrade the properties of the colour centre.

In the following, only the negatively charged nitrogen vacancy (NV^-) colour centre in diamond will be considered [261]. It is the most-studied colour centre in diamond with an optical emission at $637\,\text{nm}$. Its unique electronic level structure makes it suitable for a wide range of applications ranging from quantum information technologies to sensing applications like the detection of electromagnetic fields or imaging of biological samples [69, 70, 262, 263]. There is a large number of experimental protocols to control both the spin states through microwave fields, the radiative transitions with light fields, and to exploit the interaction with nuclear spins. The long coherence times of the electronic spin together with the ability to couple to long-lived nuclear spins make the negatively charged nitrogen vacancy colour centre in diamond an outstanding two-level system for quantum information processing [264].

2.4.1 Structure of the Nitrogen Vacancy Colour Centre

The nitrogen vacancy colour centre in diamond is formed by a substitutional nitrogen atom and an adjacent vacant lattice position perturbing the otherwise perfect crystal structure of the carbon atoms. This configuration is depicted in figure 2.3(a). The nitrogen vacancy colour centre is thus always aligned along an equivalent [111] axis with respect to the crystallographic coordinates. In the tetrahedral lattice structure of diamond, this corresponds to four possible orientations. A suitable coordinate system describing the nitrogen vacancy centre can be defined as $x = 1/\sqrt{2}\,[\bar{1}10]$, $y = 1/\sqrt{6}\,[\bar{1}\bar{1}2]$, and $z = 1/\sqrt{3}\,[111]$ according to literature [265] as will also be shown in section 3.1.5. The tetrahedral diamond lattice imposes a C_{3v} rotation symmetry to the nitrogen vacancy colour centre due to the nearest neighbour configuration of the carbon atoms.
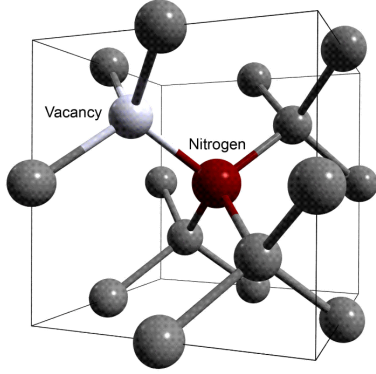
(a) Tetragonal diamond lattice with embedded nitrogen and adjacent vacant lattice position.
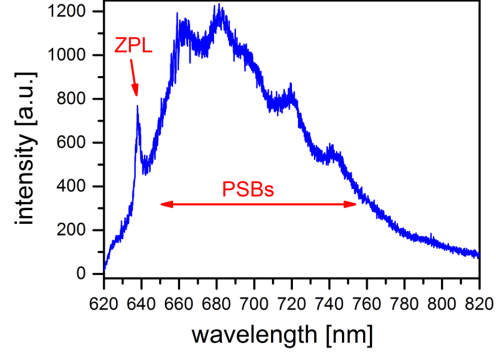
(b) Emission spectrum of the nitrogen vacancy colour centre with zero phonon line at 637 nm and a broad phononic sideband.

Figure 2.3: Crystallographic structure (a) and optical emission spectrum (b) of the nitrogen vacancy colour centre in diamond. Both figures taken from reference [266].

The emission of the nitrogen vacancy colour centre is shown in figure 2.3(b). In measurements at cryogenic temperatures, the zero phonon line at 637 nm appears much more prominent in the optical spectrum than at room temperature as it becomes narrower what also increases the peak intensity. Besides the zero phonon line, there is a large vibronic sideband spectrum characterising the nitrogen vacancy colour centre emission. The coupling to lattice phonons gives rise to a spectral signature on the long wavelength side of the zero phonon line. This process can be described by a Huang-Rhys-model where equidistant vibronic levels with energies slightly above the ground state represent the interaction with lattice vibrations [261, 267].

The charge state of the nitrogen vacancy colour centre defines its electronic properties and thus also its emission properties. This work focusses on the more commonly employed negatively charged nitrogen vacancy colour centre. It is stable in the crystal lattice and other charge states can be converted into the negatively charged state by a suitable optical pumping scheme. In the following, the term nitrogen vacancy colour centre always describes the negative charge state.

2.4.2   Electronic Properties of the Nitrogen Vacancy Colour Centre

The electronic level structure of the negatively charged nitrogen vacancy colour centre at room temperature is depicted in figure 2.4. The left hand side of the schematic shows the triplet states whereas the right hand side shows the singlet states. The splitting between the different degenerate triplet levels with zero and non-zero spin projection are caused by a crystal field splitting of 2.88 GHz and 1.43 GHz in the ground and excited state, respectively [268–270]. The decay from the excited to the ground state
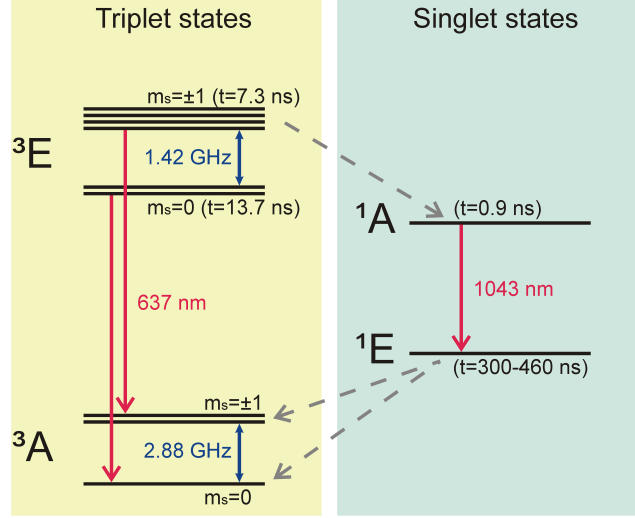
Figure 2.4: Electronic level scheme of the negatively charged nitrogen vacancy colour centre in diamond at ambient conditions. The level splittings due to spin-spin-interaction are depicted with blue arrows, the optical transitions with red arrows, and non-radiative decays with dashed grey arrows.

triplet gives rise to the optical emission at $637\,\text{nm}$ that is used for most applications of the nitrogen vacancy colour centre.

The degenerate excited triplet state with $m_s = 0$ can only directly decay to the ground triplet state via an optical transition with a lifetime of $t_{m_s=0} = 13.7\,\text{ns}$ whereas the excited triplet states with $m_s = \pm 1$ have a shorter lifetime of $t_{m_s=\pm1} = 7.3\,\text{ns}$ [271]. This deviating lifetime indicates that there is another decay channel besides the optical transition to the ground state and the doubly degenerate excited states have indeed a non-radiative decay channel to the excited singlet state with a lifetime of $0.9\,\text{ns}$ [272]. The decay of the excited singlet state is a radiative decay with an emission wavelength of $1043\,\text{nm}$ [272]. The ground singlet state has a lifetime of approximately $150 - 460\,\text{ns}$ depending predominantly on the temperature. This metastable state eventually decays to either one of the triplet ground states [272,273].

This spin-dependent inter-system crossing is an important property of the nitrogen vacancy colour centre and can be exploited experimentally for an optical detection of the spin state. The ground state levels can experimentally be distinguished into a dark state corresponding to $m_s = \pm 1$ and a bright state corresponding to $m_s = 0$. The reason is that an optical excitation will result in a much stronger optical emission into the zero phonon line at $637\,\text{nm}$ for a population in the $|0\rangle$ ground state as this is the only decay channel in that case. A population of the $|\pm1\rangle$ ground state results in a reduced intensity of the zero phonon line due to the additional decay channel via the singlet states. An emission contrast of $30 - 40\,\%$ can then be detected on the zero phonon line between an initial population of the $|0\rangle$ and the $|\pm1\rangle$ ground states, respectively [261,272]. The distinction into a "bright" and a "dark" spin state level allows for an optical readout of the nitrogen vacancy colour centre spin state. This spin-dependent fluorescence can be

exploited to optically access the spin states and is the basis for experimental protocols like optically detected magnetic resonance (ODMR).

For continuous-wave ODMR measurements, a laser with 532 nm is exciting the nitrogen vacancy colour centre while the emission is detected on the zero phonon line at 637 nm and on the phononic sidebands on its red wavelength side. A microwave field is then applied to the nitrogen vacancy colour centre leading to a drop of the emission intensity when it is resonant with the transition between the different ground state levels with zero and non-zero spin projection. This is due to the fact that the microwave excitation results in a depopulation of the "bright" $|0\rangle$ ground state to the advantage of the "dark" $|\pm 1\rangle$ ground state. At cryogenic temperatures, even single shot readouts of the spin state can be performed [271]. This technique is widely used both for sensing applications and for steps towards implementing qubit operations based on the nitrogen vacancy colour centre electronic states.

Ground State Levels (Spin States)

The ground state triplet consists of three individual levels of spin $|0\rangle$, $|+1\rangle$, and $|-1\rangle$. The splitting originating from the diamond crystal field of 2.88 GHz caused by spin-spin interaction reduces this degeneracy and causes a splitting between the $|0\rangle$ and the degenerate $|\pm 1\rangle$ states. A transition between these states can be induced by a microwave field and tested with the optically accessible distinction into a "dark" and a "bright" state. In order to exploit the nitrogen vacancy colour centre for more advanced applications, the lifetime of the spin state needs to be measured and improved.

For the ground states of the nitrogen vacancy colour centre, two different decoherence processes take place that are characterised by the time constants T_1 and T_2, respectively. The overall decoherence rate of the nitrogen vacancy colour centre ground state levels γ_{ground} is then dependent on both time constants. The first time constant T_1 describes a spin relaxation process that is caused by transitions between the different sub-levels of the ^{3}A ground state. This time constant has first been measured to > 1 ms [274] while other experiments showed spin relaxation times of 5.93 ms for bulk diamond and $100\,\mu$s for nanodiamonds [275]. The second time constant T_2 describes a dephasing of the spin. The dynamics of the spin bath in the surrounding carbon material leads to a fluctuating magnetic field that interacts with the spin state of the nitrogen vacancy colour centre. This spin bath is created by ^{13}C atoms and additional nitrogen impurities [276]. In an ideal spin-free diamond, the spin-lattice relaxation time on the order of several seconds would constitute an ultimate limit [277]. In real samples, however, the dephasing time depends very much on the purity of the sample with respect to additional spins but is typically in the order of ns to few μs [170, 175, 274, 276]. As this interaction process with the environment is a pure dephasing process and not a decay process, it can be resolved with experimental techniques [278]. For single pulse Hahn echo measurements, the time constant is in the range of tens to few hundred μs [275, 279–281]. The use of dynamical decoupling techniques can further improve the dephasing times. For pulsed dynamical decoupling from the spin bath, coherence times of 1.6 ms could be reached for single nitrogen vacancy colour centres [280], and a similar value of 2 ms was found in an ensemble measurement [282]. Another possibility is a continuous wave dynamical

decoupling technique where the spin states are addressed continuously and coherently with a control field. Continuous decoupling techniques do not show such a significant improvement of dephasing times as compared to pulsed schemes. However, they are still favourable for many applications as they do not restrict the possibilities to perform arbitrary quantum gate operations or to sense quasi-static magnetic fields [163]. Employing a microwave field as control field, the dephasing time could be improved 20-fold to $50\,\mu$s [283]. Using a strain field as control led to an increase of T_2 by approximately a factor of five to values of $16.4\,\mu$s for a single spin and $15\,\mu$s for an ensemble [170,175].

As alternative to advanced measurement protocols, the diamond material itself can be engineered in order to suppress the dephasing of the spin states of the nitrogen vacancy colour centre. In a very pure diamond sample, only ^{13}C atoms interact with the ground state levels of the nitrogen vacancy colour centre due to their nuclear spin properties. Diamond material with lower ^{13}C content results in a heavily reduced interaction with the environment. By using mono-isotopic diamond, dephasing times up to $1.8\,$ms could be reached with spin echo measurements even at room temperature [277]. This is comparable to the values achieved with pulsed dynamical decoupling measurements. Combining both approaches by employing pulsed dynamical decoupling for nitrogen vacancy colour centres in mono-isotopic diamond samples, coherence times up to $0.6\,$s could be reached at cryogenic temperatures of $77\,$K [284].

Excited State Levels

The excited state triplet consists of six electronic states termed $|A_1\rangle$, $|A_2\rangle$, $|E_x\rangle$, $|E_y\rangle$, $|E_1\rangle$, and $|E_2\rangle$. In absence of thermal effects, this degeneracy is partly lifted by spin-orbit coupling resulting in doubly degenerate states, namely $|A_{1,2}\rangle$, $|E_{x,y}\rangle$, and $|E_{1,2}\rangle$ where the degeneracy between $|A_1\rangle$ and $|A_2\rangle$ is lifted by spin-spin interaction. The small but non-zero spin-orbit coupling in the nitrogen vacancy colour centre as well as the absence of inversion symmetry also make it very sensitive to electric and strain fields. Higher temperatures lead to a spin-spin interaction that mixes the excited state levels. The resulting states of non-zero spin and angular momentum $|A_1\rangle$, $|A_2\rangle$, $|E_1\rangle$, and $|E_2\rangle$ are split from the degenerate states with zero spin projection $|E_x\rangle$ and $|E_y\rangle$ by an effective crystal field of $1.42\,$GHz. The Fourier-limited decay rates of the excited states can directly be derived from the lifetime as $\gamma = 1/t$. With the values of the lifetimes $t_{m_s=0} = 13.7\,$ns and $t_{m_s=\pm1} = 7.3\,$ns [271], decay rates of $\gamma_{m_s=0} = 73\,$MHz and $\gamma_{m_s=\pm1} = 137\,$MHz can be determined for the excited state levels with zero and non-zero spin projection, respectively. As the excited states with zero spin projection will be in the centre of the analysis, $\gamma_{m_s=0} = 73\,$MHz denotes the generalised decay rate of an unperturbed nitrogen vacancy colour centre's excited state expressed as γ_0 in the remainder of the text. Besides the intrinsic dynamics of the nitrogen vacancy colour centre described by this decay rate, further effects lead to a broadening of the zero phonon line in a non-perfect diamond lattice at ambient temperatures.

The dynamic Jahn-Teller effect causes a dephasing of the excited state triplet [285]. This effect describes the coupling of degenerate states to vibrational modes of the diamond lattice and the energy potential of the electronic levels is changed by this interaction. Considering both linear and quadratic coupling terms between the triplet states

and phononic modes of E-type, the energy potential transforms to a Mexican-hat shape with three distinct minima at the angles 0, $2\pi/3$, and $4\pi/3$. The minimal energy of this potential is lower than that for the unperturbed nitrogen vacancy colour centre. The barrier between the minima is approximately $10\,\text{meV}$, meaning that the system would be trapped in one of the minima for phonon energies below this threshold. This is also called static Jahn-Teller effect. The e-type vibrational modes of the diamond lattice, however, have an energy of $71\,\text{meV}$. For these parameters, tunnelling between the different minima occurs and results in the dynamic Jahn-Teller effect. A two-phonon Raman process of E-type vibrational modes can then stimulate transitions between the $|E_x\rangle$ and $|E_y\rangle$ excited state levels. One of these states' lifetime is reduced by this process and a dephasing of the optical transition takes place. This is then visible as homogeneous broadening of the zero phonon line. The effective linewidth γ_{eff} of the zero phonon line can then be described as

$$\gamma_{\text{eff}} = \gamma_0 + \gamma^* \tag{2.23}$$

with γ_0 being the decay rate of the excited state and γ^* the line broadening associated with pure dephasing. The pure dephasing for nitrogen vacancy colour centres in diamond has been measured to $\gamma^* = 15\,\text{THz}$ at room temperature and $\gamma^* = 30\,\text{GHz}$ at cryogenic temperatures [267]. The temperature dependence indicates that the lower phonon population at cryogenic temperatures reduces the linewidth broadening. Even lower values down to negligible dephasing for temperatures below $10\,\text{K}$ were reported in a different reference [286] what could also be reproduced in a theoretical model [287].

Besides this pure dephasing, also spectral diffusion takes place. Local electric fields lead to a Stark shift of the nitrogen vacancy colour centre. These fields are typically created by single charges in close proximity, typically either charges trapped at the surface of the diamond or ionised substitutional nitrogen atoms. As the electronic environment of the nitrogen vacancy colour centre created by these charges fluctuates, the zero phonon line shows jumps. These jumps are much faster than typical integration times in spectroscopy and inhomogeneous linebroadening occurs. This effect can be suppressed when employing diamond of high crystalline quality and when avoiding nitrogen vacancy colour centres that are located close to the material surface. In addition, the common re-pump with $532\,\text{nm}$ required to transfer nitrogen vacancy colour centres back to the desired negatively charged state should be substituted with a pumping scheme working at $575\,\text{nm}$ [288]. Thus, the ionisation of substitutional nitrogen can be avoided and spectral diffusion can drastically be reduced.

2.4.3 Creation of Nitrogen Vacancy Colour Centres

The formation of colour centres in diamond requires the incorporation of nitrogen impurities in the material and the co-localisation of a vacant lattice position to obtain the configuration shown in figure 2.3(a). Nitrogen impurities can be introduced to the diamond matrix either during the diamond growth process or in an additional implantation step. The incorporation of nitrogen atoms during the formation of diamond is often a side-effect of the growth conditions. Diamond created in a high pressure high temperature (HPHT) processes typically has rather high densities of nitrogen impurities ($20-200\,\text{ppm}$) whereas diamond grown by chemical vapour deposition (CVD) usually

has a much lower nitrogen pollution ($0.05 - 10\,\mathrm{ppm}$) [279]. During diamond growth in a CVD process, the plasma parameters can be engineered such that the incorporation of nitrogen impurities is stimulated. This technique is typically used for so-called delta-doping where thin layers with high nitrogen concentration are grown into a diamond sample. This results in nitrogen vacancy colour centres that are located in a defined layer of the sample with a precision of few nm [289, 290]. Alternatively, nitrogen can be introduced to the diamond material by ion implantation. Highly energetic nitrogen atoms are accelerated onto a diamond sample and remain inside the material [291, 292]. For both incorporation methods, the nitrogen impurities need to be paired with adjacent lattice vacancies in order to form nitrogen vacancy colour centres. This activation step is typically done by irradiation with electrons, high-temperature annealing, or a combination of both [33, 86, 276, 289].

For the interaction of colour centres with photonic or phononic structures, the orientation of the colour centres and their precise positioning are crucial in order to achieve a good coupling. Delta-doping allows the precise localisation of defect centres in the vertical direction and an improved coupling to photonic structures has been demonstrated with this technique [82]. While the depth of implanted nitrogen vacancy colour centres can in principle be controlled by varying the implantation energy, the resulting precision of the vertical positioning cannot compete with delta-doping of nitrogen vacancy colour centres during growth. The lateral resolution, however, can be improved drastically by reducing the implanted area. This can be achieved by either using an aperture to reduce the implantation spot size [83, 84] or by using a focused ion beam technique so that the small diameter is inherent to the method [85]. When combining the delta-doping technique for the incorporation of colour centres providing a good vertical resolution and activating them with focused electron beam irradiation providing a good lateral resolution, a very precise localisation of nitrogen vacancy colour centres within a volume as small as $450\,\mathrm{nm} \times 450\,\mathrm{nm} \times 4\,\mathrm{nm}$ could be achieved [86]. Besides the targeted creation, also a measurement of the exact position of single nitrogen vacancy colour centres after formation can facilitate their integration into photonic or phononic structures [293]. High-resolution imaging like STED microscopy can determine the location of a single nitrogen vacancy colour centre with a resolution down to few nanometres [87].

Besides a precise localisation of nitrogen vacancy colour centres, also their orientation is a crucial factor for the interaction with other degrees of freedom. The orientation of nitrogen vacancy colour centre's symmetry axis is determined to an equivalent [111] lattice direction through the structure of diamond what corresponds to four possible orientations. This number of possible orientations can be reduced for nitrogen vacancy colour centres incorporated during diamond growth to two directions for (110)-oriented samples [88] and (100)-oriented samples [294], and even a single orientation for (111)-oriented samples [89, 90]. This deterministic orientation could in principle be combined with a delta-doping technique so that oriented nitrogen vacancy colour centres are created in a defined depth inside the bulk of the diamond. However, a combination with a localised activation technique is not possible in this case, as the orientation results from the fact that the incorporation of a nitrogen atom is followed by the incorporation of a vacancy along the growth direction. There is no technique to date that would allow the creation of oriented nitrogen vacancy colour centres with a high lateral resolution.

2.5   Coupling between Emitter and Optical Cavity

Introducing a two-level-system into an optical resonator will give rise to an interaction between these different degrees of freedom when the transition frequency of the emitter is on resonance with the cavity field. The coupling can be described such that the optical resonator increases the local density of states in the modal volume of the resonator field. This increased density of optical states leads to a higher emission rate into the cavity mode. These additional photons further increase the photon population of the optical resonator what corresponds to a back-action of the emitter on the cavity field. This coupling between an emitter and an optical cavity field will here be described with a focus on the interaction between a photonic crystal and a colour centre in diamond. The theoretical description can be found in any standard literature on this topic. The specific formalism as described here is adapted from reference [295].

On the single particle level, the interaction between an emitter and an optical resonator field can be described by a Jaynes-Cummings-Hamiltonian. A perfect spectral overlap between the optical resonator field and the emitter is assumed such that ω_{opt} describes not only the frequency of the cavity field but also the zero phonon line frequency of the emitter $\omega_{\mathrm{ZPL}} = \omega_{\mathrm{opt}}$. For a perfect dipole orientation of the emitter parallel to the resonator axis and an ideal positioning in the maximum of the optical resonator field, the Hamiltonian of the coupled system is given as

$$H_{\mathrm{J-C}} = \hbar\omega_{\mathrm{ZPL}}\widehat{\sigma}_z + \hbar\omega_{\mathrm{opt}}\widehat{a}^\dagger\widehat{a} + i\hbar g_{\mathrm{F},0}\left(\widehat{a}^\dagger\widehat{\sigma} - \widehat{\sigma}^\dagger\widehat{a}\right) \tag{2.24}$$

Here $\widehat{\sigma}^\dagger = |e\rangle\langle g|$ and $\widehat{\sigma} = |g\rangle\langle e|$ are the raising and lowering operators for the optical transition of an emitter with ground state $|g\rangle$ and excited state $|e\rangle$, and the population operator is given by $\widehat{\sigma}_z = 1/2\left(|e\rangle\langle e| - |g\rangle\langle g|\right)$. $\widehat{a}$ and $\widehat{a}^\dagger$ denote the photon creation and annihilation operators and $g_{\mathrm{F},0}$ is the single photon coupling constant. The first term of the Hamiltonian describes the two-level system, the second term the optical resonator mode, and the third term represents the interaction between the internal and the optical degree of freedom. For non-perfect orientation of the emitter with respect to the cavity field, a factor of $\cos(\xi)$ reduces the single photon coupling constant $g_{\mathrm{F},0}$ where the angle ξ is the angle between the dipole and the resonator axis. Also an additional positioning factor ψ needs to be included to the interaction part when the emitter is not located in the maximum of the resonator field. It is given by the fraction of the electric field strength at the location of the emitter and the maximum of the electric field $\psi = E_{\mathrm{loc}}/|E_{\mathrm{max}}|$.

The single photon coupling constant $g_{\mathrm{F},0}$ determines the rate of the interaction. A high coupling constant indicates a fast exchange of energy between the emitter and the optical resonator field. It is given by the following expression

$$g_{\mathrm{F},0} = \frac{\mu}{\hbar}\sqrt{\frac{\hbar\omega_{\mathrm{opt}}}{2\varepsilon_{\mathrm{dia}}V_{\mathrm{opt}}}} \tag{2.25}$$

Here μ is the absolute value of the dipole matrix element for the transition between the excited state $|e\rangle$ and the ground state $|g\rangle$:

$$\mu = |q\langle e|\widehat{x}|g\rangle| \tag{2.26}$$

with $\widehat{x}$ the position operator and q the unit charge. Besides the dipole matrix element, the single photon coupling constant $g_{\mathrm{F},0}$ is only dependent on properties of the optical resonator, namely the optical resonator frequency ω_{opt}, the modal volume V_{opt}, and the dielectric constant of diamond $\varepsilon_{\mathrm{dia}}$. An alternative expression for the single photon coupling constant $g_{\mathrm{F},0}$ shows even more clearly that the interaction depends only on the free space emission properties of the colour centre and the properties of the optical resonator:

$$g_{\mathrm{F},0} = \frac{\gamma_0}{2}\sqrt{\frac{V_0}{V_{\mathrm{opt}}}} \tag{2.27}$$

Here γ_0 is the decay rate of the phonon population for the spontaneous emission in free space given as

$$\gamma_0 = \frac{\omega_{\mathrm{opt}}^3 \mu^2}{3\pi\varepsilon_0\hbar c^3} \tag{2.28}$$

In the case of the excited states of the nitrogen vacancy colour centre with zero spin projection, this decay rate is $\gamma_0 = 73\,\mathrm{MHz}$. The virtual modal volume in free space V_0 is given as

$$V_0 = \frac{3c\lambda_{\mathrm{opt}}^2\varepsilon_0}{2\pi\gamma_0\varepsilon_{\mathrm{dia}}} \tag{2.29}$$

It can thus be seen that a stronger coupling can be achieved for emitters with high spontaneous emission rates and for optical resonators with small modal volumes.

Besides increasing the single photon coupling constant, a stronger interaction can also be achieved by increasing the number of emitters or photons in the resonator. This fact can be illustrated by determining the critical emitter number N_0 as well as the intra-cavity saturation photon number $n_{\mathrm{opt},0}$. The critical emitter number is defined as

$$N_0 = \frac{2\kappa\gamma_0}{g_{\mathrm{F},0}^2} \tag{2.30}$$

It gives a direct measure for the number of emitters that need to be coupled to an optical resonator in order to obtain a measurable effect on the single photon cavity field. The intra-cavity saturation photon number $n_{\mathrm{opt},0}$ is given as

$$n_{\mathrm{opt},0} = \frac{4\gamma_0^2}{3g_{\mathrm{F},0}^2} \tag{2.31}$$

This number indicates for each set of parameters γ_0 and $g_{\mathrm{F},0}$ how many photons are needed for an emitter to be saturated by the optical cavity field. It can be seen that it is only dependent on the interaction strength and the decay rate of the emitter. This indicates that a higher photon population of the optical resonator can compensate for a fast-decaying emitter or a low single photon coupling constant.

2.5.1   Coupling Regimes

In the following, the interaction is only discussed at the level of single photons and a single emitter. In order to understand the dynamics of the coupled system better, it is crucial to determine to which extent the coupling dominates over the individual degrees of freedom. To this end, the optical resonator's loss rate κ and the free space spontaneous emission rate of the emitter γ_0 are compared to the single photon coupling constant $g_{\mathrm{F},0}$. On this basis, different coupling regimes can be identified that determine the dynamics of the integrated system.

The single photon cooperativity $C_{\mathrm{F},0}$ is an important measure for the interaction strength. It can be expressed in terms of the single photon coupling constant $g_{\mathrm{F},0}$, the decay rate of the optical resonator mode κ, and the decay rate of the colour centre's excited state levels γ_0 as

$$C_{\mathrm{F},0} = \frac{g_{\mathrm{F},0}^2}{\kappa \gamma_0} \tag{2.32}$$

The large single photon cooperativity regime $C_{\mathrm{F},0} > 1$ means that a coherent interaction is faster than the decay of both the cavity field and the photon population of the emitter. The coupling between the emitter and the resonator determines the dynamics of the system. The large cooperativity regime also implies that the critical emitter number is smaller than one, indicating that already a single emitter has a measurable effect on the optical resonator field.

The interaction is considered strong when the single photon coupling constant $g_{\mathrm{F},0}$ is larger than the individual non-resonant decay rates of emitter and optical cavity.

$$g_{\mathrm{F},0} \gg (\kappa, \gamma) \tag{2.33}$$

In this case, the emission of a photon into the optical cavity mode is a reversible process. An emitted photon can be absorbed again before it finally decays from the cavity. A common eigenstate describes the emitter and the optical resonator field showing that the interaction is a coherent process. In this regime, both the critical atom number N_0 and the intra-cavity saturation photon number $n_{\mathrm{opt},0}$ are smaller than one. Already a single photon in the optical cavity mode has a significant effect on a single emitter coupled to this optical mode as well as a single emitter shows measurable influence on the cavity field. The strong coupling regime is advantageous for many experiments in the field of quantum information processing [296] but could not be reached with diamond resonators to date. So far, the required very high optical quality factors ($Q_{\mathrm{opt}} \approx 10000$ for $V_{\mathrm{opt}} \approx 1 \, (\lambda/n)^3$) could not be realised with current nanofabrication techniques. Also, the precise positioning of a single emitter in the maximum of the optical resonator field remains challenging, especially when considering that the interaction is weaker for less-than-perfect dipole orientation and spectral overlap between the cavity field and the emitter.

2.5.2 Weak Coupling in the Purcell Regime

The weak coupling between the emitter and the optical cavity mode is also called Purcell regime where the non-resonant decay rates dominate over the coupling.

$$g_{\mathrm{F},0} < (\kappa, \gamma) \tag{2.34}$$

The emission rate is enhanced as compared to free space emission in this regime, but the emission of a photon into the optical cavity mode remains an irreversible process. Although spontaneous emission is the predominant process, light emitted into the optical resonator shows spectral and spatial characteristics corresponding to the properties of the cavity mode. A broadband emitter is then more likely to emit at the optical cavity's resonance frequency and in the direction of the optical cavity axis. The figure of merit of this interaction is the Purcell factor F_0. It is defined as the ratio of the emission rate into the resonator mode γ_{res}, and the emission rate in free space γ_0. It can also be expressed in terms of the corresponding lifetimes t_0 and t_{res} of the emitter in free space and inside the optical resonator, respectively.

$$F_0 = \frac{\gamma_{\mathrm{res}}}{\gamma_0} = \frac{t_0}{t_{\mathrm{res}}} \tag{2.35}$$

The spontaneous emission rate of an emitter in free space γ_0 is given in equation 2.28 and depends mainly on the emission frequency ω_{opt} and the absolute value of the transition's dipole matrix element μ. The emission rate in an optical resonator is given as

$$\gamma_{\mathrm{res}} = g_{\mathrm{F},0}^2 \frac{4\,Q_{\mathrm{opt}}}{\omega_{\mathrm{opt}}} \tag{2.36}$$

This calculation of the emission rate is only valid under the assumptions that the emitter is located at the maximum of the optical cavity field, with its dipole oriented parallel to the electric field of the optical cavity mode, and its emission frequency is exactly matching the resonance frequency of the cavity. The Purcell factor F_0 can then be expressed as

$$F_0 = \frac{\gamma_{\mathrm{res}}}{\gamma_0} = \frac{3\,Q_{\mathrm{opt}}\lambda_{\mathrm{opt}}\varepsilon_0}{4\pi^2 V_{\mathrm{opt}}\varepsilon_{\mathrm{dia}}} \tag{2.37}$$

In the case of solid state optical resonators, the decay rate of the emitter inside the cavity is better compared to the emission rate inside the bulk of the material. The effect of a higher density of states inside the material is then not misleadingly attributed to the emission enhancement by the optical resonator. The corrected Purcell factor F is then given by the following expression for a diamond optical resonator.

$$F = \frac{F_0}{n_{\mathrm{dia}}} = \frac{3}{4\pi^2}\frac{Q_{\mathrm{opt}}}{V_{\mathrm{opt}}}\left(\frac{\lambda_{\mathrm{opt}}}{n_{\mathrm{dia}}}\right)^3 \tag{2.38}$$

with λ_{opt} being the emission and cavity wavelength and n_{dia} the refractive index of diamond. A higher Purcell factor implies a higher emission rate and at the same time more emission into the optical cavity mode. The fraction of photons that are emitted into the optical resonator mode is given as

$$\beta = \frac{F}{1 + F} \tag{2.39}$$

It can be seen from this equation that for very high Purcell factors almost no photons are emitted into free space. The weak coupling regime has two appearances: the bad cavity and the bad emitter regime. This distinction illustrates that the effect of a lossy resonator or a fast-decaying emitter have a qualitatively different impact on the interaction.

In the bad emitter regime, the emitter's lifetime is shorter than the average lifetime of a photon in the optical cavity mode. This regime is typical for emitters that are subject to broadening mechanisms and the effective decay rate γ_{eff} needs to be considered where all sources of decoherence are included. In the case of the nitrogen vacancy colour centre, the effective decay rate γ_{eff} can be described by the sum of the Fourier-limited decay rate γ_0 and a decay rate γ^* assigned to pure dephasing (see equation 2.23). In the bad emitter regime, the different decay rates and the coupling rate compare as follows

$$\gamma_{\text{eff}} > \kappa \gg g_{\text{F},0} \tag{2.40}$$

The Purcell factor can then be transformed to the following expression:

$$F_{\text{bad emitter}} = \frac{g_{\text{F},0}^2}{\gamma_0 \left(\gamma_0 + \gamma^*\right)} \tag{2.41}$$

It can be seen from this equation that the Purcell enhancement is completely independent of the cavity decay rate κ. This illustrates the fact that even an outstanding optical resonator cannot compensate for a broadband emitter.

The bad cavity regime is characterised by a fast decay of the optical resonator mode dominating over the decay rate of the emitter and the coupling constant.

$$\kappa > \gamma_0 \gg g_{\text{F},0} \tag{2.42}$$

This is the case for lossy cavities with a poor temporal confinement of the resonator mode corresponding to low quality factors. In this case, the Purcell factor is directly proportional to the single photon cooperativity $C_{\text{F},0}$.

$$F_{\text{bad cavity}} = \frac{g_{\text{F},0}^2}{\kappa \gamma} = C_{\text{F},0} \tag{2.43}$$

In contrast to the bad emitter regime, both the emitter and the cavity decay rate still have an influence on the spontaneous emission enhancement. When working in the bad cavity regime, it is thus crucial to carefully optimise all decay rates in order to achieve a strong emission enhancement.

2.6   Optomechanical Coupling

Optomechanical coupling describes the interaction between an optical and a mechanical degree of freedom. Here, only the case of cavity-mediated coupling is considered where

both the optical and the mechanical resonator are confined to a localised cavity mode. The interaction is based on a non-dissipative coupling meaning that the interaction does not extract energy from the optomechanical system. This allows for operation at the single particle level for both photons and phonons, a feature that is required for a range of fundamental quantum mechanical experiments. The theoretical overview provided in this section is based on a more detailed description taken from reference [103].

A cavity optomechanical system can be depicted by a Fabry-Pérot resonator where one of the end mirrors is suspended on a mechanical spring or cantilever as shown in figure 2.5. The oscillatory movement of the spring causes a fluctuation of the cavity length and at the same time, radiation pressure from the cavity photons has an impact on the mechanical oscillation of the spring. The optical and mechanical fields are mutually coupled and can form common states of quantum mechanical motion.
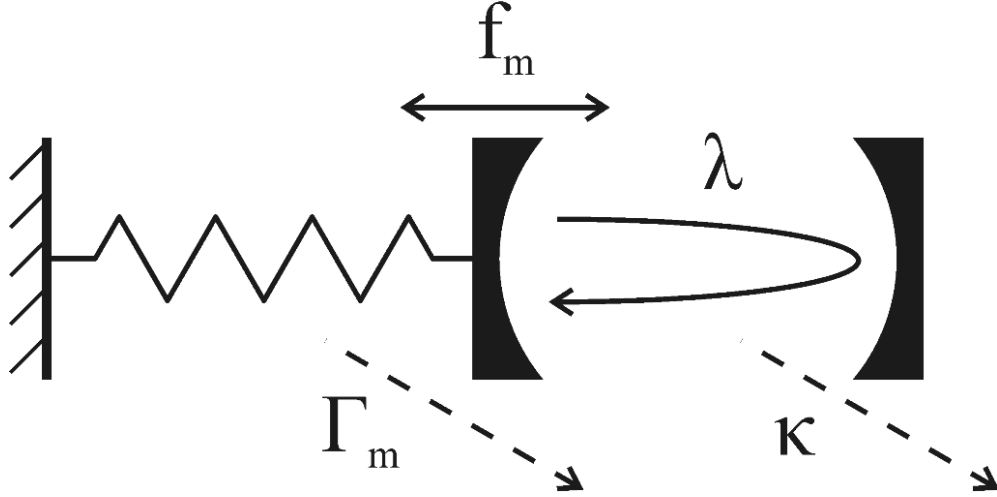
Figure 2.5: Most simple model for cavity optomechanics. One end mirror of a Fabry-Pérot resonator is attached to a mechanical oscillator. Both the optical and the mechanical resonator mode can be described independently by a resonance frequency, a spatial confinement and a loss rate. The optomechanical interaction in this case can best be understood in a feedback picture where mutual back-action leads to a collective dynamics of the coupled system.

The concept of optomechanical coupling can be depicted by a variety of physical formalisms. These different approaches are not contradictory and valid at the same time. However, some experimental signatures can better be understood with the help of a particular concept.

In a classical conception, optomechanical interaction can be understood in a feedback picture. When considering a Fabry-Pérot resonator where one of the end mirrors is suspended on a mechanical spring corresponding to the situation shown in figure 2.5, the oscillatory movement of the spring causes a fluctuation in the optical cavity length. The periodic change of the resonance conditions for the optical mode gives rise to a radiation pressure force created by cavity photons striking the end mirror. This force back-acts on the mechanical resonator but is retarded against the initial motion of the

mechanical resonator. Depending on the retardation of the radiation pressure force, this back-action force can then both cause an effective spring-softening or spring-hardening of the mechanical resonator, and either amplify or damp the mechanical oscillation.
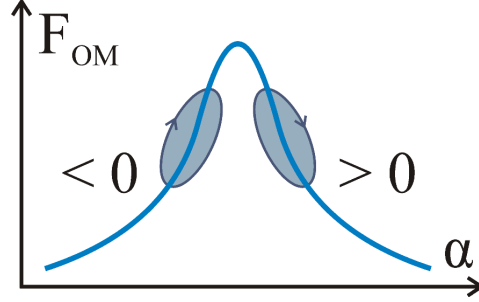
Figure 2.6: Graphical representation of the thermodynamic interpretation of optomechanical interaction. The work done by the radiation pressure force $\widehat{F}_{\mathrm{OM}}$ can be represented as closed cycle in the diagram of force against mechanical displacement α. Qualitatively, a negative sign corresponds to cooling whereas a positive surface indicates heating of the mechanical resonator. The size of the area swept during an interaction cycle determines the coupling strength. Figure adapted from reference [103].

Alternatively, this feedback loop of optomechanical interaction can be expressed as thermodynamic cycle. The mechanical oscillation can be represented by a closed trajectory in a diagram of radiation force $\widehat{F}_{\mathrm{OM}}$ against mechanical displacement α as shown in figure 2.6. If now the retardation of the radiation pressure force is considered, the trajectory of the mechanical oscillation in this diagram follows an ellipsoid instead of a line. Depending on the phase shift, this closed cycle is performed clockwise or counter-clockwise leading to optomechanical damping or amplification of the mechanical oscillation, respectively. Mechanical damping corresponds to cooling as the phonon population is decreased with every thermodynamic cycle.

Although both these formalisms are of purely classical nature, they can provide a description of optomechanical effects in the quantum regime when taking into account quantum noise. This noise adds to the retarded radiation pressure force and directly imposes a fundamental limit for optomechanical cooling. A truly quantum mechanical description, however, imposes a scattering picture where single photons and phonons exchange energy via optomechanical coupling. When a phonon is created due to the interaction, the cavity photon looses the energy required for the particle creation. In the optical transmission spectrum, this gives rise to a sideband on the long wavelength side of the optical frequency. The energy of this sideband is exactly the energy of the initial photon minus the energy of the newly created cavity phonon. In frequencies, this corresponds to a red-shift of the optical mode by exactly the mechanical resonator frequency. The opposite process of particle annihilation leads to the appearance of a short wavelength sideband. A cavity phonon is absorbed and the now higher energetic photons can be detected as a blue-detuned sideband at a frequency corresponding to the sum of the optical and mechanical resonator frequencies.

The coupled system of an optical and a mechanical system can be described by a

Hamiltonian formulation consisting of optical and mechanical resonator terms as well as an interaction part.

$$\widehat{H}_{\mathrm{OM}} = \hbar\omega_{\mathrm{opt}}\widehat{a}^{\dagger}\widehat{a} + \hbar\omega_{\mathrm{m}}\widehat{b}^{\dagger}\widehat{b} + \hbar g_{\mathrm{OM,0}}\widehat{a}^{\dagger}\widehat{a}\left(\widehat{b} + \widehat{b}^{\dagger}\right) \tag{2.44}$$

Here, ω_{opt} is the optical resonator frequency, ω_m the mechanical resonator frequency, $g_{\mathrm{OM,0}}$ the single photon coupling constant, and $\widehat{a}^{\dagger}$, $\widehat{a}$, $\widehat{b}^{\dagger}$ and $\widehat{b}$ the photonic and phononic creation and annihilation operators, respectively. The first part of equation 2.44 represents the energy stored in the optical cavity, the second part the energy stored in the mechanical cavity, and the third part describes the interaction between these two degrees of freedom. The coupling is a fundamentally non-linear process that can only be expressed by a combination of three operators in each single term. While some optomechanical protocols require this full non-linear description, most interactions can be expressed with the help of a linearised approach that will be shown in section 2.6.3.

The form of the Hamiltonian for an optomechanical system expressed in equation 2.44 resembles a Raman scattering process and the formalism is indeed the same. However, only the case of cavity optomechanics is discussed in the following where both the optical and the mechanical degree of freedom are confined to a localised resonator mode. Systems where radiation pressure forces are due to the absorption of light are not considered here. In those systems, the coupling is dissipative meaning that the interaction is based on the extraction of energy from the system. Although the interaction in those systems might seem similar, the dissipation of light destroys the coherence of the optical resonator field and reversible optomechanical interaction is not possible.

It can also be seen that the coupling linearly depends on the displacement. While this is true for most optomechanical experiments, there are geometries like for example a membrane-in-the-middle setup where the coupling depends on the square of the displacement what is advantageous for some particular applications as shown in section 2.6.5. The Hamiltonian formulation in equation 2.44 does not apply in that case and the corresponding special situation of so-called dispersive coupling is not considered in the following.

Optomechanical coupling is governed by the single photon optomechanical coupling constant $g_{\mathrm{OM,0}}$. It is a measure for the rate at which optomechanical coupling takes place. The single photon coupling constant $g_{\mathrm{OM,0}}$ describes the optical resonator frequency shift upon excitation of a single phonon in the mechanical resonator. It is defined as the product of the zero point fluctuation x_{ZPF} of the mechanical oscillator and the optical frequency shift per displacement G_{OM}.

$$g_{\mathrm{OM,0}} = x_{\mathrm{ZPF}} \cdot G_{\mathrm{OM}} \tag{2.45}$$

The zero point fluctuation x_{ZPF} is a property of the mechanical motion as described in section 2.3 and corresponds to the maximal elongation of the mechanical resonator upon excitation of a single cavity phonon (see equation 2.21). The optical frequency shift per displacement can be expressed as the derivative of the optical frequency at mechanical equilibrium.

$$G_{\mathrm{OM}} = \frac{d\omega_{\mathrm{opt}}}{d\alpha}\bigg|_{\alpha=\alpha_0} \tag{2.46}$$

Here, α is an abstract parameter for the mechanical displacement with α_0 the equilibrium position of the mechanical resonator. A high value of G_{OM} indicates that already a small mechanical motion has a strong effect on the optical resonator mode.

An alternative measure is the single photon optomechanical coupling length $L_{\mathrm{OM,0}}$ defined as follows.

$$L_{\mathrm{OM,0}} = \frac{\omega_{\mathrm{opt}}}{g_{\mathrm{OM,0}}} \tag{2.47}$$

It is diffraction limited to $\lambda_{\mathrm{opt}}/2n_{\mathrm{dia}}$ with λ_{opt} the wavelength of the optical resonator mode and n_{dia} the refractive index of the cavity material diamond. While it is of little practical relevance, this expression provides an intuitive access to optomechanical coupling. It is formulated nicely in reference [156] that "$L_{\mathrm{OM,0}}$ is [...] the length over which a photon's momentum is transferred into the mechanical mode as it propagates within the structure".

The radiation pressure force $\widehat{F}_{\mathrm{OM}}$ is the derivative of the interaction part in equation 2.44 with respect to displacement.

$$\widehat{F}_{\mathrm{OM}} = -\frac{d\widehat{H}_{\mathrm{int}}}{d\widehat{x}} = \hbar G_{\mathrm{OM,0}}\widehat{a}^{\dagger}\widehat{a} \tag{2.48}$$

It is the force that an optical field exerts on the mechanical resonator through the optomechanical interaction.

2.6.1   Coupling Regimes

For a full description of the entire system consisting of an optical and a mechanical cavity mode that are mutually coupled by optomechanical interaction, the dynamics of the coupled system has to be studied. The comparison between the optomechanical coupling rate $g_{\mathrm{OM,0}}$ and the individual decay rates of the optical and the mechanical resonator κ and Γ_{m} determines to what extent the interaction dominates the optomechanical system. Different coupling regimes can then be identified on this basis, allowing to assess the experimental implementations of the interaction. The single photon optomechanical cooperativity $C_{\mathrm{OM,0}}$ is defined as

$$C_{\mathrm{OM,0}} = \frac{g_{\mathrm{OM,0}}^2}{\kappa \cdot \Gamma_{\mathrm{m}}} \tag{2.49}$$

It is an abstract measure that indicates how much the dynamics of the system are determined by the interaction. For reaching the large single photon cooperativity regime, the condition $C_{\mathrm{OM,0}} > 1$ needs to be fulfilled. In this regime, a coherent population with single photons and phonons persists during the entire interaction allowing optomechanical coupling to dominate the dynamics. This illustrates the fact that a good optomechanical coupling cannot compensate for a poor temporal confinement of the optical and mechanical resonator modes.

A more challenging condition is the strong single photon coupling regime. Here, the single photon optomechanical coupling constant $g_{\text{OM},0}$ needs to be larger than the individual decay rates of both the optical and the mechanical resonator.

$$g_{\text{OM},0} > (\kappa, \Gamma_{\text{m}}) \tag{2.50}$$

The single photon strong coupling regime is a condition required for non-linear optomechanical interaction. In this regime, the optical and the mechanical resonator share a common eigenstate and a quantum state transfer is possible [297].

An even more challenging condition to reach is the coherent coupling regime. In this case, the interaction needs to be faster than all noise processes including the thermal decoherence of the mechanical resonator.

$$g_{\text{OM},0} > (\kappa, \Gamma_{\text{th}}) \tag{2.51}$$

A coherent transfer of quantum states between photons and phonons can take place under this condition and the interaction becomes quantum coherent.

There are is only very few experiments requiring true non-linear optomechanical coupling. These include the quantum non-demolition measurement of the intra-cavity phonon number $\widehat{n}_{\text{m}} = \widehat{b^\dagger}\widehat{b}$ and the creation of a "Schrödinger cat" type entanglement. Compared to other quantum systems, the entanglement here involves a microscopic and a nearly macroscopic degree of freedom realised in the form of the optical and the mechanical resonator mode [111,112]. For optomechanical interaction, a "Schrödinger cat" state means that already a single photon is able to displace the mechanical resonator by at least a zero point fluctuation. This requires not only the single photon strong coupling regime but also that the decay rate of the optical resonator mode is lower than the mechanical oscillation frequency corresponding to the so-called resolved sideband regime.

2.6.2   Sideband Resolution

Generally, a distinction between the resolved sideband regime and the unresolved sideband regime, the so-called Doppler regime, can be made based on the sideband suppression factor κ/ω_{m}. This corresponds to the distinction between the bad and the good cavity regime in the case of Purcell enhancement (see section 2.5.2). Experimentally, the resolved sideband regime is more challenging to reach as very high optical quality resonators are difficult to manufacture in practice.

The resolved sideband regime corresponding to the good cavity limit is favourable or strictly required for many applications of optomechanical coupling and could be observed in experiments [135]. It is reached when the frequency of the mechanical oscillation ω_{m} is larger than the decay rate of the optical resonator κ.

$$\omega_{\text{m}} \gg \kappa \tag{2.52}$$

A direct signal of the mechanical resonator can then be detected in the optical cavity spectrum in the form of mechanical sidebands to the optical cavity mode.

The Doppler regime, in contrast, corresponds to the bad cavity regime. This regime is also denoted as slow motion because the mechanical frequency is much slower than the lifetime of the resonator photons.

$$\omega_{\mathrm{m}} < \kappa \qquad (2.53)$$

In the Doppler regime, the signature of optomechanical interaction cannot be detected in the optical transmission spectrum because the optical cavity linewidth is larger than the spectral separation to the mechanical resonator signature. Therefore, it is also called unresolved sideband regime.

2.6.3   Linearised Optomechanical Interaction

While single photon non-linear optomechanical interaction is interesting for testing fundamental principles of quantum mechanics, most optomechanical effects can be described with the help of a linearised approximation. In fact, not only optomechanical cooling, but also entanglement between optical and mechanical mode as well as squeezing of an optomechanical state can fully be described with the help of the linearised expressions. The purpose of this transformation is to reduce the interaction terms based on three operators in equation 2.44 to a form where the coupling can be expressed with the help of only two operators in each term. This approximation drastically reduces the complexity of the equation and allows for a much more simple but still concise characterisation of a driven optomechanical system. However, some information is obviously lost in this representation and effects that can be described based on this approximation are also denoted linear optomechanics. In the linearised approximation, the optical resonator field $\widehat{a}$ is expressed as the sum of a coherent amplitude $\bar{a}$ and a fluctuating term $\delta\widehat{a}$.

$$\widehat{a} = \bar{a} + \delta\widehat{a} \qquad (2.54)$$

The average amplitude can be described with the help of the intra-cavity photon number $\overline{n}_{\mathrm{opt}}$.

$$\bar{a} = \sqrt{\overline{n}_{\mathrm{opt}}} \qquad (2.55)$$

Strictly speaking, this linearised approximation is only valid in the limit of high photon numbers since only then the assumption of a permanent coherent amplitude of the cavity field $\bar{a}$ is valid. However, this description still holds true for experiments with very low photon numbers as long as the system is not in the single photon strong coupling regime. The mechanical oscillator cannot resolve single photons in this case and an averaged photon occupation number is a valid description.

The optomechanical interaction described in the third term of equation 2.44 can be expressed with the help of the decomposed cavity field in equation 2.54 and sorted according to the powers of $\bar{a}$.

$$\begin{aligned}
\widehat{H}_{\mathrm{int}}^{(\mathrm{lin})} &= -\hbar g_{\mathrm{OM},0} \left(\bar{a} + \delta\widehat{a}\right)^{\dagger} \left(\bar{a} + \delta\widehat{a}\right) \left(\widehat{b} + \widehat{b}^{\dagger}\right) \\
&= -\hbar g_{\mathrm{OM},0} \left|\bar{a}\right|^2 \left(\widehat{b} + \widehat{b}^{\dagger}\right) - \hbar g_{\mathrm{OM},0}(\bar{a}^*\delta\widehat{a} + \bar{a}\delta\widehat{a}^{\dagger})(\widehat{b} + \widehat{b}^{\dagger}) - \hbar g_{\mathrm{OM},0}\delta\widehat{a}^{\dagger}\delta\widehat{a}
\end{aligned} \qquad (2.56)$$

The first term of this interaction Hamiltonian describes an average radiation pressure force $\bar{F}_{\mathrm{OM}} = \hbar G_{\mathrm{OM},0} \left|\bar{a}\right|^2$. It can be expressed by a permanent shift $\delta\bar{\alpha}$ of the equilibrium displacement.

$$\delta\bar{\alpha} = \frac{\hbar G_{\mathrm{OM},0} \left|\bar{a}\right|^2}{m_{\mathrm{eff}}\omega_{\mathrm{m}}^2} \tag{2.57}$$

Adapting the equilibrium position of the mechanical oscillator accordingly, entirely absorbs this contribution and no further effects need to be considered here.

The third term of the linearised interaction Hamiltonian can be neglected as it only depends on the fluctuation $\delta\widehat{a}$ and is thus very small compared to the other terms. By omitting terms for driving, decay, and fluctuation, the Hamiltonian of the driven optomechanical resonator is then

$$\widehat{H}_{\mathrm{driven}}^{(\mathrm{lin})} = -\hbar\Delta\delta\widehat{a}^{\dagger}\delta\widehat{a} + \hbar\omega_{\mathrm{m}}\widehat{b}^{\dagger}\widehat{b} - \hbar g_{\mathrm{OM},0}\sqrt{\bar{n}_{\mathrm{opt}}}(\delta\widehat{a}^{\dagger} + \delta\widehat{a})(\widehat{b} + \widehat{b}^{\dagger}) + ... \tag{2.58}$$

Due to the permanent shift of the equilibrium displacement in equation 2.57, the laser power only determines the intra-cavity photon number $\bar{n}_{\mathrm{opt}}$ in the above equation and has no influence on the first term describing the optical resonator mode.

The optomechanical interaction in the linearised regime is governed by the effective optomechanical coupling rate of a driven cavity g_{OM}.

$$g_{\mathrm{OM}} = g_{\mathrm{OM},0} \cdot \sqrt{\bar{n}_{\mathrm{opt}}} \tag{2.59}$$

A stronger laser power and thus a higher photon population inside the resonator also leads to a stronger optomechanical interaction. If the intrinsic optomechanical coupling described by the single photon coupling rate $g_{\mathrm{OM},0}$ is not strong enough for the desired application, it can in principle be arbitrarily enhanced further by increasing the pump power. However, for cooling applications, an optomechanically [118] or thermally induced [298] bistability can occur that effectively limits the intensity of the pump field.

2.6.4 Coupling Regimes in Linear Optomechanics

Just as in the case of the pure non-linear description, also in the case of linearised optomechanical interaction different coupling regimes can be distinguished. Here they are based on a comparison of the decay rates of the optical and mechanical resonator modes on the one side and the optomechancial interaction of a driven cavity on the other side. The effective optomechanical cooperativity C_{OM} is a measure for the efficiency of optomechanical interaction.

$$C_{\mathrm{OM}} = \frac{g_{\mathrm{OM}}^2}{\kappa \cdot \Gamma_{\mathrm{m}}} \tag{2.60}$$

The large cooperativity regime is reached for values $C_{\mathrm{OM}} > 1$. This regime is required for several applications like the creation of a squeezed state of the mechanical oscillator [108, 109] or optomechanically induced transparency [144, 299].

An even more challenging condition to reach is the strong coupling regime. Here, the optomechanical interaction in the driven resonator is faster than the decay of both the optical and the mechanical resonator mode individually.

$$g_{\mathrm{OM}} > (\kappa, \Gamma_{\mathrm{m}}) \tag{2.61}$$

In this regime, the optical and the mechanical resonator share two common eigenstates: the symmetric and the antisymmetric superposition of the phononic and photonic state spectrally separated by $2\,g_{\mathrm{OM}}$. This regime could be demonstrated experimentally in a photonic and phononic crystal cavity made from silicon [141].

If the effective optomechanical coupling rate g_{OM} exceeds both the decay rate of the optical cavity and the thermal decoherence rate of the mechanical oscillator, the interaction becomes quantum coherent.

$$g_{\mathrm{OM}} > (\kappa, \Gamma_{\mathrm{th}}) \tag{2.62}$$

This means that the coupling is so strong that no photons or phonons are lost from the system before the interaction could take place. This could be demonstrated experimentally with a mean phonon number of 1.7 [143]. It should be noted here that the different coupling regimes can be reached much easier with a driven resonator in the framework of linearised optomechanical interaction than in the case of pure non-linear optomechanics. This is based on the fact that the single photon optomechanical coupling constant $g_{\mathrm{OM,0}}$ can strongly be enhanced by a strong photon population resulting in the description of the effective optomechanical coupling constant of a driven resonator g_{OM} as described in equation 2.59.

2.6.5   Driven Optomechanical Systems

The detuning $\Delta_{\mathrm{L}} = \omega_{\mathrm{L}} - \omega_{\mathrm{opt}}$ between the driving field and the optical resonator mode determines the nature of the optomechanical interaction. A blue-detuned excitation very generally leads to an increase of the energy in the optomechanical system, whereas the opposite is true for a red-detuned pump field. While the sign of the detuning determines the implications of the interaction, the fundamental description is the same for both cases. A resonant excitation does usually not change the energy stored in the coupled system but can still be used for cold damping or to detect the state of the mechanical motion. These interaction types exist independent of the parameters of the optomechanical system but the resulting effects can differ drastically depending on the sideband resolution and the coupling regime. Very generally, quantum signatures can better be detected in the resolved sideband regime whereas the Doppler regime is favourable for basic observations with less sophisticated devices or measurements based on excitation with short pulses.

There are two different effects of non-resonant optomechanical coupling related to the real and the imaginary part of the mechanical oscillator's susceptibility. The real part leads to a mechanical frequency shift δf_{m} resulting in the so-called optical spring effect, whereas the imaginary part describes optomechanical damping $\widetilde{\Gamma}_{\mathrm{OM}}$. Both effects will be described separately in the following with an emphasis on the damping aspect.

Optical Spring Effect

A frequency shift δf_{m} of the mechanical mode is associated with the optical spring effect. This will lead to an effective spring-stiffening or spring-softening of the mechanical oscillation [119,120]. Under the assumption of a weak effective optomechanical coupling

with $g_{\mathrm{OM}} \ll \kappa$, the susceptibility can be evaluated at the unperturbed mechanical frequency and δf_{m} can be expressed as

$$\delta f_{\mathrm{m}} = 2\pi g_{\mathrm{OM}}^2 \left(\frac{\Delta_{\mathrm{L}} - \omega_{\mathrm{m}}}{\kappa^2/4 + (\Delta_{\mathrm{L}} - \omega_{\mathrm{m}})^2} + \frac{\Delta_{\mathrm{L}} + \omega_{\mathrm{m}}}{\kappa^2/4 + (\Delta_{\mathrm{L}} + \omega_{\mathrm{m}})^2} \right) \tag{2.63}$$

In the Doppler regime, this can be simplified to

$$\delta f_{\mathrm{m,Doppler}} \approx 2\pi g_{\mathrm{OM}}^2 \frac{2\Delta_{\mathrm{L}}}{\kappa^2/4 + \Delta_{\mathrm{L}}^2} \tag{2.64}$$

It can be seen from these expressions that the effects of positive and negative detuning are qualitatively different. A blue-detuned pump field with $\Delta_{\mathrm{L}} > 0$ is increasing the mechanical resonance frequency. This is also termed spring-hardening in reference to the classical analogue of a mechanical oscillator. For a negative detuning $\Delta_{\mathrm{L}} < 0$ corresponding to a red-detuned driving field, the mechanical oscillation frequency is lowered what is then termed spring-softening.

In the good cavity regime of resolved sidebands, the optical spring effect vanishes completely for excitation on a sideband and pure optomechanical damping characterises the interaction. The optical spring effect can be exploited in order to create squeezed states. The detuning is then not chosen constant over time but altered such that it creates a time-dependent modulation of the mechanical frequency. This parametric driving of the mechanical mode then gives rise to a squeezed phonon state.

Optomechanical Damping

The imaginary part of the mechanical resonator's susceptibility describes an optomechanical damping whose rate is given by

$$\widetilde{\Gamma}_{\mathrm{OM}} = g_{\mathrm{OM}}^2 \left(\frac{\kappa}{\kappa^2/4 + (\Delta_{\mathrm{L}} - \omega_{\mathrm{m}})^2} - \frac{\kappa}{\kappa^2/4 + (\Delta_{\mathrm{L}} + \omega_{\mathrm{m}})^2} \right) \tag{2.65}$$

As in the case of the optical spring effect, the damping can both be positive or negative corresponding to cooling or amplification of the mechanical resonator mode. The effective damping is given by the sum of the internal decay rate of the mechanical resonator and the optomechanical damping rate

$$\widetilde{\Gamma}_{\mathrm{eff}} = \Gamma_{\mathrm{m}} + \widetilde{\Gamma}_{\mathrm{OM}} \tag{2.66}$$

For positive optomechanical damping, the decay of the mechanical oscillator is enhanced by the optomechanical interaction and effective cooling takes place. A negative optomechanical damping leads to an amplification of mechanical motion and phonons are effectively created. The sideband suppression has a strong effect on the optomechanical damping and a distinction between the Doppler regime and the resolved sideband regime is necessary. In the Doppler regime, maximal positive or negative damping can be achieved when driving the optical resonator with a detuning of $\Delta_{\mathrm{L}} = \pm\kappa/2$ corresponding to the maximal slope of the optical mode spectrum. In the resolved sideband regime, the amplification is strongest for excitation on either sideband at $\Delta_{\mathrm{L}} = \pm\omega_{\mathrm{m}}$ or

also higher order sidebands at $\Delta_{\mathrm{L}} = n \cdot \omega_{\mathrm{m}}$. This corresponds to the detuning where the optical spring effect vanishes completely. Also the maximal optomechanical damping rate that can be achieved depends on the sideband resolution.

For an optomechanical system the Doppler regime, the optomechanical damping rate simplifies to

$$\widetilde{\Gamma}_{\mathrm{OM,Doppler}} = 2\pi g_{\mathrm{OM}}^2 \frac{-4\kappa \Delta_{\mathrm{L}}}{\left(\kappa^2/4 + \Delta_{\mathrm{L}}^2\right)} \tag{2.67}$$

For the most efficient pumping at $\Delta_{\mathrm{L}} = \pm\kappa/2$, this expression further reduces to

$$\widetilde{\Gamma}_{\mathrm{OM,Doppler,max}} = \pm 8\omega_{\mathrm{m}} \left(\frac{g_{\mathrm{OM}}}{\kappa}\right)^2 \tag{2.68}$$

The inverse proportionality to the square of the optical resonator decay rate κ indicates that the optomechanical damping rate is rather low in the Doppler regime as this regime is characterised by a bad optical cavity corresponding to a large decay rate κ.

The maximal optomechanical damping rate in the resolved sideband regime is obtained for a laser resonant on either sideband $\Delta_{\mathrm{L}} = \pm\omega_{\mathrm{m}}$ and can be expressed as

$$\widetilde{\Gamma}_{\mathrm{OM,res,max}} = \pm 4 \frac{g_{\mathrm{OM}}^2}{\kappa} \tag{2.69}$$

This shows that optomechanical damping is more efficient in the regime of resolved sidebands than in the Doppler regime [128]. Taking advantage of equation 2.59 and replacing the photon population in the resonator with the help of equation 2.9 in the limit of the resolved sideband regime, the optomechanical damping can be expressed without the decay rate κ of the optical resonator

$$\widetilde{\Gamma}_{\mathrm{OM,res,max}} = \frac{P_{\mathrm{L}}}{\hbar \omega_{\mathrm{L}}} \frac{g_{\mathrm{OM,0}}^2}{\omega_{\mathrm{m}}^2} \tag{2.70}$$

Optomechanical Heating and Phonon Lasing

In the case $\Delta_{\mathrm{L}} > 0$, a blue-detuned excitation of the optical resonator, the mechanical oscillation is subject to negative damping or amplification. The excess energy that the pump field carries with respect to the optical resonator mode is transferred to additional excitation of the mechanical oscillator. For very high pump powers, the optomechanical heating rate $\widetilde{\Gamma}_{\mathrm{OM}}$ can surpass the decay rate of the mechanical oscillator Γ_{m}. This leads to an instability of the mechanical oscillator and the mechanical potential forms a double-well potential. Small fluctuations are then exponentially amplified and self-induced optomechanical oscillations occur. The optical driving field serves as pump for these back-action induced oscillations and the mechanical lasing starts at pump powers above the threshold $\widetilde{\Gamma}_{\mathrm{OM,L}}$

$$\widetilde{\Gamma}_{\mathrm{OM,L}} = \Gamma_{\mathrm{m}} \tag{2.71}$$

Optomechanical Cooling

In the case $\Delta_{\mathrm{L}} < 0$, a red-detuned excitation of the optical resonator mode, optomechanical cooling takes place. The optical excitation is then transferred into a removal of

phonons from the mechanical resonator mode through the optomechanical interaction. The sideband resolution has a strong influence on both the cooling efficiency and the phonon number that finally is present in the system. In absence of a thermal bath, the minimal excitation of the mechanical resonator mode after cooling is expressed in terms of the asymptotic minimal phonon occupation number $\overline{n}_{\mathrm{m,min}}$. This does not correspond to a realistic situation where heating from the environment limits the damping of the mechanical oscillation but it is a common figure of merit for the effectiveness of optomechanical cooling.

In the Doppler regime, the asymptotic minimal phonon occupation number $\overline{n}_{\mathrm{m,min}}$ for the most efficient optomechanical cooling with a detuning at $\Delta_{\mathrm{L}} = -\kappa/2$ is

$$\overline{n}_{\mathrm{m,min,Doppler}} = \frac{\kappa}{4\omega_{\mathrm{m}}} \tag{2.72}$$

In the Doppler regime, the phonon occupation number is thus always $\overline{n}_{\mathrm{m,min}} \gg 1$ as one can directly see when considering the relation in equation 2.53. The quantum ground state of mechanical motion is thus impossible to reach in this case. However, the cooling can be significant for high values of the effective optomechanical coupling constant g_{OM}. An increase in the optical pump power and thus the photon population of the optical mode $\overline{n}_{\mathrm{opt}}$ increases the optomechanical cooling rate. However, high pump powers also heat the sample and provoke the occurrence of a radiation-pressure induced optical bistability [118] or a thermally induced optical bistability [298].

In the case of optomechanical cooling, the asymptotic minimal phonon occupation number that can be reached with an optomechanical system in the resolved sideband regime in the absence of thermal effects is given as

$$\overline{n}_{\mathrm{m,min,res}} = \left(\frac{\kappa}{4\omega_{\mathrm{m}}}\right)^2 \tag{2.73}$$

It can be seen from this expression, that optomechanical cooling in the resolved sideband regime in principle allows reducing the population of the mechanical oscillator below a single phonon [128].

However, the thermal environment of the resonator needs to be considered as the final phonon occupation number $\overline{n}_{\mathrm{f}}$ does not only depend on the optomechanical cooling but also on the rate at which the mechanical resonator mode is populated thermally. The final phonon occupation number of an optomechanical system can generally be expressed as

$$\overline{n}_{\mathrm{f,OM}} = \frac{\widetilde{\Gamma}_{\mathrm{OM}}\overline{n}_{\mathrm{m,min}} + \Gamma_{\mathrm{m}}\overline{n}_{\mathrm{th}}}{\widetilde{\Gamma}_{\mathrm{OM}} + \Gamma_{\mathrm{m}}} \tag{2.74}$$

The temperature T_{f} that can be reached with optomechanical cooling is dependent on the temperature of the thermal bath T, the optomechanical cooling rate $\widetilde{\Gamma}_{\mathrm{OM}}$, and the damping rate of the mechanical oscillator Γ_{m}. Under the assumption of a moderate cooling rate assuring that the final temperature is large enough to neglect radiation pressure fluctuations resulting from photon shot noise, the final temperature is

$$T_{\mathrm{f}} = \frac{\Gamma_{\mathrm{m}}}{\Gamma_{\mathrm{m}} + \widetilde{\Gamma}_{\mathrm{OM}}}T \tag{2.75}$$

In a combination of cryogenic an optomechanical cooling, very low temperatures can be achieved for a system in the regime of resolved sidebands. Even the quantum ground state of the mechanical oscillator can be reached resulting in the absence of thermally excited cavity phonons in this case and phonon population numbers $\overline{n}_{\mathrm{m}} < 1$ could be shown experimentally [139,162,299]. However, photon shot noise of the pump field sets an upper limit for the temperature that can be achieved with optomechanical cooling. Reaching the quantum ground state of motion remains very challenging even with very stable lasers and a certain phonon number typically remains inside the resonator. But also for higher phonon numbers $\overline{n}_{\mathrm{m}} = 2.6$, an asymmetry in the mechanical sidebands can be detected [140]. The absorption and emission of phonons, giving rise to the red- or the blue-detuned sidebands, respectively, have different probabilities due to the limited number of phonons populating the cavity. This leads to a spectrum where the long wavelength sideband gives a stronger spectral signal than the short wavelength sideband. The ratio between the amplitudes in the blue- and the red-detuned sidebands depends on the absolute phonon population of the mechanical resonator mode $\sqrt{\overline{n}_{\mathrm{m}}}$.

$$\frac{I_{\mathrm{red}}}{I_{\mathrm{blue}}} = \frac{\sqrt{\overline{n}_{\mathrm{m}}}}{\sqrt{\overline{n}_{\mathrm{m}} + 1}} \tag{2.76}$$

Detecting this sideband asymmetry is a direct proof for entering the quantum regime of a mechanical oscillator. It confirms that the interaction indeed can be described in the scattering picture where single photons interact with single photons.

Resonant Driving of the Optical Resonator

A resonant excitation corresponding to zero detuning between the drive Laser and the optical resonator mode $\Delta_{\mathrm{L}} = 0$ allows for measuring phase shifts in the light field that is transmitted through the cavity. While a direct excitation or cooling of the mechanical resonator mode through the optical excitation is not possible in this case, there is a number of different applications for a resonantly driven optomechanical system.

Displacement Detection

Measuring the displacement α of the mechanical resonator requires interference between light transmitted through the optical resonator and a local oscillator serving as phase reference. Assuming operation in the Doppler regime, the phase shift θ of the transmitted light field is then proportional to

$$\theta \propto \frac{\alpha \cdot G_{\mathrm{OM,0}}}{\kappa} \tag{2.77}$$

The imprecision of this measurement is directly linked to the number of photons N_{phot} that contribute to the measurement. Such a measurement is limited by photon shot noise and the corresponding imprecision noise is $\delta\theta_{\mathrm{imp}} \sim 1/\sqrt{N_{\mathrm{phot}}}$. This suggests that the readout becomes arbitrarily precise for high photon numbers. This would indeed be true for instantaneous measurements with very high pump powers. However, experiments are limited by finite pump powers that can be coupled into a system. An integration over a

longer measurement time is therefore the much more realistic case and a so-called weak measurement is then performed in a continuous way. The shot noise leads to a fluctuating radiation pressure force that gives an overall jitter on the mechanical oscillation. The effect of shot noise grows with the number of photons involved in the measurement and leads to the so-called back-action noise $\delta\theta_{\mathrm{back}} \sim \sqrt{N_{\mathrm{phot}}}$. As both noise contributions are always present at the same time in the case of a non-instantaneous measurement, there is an optimal photon number for which a maximal precision can be reached. This is known as the standard quantum limit. A "precision beyond the standard quantum limit" means that the imprecision noise is below the standard quantum limit what also implies that the back-action noise is moderate. This could already be demonstrated experimentally with different optomechanical systems [126, 142, 196, 300]. In the case of optomechanical interaction, the standard quantum limit can be linked to an optimal measurement time for a displacement detection. Damping of the mechanical oscillator is the limiting factor for this detection and thus the measurement should be restricted to a timescale shorter than $1/\Gamma_{\mathrm{m}}$. This allows for a displacement measurement with a precision down to the zero point fluctuation x_{ZPF} of the mechanical oscillator. In practice, however, this is challenging to reach. The in-coupling of light is usually poor and it is very difficult to achieve high pump powers inside the optical resonator mode without increasing noise contributions above the threshold.

Quantum Non-Demolition Measurement and Cold Damping

Another application of resonantly driven optomechanical systems are optical quantum non-demolition measurements of the mechanical displacement. Here, only one quadrature is measured in contrast to the previously discussed weak displacement measures where two quadratures are detected simultaneously. By restricting the measurement to a single quadrature, the Heisenberg principle is not setting a limit. This corresponds to an idealised projection measurement and an arbitrary precision can be reached. Therefore, this type of measurement is also called quantum non-demolition detection [105, 301, 302].

In practice, this displacement measurement can be performed in two different ways. One option is to take advantage of the fact that any force applied on the mechanical resonator does not affect its position after a full oscillation period. To this end, either a measurement series with a repetition rate corresponding to the mechanical oscillation frequency, or a drive field whose intensity is modulated at this frequency can be implemented. The variance of the quadrature measured approaches zero what results in a squeezing of any states conditioned on the measurement results. The other possibility is to measure much faster than the mechanical oscillation takes place [153, 154]. This scheme is based on the application of very short but also intense Laser pulses. The optomechanical system should be in the Doppler regime for this type of measurement so that the mechanical resonator is too slow to resolve the optical measurement.

For both measurement protocols, a quantum state tomography is required. The same state needs to be prepared repeatedly and probability densities of the quadrature are measured for a large number of phases. Finally, an inverse Radon transform is applied in order to extract the Wigner density and thus the full quantum state. This has successfully been demonstrated for the vibrational modes of ions [303] and for the

oscillation of a micromechanical cantilever [154].

This type of quantum non-demolition measurement allows for a direct measurement of the mechanical motion with a very high precision. One can take advantage of this detection in order to damp the mechanical motion. The damping can precisely be adjusted to the actual oscillator motion and an active feedback control can be exploited to cool the resonator. This technique has the advantage that it does not increase the thermal noise in the resonator and is therefore also called cold damping or active feedback cooling [129]. This scheme has been investigated theoretically [116] and was realised experimentally in different optomechanical systems [117, 130–132]. The optimal regime of the optomechanical system for this application is the so-called adiabatic regime, a weak coupling in the Doppler regime. The cooling that can be achieved with this active feedback technique is limited by the measurement precision of the mechanical motion and in principle even ground state cooling is possible [129].

Measurement of the Phonon Number

A very direct proof for the quantum nature of a mechanical oscillator is the measurement of the phonon number. In contrast to the quantum non-demolition measurements discussed above, this requires the direct measurement of the square of the displacement α^2 rather than the displacement α. This value is directly proportional to the potential energy and thus the phonon number in the mechanical resonator. Such a measurement can only be achieved if the optical field couples to the square of the displacement α^2. Optomechanical systems based on dispersive coupling can be exploited for this Fock state detection. In contrast to the description of an optomechanical system given in equation 2.44, the Hamiltonian for dispersively coupled optomechanical systems depends on the mechanical displacement squared:

$$\widehat{H}_{\mathrm{OM}}^{(\mathrm{disp})} = \hbar\omega_{\mathrm{opt}}\widehat{a}^\dagger\widehat{a} + \hbar\omega_{\mathrm{m}}\widehat{b}^\dagger\widehat{b} + \hbar g_{\mathrm{OM},0}^{(2)}\widehat{a}^\dagger\widehat{a}\left(\widehat{b}+\widehat{b}^\dagger\right)^2 \tag{2.78}$$

with $g_{\mathrm{OM},0}^{(2)} = \frac{\partial^2\omega_{\mathrm{opt}}}{\partial\alpha^2}x_{\mathrm{ZFP}}^2$. By cooling the mechanical resonator close to the quantum ground state, a time-resolved measurement of the phase shift of the optical field for individual mechanical Fock states can be detected. As losses and noise substantially lower the quality of the results, the necessary condition for a successful measurement is the single photon strong coupling regime under the assumption that absorption is the dominant loss channel. However, it has been investigated theoretically that even if phonon numbers cannot directly be detected, jumps between different Fock states might still be accessible in the form of phonon shot noise [151].

2.6.6   Optomechanical Coupling in Photonic and Phononic Crystals

As discussed in the previous sections, the single photon optomechanical coupling constant $g_{\mathrm{OM},0}$ describes the rate of single photon optomechanical coupling and is the most important measure for estimating the interaction dynamics of the coupled system. In order to determine its value for a specific resonator, the frequency shift of the optical mode per mechanical displacement G_{OM} needs to be calculated as the derivative of the optical frequency ω_{opt} with respect to the mechanical displacement α at equilibrium

(see equation 2.46). In the case of geometrically more simple Fabry-Pérot resonators, the mechanical displacement directly translates in a change of the resonator length and thus the optical frequency shift. For monolithic resonator geometries like photonic and phononic crystal structures, the cavity material itself oscillates and induces a backaction on the optical resonator mode. The deformation of the material then translates in a variation of the function giving rise to optomechanical coupling described by the moving boundaries effect and the photoelastic effect.

A typical excitation of the mechanical mode causes elongations $d\alpha$ in the range of femtometers. This is very small compared to the resonator size and has no impact on the symmetry or shape of the optical mode in a photonic and phononic crystal. Therefore, the mechanical motion can be treated as small perturbation to the optical resonator mode and the first order approximation is valid. The derivative of the optical frequency ω_{opt} with respect to the mechanical displacement α evaluated at equilibrium can then be expressed as

$$\frac{d\omega_{\text{opt}}}{d\alpha} = -\frac{\omega_{\text{opt}}^{(0)}}{2} \frac{\left\langle \mathbf{E}^{(0)} \left| \frac{d\varepsilon}{d\alpha} \right| \mathbf{E}^{(0)} \right\rangle}{\left\langle \mathbf{E}^{(0)} \left| \varepsilon \right| \mathbf{E}^{(0)} \right\rangle} \tag{2.79}$$

Here, the optical frequency $\omega_{\text{opt}}^{(0)}$ and the electric field $\mathbf{E}^{(0)}$ are the properties of the unperturbed optical cavity mode. The optomechanical coupling can thus be assigned to a variation $\frac{d\varepsilon}{d\alpha}$ of the dielectric function ε due to the mechanical displacement α. In the case of a photonic and phononic crystal cavity, optomechanical interaction is based on two different contributions, the moving boundaries effect resulting from a perturbation in the spatial distribution of the electromagnetic field [304] and the photoelastic effect caused by local variations of the refractive index under the influence of mechanical strain [305]. In the following, both these contributions are evaluated individually and finally consolidated to determine the overall optomechanical coupling.

Moving Boundaries Effect

The moving boundaries effect describes a surface phenomenon that occurs when material boundaries of a monolithic optical resonator are shifted during the mechanical oscillation period [304]. This movement leads to a small change in the geometry of the photonic and phononic crystal structure resulting in a slightly different spatial distribution of the dielectric function. During the mechanical oscillation period, the photonic and phononic crystal structure then provides varying resonance conditions for the optical cavity mode. The coupling term can be expressed as surface integral over the entire photonic and phononic crystal cavity.

$$\left\langle \mathbf{E}^{(0)} \left| \frac{d\varepsilon}{d\alpha} \right| \mathbf{E}^{(0)} \right\rangle = \oint (\mathbf{u} \cdot \hat{\mathbf{n}}) \left(\Delta\varepsilon \left| \mathbf{E}_{\parallel} \right|^2 - \Delta\varepsilon^{-1} \left| \mathbf{D}_{\perp} \right|^2 \right) dS \tag{2.80}$$

Here, $\mathbf{u}$ is the mechanical displacement field caused by the oscillation of the mechanical resonator, $\hat{\mathbf{n}}$ is the surface normal vector, and $\Delta\varepsilon = \varepsilon_{\text{dia}} - \varepsilon_0$ the contrast in the dielectric constant between diamond and air with $\Delta\varepsilon^{-1} = \varepsilon_{\text{dia}}^{-1} - \varepsilon_0^{-1}$. From the side of the optical resonator mode, only the electric field component parallel to the surface $\mathbf{E}_{\parallel}$ and the electric displacement field perpendicular to the surface $\mathbf{D}_{\perp}$ contribute to

the optomechanical interaction. The resulting single photon optomechanical coupling constant originating from the moving boundaries effect $g_{\mathrm{MB},0}$ can thus be expressed as

$$g_{\mathrm{MB},0} = -x_{\mathrm{ZPF}} \frac{\omega_{\mathrm{opt}}^{(0)}}{2 \left\langle \mathbf{E}^{(0)} \middle| \varepsilon \middle| \mathbf{E}^{(0)} \right\rangle} \oint (\mathbf{u} \cdot \hat{\mathbf{n}}) \left(\Delta \varepsilon \left| \mathbf{E}_{\parallel} \right|^2 - \Delta \varepsilon^{-1} \left| \mathbf{D}_{\perp} \right|^2 \right) dS \qquad (2.81)$$

The moving boundaries effect is particularly strong when the optical cavity mode is localised near the surface of the structure and when the mechanical elongation at the surface is large. Therefore, cavity modes with large spatial extent show a strong optomechanical coupling resulting from the moving boundaries effect whereas strongly confined modes arising from the dielectric band are less affected by this surface effect.

Photoelastic Effect

The photoelastic effect describes a local variation of the refractive index under the influence of strain in the material. Due to this change in the material's optical density, the propagation of the optical mode is affected by the locally varying dielectric function during the mechanical oscillation period. The optomechanical coupling term attributed to the photoelastic effect can be expressed as volume integral over the photonic and phononic crystal structure.

$$\left\langle \mathbf{E}^{(0)} \middle| \frac{d\varepsilon}{d\alpha} \middle| \mathbf{E}^{(0)} \right\rangle = - \varepsilon_0 \varepsilon_{\mathrm{dia}}^2 \int \left[\sum_{\mathrm{i} \neq \mathrm{j}} p_{44} E_\mathrm{i} E_\mathrm{j} \epsilon_{\mathrm{ij}} \right] dV$$
$$- \frac{1}{2} \varepsilon_0 \varepsilon_{\mathrm{dia}}^2 \int \left[\sum_{\mathrm{i} \neq \mathrm{j} \neq \mathrm{k}} \left| E_\mathrm{i} \right|^2 \left(p_{11} \epsilon_{\mathrm{ii}} + p_{12} \left(\epsilon_{\mathrm{jj}} + \epsilon_{\mathrm{kk}} \right) \right) \right] dV \qquad (2.82)$$

Here, ε_0 is the vacuum permittivity, $\varepsilon_{\mathrm{dia}}$ the standard dielectric constant of diamond, ϵ_{ij} the components of the strain tensor imposed by the mechanical oscillation and p_{11}, p_{12}, and p_{44} the photoelastic constants of diamond, a material property given in section 2.1. The resulting single photon optomechanical coupling constant $g_{\mathrm{PE},0}$ issuing from the photoelastic effect can then be expressed as

$$g_{\mathrm{PE},0} = x_{\mathrm{ZPF}} \frac{\varepsilon_0 \varepsilon_{\mathrm{dia}}^2 \omega_{\mathrm{opt}}^{(0)}}{2 \left\langle \mathbf{E}^{(0)} \middle| \varepsilon \middle| \mathbf{E}^{(0)} \right\rangle} \left(\int \left[\sum_{\mathrm{i} \neq \mathrm{j}} p_{44} E_\mathrm{i} E_\mathrm{j} \epsilon_{\mathrm{ij}} \right] dV \right.$$
$$\left. + \frac{1}{2} \int \left[\sum_{\mathrm{i} \neq \mathrm{j} \neq \mathrm{k}} \left| E_\mathrm{i} \right|^2 \left(p_{11} \epsilon_{\mathrm{ii}} + p_{12} \left(\epsilon_{\mathrm{jj}} + \epsilon_{\mathrm{kk}} \right) \right) \right] dV \right) \qquad (2.83)$$

The photoelastic effect is a volume effect occurring in the bulk of the material. It is strong if the optical cavity field is concentrated in material regions where the mechanical oscillations induce maximum strain. Therefore, strongly confined modes with high local field intensities are generally most suitable for optomechanical coupling based on the photoelastic effect.

Overall Optomechanical Coupling

Very generally, structures optimised for a strong moving boundaries effect exhibit a rather weak photoelastic effect and vice versa, as for the moving boundaries effect the optical field ideally is localised near the diamond surface whereas the photoelastic effect is particularly strong when the electric field is concentrated in the bulk of the material. For both effects individually, the symmetries of the optical and mechanical cavity modes play a crucial role for the strength of the optomechanical coupling. Local optomechanical coupling effects can vanish if the individual contributions at different locations of the photonic and phononic crystal cavity have different signs due to a respective negative or positive elongation of the optical or mechanical cavity field. Fully symmetric optical and mechanical modes mostly avoid this reduction of the interaction strength and allow for good optomechanical coupling. This can also be confirmed with results from numerical modelling shown in section 3.3.2.

The overall optomechanical coupling is determined by the consolidated coupling arising from both the moving boundaries and the photoelastic effect. To this end, the phase shift between the two effects needs to be considered [257]. As both effects can show maximal positive or negative coupling at different times of the mechanical oscillation period, they might at least partly cancel out. If they have opposite signs at maximum elongation, the overall optomechanical coupling is reduced to the difference between the individual effects, whereas the overall coupling can also consist of the sum of both effects when they are acting in phase. This would lead to an even stronger coupling than both contributions could provide individually. In the structures considered here, the contributing effects are out of phase for the most suitable mechanical resonator mode and the photoelastic effect is substantially stronger than the moving boundaries effect (see section 3.3.2). For achieving high optomechanical coupling constants, the photoelastic effect should further be enhanced and the moving boundaries effect is to be suppressed. For the design of the optomechanical resonator this means that strongly confined fundamental modes of high symmetry should be exploited. As additional benefit, these are also the modes that allow for reaching high optical and mechanical quality factors and that are best suitable for strain coupling.

2.7 Strain Coupling

Strain coupling describes the interaction between an emitter and a mechanical resonator. Here, only the case of direct strain coupling is considered where no other degree of freedom is required to mediate the interaction. This is an inherent feature of solid state two-level systems and the description will be limited to the interaction of a localised mechanical resonator mode and a single nitrogen vacancy colour centre in diamond.

In a classical description, the effect of strain on the nitrogen vacancy colour centre can be understood by considering the deformation of electronic orbitals in a strained material. Static strain permanently deforms the local environment of the colour centre and shifts the different electronic levels. The interaction is stronger for electrons with a larger distance to the centre and accordingly, the excited states couple stronger to the mechanical motion than the ground state levels. A dynamic strain leads to a

dynamic modulation of the deformation and a constantly varying level structure. The deformation of the colour centre's orbital structure will also back-act on the mechanical oscillator. A strained colour centre creates a local charge perturbation and the ions of the surrounding crystal will feel a back-action force. This feedback is retarded against the initial motion and can thus lead to either damping or amplification of the mechanical oscillation.

In a quantum mechanical description, a scattering picture can be used to describe strain coupling. The individual phonons populating the mechanical resonator mode interact with the individual electrons of the nitrogen vacancy colour centre. Phonon creation or annihilation during a dipole transition alternates the effective level structure of the emitter and an shift corresponding to the phononic energy will occur. Also in this picture, the interaction will be stronger for the excited states as their interaction cross-section with the mechanical oscillation is larger due to their larger spatial extension.

In the following, a Hamilton formalism will be used in order to describe the strain coupling interaction based on a symmetric strain tensor. As only symmetric parts of the strain tensor affect the structure of a defect and antisymmetric components only cause a rotation, this assumption should be valid [306]. In the internal coordinate system of the nitrogen vacancy colour centre given in section 2.4.1, the strain tensor ϵ can then be expressed based on the individual entries ϵ_{ij} as

$$\epsilon = \begin{pmatrix} \epsilon_{xx} & \epsilon_{xy} & \epsilon_{xz} \\ \epsilon_{xy} & \epsilon_{yy} & \epsilon_{yz} \\ \epsilon_{xz} & \epsilon_{yz} & \epsilon_{zz} \end{pmatrix} \tag{2.84}$$

For reasons of clarity, the interaction with the ground and excited states will be described in separate paragraphs. To quantify the effect of strain coupling on the optical transition, both contributions need to be considered in principle. However, as the effect is orders of magnitude stronger for the excited state levels $|E_x\rangle$ and $|E_y\rangle$, the ground state coupling can be neglected for this purpose. Without loss of generality, the orientation of the nitrogen vacancy colour centre is assumed to be along the [111] axis with respect to the crystallographic coordinates for simplicity. The results obtained from this description can equally be applied to its other three possible orientations.

2.7.1   Coupling to the Ground State Levels

The strain coupling between the ground state levels of a nitrogen vacancy colour centre and a mechanical resonator mode can best be described in a Hamiltonian formulation. There are two formalisms that can be used in order to describe this interaction. The most widely used description results from a purely phenomenological approach where the corresponding strain coupling coefficients have been found in independent measurements by two different teams [163, 173, 174]. Very recently, an alternative approach has been published that is based on a group theoretical calculation involving the intrinsic symmetry properties of the nitrogen vacancy colour centre [307]. This more complete description of the interaction between an arbitrary strain field and the nitrogen vacancy colour centre is drawing on early theoretical work describing the electronic structure of

the colour centre [265]. Here, both formalisms are presented and in section 3.4.1, the interaction is modelled independently with both approaches.

Phenomenological Description

In the purely phenomenological description, the interaction between the ground state levels of the nitrogen vacancy colour centre and a strain field in the absence of a magnetic field can be described by the following Hamiltonian.

$$\widehat{H}_{\text{strain,ground,pheno}} = D_0\widehat{S}_z^2 + \hbar\omega_{\text{m}}\widehat{b}^\dagger\widehat{b} + \widehat{H}_\parallel + \widehat{H}_\perp \tag{2.85}$$

Here, $D_0 = 2.88\,\text{GHz}$ is the zero-field splitting of diamond that lifts the degeneracy between the $|0\rangle$ and $|\pm1\rangle$ states, ω_{m} is the oscillation frequency of the mechanical resonator, $\widehat{S}_z$ the component of the nitrogen vacancy spin along the [111] axis, and $\widehat{b}$ and $\widehat{b}^\dagger$ are the phonon creation and annihilation operators. The interaction part consists of two different contributions, $\widehat{H}_\parallel$ and $\widehat{H}_\perp$. These interaction Hamiltonians for strain along and perpendicular to the symmetry axis of the nitrogen vacancy colour centre are given by the following equations.

$$\widehat{H}_\parallel = g_\parallel \widehat{S}_z^2 \left(\widehat{b} + \widehat{b}^\dagger\right) \tag{2.86}$$

$$\widehat{H}_\perp = g_\perp \left(e^{i\phi}\widehat{S}_+^2 + e^{-i\phi}\widehat{S}_-^2\right)\left(\widehat{b} + \widehat{b}^\dagger\right) \tag{2.87}$$

Here , $\widehat{S}_+$ and $\widehat{S}_-$ are the spin raising and lowering operators defined as $\widehat{S}_\pm = \widehat{S}_x \pm i\widehat{S}_y$ and the angle ϕ is determined by the relation $\tan(\phi) = \epsilon_{xx}/\epsilon_{yy}$. The strain coupling constants $g_\parallel$ and $g_\perp$ describe the interaction rate between the ground state levels of the nitrogen vacancy colour centre and axial or radial strain field contributions of a mechanical resonator, respectively. This distinction takes into account that axial strain $\epsilon_\parallel = \epsilon_{zz}$ (along [111]) and radial strain $\epsilon_\perp = \sqrt{\epsilon_{xx}^2 + \epsilon_{yy}^2}$ (perpendicular to [111]) have qualitatively different effects on the nitrogen vacancy colour centre. Axial strain causes an additional splitting between the $|0\rangle$ and the $|\pm1\rangle$ states similar to the effect of the crystal field splitting D_0. Radial strain, in contrast, mixes the $|+1\rangle$ and $|-1\rangle$ levels and causes a splitting of the resulting mixed states with non-zero spin projection. This allows for driving the forbidden transitions between the states $m_s = +1$ and $m_s = -1$ when addressing the ground state of the nitrogen vacancy colour centre with a strain field. The strain coupling constants to the nitrogen vacancy colour centre ground state for the mechanical strain fields $\epsilon_\parallel$ and $\epsilon_\perp$ are given by the following equations

$$g_\parallel = d_\parallel\epsilon_\parallel \tag{2.88}$$

$$g_\perp = d_\perp\epsilon_\perp/2 \tag{2.89}$$

with $d_\parallel$ and $d_\perp$ as the axial and radial strain coupling coefficients, respectively. A higher phonon population of the mechanical resonator mode leads to a stronger coupling to the nitrogen vacancy colour centre in analogy to the non-linear interaction in the case of optomechanical interaction. For a strain field corresponding to the zero point motion of the mechanical oscillator, the above expressions correspond to the single phonon

strain coupling constants. The strain coupling coefficients $d_\parallel$ and $d_\perp$ are properties of the nitrogen vacancy colour centre and have been determined in measurements by two teams independently [173,174]. The corresponding values are given in table 2.1 where it can be seen that the two sets of values are in the same range but do not exactly match.

	Basel	UCSB
$d_\parallel$	$5.46 \pm 0.31\,\mathrm{GHz}$	$13.4 \pm 0.8\,\mathrm{GHz}$
$d_\perp$	$-19.63 \pm 0.40\,\mathrm{GHz}$	$-21.5 \pm 1.2\,\mathrm{GHz}$

Table 2.1: Strain coupling coefficients for the ground state levels of the nitrogen vacancy colour centre reported in reference [173] (Basel) and in reference [174] (UCSB).

Possible explanations for the deviating values as given by the authors are that the measurement techniques employed by the two groups are subject to unwanted side-effects to a different extent, and that some of the samples used in the underlying experiments do have non-perfect properties with respect to emitter homogeneity. Despite the fact that the discrepancies appear quite significant especially for $d_\parallel$, both groups confirm that the values are in good agreement. In an independent work, experimental results for $d_\parallel$ obtained from hydrostatic measurements seem to confirm the higher values reported in reference [174] whereas the corresponding theoretical calculations suggest that the lower values reported in reference [173] are more trustworthy [308]. Therefore, both sets of strain coupling coefficients are used in this work and all results are given for both values.

Group Theoretical Description

The description of strain coupling to the ground state levels of the nitrogen vacancy colour centre derived from group theoretical calculations is taken from reference [307]. The description is based on the stress tensor components expressed in the crystallographic coordinates $X = [100]$, $Y = [010]$, and $Z = [001]$. The nitrogen vacancy colour centre is described by the coordinates $x' = 1/\sqrt{6}\,[\bar{1}\bar{1}2]$, $y' = 1/\sqrt{2}\,[1\bar{1}0]$, and $z' = 1/\sqrt{3}\,[111]$. In contrast to the coordinates used throughout this work ($x = 1/\sqrt{2}\,[\bar{1}10]$, $y = 1/\sqrt{6}\,[1\bar{1}\bar{2}]$, and $z = 1/\sqrt{3}\,[111]$), this coordinate system is left-handed. This means that the rotations performed in the process of deriving the formalism do not properly perform the intended coordinate transformations. The consequences of this inconsistency will be discussed in section 3.4.1 where also the results from numerical modelling are shown. According to the formalism in reference [307], the Hamiltonian for the ground state levels of the nitrogen vacancy colour centre coupling to a mechanical resonator mode in absence of a magnetic field, can be noted as follows.

$$\widehat{H}_{\mathrm{strain,ground,group}} = D_0 \left(\widehat{S}_{z'}^2 - \frac{2}{3} \right) + \hbar\omega_\mathrm{m}\widehat{b}^\dagger\widehat{b} + \widehat{H}_{\mathrm{M_x}} + \widehat{H}_{\mathrm{M_y}} + \widehat{H}_{\mathrm{M_z}} \qquad (2.90)$$

Here, $D_0 = 2.88\,\mathrm{GHz}$ is the zero-field crystal splitting, ω_m the resonance frequency of the mechanical oscillation, $\widehat{b}$ and $\widehat{b}^\dagger$ are the phonon creation and annihilation operators and $\widehat{S}_{z'}$ is the component of the electron spin operator along the symmetry axis of the

nitrogen vacancy colour centre. The interaction is described by the terms $\widehat{H}_{M_x}$, $\widehat{H}_{M_y}$, and $\widehat{H}_{M_z}$ given by the following equations

$$\widehat{H}_{M_x} = -g_{M_x}\left(\widehat{S}_{y'}^2 - \widehat{S}_{x'}^2\right)\left(\widehat{b} + \widehat{b}^\dagger\right) \tag{2.91}$$

$$\widehat{H}_{M_y} = g_{M_y}\left(\widehat{S}_{x'}\widehat{S}_{y'} + \widehat{S}_{y'}\widehat{S}_{x'}\right)\left(\widehat{b} + \widehat{b}^\dagger\right) \tag{2.92}$$

$$\widehat{H}_{M_z} = g_{M_z}\left(\widehat{S}_{z'}^2 - 2/3\right)\left(\widehat{b} + \widehat{b}^\dagger\right) \tag{2.93}$$

$\widehat{S}_{x'}$, $\widehat{S}_{y'}$, and $\widehat{S}_{z'}$ are the components of the dimensionless spin operator $\widehat{S}$ defined in the coordinate system x', y', and z' used to describe the nitrogen vacancy colour centre in the original article. g_{M_x}, g_{M_y}, and g_{M_z} are the strain coupling constants that determine the single phonon interaction strength. Qualitatively, g_{M_z} describes an additional splitting between the ground state levels of zero and non-zero spin projection $|0\rangle$ and $|\pm 1\rangle$. Strain coupling also leads to a splitting $\Delta_\pm$ between the states $|-1\rangle$ and $|+1\rangle$. This splitting can be determined as $\Delta_\pm = 2 \cdot g_{M_\Delta}$ with the help of an overall strain coupling constant g_{M_Δ}.

$$g_{M_\Delta} = \sqrt{g_{M_x}^2 + g_{M_y}^2} \tag{2.94}$$

The individual strain coupling constants are given as function of the stress field components acting on the nitrogen vacancy colour centre. In this case, they are expressed in the external system defined by the crystallographic coordinates X, Y, and Z. This is different from the previously shown formalism where the interaction was evaluated based on the strain field expressed in the internal system defined by the colour centre coordinates. The authors of the original article justify this difference with the argument that the assumption of isotropy is not strictly given in the case of diamond. Despite the fact that the raw data of the simulation are based on a isotropic material counteracting this intention, the exact formalism of the original article needs to be followed in order to obtain a complete and meaningful description. The individual strain coupling constants are given by the following equations.

$$g_{M_x} = b\left(2\sigma_{ZZ} - \sigma_{XX} - \sigma_{YY}\right) + c\left(2\sigma_{XY} - \sigma_{YZ} - \sigma_{ZX}\right) \tag{2.95}$$

$$g_{M_y} = \sqrt{3}\left[b\left(\sigma_{XX} - \sigma_{YY}\right) + c\left(\sigma_{YZ} - \sigma_{ZX}\right)\right] \tag{2.96}$$

$$g_{M_z} = a_1\left(\sigma_{XX} + \sigma_{YY} + \sigma_{ZZ}\right) + 2a_2\left(\sigma_{YZ} + \sigma_{ZX} + \sigma_{XY}\right) \tag{2.97}$$

Here, σ_{IJ} are the entries of the stress tensor describing the mechanical oscillation at the position of the colour centre expressed in terms of the external coordinates of the crystallographic axes. As the model is based on an isotropic medium, a symmetric strain tensor will be used to calculate the strain coupling constants such that $\sigma_{IJ} = \sigma_{JI}$. The strain coupling coefficients a_2, b, and c have been determined in measurements described in the article, whereas the value for a_1 has been adopted as reference from a previous measurement performed with the help of hydrostatic pressure [308]. The corresponding values are listed in table 2.2.

This gives a full description of strain coupling to the ground state levels of the nitrogen vacancy colour centre that will be used for modelling the interaction with the diamond

a_1	$4.86 \pm 0.02 \cdot 10^{-3}\,\mathrm{Hz/Pa}$
a_2	$-3.7 \pm 0.02 \cdot 10^{-3}\,\mathrm{Hz/Pa}$
b	$-2.3 \pm 0.03 \cdot 10^{-3}\,\mathrm{Hz/Pa}$
c	$3.5 \pm 0.03 \cdot 10^{-3}\,\mathrm{Hz/Pa}$

Table 2.2: Strain coupling coefficients for the ground state levels of the nitrogen vacancy colour centre reported in reference [307].

structure as shown in section 3.4.1. However, the results need to be interpreted with a certain amount of reservation due to the inconsistency related to the left-handed coordinate systems at the basis of the derivation.

2.7.2   Coupling to the Excited State Levels

The description of the interaction between strain and the excited state levels of the nitrogen vacancy colour centre is taken from references [176], and [163]. The description is based on a complete theoretical model [309] that was reformulated and expressed more generally later on [306]. The strain coupling coefficients are achieved by fitting measured data to this theoretical description. The description is limited to the excited states with zero spin projection $|E_x\rangle$ and $|E_y\rangle$, as experimental data for the coupling coefficients are not available for the other electronic levels.

Due to the C_{3v} symmetry of the nitrogen vacancy colour centre, only strain of symmetries corresponding to A_1, E_1 and E_2 phonon modes needs to be considered. The interaction between a strain field and the excited state levels $|E_x\rangle$ and $|E_y\rangle$ with $m_s = 0$ can then be described by the following Hamiltonian:

$$\widehat{H}_{\mathrm{strain,excited}} = \hbar\omega_{\mathrm{ZPL}} \left(|E_x\rangle \langle E_x| + |E_y\rangle \langle E_y|\right) + \hbar\omega_m \widehat{b}^\dagger\widehat{b} + \widehat{H}_{\mathrm{A_1}} + \widehat{H}_{\mathrm{E_1}} + \widehat{H}_{\mathrm{E_2}} \quad (2.98)$$

Here, ω_{ZPL} is the transition frequency from the excited states $|E_x\rangle$ and $|E_y\rangle$ to the ground state $|0\rangle$, ω_{m} is the resonance frequency of the mechanical resonator and $\widehat{b}$ and $\widehat{b}^\dagger$ are the phonon creation and annihilation operators. The different interaction terms $\widehat{H}_{\mathrm{A_1}}$, $\widehat{H}_{\mathrm{E_1}}$, and $\widehat{H}_{\mathrm{E_2}}$ describe the strain coupling to phonons of different symmetry and are defined as:

$$\widehat{H}_{\mathrm{A_1}} = g_{\mathrm{A_1}} \left(|E_x\rangle \langle E_x| + |E_y\rangle \langle E_y|\right) \left(\widehat{b} + \widehat{b}^\dagger\right) \quad (2.99)$$

$$\widehat{H}_{\mathrm{E_1}} = g_{\mathrm{E_1}} \left(|E_x\rangle \langle E_x| - |E_y\rangle \langle E_y|\right) \left(\widehat{b} + \widehat{b}^\dagger\right) \quad (2.100)$$

$$\widehat{H}_{\mathrm{E_2}} = g_{\mathrm{E_2}} \left(|E_x\rangle \langle E_y| + |E_y\rangle \langle E_x|\right) \left(\widehat{b} + \widehat{b}^\dagger\right) \quad (2.101)$$

Here, $g_{\mathrm{A_1}}$, $g_{\mathrm{E_1}}$, and $g_{\mathrm{E_2}}$ are the strain coupling constants for phonons of the corresponding symmetry, and $\widehat{b}$ and $\widehat{b}^\dagger$ are the phonon creation and annihilation operators. This equation is only valid for the assumption that the ground state is defined at zero energy

so that the mixing of the excited states with the ground state can be neglected. Strain with A_1-symmetry maintains the C_{3v} symmetry of the nitrogen vacancy colour centre and leads to a uniform shift of the excited state levels with respect to the ground state. Strain with E-type symmetry breaks the symmetry of the nitrogen vacancy colour centre and leads to a mixing and splitting of the excited state levels $|E_x\rangle$ and $|E_y\rangle$. The degeneracy is then lifted and the splitting between the excited state levels Δ_{xy} can be expressed as $\Delta_{xy} = 2 \cdot g_{E_\Delta}$ with an overall strain coupling constant including all contributions from strain of E-type symmetry.

$$g_{E_\Delta} = \sqrt{g_{E_1}^2 + g_{E_2}^2} \tag{2.102}$$

The individual strain coupling constants are given explicitly as

$$\begin{aligned}
g_{A_1} &= \lambda_{A_1}\epsilon_{zz} + \lambda_{A_1'}\left(\epsilon_{xx} + \epsilon_{yy}\right) & \text{(2.103)} \\
g_{E_1} &= \lambda_E\left(\epsilon_{yy} - \epsilon_{xx}\right) + \lambda_{E'}\left(\epsilon_{xz} + \epsilon_{zx}\right) & \text{(2.104)} \\
g_{E_2} &= \lambda_E\left(\epsilon_{xy} + \epsilon_{yx}\right) + \lambda_{E'}\left(\epsilon_{yz} + \epsilon_{zy}\right) & \text{(2.105)}
\end{aligned}$$

Here, ϵ_{ij} are the strain tensor components of the mechanical resonator field expressed in the internal coordinates describing the nitrogen vacancy colour centre ($x = 1/\sqrt{2}\,[\bar{1}10]$, $y = 1/\sqrt{6}\,[\bar{1}\bar{1}2]$, and $z = 1/\sqrt{3}\,[111]$). For obtaining the single phonon coupling constants, the strain tensor needs to correspond to an elongation by the zero point motion. This fact indicates that an increase of the mechanical oscillator's phonon population will also enhance the strain coupling interaction. The excited state strain coupling coefficients λ_{A_1}, $\lambda_{A_1'}$, λ_E, and $\lambda_{E'}$ were determined experimentally [176].

λ_{A_1}	$-1.95 \pm 0.29\,\text{PHz}$
$\lambda_{A_1'}$	$2.16 \pm 0.32\,\text{PHz}$
λ_E	$-0.85 \pm 0.13\,\text{PHz}$
$\lambda_{E'}$	$0.02 \pm 0.01\,\text{PHz}$

Table 2.3: Strain coupling coefficients for the excited state levels $|E_x\rangle$ and $|E_y\rangle$ of the nitrogen vacancy colour centre reported in reference [176].

The corresponding values are given in table 2.3. These results are in agreement with previous estimations that the coupling coefficients are in the range of approximately $2\,\text{PHz}$ and that $\lambda_{E'}$ is negligible as compared to the other coefficients [306]. Under the assumption of a symmetric strain tensor, the coupling constants g_{E_1} and g_{E_2} reduce to the following expressions:

$$g_{E_1} = \lambda_E\left(\epsilon_{yy} - \epsilon_{xx}\right) + 2\lambda_{E'}\epsilon_{xz} \tag{2.106}$$

$$g_{E_2} = 2\lambda_E\epsilon_{xy} + 2\lambda_{E'}\epsilon_{yz} \tag{2.107}$$

In addition to a splitting, also the polarisation of the transition is affected by strain. According to literature [176], the rotation angle of the polarisation θ is defined by the

following relation

$$\tan\left(2\theta\right) = \frac{g_{E_2}}{g_{E_1}} \tag{2.108}$$

However, as the different radial strain coupling contributions cannot be isolated or controlled individually, the polarisation cannot be controlled at the same time and independently from an energy shift of the electronic levels. Only when the spin-orbit coupling of $5.5\,\mathrm{GHz}$ would be surpassed by strain coupling, the polarisation properties of the nitrogen vacancy colour centre's optical transition would significantly change [306]. There is no device known to date where strain-coupling on the single phonon level is so strong that the description via a polarisation rotation would not be valid.

2.7.3   Coupling Regimes

In the following, the distinction between the ground and excited state strain coupling constants will be omitted. A generalised strain coupling constant g_{SC} is employed to quantify the interaction strength and the abstract decay rate γ_{NV} describes the coherence time of the two-level system. In the case of ground state strain coupling, it corresponds to the spin decoherence rate γ_{ground} whereas it denotes the radiative decay rate γ_0 in the case of the excited state levels $|E_x\rangle$ and $|E_y\rangle$.

The strain coupling constants are not generally expressed at the single phonon level. The phonon energies are low as compared to typical bath temperatures and the mechanical mode will be subject to thermal population. This means that the strain coupling interaction is inherently non-linear in contrast to the optomechanical interaction. An expression on the single phonon level is thus only relevant to obtain an absolute scaling that allows to compare the interaction strength in fundamentally different devices. The single phonon strain coupling constant $g_{SC,0}$ can be obtained in two ways. It can either be calculated by scaling the population of the mechanical mode to a single phonon such that the components of the strain tensor inherently correspond to a single phonon excitation, the zero point fluctuation. Alternatively, the following relation with the phonon population number of the mechanical mode $\overline{n}_m$ can be used:

$$g_{SC} = \sqrt{\overline{n}_m}\, g_{SC,0} \tag{2.109}$$

In the following, all figures of merit are expressed at the multi-phonon level. The strain coupling cooperativity C_{SC} gives a measure on the dynamics of the coupled system. In the large strain coupling cooperativity regime $C_{SC} > 1$, the interaction governs the dynamics of the coupled system. The cooperativity is defined as

$$C_{SC} = \frac{g_{SC}^2}{\gamma_{NV}\Gamma_m} \tag{2.110}$$

with Γ_m being the decay rate of the mechanical resonator. By inserting the expression for the mechanical decay rate given in equation 2.16, the strain coupling cooperativity can be expressed explicitly as

$$C_{SC} = \frac{2\pi g_{SC}^2 Q_m}{\gamma_{NV} f_m} \tag{2.111}$$

The large cooperativity regime $C_{\text{SC}} > 1$ is required for applications like single phonon routing or for generating long-range interaction between distant nitrogen vacancy colour centres [25, 310] An even stricter condition, the strong strain coupling regime can be reached when the strain coupling constant is larger than the individual decay rates of both the mechanical resonator and the emitter.

$$g_{\text{SC}} > (\gamma_{\text{NV}}, \Gamma_{\text{m}}) \qquad (2.112)$$

The nitrogen vacancy colour centre and the mechanical resonator share a common eigenstate in this case. The even stricter condition of coherent strain coupling also takes into account that the mechanical resonator mode is not only subject to damping but also to a thermal decoherence process.

$$g_{\text{SC}} > (\gamma_{\text{NV}}, \Gamma_{\text{th}}) \qquad (2.113)$$

In this case, the interaction becomes quantum coherent and the exchange of energy between the mechanical resonator mode and the nitrogen vacancy colour centre is reversible. Besides increasing the interaction strength by increasing the phonon population of the mechanical mode, also the number of emitters can enhance the strain coupling. The collective strain coupling constant is defined as

$$g_{\text{SC,eff}} = g_{\text{SC}} \sqrt{N_{\text{NV}}} \qquad (2.114)$$

with N_{NV} the number of nitrogen vacancy colour centres involved in the interaction. This situation will not be investigated further in this work as the focus here is on the single-particle interaction.

As in the case of optomechanical coupling, not only the interaction strength but also the sideband resolution is characterising the interaction. In the case of strain coupling, resolved sidebands mean that the mechanical frequency is larger than the linewidth of the two-level-system.

$$\omega_{\text{m}} > \gamma_{\text{NV}} \qquad (2.115)$$

In the case of coupling to the orbital states of the nitrogen vacancy colour centre, the mechanical frequency needs to be larger than the linewidth of the optical transition and can be detected in the optical spectrum of the colour centre in the form of mechanical sidebands to the zero phonon line.

2.7.4 Driven Strain Coupled Systems

The applications of strain coupled systems in the context of hybrid quantum systems and for sensing tasks are various. While they come in various different manifestations, the fundamental requirement for all of them is a control field to exploit the interaction. Many experimental protocols are based on mechanically driven strain coupled systems. Coherent control of the nitrogen vacancy colour centre spin states [167] as well as the observation of a phononic Mollow triplet structure [168] could be achieved with the help of an actuated mechanical resonator interacting with the nitrogen vacancy colour centre through magnetically mediated strain coupling. Also strong driving, accessing

the dipole-forbidden transition $|+1\rangle$ to $|-1\rangle$, and continuous dynamical decoupling could be demonstrated with the ground state levels of the nitrogen vacancy colour centres coupling to a mechanical oscillation [170, 175]. However, there is no technique available to date that would allow to drive a mechanical resonator with frequencies of several GHz. The phononic crystal structure investigated in this work can therefore not directly be actuated and the investigation of mechanically driven strain coupled systems is not relevant to study the interaction in the considered diamond structure. The following analysis will thus be restricted to the interaction between a passive mechanical cavity mode and a driven transition between different electronic levels of the nitrogen vacancy colour centre.

As in the case of optomechanical interaction, the cooling of the mechanical resonator mode is the most prominent example for the application of strain coupling. In contrast to the simple situation with a single optical resonator mode, the situation is much more complex for the interaction of a mechanical cavity mode with the nitrogen vacancy colour centre. The different ground and excited state levels shown in figure 2.4 can be exploited in various experimental protocols. Generally, the use of the ground state levels brings the advantage of very long coherence times. However, the optical access channel to the excited state levels allows for a practical implementation with standard optical techniques, and the high strain coupling constants to the exciting state levels facilitate reaching a strong interaction.

Cooling based on the Ground State Levels

A cooling procedure based on the ground state levels of the nitrogen vacancy colour centre has been proposed in reference [164]. This protocol requires the generation of dressed spin states what can be achieved by applying a microwave field on the transition between the $|0\rangle$ and $|\pm1\rangle$ levels with a Rabi frequency Ω and a detuning Δ_{MW}. The resulting states $|d\rangle$, $|g\rangle$, and $|e\rangle$ are given by the following projections of the spin state levels of the nitrogen vacancy colour centre with $\tan\theta = -\sqrt{2}\Omega/\Delta_{\mathrm{MW}}$.

$$|d\rangle = \frac{1}{\sqrt{2}}\left(|+1\rangle - |-1\rangle\right) \tag{2.116}$$

$$|g\rangle = \cos\theta\,|0\rangle - \frac{1}{\sqrt{2}}\sin\theta\left(|+1\rangle + |-1\rangle\right) \tag{2.117}$$

$$|e\rangle = \sin\theta\,|0\rangle + \frac{1}{\sqrt{2}}\cos\theta\left(|+1\rangle + |-1\rangle\right) \tag{2.118}$$

When the mechanical resonator frequency ω_{m} is resonant on the transition between the dressed states $|g\rangle$ and $|d\rangle$, the Hamiltonian of the coupled system takes the form of an effective Jaynes-Cummings interaction. The coupling constant then corresponds to the strain coupling constant $g_{\parallel}$ expressing the interaction between the ground state levels of the nitrogen vacancy colour centre and strain along the [111] axis. The dressed state $|g\rangle$ can then be excited to the dressed state $|d\rangle$ upon removal of a phonon from the mechanical resonator corresponding to the transition $|g\rangle\,|n\rangle \rightarrow |d\rangle\,|n-1\rangle$. An optical re-pump can then re-initialise the system without adding energy so that this process can be repeated and an effective cooling of the mechanical mode is possible. As this cooling

protocol is based on the spin state levels with very long coherence times, it is very stable against external noise. The cooling rate associated with this protocol depends on the strain coupling constant $g_\parallel$ and the decay rate of the ground state levels γ_{ground} as follows

$$\widetilde{\Gamma}_{\text{SC,ground}} \sim \frac{g_\parallel^2}{\gamma_{\text{ground}}} \tag{2.119}$$

The final phonon occupation number of the mechanical resonator mode that can be achieved with this cooling scheme is

$$\overline{n}_{\text{f,SC,ground}} \sim \frac{\overline{n}_{\text{th}}\omega_{\text{m}}}{Q_{\text{m}}\widetilde{\Gamma}_{\text{SC,ground}}} = \frac{k_{\text{B}}T\gamma_{\text{ground}}}{Q_{\text{m}}\hbar g_\parallel^2} \tag{2.120}$$

This means that a good confinement of the mechanical resonator mode allowing for a high strain coupling constant, and a slowly decaying mechanical resonator are favourable for reaching low phonon numbers. However, a large decay rate of the nitrogen vacancy colour centre and a high temperature of the thermal bath counteract an effective reduction of the phonon number.

Cooling based on the Excited State Levels with Zero Spin Projection

For the excited state levels, there are two different cooling protocols that have been described in a theoretical proposal [311]. On the one hand, classical sideband cooling is also possible based on the excited state levels. The higher strain coupling constants potentially allow for a more efficient cooling compared to the above-mentioned protocol based on the ground state levels. On the other hand, a more advanced scheme has been worked out that exploits the doublet structure of the excited state levels $|E_x\rangle$ and $|E_y\rangle$.

For the first cooling protocol, the resolved sideband regime of strain coupling to the excited state levels is advantageous. The optical transition between the $|0\rangle$ ground state and the excited state levels with zero spin projection $|E_x\rangle$ and $|E_y\rangle$ is driven with a detuning $\Delta_{\text{L}} = -\omega_{\text{m}}$. The cooling rate that can be achieved with this sideband cooling is then dependent on the coupling constant g_{E_1} corresponding to the relative shift of the excited state levels of the nitrogen vacancy colour centre and the optical Rabi frequency Ω.

$$\widetilde{\Gamma}_{\text{SC,side}} = \frac{g_{\text{E}_1}^2 \Omega^2}{\gamma_0 \omega_{\text{m}}^2} \tag{2.121}$$

It can be seen that the proportionality of the cooling rate to $1/\omega_{\text{m}}^2$ is a disadvantage for the high mechanical frequencies in phononic crystal structures. However, the large coupling constants that can be achieved through the strong spatial confinement of the mechanical mode can mitigate the lower cooling rates.

The second cooling protocol based on the doublet structure of the excited state levels works best when the splitting between the electronic levels with zero spin projection corresponds to the frequency of the mechanical resonator mode ω_{m}. The transition between the ground state and the lower level $|E_y\rangle$ is resonantly excited by a driving laser at Rabi frequency Ω. This state can then either directly decay back to the ground state or decay via a phonon-induced transition from the second excited state level $|E_x\rangle$.

This decay via the state $|E_x\rangle$ removes a phonon from the mechanical resonator mode. Under the assumption of a weak collective coupling, the cooling rate of the mechanical resonator mode can then be expressed as

$$\widetilde{\Gamma}_{\mathrm{SC,doublet}} = 4\frac{g_{\mathrm{E}_2}^2 \Omega^2}{\gamma_0^3} \tag{2.122}$$

In contrast to the sideband cooling protocol, the cooling rate does not depend on the mechanical resonator frequency ω_{m} and can be maximised by saturating the optical transition with $\Omega \approx \gamma_0$. This makes this resonant cooling protocol exploiting the doublet structure of the excited state levels more efficient than classical sideband cooling.

To achieve optimal cooling, the optical transition should be saturated $\Omega = \gamma_0$ in the case of doublet cooling while the optical transition should best be driven at the mechanical resonance frequency $\Omega = \omega_{\mathrm{m}}$ in the case of sideband cooling. Assuming that the strain coupling constants g_{E_1} and g_{E_2} are of the same order, the cooling rates compare as

$$\frac{\widetilde{\Gamma}_{\mathrm{SC,doublet}}}{\widetilde{\Gamma}_{\mathrm{SC,side}}} = 4\frac{\omega_{\mathrm{m}}^2}{\gamma_0^2} \tag{2.123}$$

Interestingly, the final phonon occupation number does not depend on the choice of the cooling protocol. Under the assumption that the strain coupling constants g_{E_1} and g_{E_2} are comparable and that the optimal cooling rate is reached in both cases, the final population of the mechanical resonator mode is given as

$$\overline{n}_{\mathrm{f,doublet}} = \overline{n}_{\mathrm{f,side}} = \frac{\gamma_0 k_{\mathrm{B}} T}{Q_{\mathrm{m}} \hbar g_{\mathrm{E}}^2} \tag{2.124}$$

The phonon occupation number can thus best be reduced with a high quality mechanical resonator that strongly couples to the nitrogen vacancy colour centre. Also cryogenic temperatures help with reaching low phonon numbers as the thermal population of the mechanical resonator is then slower as compared to higher temperatures.

Cooling based on the Excited State Levels with Non-Zero Spin Projection

As alternative to the above-mentioned possibilities for cooling the mechanical resonator, the excited state levels with non-zero spin projection could be exploited to this end. A stimulated Raman transition between different ground state levels via the excited state has been investigated in a theoretical proposal [25]. This protocol combines the advantages of the above-mentioned cooling schemes working with either the ground or excited state levels, namely the long coherence times of the ground state levels and the strong strain coupling constants of the excited state levels. This protocol requires that the ground state levels with non-zero spin projection $|-1\rangle$ and $|+1\rangle$ are energetically split. A stimulated Raman transition via an excited state with non-zero spin projection is stimulated by two driving fields connecting the ground states $|-1\rangle$ and $|+1\rangle$ to the virtual excited state level. These fields have relative detuning $\Delta_{|-1\rangle} = \Delta_{\mathrm{L}} + \omega_{\mathrm{m}}/2$ and $\Delta_{|+1\rangle} = \Delta_{\mathrm{L}} - \omega_{\mathrm{m}}/2$ from the respective transitions to the excited state level such that a phonon is removed upon the transition between the ground state levels. As this cooling

protocol is based on the stimulated Raman transition via an excited state with non-zero spin projection, the couplings cannot directly linked to the strain coupling constants derived in section 2.7.2 and calculated for the diamond photonic and phononic crystal structure in section 3.4.2.

Phonon Lasing based on the Excited State Levels with Zero Spin Projection

Besides phonon annihilation, also phonon creation is a possible application of strain coupling to the nitrogen vacancy colour centre. While the generation of phonons in the optical resonator is a simple heating process, it is also possible to generate a coherent phonon field similar to a lasing process in the case of photons. This possibility has been shown theoretically for the protocol exploiting the doublet structure of the excited state levels. In that case, the transition between the ground state and the excited state with higher energy needs to be driven resonantly. For sufficiently high pump powers, the creation of phonons is not just a heating process but the mechanical resonator can be driven into a coherent state if the intrinsic damping of the mechanical resonator is overcome by the mechanical actuation via strain coupling. Under the assumptions of weak driving and a dominant strain coupling constant g_{E_2}, the lasing threshold is reached for the driving strength Ω.

$$\Omega = \sqrt{\frac{\gamma_0^3 \Gamma_{\mathrm{m}}}{4 g_{\mathrm{E}_2}^2}} \tag{2.125}$$

It can be seen from this equation, that the threshold is challenging to reach especially in the case of a bad mechanical cavity. High strain coupling constants and a good temporal confinement of the mechanical oscillation, in contrast, could make phonon lasing possible. Driving the optical transition of the nitrogen vacancy colour centre into saturation will also result in a saturation of the phonon creation. For very strong driving fields, the system even looses the resonance condition and the lasing effect vanishes completely.

2.8 Hybrid Interaction between Three Degrees of Freedom

In order to study the overall interaction in the diamond structure investigated in this work, the hybrid coupling between all three degrees of freedom is considered. The corresponding work has been performed in a collaboration with the theoretical physics department and can be found in reference [312]. The description of the hybrid interaction is based on a theoretical model including an additional optical cavity mode that interacts with both the optical transition of the nitrogen vacancy colour centre and the mechanical resonator mode that are interacting via strain coupling. The formalism is inspired by an earlier work that did not include the interaction with the optical resonator mode [311]. The study investigates the possibilities for cooling a mechanical resonator mode by means of strain coupling to an optically driven nitrogen vacancy colour centre. An additional passive optical resonator mode is resonant on or slightly detuned from the radiative decay from the excited states $|E_x\rangle$ and $|E_y\rangle$. The notation of the original

article is adapted to the conventions used throughout this work and deviates partially from the formalism in the published version.

The dynamics of the coupled system can be described by the master equation $\partial_t \rho = \widehat{\mathcal{L}} \rho$ with the density matrix of the coupled system ρ. Under the condition $\hbar = 1$, the super-operator $\widehat{\mathcal{L}}$ is given by

$$\widehat{\mathcal{L}} = -i \left[\widehat{H}, \rho \right] + \widehat{\mathcal{L}}_{\mathrm{dis}} \rho \tag{2.126}$$

Here, $\widehat{H}$ is the Hamiltonian operator of the coupled system and the Liouville operator $\widehat{\mathcal{L}}_{\mathrm{dis}}$ describes dissipation processes. The detailed expression for the Hamiltonian operator of the coupled hybrid system is

$$
\begin{aligned}
\widehat{H}_{\mathrm{hybrid}} \ = \ & \hbar \omega_{\mathrm{m}} \widehat{b}^\dagger \widehat{b} + g_{\mathrm{OM},0} \widehat{a}^\dagger \widehat{a} \left(\widehat{b} + \widehat{b}^\dagger \right) + \widehat{H}_{\mathrm{A}_1} + \widehat{H}_{\mathrm{E}_1} + \widehat{H}_{\mathrm{E}_2} \\
+ \ & \hbar \left(\omega_y - \omega_{\mathrm{L}} \right) |E_y\rangle \langle E_y| + \hbar \left(\omega_x - \omega_{\mathrm{L}} \right) |E_x\rangle \langle E_x| + \hbar \left(\omega_{\mathrm{opt}} - \omega_{\mathrm{L}} \right) \widehat{a}^\dagger \widehat{a} \\
+ \ & \frac{\Omega}{2} |E_y\rangle \langle A| + \left(g_x |E_x\rangle \langle A| + g_y |E_y\rangle \langle A| \right) \widehat{a} + h.c.
\end{aligned}
\tag{2.127}
$$

The first term describes the mechanical resonator mode, the second term the optomechanical interaction, and the remaining terms in the first line take into account for the strain coupling between the excited states $|E_x\rangle$ and $|E_y\rangle$ and the mechanical resonator mode specified in equations 2.99, 2.100, and 2.101. The remaining terms describe the dynamics of the driven nitrogen vacancy colour centre with ω_x (ω_y) the frequency of the transition between the ground state $|A\rangle$ and the excited state $|E_x\rangle$ ($|E_y\rangle$) and its interaction with the passive optical resonator mode. A laser with frequency ω_{L} drives the transition between the ground state $|A\rangle$ and the excited state $|E_y\rangle$ with Rabi frequency Ω, and the passive optical cavity with resonance frequency ω_{opt} drives the transition between the ground state $|A\rangle$ and the excited state $|E_x\rangle$ ($|E_y\rangle$) with the vacuum Rabi frequency g_x (g_y). To simplify the formalism, the polarisation of the optical resonator mode has been chosen such that it only interacts with one of the excited state levels, here set to $|E_y\rangle$.

In addition to the conservative terms included in the Hamiltonian, irreversible processes take place. These are summarised by $\widehat{\mathcal{L}}_{\mathrm{dis}}$ and can be modelled by a Born-Markov process. The individual terms describing the dissipation processes included in the model are:

- $\widehat{\mathcal{L}}_{\gamma_0}$ the spontaneous radiative decay of the excited states $|E_x\rangle$ and $|E_y\rangle$ to the ground state $|A\rangle$ with the rate γ_0

- $\widehat{\mathcal{L}}_{\gamma^*}$ the pure dephasing of the electronic coherences with the rate γ^*

- $\widehat{\mathcal{L}}_{\kappa}$ the of the optical resonator with the rate κ

- $\widehat{\mathcal{L}}_{\Gamma_{\mathrm{th}}}$ the decoherence of the mechanical resonator mode with the rate Γ_{th}

They can best be expressed with the help of the following formulation based on the operator $\widehat{o} = |A\rangle \langle \xi| , |\xi\rangle \langle \xi| , \widehat{a}, \widehat{b}, \widehat{b}^\dagger$.

$$\mathcal{D} \left[\widehat{o} \right] \rho = 2 \widehat{o} \rho \widehat{o}^\dagger - \widehat{o}^\dagger \widehat{o} \rho - \rho \widehat{o}^\dagger \widehat{o} \tag{2.128}$$

The individual terms are then:

$$\widehat{\mathcal{L}}_{\gamma_0} \;=\; \frac{\gamma_0}{2} \sum_{\xi=E_x,E_y} \mathcal{D}\left[|A\rangle\langle\xi|\right] \tag{2.129}$$

$$\widehat{\mathcal{L}}_{\gamma^*} \;=\; \frac{\gamma^*}{2} \sum_{\xi=E_x,E_y} \mathcal{D}\left[|\xi\rangle\langle\xi|\right] \tag{2.130}$$

$$\widehat{\mathcal{L}}_{\kappa} \;=\; \frac{\kappa}{2}\mathcal{D}\left[\widehat{a}\right] \tag{2.131}$$

$$\widehat{\mathcal{L}}_{\Gamma_{\mathrm{th}}} \;=\; \frac{\Gamma_{\mathrm{th}}+\Gamma_{\mathrm{m}}}{2}\mathcal{D}\left[\widehat{b}\right] + \frac{\Gamma_{\mathrm{th}}}{2}\mathcal{D}\left[\widehat{b}^{\dagger}\right] \tag{2.132}$$

In order to facilitate the description and to identify the parameter sets of interest, the relative detuning Δ_{L}, Δ_{opt}, and Δ_{xy} of the laser field ω_{L}, the optical resonator ω_{opt}, and the second colour centre transition ω_x from the transition ω_y were introduced.

$$\Delta_{\mathrm{L}} \;=\; \omega_{\mathrm{L}} - \omega_y \tag{2.133}$$

$$\Delta_{xy} \;=\; \omega_x - \omega_y \tag{2.134}$$

$$\Delta_{\mathrm{opt}} \;=\; \omega_{\mathrm{opt}} - \omega_y \tag{2.135}$$

The coupling constants both for the optomechanical and the strain coupling interaction are in the order of MHz and thus much smaller than the mechanical mode frequency in the range of GHz. A second order perturbation approach is thus justified and can be exploited in the detailed calculations that are not shown here but can be found in the published article. To investigate the dynamics of the hybrid interaction in the coupled system, the cooling rate $\widetilde{\Gamma}_{\mathrm{hybrid}}$, the asymptotic minimal phonon occupation number in the absence of a thermal bath $\overline{n}_{\mathrm{m,min,hybrid}}$, and the final phonon occupation number $\overline{n}_{\mathrm{f,hybrid}}$ are evaluated for different values of the detuning Δ_{L} between the driving Laser and the optical transition of the nitrogen vacancy colour centre. The corresponding results are shown in section 3.5.

Chapter 3

Numerical Modelling

This chapter shows all results from numerical modelling and the methods that have been used to this end. First, the photonic and phononic crystal structure is presented and all simulation methods used for modelling both the optical and mechanical resonator modes as well as optomechanical interaction and strain coupling are introduced. Then, the optical properties of the photonic and phononic crystal structure are shown including the photonic band structure, the optical resonator mode and gratings for in- and out-coupling of light. Based on the structure with optimal optical properties, the mechanical properties of this structure are studied starting from a band structure analysis. The properties of localised mechanical resonator modes and their optomechanical interaction with the optical resonator mode are investigated to find a suitable mechanical cavity mode that strongly couples to other degrees of freedom. Strain coupling is then evaluated based on separate descriptions for the interaction with the ground and excited states of the nitrogen vacancy colour centre. Different experimentally relevant orientations of the diamond sample are considered to identify the most interesting cases and the obtained results are critically assessed to review the derivation of the formalisms used to describe the interaction. Finally, the hybrid interaction between all three degrees of freedom is investigated where in particular the influence of the optical resonator mode and of dephasing on the cooling performance is studied.

3.1 Methods

3.1.1 Structure Geometry

The structure investigated in this work is a one-dimensional photonic and phononic crystal cavity made from single crystal diamond. It is built up from equally sized unit cells each containing a single circular hole as depicted in figure 3.1(b). The parameters used to describe the geometric dimensions of the unit cell are the lattice constant a, the hight h, the width w, and the hole radius r. To build a resonator structure, a variation in the regular pattern needs to be introduced in order to confine an optical resonator mode. In the photonic and phononic crystal cavity investigated in this work, the hole size is varied such that there are larger holes in the centre of the structure and smaller holes towards the edges as shown in figure 3.1(a). The orientation of the structure is such that the photonic crystal structure is aligned along the x-axis with a distance between neighbouring holes corresponding to the lattice constant a. The y-axis is perpendicular to x within the sample plane, and z is normal to the diamond surface. The origin for the coordinate system is chosen to be in the centre of the structure such that the innermost holes are placed at a distance of $x = \pm 0.5\,a$. The radius of an arbitrary hole is given through the following equation.

$$r_\mathrm{i} = r_0 \cdot (1 - Cx_\mathrm{i}^2) \tag{3.1}$$

Here r_0 is the (virtual) maximal hole radius for a hole placed in the exact centre of the structure, x_i is the distance of the hole to the centre of the structure expressed in units of the lattice constant a, and C is a dimension-less parameter determining the decrease of hole radii. The hole spacing is kept constant over the entire structure. The centre of

(a) Photonic and phononic crystal structure.

(b) Unit cell of the photonic and phononic crystal.

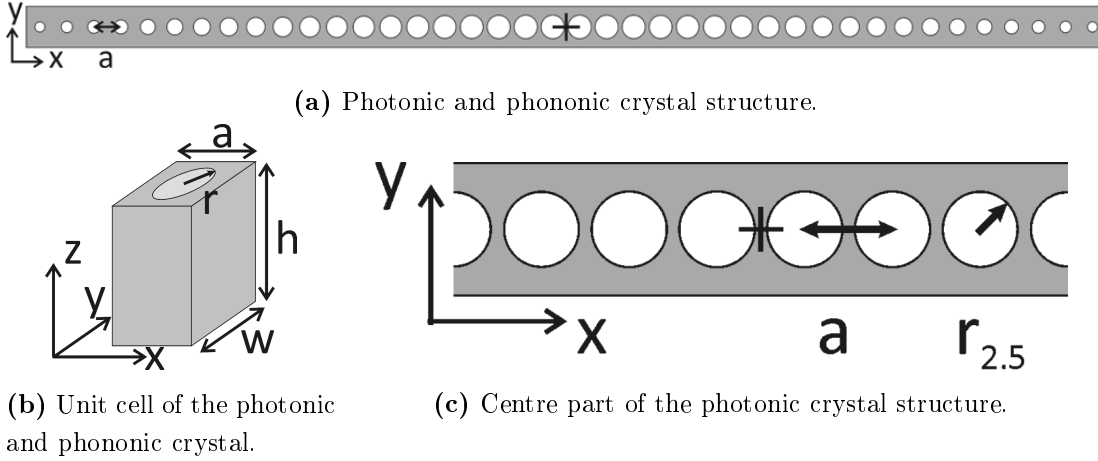**(c)** Centre part of the photonic crystal structure.

Figure 3.1: Photonic and phononic crystal structure investigated in this work. The individual figures show the entire structure (a), the unit cell (b), and the centre part (c). The coordinates x, y, and z are indicated in all figures. The origin (0/0/0) is chosen to be in the centre of the structure as indicated with a cross. The hole radius decreases quadratically from the centre of the structure and is parametrised with the corresponding hole position.

such a structure is depicted in figure 3.1(c) to illustrate the choice of coordinates and the determination of hole radii. The structure investigated in this work has a photonic and phononic crystal pattern consisting of $L = 20$ holes to each side from the centre.

3.1.2   Modelling of Optical Properties

The optical properties of the photonic and phononic crystal structures are investigated in finite-difference time-domain (FDTD) simulations [313]. Arbitrarily shaped photonic structures consisting of different materials with their individual optical properties can be modelled with this technique. FDTD simulations require a spatial lattice where Maxwell's equations are solved in discrete steps and the electromagnetic fields can propagate over time. The programme used to implement the simulation of photonic crystal cavities is an open-source programme called MEEP (MIT Electromagnetic Equation Propagation) [314].

A spatial discretisation of the simulation area is required for all FDTD methods and usually a Yee lattice [316] is used to subdivide the simulation cell into small compartments, referred to as voxels. In FDTD calculations, the grid always subdivides the simulation area into rectangular voxels and only rectangular simulation areas can be modelled. The particularity of a Yee grid is that the different components of the electromagnetic field are stored at different locations. The electric field components are always stored at the edges of a voxel whereas the magnetic field is stored at its faces. The unit cell of a Yee lattice is depicted in figure 3.2 along with the discrete coordinates of the corner points as well as the electric and magnetic field components at their respective locations in the grid. This particular design of the unit cell facilitates the numerical processing as the evolution of the magnetic (electric) field can only be
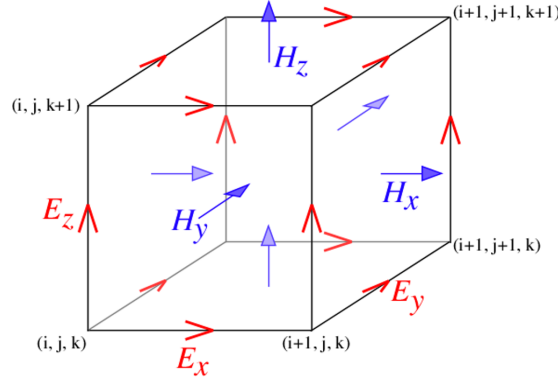
Figure 3.2: Schematic of a Yee Lattice. Magnetic field components (blue) are evaluated at the voxel faces whereas electric field components (red) are calculated at its edges. Figure taken from reference [315]

solved with the help of the curl of the electric (magnetic) field. By localising the field components at different parts of the simulation cell, the respective curls are intuitively evaluated at the spatial points where they are needed for further processing. This is a very advantageous automatism that reduces the calculation time and also explains why this method is preferred over the finite element method (FEM) for time-dependent electromagnetic or fluid dynamics problems. To avoid a simultaneous calculation of fields that depend on each other, the electric field is only calculated at every second step with the magnetic field being evaluated in the intermediate steps. If both the electric and the magnetic field need to be evaluated simultaneously, both fields are interpolated at the centre of the voxel.

To obtain reliable results in an adequate computation time, the resolution of the simulation grid needs to be adjusted to the requirements of the physical model. On the one hand, the resolution has to be sufficiently high to reliably render the structure on the simulation grid and represent all details of the dielectric distribution. On the other hand, if the resolution is too fine, numerical singularities risk to distort the result and in addition, the computation time becomes unnecessarily long. A suitable resolution for the simulations in this work is a resolution of 20 to 24 grid points per unit length a describing to the hole spacing. In MEEP, the modelling of the dielectric structure is supported by a sub-pixel averaging algorithm that helps with smoothing material borders, avoids numerical discontinuities, and allows for continuous distributions even on the discrete lattice [317,318]. In FDTD calculations, the temporal resolution is closely linked to the spatial resolution. To achieve a stable simulation, the size of the discrete temporal steps Δt should not exceed the equivalent spatial resolution Δx. In particular, the time steps measured in units of a/c should obey the relation $\Delta t < \Delta x \sqrt{dimension}$ [313]. This is ensured with the standard setting in MEEP $\Delta t < 0.5\Delta x$ meaning that an increase in spatial resolution automatically also refines the temporal stepping.

Furthermore, the boundary conditions need to be chosen carefully so that no unwanted numerical reflections from the borders of the unit cell influence the simulation. Therefore, the edges of the unit cell require particular attention in order to obtain re-

liable results. Absorbing boundaries, where all field components reaching the edges of the simulation cell vanish, are the necessary condition so that no reflections perturb the optical resonator mode. This can be achieved by introducing so-called perfectly matched layers (PML), an artificial material covering the sides of the simulation cell. This material's permittivity and permeability are of purely complex nature leading to a strong absorption in this area. All electromagnetic fields thus vanish towards the edges of the simulation cell and with this technique, the real situation of a free-standing photonic structure can be modelled without an extremely large simulation cell. However, a considerable distance to the resonator and a sufficient thickness are required to avoid field reflections at the boundaries of the simulation cell. All simulations in this work are performed with a perfectly matched layer thickness of unit size a.

The use of symmetry conditions helps with reducing simulation times as well as with selecting specific resonator modes. The simulations in this work focus on transversal electric optical modes where the electric field is perpendicular to the surface of the diamond slab. This can be implemented in the simulation by introducing an even mirror symmetry in the z-direction with respect to the origin. To efficiently model the preferred resonator mode of the photonic crystal structure investigated in this work, an odd symmetry in the x-direction and an even symmetry in the y-direction are chosen to shorten computation times. This corresponds to an even mode of the optical resonator, the mode type that also brings the advantage of good optomechanical interaction as the individual coupling contributions do not cancel out in this case (see section 2.6.6). The entire simulation cell is depicted in figure 3.3. It includes the photonic crystal structure, the perfectly matched layers with artificially absorbing material on the boundaries, the symmetry planes and the dipole source. The overall size of the simulation cell is to scale with the diamond structure.
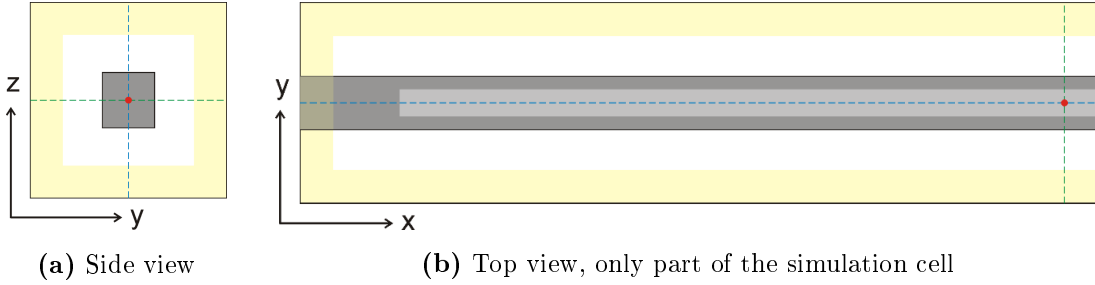

(a) Side view   **(b)** Top view, only part of the simulation cell

Figure 3.3: Simulation cell of the optical simulation in side view (a) and top view (b). The dimensions are $46\,a \times 6\,a \times 6\,a$ and all components are to scale. The red dot indicates the dipole source placed in the centre of the structure at coordinates (0/0/0). The yellow area shows the perfectly matched layers consisting of artificially absorbing material. The dotted green (blue) lines indicate even (odd) symmetry planes. The diamond structure is represented by the grey rectangle with the lighter coloured area indicating the region of the photonic and phononic crystal structure.

In the optical simulation, all physical constants, namely the speed of light c, the vacuum permittivity ε_0, and the vacuum permeability μ_0 are set to unity. This implies

that all values calculated are dimensionless as well. Advantage is also taken of the scale invariance of Maxwell's equations and all parameter values are expressed in units of a, the unit length in the simulation cell. By convention, the unit length a is set to the lattice constant determining the distance between neighbouring holes in a photonic crystal structure as shown in figure 3.1. This also implies that all simulation results are independent of scale and the optical resonator mode can be matched to any desired wavelength by adjusting the overall size of the structure.

The spatial confinement of the optical resonator modes is directly evaluated during the simulation. The electric field of the cavity mode is known from the calculations and with the help of an integration and the evaluation of the maximal field strength, the relation from equation 2.3 can be exploited to determine the modal volume V_{opt} of the optical resonator mode. To determine the temporal confinement of the optical resonator modes, the decay of the electromagnetic field in the photonic crystal has to be determined. To this end, a dipole point source exciting the y-component of the electric field is used to efficiently address the optical resonator modes. This dipole source generates a Gaussian-shaped pulse with predefined centre frequency and bandwidth. The central frequency of the excitation pulse is adapted to the resonator mode in an iterative procedure and corresponds to $0.3 \cdot 2\pi\,c/a$ for the simulations in this work. The width is chosen as $0.03 \cdot 2\pi\,c/a$ corresponding to $10\,\%$ of the absolute frequency. After the source is turned off, the simulated fields need to be given sufficient decay time to avoid numerical singularities. After 400 time-steps, the detection of the optical resonator modes is started in the simulations in this work. In MEEP, the detection of the optical resonator modes is implemented with HARMINV, an algorithm based on a filter diagonalisation method [319, 320]. With this technique, any signal consisting of a sum of sinusoids is decomposed into its individual components and the individual waves' frequencies, decay rates, amplitudes, and phases are evaluated. Based on the principle that the filter diagonalisation method identifies the eigenvalues of a small matrix, it gives very reliable results for signals that consist of a limited number of oscillating modes and little noise. This is well justified in the case of photonic crystal cavities and thus the accuracy of this method is better than a direct Fourier transformation. The different field components $f\,(t)$ are expressed as a sum of different harmonic oscillations.

$$f\,(t) = \sum_{\mathrm{n}} A_{\mathrm{n}} \mathrm{e}^{-i\omega_{\mathrm{opt,n}}t} \tag{3.2}$$

The amplitude A_{n} as well as the frequency $\omega_{\mathrm{opt,n}}$ of the optical modes are complex values. The optical quality factor Q_{opt} can then be found by comparing the real and complex parts of the optical mode frequency according to equation 2.5. The detection of the fields is only possible at points with a sufficient excitation. Therefore, a point in the centre of the photonic structure that is not coinciding with nods of the electromagnetic field or placed on a symmetry axis is best suited. All optical resonator modes can then be detected and their optical quality factors can be determined. In previous work, other methods have been tested in order to confirm the reliability of this method and showed consistent values [321].

Besides confined optical resonator modes, also structures to couple light into and out of the diamond structure are required. These are not investigated based on the

simulation cell shown in figure 3.3, but a slightly deviating geometry described in detail in reference [322] is used to this end. Here, only a diamond structure without photonic and phononic crystal pattern is modelled where an additional grating structure in the diamond membrane allows for in- and out-coupling of light. An electromagnetic field with the symmetry properties of the optical cavity mode is generated in the diamond air-bridge, and its propagation through the grating structure is detected. The performance of the grating is evaluated based on the detection of the electromagnetic flux through specified surfaces, determined as integral of the Poynting vector over the surface. In an initial step, the diamond structure is modelled without grating to obtain a scaling for the electromagnetic fluxes in absence of the coupling structure. In a second step, the grating is added to the model and the resulting electromagnetic fluxes are calculated based on the scaling obtained in the first simulation. Finally, the efficiency of the device is determined in term of the electromagnetic field that is radiated in vertical direction compared to the electromagnetic field that propagates through the airbridge structure towards the clamping. The details of this method are specified in [322] and will not further be described here.

3.1.3 Modelling of Mechanical Properties

The mechanical properties of the photonic and phononic crystal structure are modelled with the finite element method (FEM). Similar to the FDTD method, the finite element method is based on a spatial discretisation of the structure, and the simulation area has to be subdivided into smaller volume sections by a simulation grid. The underlying physical equations are solved individually for each grid element and then interpolated over the entire structure. To model the mechanical properties of the photonic and phononic crystal structure investigated in this work, the equation of motion expressed as eigenfunction of the mechanical displacement in equation 2.10 is solved in the finite element calculation. The mechanical band structures supported by each unit cell of the photonic and phononic crystal structure can then be retrieved as solution to this equation. To find the mechanical resonator modes, an eigenmode analysis is performed over the entire structure geometry. The mode profile can be visualised to identify resonances that are suitable for interaction with other degrees of freedom. To implement this method, the commercially available software COMSOL is used along with its "structural mechanics" expansion pack.
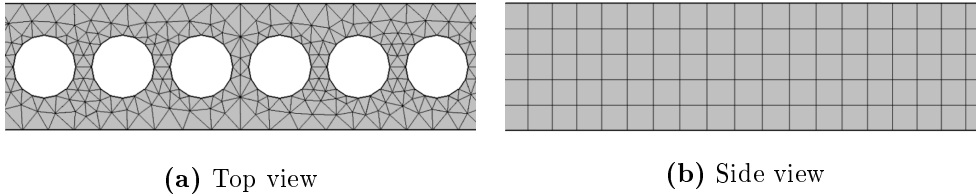

(a) Top view   **(b)** Side view

Figure 3.4: Centre of the phononic crystal structure discretised for finite element modelling with a swept mesh based on a triangular lattice in top view (a) and side view (b).

In contrast to other simulation methods like FDTD, FEM allows adaptive meshing where a higher resolution is chosen around geometric details like strong curvatures or edges, and a lower resolution in the bulk of the material. It is also possible and widely used to only mesh and model the area of interest when non-standard shapes are concerned. This opens the possibility to refine the resolution in the areas of interest but also save computation time by a rather coarse grid in homogeneous areas. Thereby, also large structures with small but crucial details can be modelled with sufficiently fine resolution in relatively short simulation times. However, an irregular lattice makes it difficult to determine the resolution of the mesh. It thus needs to be assured that the resolution is sufficiently precise to generate a reliable result for the physical problem in question. A suitable meshing is reached when the simulation results remain constant also for a slightly coarser mesh. The grid type used for most simulations in this work is a swept mesh. It is chosen because it facilitates the exploitations of symmetry conditions in order to shorten the computation time, or to select mechanical modes of defined symmetry. A triangular lattice is adapted to the structure in two dimensions and extruded to the third dimension. This mesh is depicted in figure 3.4 with the resolution used for all calculations that are performed to obtain the resonance frequency and oscillation pattern of a mechanical resonator mode. The geometry used for the evaluation of the mechanical quality factor, however, makes the use of a swept mesh impossible and in this case a tetrahedral lattice is used. The results for the mechanical properties of the photonic and phononic crystal structure obtained with different meshes have been compared and no differences besides small numerical deviations in the exact value of the mode frequency could be detected.

The FEM model of the structure in COMSOL is based on real units, in contrast to the dimensionless FDTD implementation with the programme MEEP. This means that the results obtained from mechanical modelling are not directly scalable in contrast to the structure's optical properties that are expressed in abstract units. All parameters in the mechanical simulation are expressed as absolute values with the corresponding unit. Scaling of the modelling results to a deviating overall size of the structure needs to be done in an additional step. As in the case of the optical resonator mode, an overall smaller resonator will result in a higher frequency of the cavity mode and a better spatial confinement expressed as smaller effective mass.

In the case of the mechanical simulation, scaling is also important with respect to the maximal elongation of the resonator's amplitude during the oscillation cycle. To calculate the full strain tensor generated by the mechanical oscillation at a defined point in the diamond structure, a universal scaling is required in order to obtain comparable results. A suitable measure is the excitation of the mechanical resonator with a single phonon. This results in a maximal displacement corresponding to the zero point fluctuation x_{ZPF} of the mechanical resonator. In order to implement this universal measure, the simulations are performed in two steps. In an initial run, an arbitrary elongation is used to excite the mechanical oscillation and the maximal displacement is retrieved from the model. In a second step, the excitation is adapted proportionally such that the resulting maximal displacement corresponds to the zero point fluctuation x_{ZPF} of the mechanical resonator. With this method, a universal scaling can be implemented to the mechanical model that makes the results not only comparable with each other but

also allows for benchmarking against fundamentally different resonator geometries.

Besides the frequency and shape of the mechanical resonator mode, also the spatial and temporal confinement of the oscillation are extracted from the numerical model. This allows to assess the performance of the photonic and phononic crystal structure with respect to its mechanical properties. The spatial confinement of the mechanical resonator mode is directly extracted from the simulation by implementing equation equation 2.11 defining the effective mass m_{eff} in the finite element model. As the displacement field is fully determined in the model, the effective mass can directly be calculated based on an integration over the entire structure. The temporal confinement of the resonator modes can be calculated with the aid of an artificially absorbing material that damps the mechanical oscillation. The mechanical quality factor can be extracted from the simulation by either adding artificially absorbing material to the edges of the phononic crystal structure, or by introducing a homogeneous absorption over the diamond material. Under the assumption that experiments are performed in vacuum and at low temperatures with structures fabricated from samples of high crystalline quality, clamping losses are the dominant loss channel and other damping mechanisms like friction at the surface are not investigated in this work. Therefore, the quality factor is best represented by an artificially absorbing material as supporting structure for the phononic crystal cavity. This can either be a flat membrane representing the real sample geometry as used in reference [323], or half-spheres with which this technique has originally been introduced for the determination of the mechanical quality factor of photonic and phononic crystal structures [251]. Flat membranes should preferably be used when the effect of shielding structures that can strongly increase the quality factor of localised mechanical resonator modes are investigated, like for example the structures presented in reference [236]. In this work, however, all results were obtained with artificially absorbing half-spheres attached to the end facets of the phononic crystal cavity as shown in figure 3.5. The artificially absorbing material is implemented by
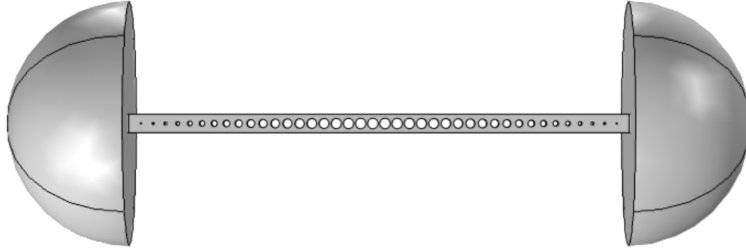

Figure 3.5: Technique used to determine the mechanical quality factor of localised mechanical resonator modes. The half-spheres attached to the phononic crystal structure are made of an artificially absorbing material representing clamping losses.

adding an imaginary part to both Young's modulus $E_{\text{abs}} = E\left(1 + \eta i\right)$ and Poisson's ratio $\nu_{\text{abs}} = \nu\left(1 + \eta i\right)$ with $\eta = 0.5$. The mechanical resonator frequency then also gains an imaginary part and the relation of the real and the complex parts of the oscillator frequency gives the mechanical quality factor Q_{m} according to equation 2.13. Alternatively, the energy stored in the mechanical oscillation can be evaluated as a

function of the excitation frequency. This generates a Lorentzian peak whose centre frequency corresponds to the resonance frequency ω_m of the mode. The mechanical quality factor is then defined as the inverse of the relative peak width according to equation 2.14. With this second method, care needs to be taken when several resonator modes have only slightly different frequencies and the peaks overlap. This analysis has been performed for comparison and values consistent to the exploitation of the real and complex frequency contributions were obtained. This is shown in detail for similar calculations in reference [323].

3.1.4   Calculation of Optomechanical Coupling

To calculate the optomechanical interaction strength in photonic and phononic crystal cavity structures, both the electromagnetic field resulting from the FDTD simulation of the optical mode, and the strain field obtained from FEM modelling of the mechanical mode need to be integrated into a single model. This is due to the fact that the respective coupling constants $g_{\mathrm{MB},0}$ and $g_{\mathrm{PE},0}$ for the moving boundaries and the photoelastic effect are calculated based on overlap integrals between the optical and mechanical cavity fields explicitly expressed in equations 2.80 and 2.82. As the optical and the mechanical properties of the structure are simulated with different programmes, the optomechanical interaction cannot be evaluated directly. With both methods working based on fundamentally different spatial meshes, particular care has to be taken when combining the electromagnetic and the strain field following the real geometric patterns imposed by the photonic and phononic crystal structure.

The method applied in this work starts with extracting all components of the electric and the magnetic field from the optical simulation at every grid point of the simulation. It is important to choose a suitable time step so that the optical resonator mode could fully evolve already, but the electromagnetic field did not decay below a critical threshold, yet. For the simulations performed in this work, an evolution time of 300 time steps after stopping of the dipole source showed to be a good choice. At the same time step, an integration over the entire electromagnetic field needs to be performed so that the optomechanical coupling can be scaled to the excitation of a single photon. The extracted values for the electromagnetic field components are given in coordinates of the Yee lattice. An additional transformation step is then required to project the field on the actual coordinates of the structure in the mechanical simulation. All components of the electromagnetic field are mapped to the coordinates of the structure expressed in real units, so that they are compatible with the FEM model. For this step, the resolution of the FDTD simulation is crucial as it determines the coordinates of each point on the Yee lattice. The resulting field function of the optical resonator mode is then imported to the FEM model. Only a structure with the exactly same geometrical parameters as in the optical model will give a meaningful result for the optomechanical interaction. After this procedure, the FEM simulation can be started with the full information about the optical cavity modes being available when performing the mechanical simulation. The overlap integrals between the optical and mechanical resonator fields required to determine the optomechanical interaction strength can then be calculated based on the newly obtained strain field. While this method is tedious, it ensures that

all optical and mechanical properties of the structure can be determined with tested and reliable methods. The resulting single photon optomechanical coupling constants for the moving boundaries and the photoelastic effect $g_{\mathrm{MB},0}$ and $g_{\mathrm{PE},0}$ are then based on realistic cavity fields.

3.1.5   Calculation of Strain Coupling

To calculate the strain coupling in the diamond structure investigated in this work, the full strain or stress tensor extracted from the mechanical simulation is in principle sufficient. However, meaningful and comparable results can only be obtained when the scaling of the mechanical excitation as well as the orientation and positioning of the nitrogen vacancy colour centre with respect to the phononic crystal structure are properly chosen. To achieve the single phonon strain coupling constants, the excitation of the mechanical resonator mode has to be scaled such that the maximal elongation corresponds to the zero point fluctuation. This can be assured by a two-step calculation described in section 3.1.3. Also, the positioning of a single nitrogen vacancy colour centre inside the diamond structure has a strong impact on the result. As the strain coupling constants are proportional to the mechanical displacement at the position of the emitter, the points of maximal strain also result in maximal strain coupling. For the structure investigated in this work, this corresponds to selected points on the diamond surface of the innermost holes. However, the optical properties of a colour centre close to the surface are poor and the interaction with the optical resonator mode is much weaker than for a more central position. Therefore, a much fairer location is the exact centre of the diamond structure. This also ensures a good comparability of all simulations as a slight variation of the geometric parameters does not shift the colour centre position considered in the modelling. The nitrogen vacancy colour centre is thus always positioned in the exact centre of the diamond structure at coordinates (0/0/0) but it should be kept in mind that considerably higher single phonon strain coupling constants could be reached at other positions.

As described in section 2.4, the nitrogen colour centre is always aligned along an equivalent [111] direction in the tetrahedral diamond lattice. In order to ensure comparable and unambiguous results, an exact [111] orientation is chosen in the model. Suitable axes creating a right-handed coordinate system respecting this orientation can be defined as x along $[\bar{1}10]$, y along $[\bar{1}\bar{1}2]$ and z along $[111]$ according to literature [265]. This coordinate system is depicted in figure 3.6.

The orientation of the diamond structure with respect to the nitrogen vacancy colour centre is adapted to realistic experimental possibilities. As described in section 2.1, diamond samples are available with orientations corresponding to either (100), (110), and (111) surfaces. The most common sample type is a (100) surface orientation typically described as (001) diamond sample. In this case, the angle between the colour centre axis and the surface normal vector corresponds to an angle of 54.7°. A suitable coordinate system to describe a photonic and phononic crystal resonator with this orientation is given by the crystallographic axes with $X = [100]$, $Y = [010]$, and $Z = [001]$. A more interesting orientation with respect to the optical properties is a (111) surface. In this case, the nitrogen vacancy colour centre is perpendicular to the surface and its dipole
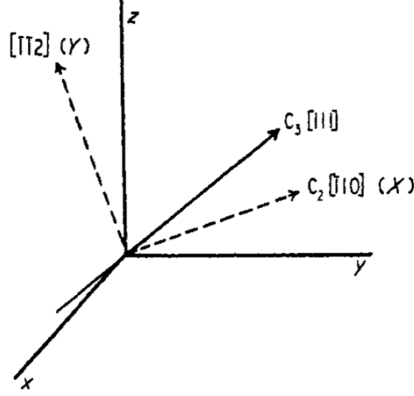
Figure 3.6: Coordinates representing the orientation of the nitrogen vacancy colour centre. Figure taken from reference [265].

orientation is optimal with regard to optical measurements. This orientation can best be described with the coordinate system depicted in figure 3.6. Both these orientations are considered for the evaluation of strain coupling in this work to assure a complete study of the most relevant cases. In addition, all possible rotations of the structure within these sample planes are considered in order to identify the perfect alignment of the structure. The strain tensor originating from the mechanical resonator mode is expressed in the coordinates shown in figure 3.6 corresponding to the internal coordinate system of the colour centre. For a transformation between the internal and external coordinates, a rotation based on the transformation matrix T is performed.

$$T = \begin{pmatrix} -\frac{1}{2}\sqrt{2} & -\frac{1}{6}\sqrt{6} & \frac{1}{3}\sqrt{3} \\ \frac{1}{2}\sqrt{2} & -\frac{1}{6}\sqrt{6} & \frac{1}{3}\sqrt{3} \\ 0 & \frac{1}{3}\sqrt{6} & \frac{1}{3}\sqrt{3} \end{pmatrix} \tag{3.3}$$

For the transformation from the crystallographic axes $X = [100]$, $Y = [010]$, and $Z = [001]$ to the coordinate system of the colour centre $x = 1/\sqrt{2}\,[\bar{1}10]$, $y = 1/\sqrt{6}\,[\bar{1}\bar{1}2]$, and $z = 1/\sqrt{3}\,[111]$, the strain tensor is rotated according to $\epsilon_{int} = T\epsilon_{ext}T^{-1}$. For the inverse transformation, the required operation is $\epsilon_{ext} = T^{-1}\epsilon_{int}T$.

All results are evaluated for both sample types with all possible orientations of the diamond structure within the sample surface. Based on these tensors, the strain coupling constants are calculated based on equations 2.88 and 2.89 originating from a phenomenological description of coupling to the ground state levels and based on equations 2.103, 2.104, and 2.105 for strain coupling to the excited state levels of the nitrogen vacancy colour centre. Strain coupling to the ground state levels base on the group theoretical description is evaluated based on the stress tensor generated by the photonic and phononic crystal structure expressed in the crystallographic coordinates. Here, equations 2.95, 2.96, and 2.97 are exploited to determine the corresponding strain coupling constants.

3.2   Optical Properties and Purcell Enhancement

3.2.1   Optical Band Structure

The optical band structure of a photonic crystal can be retrieved by modelling the optical properties of the unit cell. Periodic boundary conditions allow to study an infinite structure with a perfect lattice of equally spaced and sized holes. The method and results have been shown in previous work [321] and will only shortly be summarised here. The band structure of the unit cell and the mode shape of the first guided modes analysed at the X-point is shown in figure 3.7. It can be seen that only the dielectric band is fully below or along the light line that defines the area of index guiding in the z-direction. The mode profiles of the two lowest order bands reveal that the field is indeed mainly localised inside the diamond material for the dielectric band, and predominantly in leaky modes outside the structure for the air band. While the shape of the band structure remains unchanged for a different choice of parameters, the absolute numbers of the frequencies vary along with the exact geometric dimension of the unit cell. Qualitatively, the frequencies of the modes at the X-point are higher for larger hole radii and smaller for a larger width or height of the structure. The difference between the dielectric and the air band at the X-point is called mode gap. Based on this frequency gap between the individual bands, a localised mode can be confined. As starting point, the changes in the frequencies at the X-point are determined for a variation of the geometric parameters. The corresponding mode gap analysis will not be shown here but can be found on pages 47-48 in reference [321].

3.2.2   Optical Resonator Mode and Purcell Enhancement

Based on the desired band structure in a perfectly periodic structure, a cavity mode can be localised by introducing a defect to the structure. For the one-dimensional photonic crystal structure investigated in this work, the so-called mode gap effect is exploited to confined an optical resonator mode in the centre of the structure. This has the advantage over mode confinement by creating an optical band gap that the mode shape of the localised mode is known as it corresponds to the guided mode it arises from (see section 2.2.2). The structure investigated in this work is designed to reach high optical quality factors and at the same time low modal volumes. This can best be achieved with an inverse design approach where the optimal resonator field is chosen and the photonic crystal pattern is constructed accordingly. The electric field of the cavity mode should have a Gaussian shape to assure high optical quality factors. The mode should arise from the dielectric band for two reasons. First of all, out-of-plane radiation due to non-perfect index guiding can best be suppressed by reducing the overlap with the light cone that is already substantially lower for the dielectric band than for all other bands. In addition, the interaction with other degrees of freedom can be enhanced when the cavity field is mostly localised inside the diamond material. Both a Gaussian field envelope and a cavity mode arising from the dielectric band can be achieved with two different kinds of one-dimensional photonic crystal patterns: cavities where the radii of the holes decrease from the centre of the structure or where the hole spacing increases from the
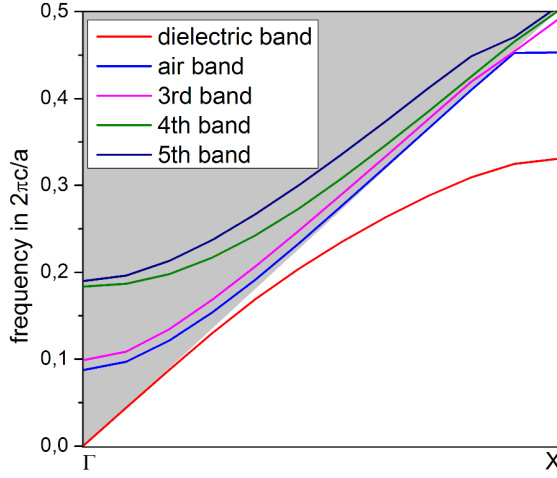
(a) Band structure of a one-dimensional photonic crystal structure. The grey shaded area indicates the light cone.

(b) Mode profile of the air band at the X-point.

(c) Mode profile of the dielectric band at the X-point.

Figure 3.7: Optical band structure analysis of a perfectly periodic photonic crystal structure with parameters width $w = 1.00\,a$, hole radius $r = 0.40\,a$, and infinite height $h = \infty$. The band structure in the first Brillouin zone is shown in (a). (b) and (c) show the corresponding profiles of the guided modes in the air band and in the dielectric band, respectively.

centre of the structure. With quadratically decreasing hole radii, a very good mode confinement that can be measured in high quality factors and a reasonable robustness against fabrication tolerances can be achieved. This design can be parametrised with the height h and the width w of the diamond structure, the (virtual) maximal hole radius in the centre of the structure r_0, a dimensionless parameter C indicating the variation of hole size along the structure, and the number of holes to each side from the centre L (see section 3.1.1). The radius of each hole r_i is given as function of x_i, the hole distance from the centre of the structure measured in units of the constant hole spacing a.

$$r_i = r_0 \left(1 - C x_i^2\right) \tag{3.4}$$

To assure a good confinement of the optical mode, the photonic crystal pattern is chosen comparably large with $L = 20$ holes to each side from the centre. Only the fundamental mode with a single maximum in the centre of the structure is considered. This assures a strong spatial confinement of the mode and allows for good interaction with other degrees of freedom. The electric field components of the resulting optical resonator mode are shown in figure 3.8.

It can be seen from the distribution of the cavity field that it is an even resonator mode. These are optical resonator modes with a polarisation perpendicular to the x-axis. In that case, the y-component of the electrical field vanishes in the far field. The symmetry conditions that should thus be chosen in order to reduce the computation times for further simulations are an odd symmetry in the y-direction and an even symmetry in
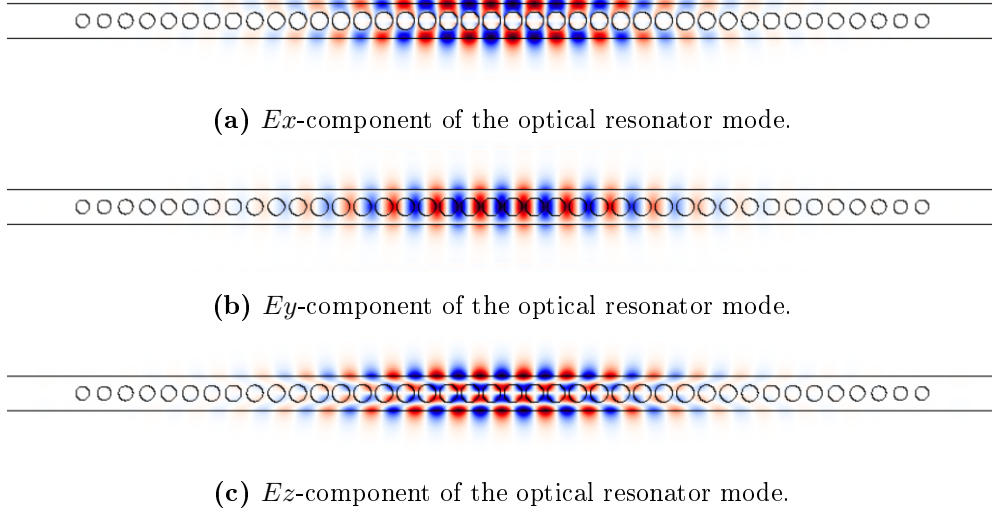
(a) *Ex*-component of the optical resonator mode.

(b) *Ey*-component of the optical resonator mode.

(c) *Ez*-component of the optical resonator mode.

Figure 3.8: Spatial distribution of the electric field components of the optical resonator mode. The parameters of the structure are $w = 1.60\,a$, $h = 1.70\,a$, $r_0 = 0.40\,a$, and $C = 0.0007$. All field distributions are retrieved at half height of the structure corresponding to $z = 0$.

the x-direction.

In addition to the properties of the optical resonator mode, also the interaction with a colour centre situated inside the diamond structure can be investigated based on the simulation results. The effective Purcell factor F only depends on the properties of the optical resonator mode as positioning and dipole orientation are standardised for this measure. It can thus directly be retrieved from the confinement of the optical cavity mode. A parameter study is performed with the aim to increase the optical quality factor Q_{opt}. The optimal values for all parameters are summarised in table 3.1 along with the resulting temporal and spatial confinement of the optical mode in terms of the quality factor Q_{opt} and the modal volume V_{opt}, and the Purcell factor F determining the interaction with a colour centre located inside the structure.

| w	h	r_0	C	Q_{opt}	V_{opt}	F
$1.60\,a$	$1.70\,a$	$0.42\,a$	0.0007	1.4×10^7	$2.0\,(\lambda/n)^3$	5.3×10^5

Table 3.1: Optimal set of parameters width w, height h, radius r_0, and scalar C for the optical resonator structure. The performance of the structure is indicated in terms of the figures of merit for the temporal and spatial mode confinement V_{opt} and Q_{opt}, and the effective Purcell factor F describing the interaction of the photonic crystal structure with a colour centre placed in its centre.

As these parameters are expressed in units of the lattice constant a, also the frequency of the resonator mode is given in this relative scale. For the parameters given in table 3.1, the frequency of the optical mode is $\omega_{\mathrm{opt}} = 0.3011 \cdot 2\pi\,c/a$. The resonator mode matches

the emission of the nitrogen vacancy colour centre at 637 nm for a lattice constant $a_{NV} = 192$ nm, but some of the structures considered in section 3.3 are designed with a unit length $a_{SiV} = 223$ nm to match the zero phonon line of the negatively charged silicon vacancy colour centre (SiV) at 738 nm.

3.2.3 Gratings for In- and Out-Coupling

To couple light in and out of the photonic crystal resonator, so-called grating couplers are added to both sides of the diamond structure. These grating couplers are necessary for a transmission or reflection measurement of the optical cavity mode that have to be performed in order to detect optomechanical interaction. To obtain in- and out-coupling structures that allow for a measurement of the above-mentioned optical resonator mode, the properties of the grating couplers need to match those of the photonic crystal structure. All structures are fabricated in a diamond membrane by removing material. The resulting photonic crystal structure has the same thickness as the remaining diamond membrane. Therefore, a diamond airbridge of width $w = 1.60\,a$ and height $h = 1.70\,a$ corresponding to the optimal parameters of the optical resonator clamped to a diamond membrane of same height is the basis for the model. The in- and out-coupling structures
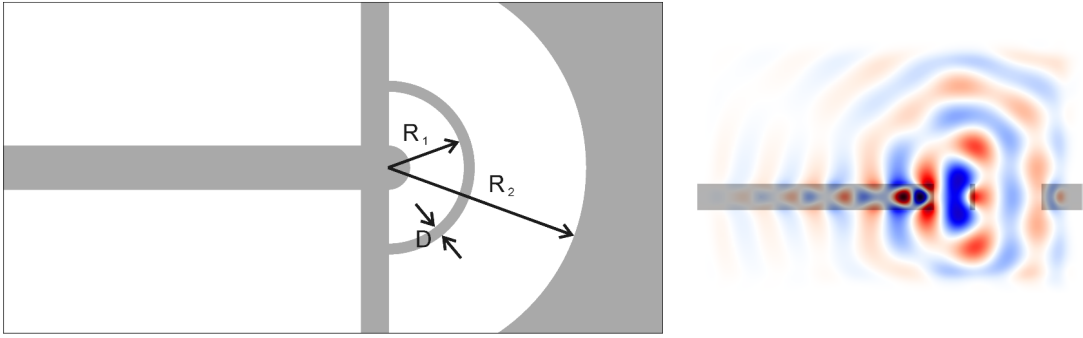
(a) Top view of round grating couplers with dimensions corresponding to the size of the simulation cell.

(b) Side view at $y = 0$ with Ey-component of the optical field.

Figure 3.9: Round grating couplers. (a) Top view of the structure with the ideal set of parameters $R_1 = 2.75\,a$, $R_2 = 7.20\,a$, and $D = 0.40\,a$. (b) Side view of the structure with parameters $R_1 = 2.95\,a$, $R_2 = 7.40\,a$, and $D = 0.40\,a$.

in the surrounding diamond material are designed such that they can be fabricated with the same techniques as the photonic crystal pattern. This implies that all structures are continuously patterned through the entire diamond membrane and have vertical side-walls in the ideal case. An optical field with a frequency of $\omega_{opt} = 0.3011 \cdot 2\pi\,c/a$ and with suitable symmetry, corresponding to the resonator mode, is then guided through the diamond waveguide and diffracted at the coupler structure.

The performance of the grating couplers is evaluated based on the electromagnetic flux emitted in the vertical direction as percentage of the electromagnetic flux transmit-

ted through the diamond airbridge onto the coupler structure. This method tends to overestimate the fraction of light coupled out of the diamond structure as emission under non-vertical angles is included in the coupling efficiency, but cannot be exploited experimentally. However, this method still gives a good estimate of a structure's performance and allows for comparison between different designs.
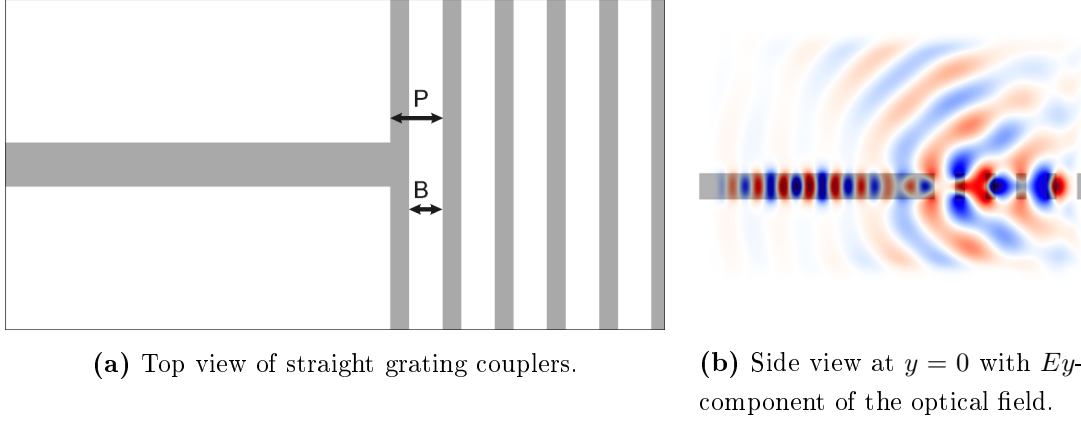

(a) Top view of straight grating couplers.

(b) Side view at $y = 0$ with Ey-component of the optical field.

Figure 3.10: Straight grating couplers in top view with indication of parameters (a) and side view with electrical field (b). The dimensions of both images correspond to the simulation cell and the couplers are shown with the ideal parameters $P = 1.90\,a$ and $B = 1.20\,a$.

The first design considered in this work are round grating couplers consisting of half-circles as shown in figure 3.9(a). A similar structure has already been described in literature [324]. The geometry is parametrised through two radii R_1 and R_2, and the width D of the diamond half-circle in the middle of the structure. The Ey-component of the electromagnetic field that is out-coupled in the vertical direction by this structure is shown in figure 3.9(b). For the optimal set of parameters $R_1 = 2.65\,a$, $R_2 = 5.30\,a$, and $D = 0.40\,a$, an efficiency of $25\,\%$ can be determined for this structure design. However, this design is not based on standard simple geometrical shapes that can be directly transferred to a pattern for focused ion beam milling. The fabrication of this structure is thus only possible with decreased resolution and at the cost of stronger mask erosion.

Therefore, a second design for straight grating couplers consisting of five trenches patterned in the diamond membrane is studied. This structure is shown in figure 3.10(a). The parameters used to describe this structure are the pitch P and the thickness of the air trenches B. Figure 3.10(b) shows the Ey-component of the electromagnetic field that is diffracted at a straight grating coupler. For the optimal set of parameters $P = 1.90\,a$ and $B = 1.20\,a$, also this design reaches $25\,\%$ out-coupling efficiency. Straight grating couplers are thus used for sample fabrication as they are better suited for patterning with standard focused ion beam milling and show a comparable performance as the round grating couplers.

3.3 Mechanical Properties and Optomechanical Interaction

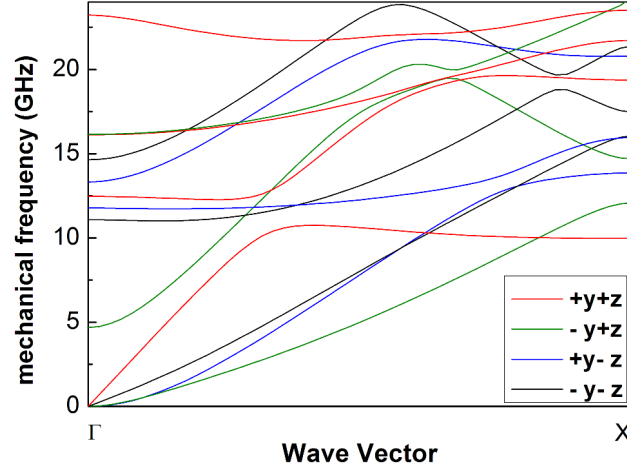### 3.3.1 Mechanical Band Structure

Figure 3.11: Acoustic band structure of a diamond phononic crystal with dimensions width $w = 1.60\,a$, height $h = 1.70\,a$, and hole radius $r = 0.42\,a$ as listed in table 3.1 for a unit length of $a = 223\,\mathrm{nm}$. The symmetries are indicated with $+$ denoting even and $-$ denoting odd symmetry in the respective direction.

As in the case of the optical properties, the mechanical band structure can be determined by studying the unit cell of the phononic crystal structure. Periodic boundary conditions allow to study an infinite phononic crystal in order to determine its acoustic band structure. The parameters to obtain ideal optical properties of the diamond structure are chosen as basis for the mechanical band structure analysis. These are width $w = 1.60\,a$ and height $h = 1.70\,a$ of the diamond structure. The absolute dimensions of the structure are scaled to a length of the unit cell $a = 223\,\mathrm{nm}$ such that the optical cavity mode is on resonance with the emission of the silicon vacancy colour centre at $738\,\mathrm{nm}$.

The full mechanical band structure is shown in figure 3.11. A clear symmetry of the modes in the x-direction cannot be determined, but modes arising from the Γ-point correspond to modes with even symmetry and modes arising from the X-point correspond to odd symmetry. No symmetry can be identified for all intermediate wave vectors. It can be seen that there is no full band gap for all symmetry conditions. However, when choosing a single symmetry condition, even a full band gap can be observed. Due to their better suitability for optomechanical interaction, fully symmetric modes with even symmetry in y- and z-direction should be chosen for further analysis.

Figure 3.12 only shows these fully symmetric mechanical bands and the corresponding mode profiles of the lowest order modes of defined symmetry G_2, G_3, X_1, and X_2. A band gap can be identified for frequencies ranging from 10 to 12 GHz for the parameter set given in table 3.1. However, this band structure changes for different sets of parameters and the band gap shifts accordingly. Therefore, an analysis for varying parameters
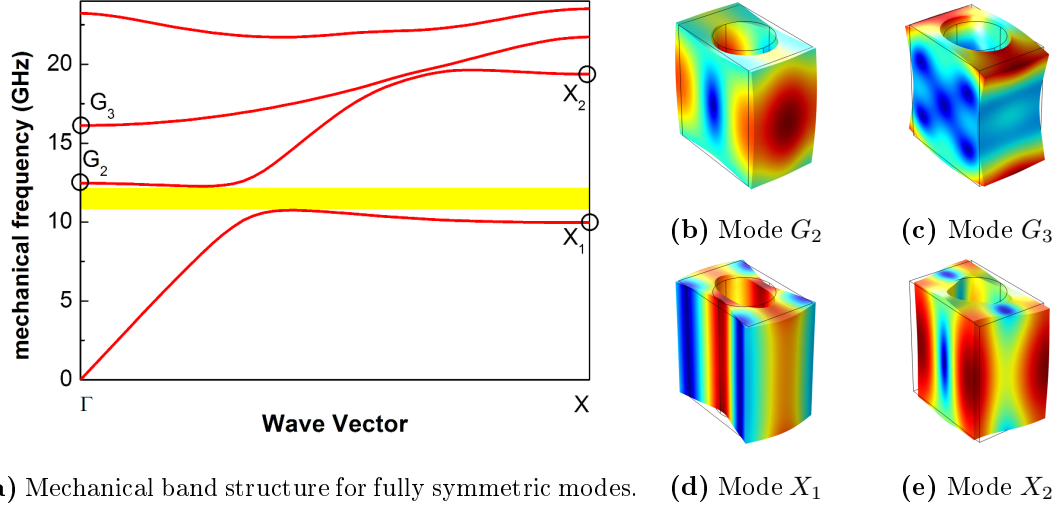
of the structure needs to be performed.

(a) Mechanical band structure for fully symmetric modes.

(b) Mode G_2

(c) Mode G_3

(d) Mode X_1

(e) Mode X_2

Figure 3.12: Mechanical band structure analysis considering only fully symmetric modes for a diamond phononic crystal with dimensions width $w = 1.60\,a$, height $h = 1.70\,a$, and hole radius $r = 0.42\,a$ as listed in table 3.1 for a unit length of $a = 223\,\text{nm}$. (a) Mechanical band structure, where the lowest order modes at the X- and the Γ-point are identified and the band gap is depicted as yellow area. (b)-(e) Profiles of the lowest order fully symmetric mechanical modes at the X- and at the Γ-point. The displacement fields are not to scale.

As the photonic and phononic crystal structure's design is based on a variation of hole radii, this parameter is given most attention. A more comprehensive overview is given in reference [323]. Figure 3.13 shows the frequencies of the lowest order modes at the X- and at the Γ-point for different hole radii. It can be seen that the frequencies are generally lower for larger holes and that modes arising from the Γ-point and modes arising from the X-point are affected nearly equally strong. These results confirm that it is indeed possible to create a localised mechanical resonator mode through a variation of hole radii.

The properties of this cavity mode, however, will be determined by the oscillation of the unit cell. For X-type modes, neighbouring unit cells are oscillating out of phase and the resulting optomechanical interaction will be comparatively low. Therefore, a mode arising from the Γ-point should be chosen as basis for a localised mechanical resonator mode. Comparing only the lowest order modes G_2 and G_3, it can be seen from figures 3.12 (b) and (c) that the maximum of the displacement field of mode G_2 is localised at the side of the unit cell whereas for mode G_3 it is localised at the edges of the unit cell. For an optimal interaction with the optical resonator mode, the mechanical cavity mode should be based on the mode G_2.
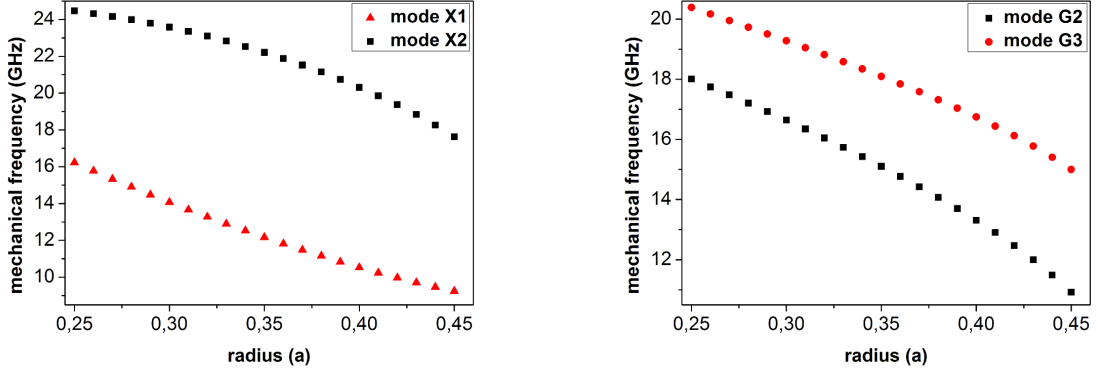
(a) Frequencies of modes at the X-point.

(b) Frequencies of modes at the Γ-point.

Figure 3.13: Frequency shift of the mechanical modes for different hole radii based on the band structure shown in figure 3.12. (a) Frequency map for mechanical modes arising from the X-point. (b) Frequency map for mechanical modes arising from the Γ-point.

3.3.2 Mechanical Resonator Mode and Optomechanical Coupling

The properties of localised mechanical resonator modes are studied based on a photonic and phononic crystal structure with the parameters given in table 3.1. As scaling for the structure, a lattice constant of $a = 223$ nm is chosen such that the optical resonator mode matches the zero phonon line of the silicon vacancy colour centre at 738 nm. Along with the mechanical mode properties, the optomechanical coupling constants $g_{\mathrm{PE},0}$, $g_{\mathrm{MB},0}$, and $g_{OM,0}$ can directly be determined as the optical properties are included to the mechanical simulation beforehand as explained in section 3.1.4.

Mode Overview

With this structure design, a variety of localised mechanical modes can be detected with frequencies ranging from MHz to several tens of GHz. Figure 3.14 shows the mechanical displacement field for a selection of localised mechanical resonator modes. It can clearly be seen from the displacement fields that the spatial localisation is much better for some modes than for others. Also the symmetry of the unit cell oscillations retrieved from mechanical band structure analysis can be recognised in the displacement fields of the different localised modes. When comparing the modes arising from the Γ-point G_2 and G_3 to the modes arising from the X-point X_1 and X_2 it can be seen, that neighbouring unit cells are oscillating in phased for the Γ-type modes and out of phase for the X-type modes. Also the modes with odd symmetry in at least one direction, termed O_i, can be tracked back to the corresponding points in the band structure. The mode O_1, for example, is arising from the Γ-point and shows odd symmetry in y- and even symmetry in z-direction. It can thus directly be linked to the second order band depicted as green line in figure 3.11.

To determine the spatial and temporal localisation, the effective mass m_{eff} and the mechanical quality factor Q_m need to be determined. Table 3.2 shows these values

(a) Localised mode G_2 **(b)** Localised mode G_3 **(c)** Localised mode X_1 **(d)** Localised mode X_2

(e) Localised mode O_1 **(f)** Localised mode O_2 **(g)** localised mode O_3 **(h)** Localised mode O_4
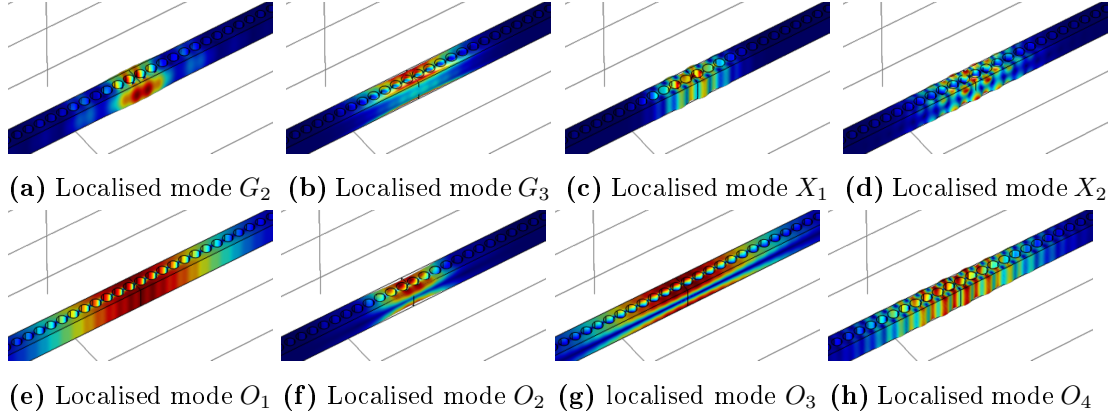
Figure 3.14: Displacement fields of localised mechanical cavity modes. The fully symmetric modes arising at the X- and at the Γ-point can be identified due to their mode profile corresponding to the ones found in the unit cell studies. All modes that have an odd symmetry in at least one direction are termed O_i and are not further distinguished into arising from the X- or the Γ-point. The displacement fields are not to scale.

for all modes depicted in figure 3.14 along with the optomechanical coupling constants $g_{PE,0}$, $g_{MB,0}$, and $g_{OM,0}$. It can be seen that the temporal and spatial confinement of the mechanical resonator modes are independent of each other. When comparing the effective masses to the profiles of the displacement field, small effective masses can indeed be correlated with a small spatial extent of the resonator modes.

To determine the overall optomechanical coupling, the contributions from both the photoelastic effect $g_{PE,0}$ and the moving boundaries effect $g_{MB,0}$ need to be considered. The single photon overall optomechanical coupling constant is the sum of the individual contributions. As both effects might add up or at least partly cancel out depending on the phase relation, the signs need to be respected in order to obtain a reliable result as shown in section 2.6.6. For the optomechanical coupling constants it is obvious that only fully symmetric modes arising from the Γ-point provide a reasonable interaction strength. Not only the overall coupling is weak for all other modes, but also the individual contributions from the photoelastic and the moving boundaries effect are comparably low. This is due to the fact that contributions from some parts of the structure at least partly cancel out with contributions from other parts of the structure as they have different signs. In order to achieve a strong optomechanical interaction, either the mode G_2, or the mode G_3 should be chosen. While the mode G_3 shows the best overall confinement, the selection of a suitable resonator mode should also be based on the shape of the displacement field to ensure a good strain coupling to colour centres located in the middle of the structure. As the areas of largest displacement are located at the edges of the diamond structure for the mode G_3, the strain coupling is expected to be low. In addition, modes of lower frequency should be preferred with respect to measuring. In the most simple setup to detect optomechanical interaction, a homodyne measurement, the mechanical resonance is visible in the intensity noise of the optical transmission spectrum through the diamond structure. This requires an optical detector

	f_m	m_eff	Q_m	$g_{\mathrm{PE},0}$	$g_{\mathrm{MB},0}$	$g_{OM,0}$
G_2	12.44	143	1.4×10^6	1.16×10^6	-7.15×10^4	1.09×10^6
G_3	16.26	63	1.7×10^7	3.92×10^5	-3.71×10^4	3.55×10^5
X_1	10.14	200	3.2×10^6	467	-1820	-1354
X_2	21.04	60	1.4×10^6	191	-664	-449
O_1	5.17	606	4.6×10^5	2328	8632	10960
O_2	11.10	117	6.7×10^6	-222	-2411	-2633
O_3	14.87	309	8.4×10^5	-79	300	221
O_4	15.46	251	4.4×10^5	187	-797	-547

Table 3.2: Mechanical resonator mode frequencies f_m in GHz and figures of merit for all localised mechanical cavity modes shown in figure 3.14 with dimensions as listed in table 3.1. The temporal and spatial confinement of the mechanical resonator mode are expressed in terms of effective mass m_eff given in femtograms fg, and the mechanical quality factor Q_m. The optomechanical coupling constants $g_{\mathrm{PE},0}$, $g_{\mathrm{MB},0}$, and $g_{OM,0}$ are given in units of $\mathrm{Hz} \cdot 2\pi$.

that can actually provide a temporal resolution of the spectrum covering the mechanical oscillation frequency. As the temporal resolution of optical detectors is a critical point and typically limited to few GHz in standard devices, the mechanical resonator mode should have a frequency that is as low as possible. This also shows that a photonic and phononic crystal resonator based on a design with larger holes in the centre is preferable over a design with smaller holes in the centre as presented in reference [323]. The mechanical resonance frequencies will be lower by design and facilitate measurements. In the following, only the localised mode G_2 will be considered and further investigated.

Higher Order Modes

(a) Second order mode $f_\mathrm{m} = 12.47\,\mathrm{GHz}$ **(b)** Third order mode $f_\mathrm{m} = 12.63\,\mathrm{GHz}$ **(c)** Fourth order mode $f_\mathrm{m} = 12.78\,\mathrm{GHz}$ **(d)** Fifth order mode $f_\mathrm{m} = 12.97\,\mathrm{GHz}$
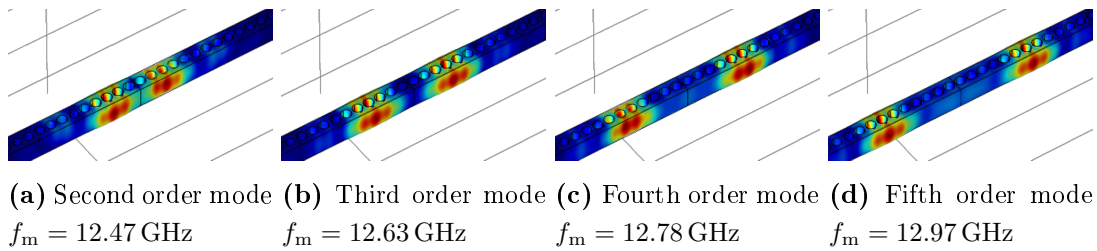
Figure 3.15: Displacement fields of higher order mechanical cavity modes arising from the fundamental mode G_2 and the corresponding mechanical resonance frequencies f_m. The displacement fields are not to scale.

In addition to the fundamental modes shown in figure 3.14, also higher order modes appear for each of these different fundamental modes. Figure 3.15 shows the higher order modes of G_2-type. The spatial confinement is obviously much lower and these

modes are not of further interest with respect to optomechanical interaction or strain coupling. It is, however, important to know the mechanical resonance frequencies so that the different modes can be identified in a mechanical mode spectrum of the photonic and phononic crystal structure. In addition, higher order modes could become more important in the case that fabricated samples are less than perfect. For example in the case of strain coupling, a localisation of a single colour centre in the exact middle of the structure cannot easily be realised (see section 2.4.3). The interaction might then effectively take place with a higher order mechanical mode that provides a much stronger strain field at the position of the colour centre.

Optimisation of Optomechanical Coupling

In the next step, the parameters of the structure are modified in order to increase optomechanical interaction. This can in principle be achieved by two different strategies. Either the stronger contribution from the photoelastic effect $g_{\mathrm{PE},0}$ can further be increased, or the contribution from the moving boundaries effect $g_{\mathrm{MB},0}$ can be reduced in its absolute value. A parameter study of the photonic and phononic crystal structure is performed to this end. The optimal parameters are shown in table 3.3 along with the figures of merit for both the optical and the mechanical resonator mode as well as the resulting optomechanical coupling constants. It can be seen when comparing this set of parameters to the one listed in table 3.1, that especially a stronger variation of hole radii expressed in a larger value of C increases the optomechanical interaction. The stronger optomechanical interaction results mainly from a better spatial confinement of both the optical and the mechanical resonator mode. This improvement, however, comes at the cost of reducing the temporal confinement of both resonator modes and especially the quality factor of the optical resonator mode drops by almost two orders of magnitude. There is no optimal solution for this dilemma and the choice of parameters should always be adapted to the specific aim.

w	h	r_0	C	Q_{opt}	V_{opt}	Q_{m}	m_{eff}	$g_{\mathrm{PE},0}$	$g_{\mathrm{MB},0}$	$g_{\mathrm{OM},0}$
1.50	1.64	0.43	0.0023	$5.5 \cdot 10^5$	0.98	$4.4 \cdot 10^5$	112	1.91	-0.09	1.82

Table 3.3: Optimal set of parameters for the photonic and phononic crystal resonator structure to achieve maximal optomechanical interaction. The parameters width w, height h, and radius r_0 are expressed in units of the lattice constant $a = 223\,\mathrm{nm}$. The figures of merit for the temporal and spatial mode confinement are indicated in terms of V_{opt} in $(\lambda/n)^3$, m_{eff} in fg, Q_{opt}, and Q_{m}. The optomechanical coupling constants $g_{\mathrm{PE},0}$, $g_{\mathrm{MB},0}$, and $g_{OM,0}$ are expressed in units of MHz $\cdot 2\pi$. The mechanical resonance frequency is $f_{\mathrm{m}} = 12.02\,\mathrm{GHz}$ and the optical resonator wavelength is $707\,\mathrm{nm}$.

Besides only varying the parameters of the structure, also the entire design can be modified in order to improve the performance of the photonic and phononic crystal cavity. This could also circumvent the trade-off between a good temporal confinement of the modes on the one side and a good spatial confinement and thus better optomechanical coupling on the other side. When considering again the mechanical bandgap analysis

shown in figure 3.13b, it can be seen that the very small holes far from the centre of the photonic and phononic crystal resonator do not provide an effective bandgap for the localised mechanical resonator mode. The same is true for the optical mode gap (see reference [321]). When adapting the design of the structure such that the hole sizes are more uniform across the structure, a better confinement of both the optical and the mechanical resonator mode could be expected. In addition to a performance improvement, this modification of the photonic and phononic crystal design facilitates sample fabrication. Especially the very small holes at the edges of the structure cause difficulties with respect to patterning due to the extremely high aspect ration (see 4.1.2. It is thus advantageous to avoid the smallest hole radii also with respect to a practical implementation.

(a) Original structure design.

(b) Modified desgin with only $K = 12$ holes of variable size.
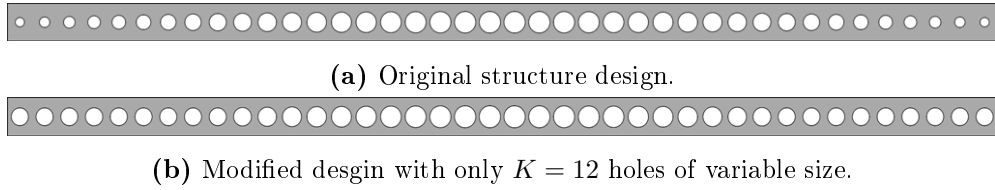
Figure 3.16: Design modification of the photonic and phononic crystal structure by introduction of a mirror section. The parameters are width $w = 1.50\,a$, height $h = 1.64\,a$, radius $r_0 = 0.43\,a$, and scalar $C = 0.0015$.

However, the largest optomechanical coupling constants can be reached with a strong variation of hole radii. The modification of the structure should thus not change the distribution of hole radii in the centre of the structure where the interaction strength is determined, while at the same time the very small hole radii on the edges of the photonic and phononic crystal pattern should be avoided. To this end, the photonic crystal is varied such that only a limited number K of all holes on each side of the structure has the radii given by the formula in equation 3.4, while the outermost holes have the constant radius $r_{K-0.5}$. This design variation is shown in figure 3.16.

The performance of the structure is evaluated for different values of K. The spatial localisation of both the optical and mechanical resonator modes of $V_{\text{opt}} = 1.5\,(\lambda/n)^3$ and $m_{\text{eff}} = 143\,\text{fg}$ as well as the optomechanical coupling strength with $g_{\text{OM},0} = 1.53\,\text{MHz}\cdot2\pi$ remain unchanged for values of $K \geq 7$. The optical and mechanical quality factors, however, are affected by this design modification. Figure 3.17 shows both the optical and the mechanical quality factor for different values of K, corresponding to a different number of holes with constant radius. It can be seen that both quality factors indeed increase for larger hole radii on the edges of the structure. Especially the mechanical quality factor, plotted on a logarithmic scale, increases by several orders of magnitude while the optical quality factor more than doubles. The increase of radii on the edges of the structure is thus acting as mirror section that provides an optical and a mechanical mode gap for the resonance frequencies of the localised mode. With this modified structure, it is thus possible to obtain at the same time very high quality factors and a high optomechanical coupling constant.
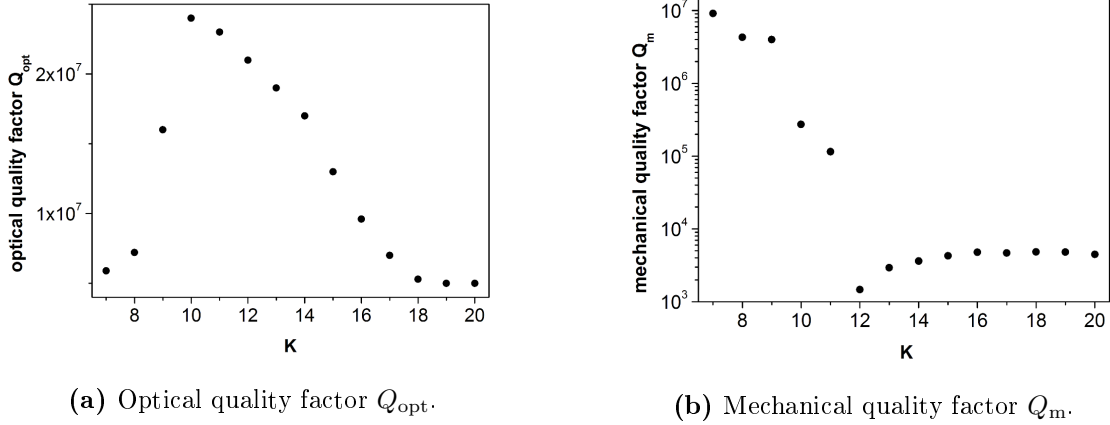
(a) Optical quality factor Q_{opt}.

(b) Mechanical quality factor Q_{m}.

Figure 3.17: Optical and mechanical quality factors for the same structure but with different number of holes with variable radius K. (a) Optical Quality factor Q_{opt} plotted on linear scale. (b) Mechanical quality factor Q_{m} plotted on logarithmic scale. The parameters of the structure are width $w = 1.50\,a$, height $h = 1.64\,a$, radius $r_0 = 0.43\,a$, and scalar $C = 0.0015$.

Scalability

The scalability of the optical resonator properties is a direct consequence of the scalability of Maxwell's equations expressed as eigenfunction of the electric field in equation 2.2. The same is true for the mechanical displacement field in equation 2.10. Therefore, both the optical and mechanical properties can be transferred to the same structure geometry but with deviating overall dimensions. Both the optical and the mechanical resonator mode scale with the inverse of the lattice constant $\omega_{\mathrm{opt}} \sim 1/a$ and $f_{\mathrm{m}} \sim 1/a$. The modal volume and the effective mass are volume measures and scale with the cubic lattice constant $V_{\mathrm{opt}} \sim a^3$ and $m_{\mathrm{eff}} \sim a^3$. Even the optomechanical interaction is scalable and the optomechanical coupling constants scale with the inverse of the effective mass $g_{\mathrm{OM}} \sim 1/m_{\mathrm{eff}}$ what is equivalent to the inverse to the cubic lattice constant $g_{\mathrm{OM}} \sim 1/a^3$. All simulations on optomechanical coupling in this work are based on a structure scaled to match the zero phonon line of the silicon vacancy colour centre at $738\,\mathrm{nm}$.

In order to investigate the interaction in a monolithic resonator where a nitrogen vacancy colour centre, an optical, and a mechanical resonator are mutually coupled, the results need to be transferred to the smaller overall dimensions of a structure matching the zero phonon line of a nitrogen vacancy colour centre at $637\,\mathrm{nm}$. The simulations are performed for both overall structure sizes in order to verify the scalability also in the numerical model as shown in tables 3.4 (a) and (b) for slightly deviating parameters of the structure. The figures of merit of the mechanical resonator and the optomechanical coupling constants are evaluated for an absolute strcutre size adjusted to match the zero phonon line of either the silicon vacancy colour centre or the nitrogen vacancy colour centre in diamond. The full scalability of the values in table 3.4(a) is not given due to limited numerical precision of the mechanical simulation. To test whether this is a general feature of the mechanical model or whether this result can be attributed to numerical imprecision, this comparison is repeated for a slightly different set of pa-

	SiV	NV
λ	738 nm	637 nm
a	223 nm	192 nm
f_{m}	12.4 GHz	14.4 GHz
m_{eff}	143 fg	69 fg
x_{ZPF}	2.17 fm	2.89 fm
$g_{\mathrm{PE},0}$	1.16	2.40
$g_{\mathrm{MB},0}$	−0.07	−0.15
$g_{\mathrm{OM},0}$	1.09	2.26

(a) Parameters as in table 3.1.

	SiV	NV
λ	762 nm	637 nm
a	223 nm	186 nm
f_{m}	13.2 GHz	15.9 GHz
m_{eff}	147 fg	85 fg
x_{ZPF}	2.08 fm	2.50 fm
$g_{\mathrm{PE},0}$	0.82	1.41
$g_{\mathrm{MB},0}$	−0.01	−0.02
$g_{\mathrm{OM},0}$	0.80	1.39

(b) Slightly smaller hole radius $r_0 = 0.40\,a$.

Table 3.4: Scalability of a photonic and phononic crystal resonator designed to match the zero phonon line of either the silicon vacancy colour centre at 738 nm or the nitrogen vacancy colour centre at 637 nm. (a) Parameters as in table 3.1. (b) Parameters as in table 3.1 but with slightly smaller hole radius $r_0 = 0.40\,a$. The results of the optical simulation are independent from the overall structure size. The values for the zero point fluctuation x_{ZPF} are evaluated based on the results for the effective mass m_{eff}. The optomechanical coupling constants $g_{\mathrm{PE},0}$, $g_{\mathrm{MB},0}$, and $g_{\mathrm{OM},0}$ are expressed in units of $\mathrm{MHz} \cdot 2\pi$.

rameters and the results are shown in table 3.4(b). It can be seen from the resulting figures of merit for the mechanical resonator and for optomechanical interaction, that the results are indeed scalable and that a smaller structure provides better spatial mode confinement and higher optomechanical coupling constants.

With the help this scalability test it can be confirmed that, despite small numerical variations for specific sets of parameters, all results can be converted to different structure dimensions due to the scalability of the underlying physical equations. The results shown in this section for structure dimensions adapted to match the zero phonon line of the silicon vacancy colour centre at 738 nm can thus be transferred to structures designed to interact with the nitrogen vacancy colour centre in diamond.

**Full Stress and Strain Tensors of the Mechanical Resonator Mode**

While the mode profile gives some hints on the mechanical displacement field, only the knowledge of the full stress tensor σ of the mechanical resonator mode provides the full information about the mechanical oscillation. It is thus a prerequisite for the evaluation of strain coupling. In order to assure good comparability, the tensor is only evaluated at the centre of the structure at coordinates $(0/0/0)$. This the most favourable position of the nitrogen vacancy colour centre when also a coupling to the optical resonator mode is required at the same time as, for example, in the case of the hybrid interaction. In addition, good optical properties of the emitter can only be obtained when a certain distance to the surface of the sample is respected. Therefore, strain coupling will only be evaluated for this position despite the fact that strain coupling could potentially be

larger at other locations, as the areas of maximal stress are located at the sidewalls of the innermost holes.

For the parameters of the photonic and phononic crystal structure given in table 3.1, scaled to match the zero phonon line of the nitrogen vacancy colour centre in diamond with $a = 192\,\text{nm}$, the mechanical elongation is adapted to correspond to the zero point fluctuation $x_{\text{ZPF}} = 2.89\,\text{fm}$. The resulting stress tensor σ then expresses the per-phonon-stress created by the mechanical oscillation in the centre of the diamond structure. For a structure oriented according to the crystallographic axes X, Y, and Z as sketched in figure 3.1, the full stress tensor σ retrieved from numerical modelling of the mechanical resonator mode is given as

$$\sigma = \begin{pmatrix} -1.7096 & 3354.6969 & 13.8899 \\ 3354.6969 & 50184.3247 & 1.4539 \\ 13.8899 & 1.452 & 2212.8153 \end{pmatrix} \text{Pa} \tag{3.5}$$

It can be seen from this stress tensor with a predominant component σ_{YY} that the oscillation is indeed a breathing mode as expected from the mode profile shown in figure 3.14 (a). To test the optimal orientation of the structure with respect to the nitrogen vacancy colour centre, different orientations of the photonic and phononic crystal resonator are considered. The strain tensor is evaluated for photonic and phononic crystal resonators fabricated in a sample with surface planes (001) and (111). The coordinate systems describing the structure in the different sample planes are the crystallographic axes $X = [100]$, $Y = [001]$, and $Z = [001]$ for (001) samples, and the coordinates $x = 1/\sqrt{2}\,[\bar{1}10]$, $y = 1/\sqrt{6}\,[\bar{1}\bar{1}2]$, and $z = 1/\sqrt{3}\,[111]$ for (001) samples as shown in figure 3.6 and also used to describe the nitrogen vacancy colour centre. All possible orientations of the photonic and phononic crystal structure within these sample planes are considered. For a (001) surface sample, $0°$ means that the periodicity of the photonic and phononic crystal structure is oriented along the X-axis along [100] as depicted in figure 3.1 and all other angles are defined through a counter-clockwise rotation around the Z-axis along [001]. The stress tensor given in equation 3.5 is obtained for an orientation of $0°$ in this case. For a (111) sample surface, $0°$ means that the long side of the diamond structure is pointing in the x-direction along [$\bar{1}$10] and all other angles are defined through a counter-clockwise rotation around the z-axis [111]. The full single phonon stress tensors for a photonic and phononic crystal structure scaled to match the zero phonon line of the nitrogen vacancy colour centre at $637\,\text{nm}$ is graphically represented in figure 3.18 for both sample surfaces and all orientations of the structure in the sample planes. It can be seen that the entries for XZ, YZ, and ZZ remain constant for all possible orientations of the structure in a (001) sample. The XX- and the XY-component are equivalent for a rotation by $90°$ what would be expected for a structure aligned according to the crystal lattice coordinates. For the structure in a (111) sample plane, the diagonal entries XX, YY, and ZZ as well as the off-diagonal entries XY, XZ, and YZ are equivalent under a rotation by $60°$. This can also be tracked back to the relative orientation of the structure with respect to the crystal lattice coordinates. The stress field analysis is the basis to evaluate strain coupling. In the case of strain coupling to the ground state levels evaluated based on the group theoretical description, the values that are graphically represented in figure 3.18 are directly used for the deter-
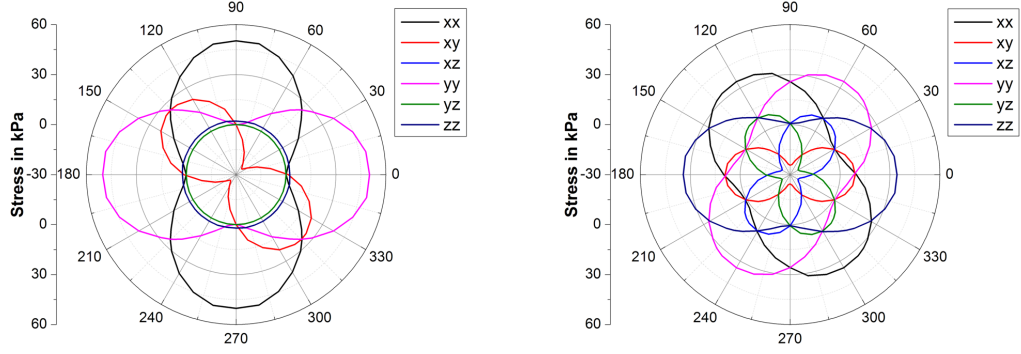
(a) Components of the single phonon stress tensor for phononic crystal structure fabricated in a (001) sample.

(b) Components of the single phonon stress tensor for phononic crystal structure fabricated in a (111) sample.

Figure 3.18: Components of the full single phonon stress tensor of the mechanical resonator mode expressed in the crystallographic coordinates X, Y, and Z. The remaining components are given by the symmetry of the stress tensor through the relation $\sigma_{\mathrm{IJ}} = \sigma_{\mathrm{JI}}$. The structure has the parameters listed in table 3.1 with a lattice constant $a = 192\,\mathrm{nm}$.

mination of the coupling constants $g_{\mathrm{M_x}}$, $g_{\mathrm{M_y}}$, and $g_{\mathrm{M_z}}$. For all other cases, the strain field acting on the nitrogen vacancy colour centre first needs to be derived from this stress field expressed in the crystallographic coordinates. The assumption of a linear elastic material is valid for diamond and the proportionality between the stress field σ and the strain field ϵ defined by Young's modulus E given in equation 2.1 can be exploited to obtain also the full strain tensor created by the mechanical resonator mode. For a photonic crystal structure in the (001) sample plane under 0°, the full single-phonon strain tensor ϵ is given as

$$\epsilon = 10^{-9} \cdot \begin{pmatrix} -0.0017 & 3.2413 & 0.0134 \\ 3.2413 & 48.4873 & 0.0014 \\ 0.0134 & 0.0014 & 2.1380 \end{pmatrix} \tag{3.6}$$

For all other orientations, the proportionality can be evaluated accordingly, but the qualitative information does not deviate from the results shown in figure 3.18.

3.4   Strain Coupling

In order to evaluate strain coupling, particular attention needs to be paid to the relative orientation between the nitrogen vacancy colour centre and the strain field created by the mechanical resonator mode. The effective interaction depends on the strain expressed in the coordinates of the colour centre. Especially the qualitatively different effects of strain axial or radial to the nitrogen vacancy colour centre axis [111] needs to be represented in the model. To this end, the strain field is expressed in the internal coordinates of the nitrogen vacancy colour centre graphically represented in figure 3.6.

For both sample surfaces and all possible orientations of the diamond structure, the strain field created by the mechanical resonator mode acting on a nitrogen vacancy colour centre oriented along the axis [111] is evaluated. The individual entries of the corresponding strain tensor expressed in the internal coordinate system of the nitrogen vacancy colour centre $x = 1/\sqrt{2}\,[\bar{1}10]$, $y = 1/\sqrt{6}\,[\bar{1}\bar{1}2]$, and $z = 1/\sqrt{3}\,[111]$ are shown in figure 3.19.
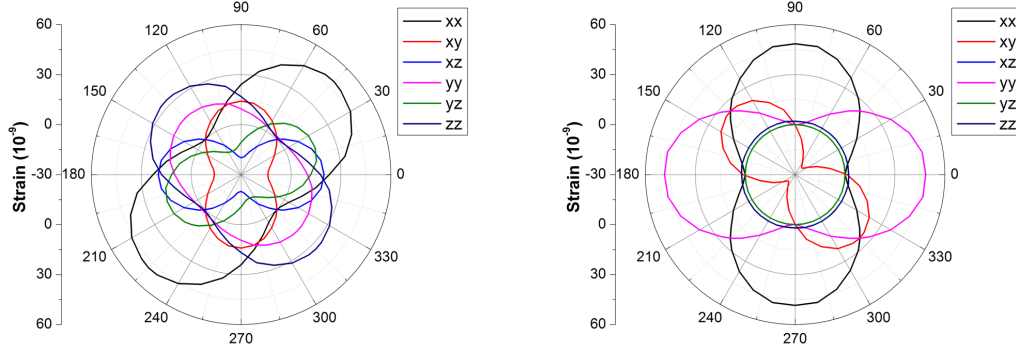
(a) Components of the single phonon strain tensor acting on a nitrogen vacancy colour centre for a phononic crystal structure fabricated in a (001) sample.

(b) Components of the single phonon strain tensor acting on a nitrogen vacancy colour centre for a phononic crystal structure fabricated in a (111) sample.

Figure 3.19: Components of the full single phonon strain tensor of the mechanical resonator mode expressed in the internal coordinate system of the nitrogen vacancy colour centre depicted in figure 3.6. The remaining components are given by the symmetry of the stress tensor through the relation $\epsilon_{ij} = \epsilon_{ji}$. The structure has the parameters width $w = 1.60\,a$, height $h = 1.70\,a$, radius $r_0 = 0.42\,a$, scalar $C = 0.0007$ as indicated in table 3.1 with a lattice constant $a = 192\,\mathrm{nm}$.

It can be seen from this graphical representation, that the angle between the colour centre axis and the diamond structure is crucial for the evaluation of strain coupling. The strain tensor components involving the surface normal direction xz, yz, and zz are constant for all possible orientations of the phononic crystal resonator in the (111) sample and also the rotational symmetry under $90°$ is maintained for the components xx and yy. For the (001) sample, the angle of $54.7°$ between the colour centre axis and the surface normal vector does not allow for obvious rotational symmetries between the individual tensor entries. However, the projection of the colour centre axis [111] in the plane can be recognised in the maximum of the xx component under $45°$ and the maximum of the yy and the zz components under $135°$. These strain fields acting on a single nitrogen vacancy colour centre located in the middle of the diamond structure are the basis for the evaluation of strain coupling to the ground state levels based on the phenomenological description, and to the excited state levels.

3.4.1 Strain Coupling to the Ground State Levels

Evaluation based on Phenomenological Description

The strain coupling constants for the interaction between the mechanical resonator mode and the ground state levels of the nitrogen vacancy colour centre $g_\parallel$ and $g_\perp$ are evaluated based on equations 2.88 and 2.89 issuing from the purely phenomenological description. The strain coupling coefficients used for the calculations can be found in table 2.1. For reasons of clarity, only the strain coupling constants obtained based on the strain coupling reported in reference [174] are shown in the graphical representations. The values reported in reference [173] are only considered for comparison of the absolute values for the strain coupling coefficients. The axial strain coupling constant $g_\parallel$ causing a shift of the $|\pm 1\rangle$ levels with respect to the $|0\rangle$ level of the nitrogen vacancy colour centre ground state is shown in figure 3.20 for a photonic and phononic crystal structure fabricated in a (001) and in a (111) sample. It can be seen that the strain coupling constant $g_{\parallel,111} = 30\,\mathrm{Hz}$ is constant for all possible orientations of the structure within the sample plane. This is expected because the colour centre is aligned along the surface normal of the diamond membrane, and a rotation of the structure in the plane should not change the axial strain coupling constant in this case. For a structure fabricated in a (001) diamond sample, the values for the axial strain coupling constant vary between $g_{\parallel,001,\mathrm{min}} = 10\,\mathrm{Hz}$ and $g_{\parallel,001,\mathrm{max}} = 447\,\mathrm{Hz}$. Maximal strain coupling occurs for a rotation of 135° of the photonic and phononic crystal structure with respect to the crystallographic X-axis [100], whereas minimal coupling can be found under an angle of 45°. This can be explained based on the strain field acting on the nitrogen vacancy colour centre shown in figure 3.19(a). Only the zz-component of the strain tensor is relevant for the evaluation of $g_\parallel$, and the value of this tensor entry varies accordingly upon rotation of the diamond structure in the sample plane. Considering the mode profile of the mechanical resonator mode G_2, a breathing mode, the predominant displacement is perpendicular to the photonic crystal pattern. The strain coupling constant $g_\parallel$ can be maximised when the projection of the mechanical oscillation on the axis of the nitrogen vacancy colour centre is highest. This is true for the angle of 135°, while the mechanical oscillation is mainly perpendicular to the symmetry axis of the nitrogen vacancy colour centre [111] for an orientation of the diamond structure of 45° in a (001) sample plane. To achieve an overall very high strain coupling constant $g_\parallel$, the photonic and phononic crystal structure should thus be fabricated in a (001) type sample under an angle of 135° with respect to the crystallographic coordinates. The coupling constants that are obtained based on the strain coupling coefficients reported in reference [173] are $g_{\parallel,111,\mathrm{Basel}} = 12\,\mathrm{Hz}$ for a (111) sample and vary between $g_{\parallel,001,\mathrm{Basel,min}} = 4\,\mathrm{Hz}$ and $g_{\parallel,001,\mathrm{Basel,max}} = 182\,\mathrm{Hz}$ for a diamond structure fabricated in a (111) sample surface.

The strain coupling constant $g_\perp$ causing a mixing and splitting of the $|+1\rangle$ and $|-1\rangle$ ground state levels of the nitrogen vacancy colour centre under the interaction with the photonic and phononic crystal resonator is shown in figure 3.21 for a (001) and a (111) sample for all possible orientations of the diamond structure. It can be seen that the values obtained for the radial strain constant $g_\perp$ are generally higher than the coupling constants $g_\parallel$ for axial strain. For a photonic and phononic crystal structure fabricated
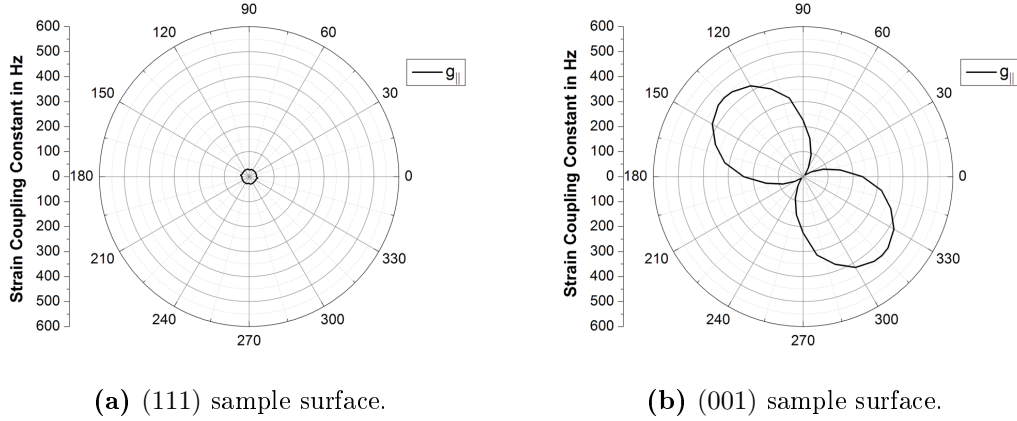
(a) (111) sample surface.   **(b)** (001) sample surface.

Figure 3.20: Strain coupling constant describing axial strain $g_\parallel$ for the interaction between the ground state levels of a nitrogen vacancy colour centre oriented along the axis [111] and a phononic crystal structure. All possible orientations of the diamond structure in a (111) sample surface (a) and in a (001) sample surface (b) are considered. The structure has the parameters shown in table 3.1 with a lattice constant $a = 192\,\text{nm}$.

in a (111) diamond sample, the interaction strength varies between $g_{\perp,111,\text{min}} = 372\,\text{Hz}$ under equivalent 45° angles, and $g_{\perp,111,\text{max}} = 522\,\text{Hz}$. The maximal values occur for an orientation of the photonic and phononic crystal pattern along the coordinates x and y in the coordinate system describing the nitrogen vacancy colour centre shown in figure 3.6. For the same structure fabricated in a (001) sample plane, the strain coupling constants for radial strain vary between $g_{\perp,001,\text{min}} = 184\,\text{Hz}$ and $g_{\perp,001,\text{max}} = 526\,\text{Hz}$ where the highest values can be achieved for an angle of 45°. The predominant oscillation perpendicular to the direction of periodicity of the hole pattern is then oriented along the projection of the colour centre axis [111] in the sample plane. This result fits well with the results for axial strain in the (001) sample plane where the minimal values for the axial strain coupling constant $g_{\parallel,001}$ occur under the same orientation of 45°. In general, very high radial strain coupling constants $g_\perp \geq 500\,Hz$ can be achieved for both sample types. When a precise orientation of the photonic and phononic crystal structure cannot be assured for technical reasons, a (111) sample surface is to prefer as the variation of the strain coupling constant for different orientations is smaller than for a (001) sample surface. As comparison, the values for the radial strain coupling constants obtained based on the strain coupling coefficients reported in reference [173] vary between $g_{\perp,111,\text{Basel,min}} = 340\,\text{Hz}$ and $g_{\perp,111,\text{Basel,max}} = 476\,\text{Hz}$ for a structure fabricated in a (111) sample surface, and $g_{\perp,001,\text{Basel,min}} = 168\,\text{Hz}$ and $g_{\perp,001,\text{Basel,max}} = 480\,\text{Hz}$ for a (001) diamond sample.

Evaluation based on Group Theoretical Description

Besides the purely phenomenological approach to strain coupling, also the description obtained from group theoretical calculations reported in reference [307] is used in order to determine the strain coupling constants for the interaction between the ground state
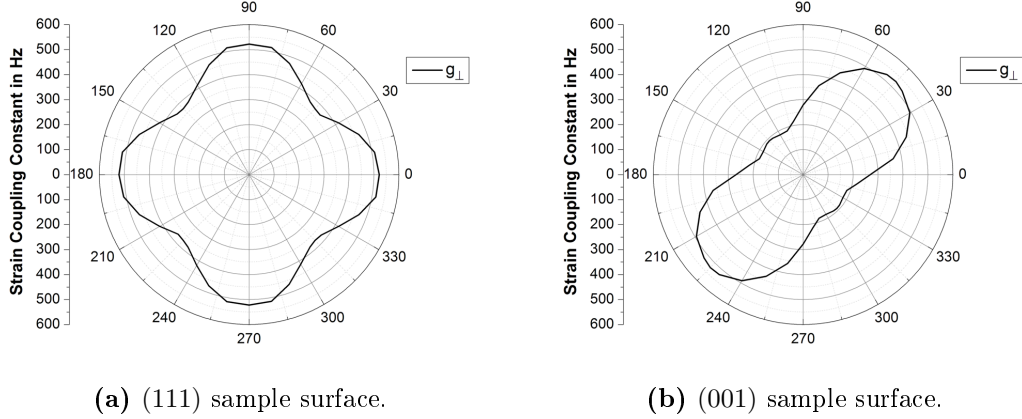
(a) (111) sample surface.   **(b)** (001) sample surface.

Figure 3.21: Strain coupling constant describing radial strain $g_\perp$ for the interaction between the ground state levels of a nitrogen vacancy colour centre oriented along the axis [111] and a phononic crystal structure. All possible orientations of the diamond structure in a (111) sample surface (a) and in a (001) sample surface (b) are considered. The structure has the parameters shown in table 3.1 with a lattice constant $a = 192\,\mathrm{nm}$.

levels of the nitrogen vacancy colour centre and a diamond photonic and phononic crystal structure. The strain coupling constants $g_{\mathrm{M_x}}$, $g_{\mathrm{M_y}}$, and $g_{\mathrm{M_z}}$ are determined based on equations 2.95, 2.96, and 2.97. The values for the corresponding strain coupling coefficients are listed in table 2.2. The effective splitting $\Delta_\pm$ between ground state levels $|+1\rangle$ and $|-1\rangle$ is evaluated based on the effective strain coupling constant $g_{\mathrm{M_\Delta}}$ given by equation 2.94. In contrast to the direct evaluation based on the full strain tensor acting on the nitrogen vacancy colour centre shown in figure 3.19 used in the purely phenomenological description of strain coupling to the ground state levels and for the description of strain coupling to the excited state levels, the strain coupling constants here are evaluated based on the stress tensor expressed in the crystallographic coordinates of the diamond structure as shown in figure 3.18. As already pointed out in section 2.7.1, this particularity originates from the form of the underlying equations and cannot be adapted here despite the fact that the left-handed coordinate system used in the derivation of the coupling constants will influence the results.

Figure 3.22 shows the single phonon strain coupling constant $g_{\mathrm{M_z}}$ that indicates the additional splitting between the ground state levels with non-zero spin projection $|\pm1\rangle$ and the ground state level with zero spin projection $|0\rangle$. When looking at figure 3.22(a), the strain coupling constant $g_{\mathrm{M_z}}$ is in principle independent from the orientation of the diamond structure in the (111) sample plane as in the case for the corresponding value $g_{\parallel,111}$ from the phenomenological description. However, slight variations of the numerical value indicate that the limited precision of the corresponding strain coupling coefficients a_1 and a_2 retrieved from experimental data prevent a strictly constant value even though the underlying stress tensor does not show these discontinuities. However, the differences remain small and are still within the uncertainty range given for the experimentally determined strain coupling coefficients. The absolute value $g_{\mathrm{M_z},111} = 430\,\mathrm{Hz}$, however,

(a) (111) sample surface.   **(b)** (001) sample surface.
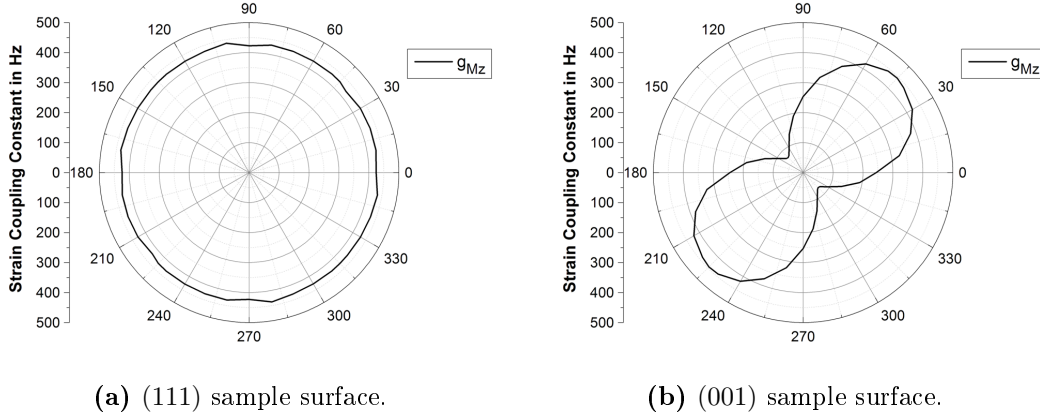
Figure 3.22: Strain coupling constant describing axial strain g_{M_z} for the interaction between the ground state levels of a nitrogen vacancy colour centre oriented along the axis [111] and a phononic crystal structure. All possible orientations of the diamond structure in a (111) sample surface (a) and in a (001) sample surface (b) are considered. The structure has the parameters shown in table 3.1 with a lattice constant $a = 192\,\text{nm}$.

is more than a factor of ten larger than the values obtained for $g_{\parallel,111} = 30\,\text{Hz}$. This indicates that the group theoretical description does not reproduce the results obtained from a direct measurement.

It can be seen from figure 3.22(b) that the strain coupling constant g_{M_z}, determining the additional splitting between the ground state levels with zero and non-zero spin projection, depends on the orientation for a structure fabricated in a (001) sample plane. It varies between $g_{M_z,001,\text{min}} = 70\,\text{Hz}$ under $135°$ and $g_{M_z,001,\text{max}} = 445\,\text{Hz}$ under $45°$. These absolute values are comparable to the values obtained for $g_{\parallel,001}$ from the phenomenological description what was also evaluated in the original article presenting the group theoretical description in order to prove the consistency of the phenomenological description with their calculations [307]. However, when comparing figures 3.20(b) and 3.22(b), minimal and maximal strain coupling occur at different orientations of the diamond structure in the sample plane with a shift of $90°$. Considering again the oscillation pattern of the mechanical resonator mode, the results obtained from the phenomenological description are more trustworthy. The reason for this mismatch is probably that the coordinate system used in the derivation of equation 2.97 is left-handed, in contrast to the right-handed crystal coordinates. A projection of the stress field created by the mechanical resonator mode would thus require an inversion besides the pure rotation of the coordinates. As the choice of coordinate system probably only accidentally resulted in a left-handed orientation, this additional transformation step is not included in the derivation.

Figure 3.23 shows the strain coupling constants g_{M_x} and g_{M_y} as well as their combined effect g_{M_Δ} indicating the splitting between the levels with non-zero spin projection $|+1\rangle$ and $|-1\rangle$. For a photonic and phononic crystal fabricated in a (111) sample plane, the individual strain coupling constants g_{M_x} and g_{M_y} vary between $g_{M_{x/y},111,\text{min}} = -61\,\text{Hz}$
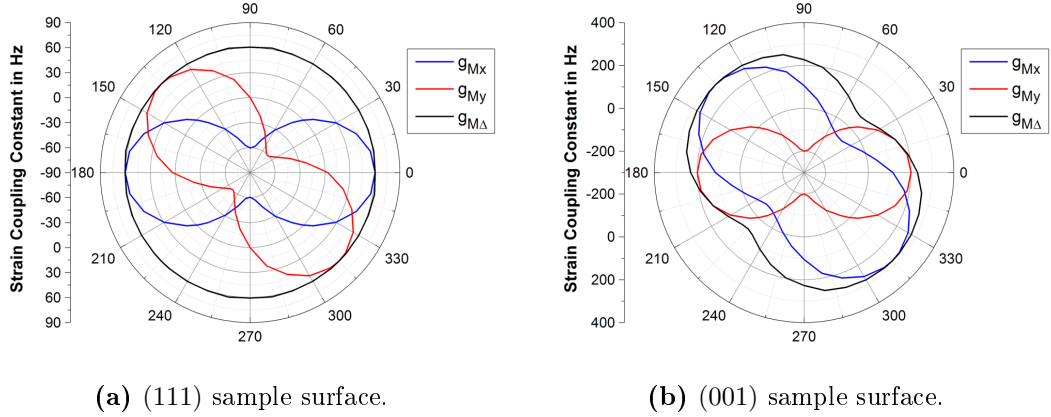
(a) (111) sample surface. **(b)** (001) sample surface.

Figure 3.23: Strain coupling constants describing radial strain $g_{\mathrm{M_x}}$, $g_{\mathrm{M_y}}$, and $g_{\mathrm{M_\Delta}}$ for the interaction between the ground state levels of a nitrogen vacancy colour centre oriented along the axis [111] and a phononic crystal structure. All possible orientations of the diamond structure in a (111) sample surface (a) and in a (001) sample surface (b) are considered. The structure has the parameters shown in table 3.1 with a lattice constant $a = 192\,\mathrm{nm}$.

and $g_{\mathrm{M_{x/y}},111,\mathrm{max}} = 61\,\mathrm{Hz}$ for different orientations of the diamond structure. The overall strain coupling constant determining the measurable splitting, however, is constant and has a value of $g_{\mathrm{M_\Delta},111} = 61\,\mathrm{Hz}$. The absolute value deviates strongly from the numbers found for the phenomenological description ranging from $g_{\perp,111,\mathrm{min}} = 372\,\mathrm{Hz}$ to $g_{\perp,111,\mathrm{max}} = 522\,\mathrm{Hz}$. In addition, the variation of the strain coupling constant $g_{\perp,111}$ for different orientations of the diamond structure is not represented in the results obtained from the group theoretical calculation. However, it cannot clearly be determined here whether the group theoretical calculation can better account for strain fields that are not aligned with the x- and y-axes of the colour centre. That the interaction between the mechanical resonator mode and a single nitrogen vacancy colour centre aligned along the surface normal of the diamond structure is independent of the rotation of the diamond structure with respect to the embedded colour centre might very well be a valid qualitative result. If this would be true, this result would show that the full group theoretical description might indeed improve the understanding of strain coupling obtained from the phenomenological description.

For the same structure fabricated in a (001) diamond sample, the individual strain coupling constants vary between $g_{\mathrm{M_x},001,\mathrm{min}} = -70\,\mathrm{Hz}$ under $135°$ and $g_{\mathrm{M_x},001,\mathrm{max}} = 283\,\mathrm{Hz}$ under $45°$, and between $g_{\mathrm{M_y},001,\mathrm{min}} = -200\,\mathrm{Hz}$ under $90°$ and $g_{\mathrm{M_y},001,\mathrm{max}} = 200\,\mathrm{Hz}$ under $0°$, respectively. The resulting splitting between the ground state levels $|+1\rangle$ and $|-1\rangle$ varies between $g_{\mathrm{M_\Delta},001,\mathrm{min}} = 70\,\mathrm{Hz}$ under $135°$ and $g_{\mathrm{M_\Delta},001,\mathrm{max}} = 283\,\mathrm{Hz}$ under $45°$. Here again, the absolute values almost match the strain coupling constants determined by the phenomenological description and only deviate by a factor of approximately two. The orientations of the diamond structure found for minimal and maximal interaction based on the group theoretical calculations, however, cannot plausibly be explained by the mode profile of the phononic crystal mode.

It remains to conclude that the group theoretical derivation of the strain coupling constants might give valuable information about the underlying mechanisms. However, a proper definition of right-handed coordinate systems both for the description of the nitrogen vacancy colour centre and the externally accessible diamond structure is crucial in order to obtain reliable results that can be reproduced experimentally.

3.4.2   Strain Coupling to the Excited State Levels

The calculation of the strain coupling constants g_{A_1}, g_{E_1}, and g_{E_2} between the excited states of the nitrogen vacancy colour centre and the mechanical oscillation of the diamond photonic and phononic crystal structure is based on equations 2.103, 2.104, and 2.105. The resulting splitting Δ_{xy} between the excited state levels $|E_x\rangle$ and $|E_y\rangle$ is determined based on the combined strain coupling constant g_{E_Δ} defined in equation 2.102. The values for the coupling coefficients are listed in table 2.3.

(a) (111) sample surface.   **(b)** (001) sample surface.
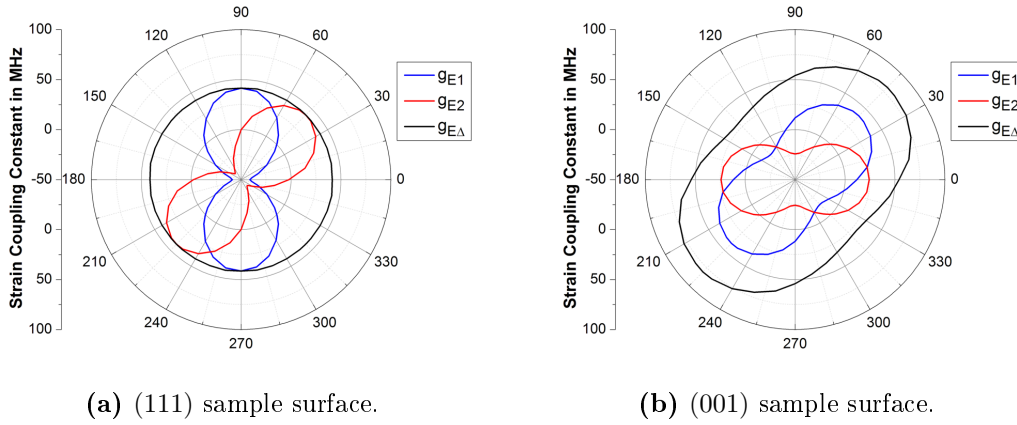
Figure 3.24: Strain coupling constants g_{E_1}, g_{E_2}, and g_{E_Δ} for the interaction between the excited state levels of a nitrogen vacancy colour centre oriented along the axis [111] and a phononic crystal structure. All possible orientations of the diamond structure in a (111) sample surface (a) and in a (001) sample surface (b) are considered. The structure has the parameters shown in table 3.1 with a lattice constant $a = 192\,\text{nm}$.

The strain coupling constants g_{E_1}, g_{E_2}, and their combined expression g_{E_Δ} for strain of E-type acting on the excited states $|E_x\rangle$ and $|E_y\rangle$ are shown in figure 3.24. The data show that the values of both coupling constants g_{E_1}, and g_{E_2} vary between $g_{E,111,\text{min}} = -41.5\,\text{MHz}$ and $g_{E,111,\text{max}} = 41.5\,\text{MHz}$ for the (111) sample surface with the respective maxima and minima being shifted by $45°$. The overall coupling constant for strain of E-type, however, has a constant value of $g_{E_\Delta,111} = 41.5\,\text{MHz}$ for all possible orientations. This confirms, that the alignment of the nitrogen vacancy colour centre along the surface normal direction of the photonic and phononic crystal structure allows to choose a random orientation of the diamond structure within the sample plane and still reach very high strain coupling constants.

For a photonic and phononic crystal structure fabricated in a (001) sample, the projection of the colour centre axis [111] in the plane is the relevant parameter for the

interaction. The strain coupling constant g_{E_1} ranging from $g_{E_1,001,\min} = -15\,\text{MHz}$ to $g_{E_1,001,\max} = 40\,\text{MHz}$ is generally higher than the strain coupling constant g_{E_2} taking values between $g_{E_2,001,\min} = -24\,\text{MHz}$ and $g_{E_2,001,\max} = 24\,\text{MHz}$. The relative maxima and minima for the two coupling constants occur for angles of $45°$ and $0°$, respectively. The overall coupling constant for strain of E-type determining the splitting between the excited state levels $|E_x\rangle$ and $|E_y\rangle$ takes values between $g_{E_\Delta,001,\min} = 15\,\text{MHz}$ under $45°$ and $g_{E_\Delta,001,\max} = 40\,\text{MHz}$ under $135°$. While the maximal value does not deviate much for both sample types, the orientation of the structure with respect to the colour centre axis [111] is crucial for a diamond structure fabricated from a (001) sample.

(a) (111) sample surface.   **(b)** (001) sample surface.
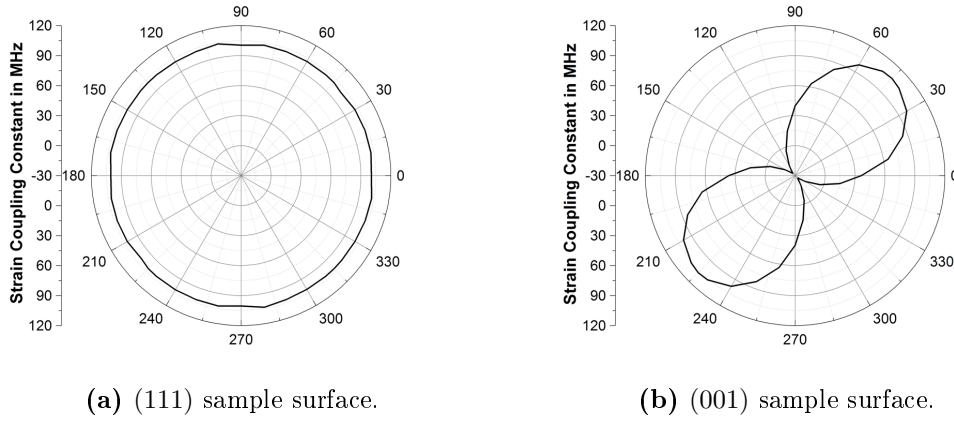
Figure 3.25: Strain coupling constant g_{A_1} for the interaction between the excited state levels of a nitrogen vacancy colour centre oriented along the axis [111] and a phononic crystal structure. All possible orientations of the diamond structure in a (111) sample surface (a) and in a (001) sample surface (b) are considered. The structure has the parameters shown in table 3.1 with a lattice constant $a = 192\,\text{nm}$.

Figure 3.25 shows the strain coupling constant g_{A_1} for the interaction between the photonic and phononic crystal structure and the excited states of the nitrogen vacancy colour centre, that causes a uniform shift of the excited state levels $|E_x\rangle$ and $|E_y\rangle$ with respect to the ground state $|A\rangle$. It can be seen from the data, that the strain coupling constant has a constant value of $g_{A_1,111} = 100\,\text{MHz}$ (with small numerical fluctuations) for all possible orientations of the diamond structure in a (111) sample plane. For a photonic and phononic crystal resonator fabricated in a (001) diamond sample, the coupling constant varies between $g_{A_1,001,\min} = -26\,\text{MHz}$ for an angle of $135°$ and $g_{A_1,001,\max} = 107\,\text{MHz}$ for an angle of $45°$. Very high strain coupling constants $g_{A_1} \geq 100\,\text{MHz}$ can be achieved with both sample types. However, a (111) sample provides the advantage that this value can be achieved for an arbitrary orientation of the photonic and phononic crystal structure.

3.5   Hybrid Interaction between Three Degrees of Freedom

In this section, the cooling of a mechanical resonator is investigated based on the theoretical description of the hybrid interaction in section 2.8. The results shown in this section were obtained from calculations principally performed by Luigi Giannelli. The model includes strain coupling of a single nitrogen vacancy colour centre to a localised mechanical resonator mode, a passive optical cavity resonant on its zero phonon line, and dephasing of the colour centre's electron spin. In contrast to the results issuing from numerical modelling shown thus far, the evaluation of hybrid interaction is a qualitative study where the individual parameters are represented by rough estimates in the correct size range but not with precise values. This is done to simplify the calculations and to obtain generally valid qualitative results that can also be applied to different systems showing similar characteristics. Another difference compared to the previous simulations is that dissipation processes are included in a more explicit way with a description based on a Born-Markov-formulation.

   The dynamics of the nitrogen vacancy colour centre are described in this model by the decay rate $\gamma_0 = 100\,\mathrm{MHz}$ and the dephasing rate $\gamma^* = 100\,\mathrm{MHz}$. The optical resonator is described by the frequency $\omega_{\mathrm{opt}} = 500\,\mathrm{MHz}$ and the decay rate $\kappa = 100\,\mathrm{MHz}$, while the mechanical resonator is characterised by the mechanical frequency $f_{\mathrm{m}} = 1\,\mathrm{GHz}$ and the decay rate $\Gamma_{\mathrm{m}} = 1\,\mathrm{kHz}$. The mechanical resonance frequency is chosen to be lower than the values in the range 10 to 20 GHz found in section 3.3.2 for the photonic and phononic crystal structure in diamond. This deviation from a more substantiated value is accepted in this particular case with the intention to avoid an interaction with other excited states besides $|E_x\rangle$ and $|E_y\rangle$ in the model. While this does not correspond to a realistic structure design, this adaptation still allows to obtain qualitative results. The axial strain coupling constant is set to zero $g_{\mathrm{A}_1} = 0$, whereas the radial strain coupling constants are chosen to be $g_{\mathrm{E}_1} = g_{\mathrm{E}_2} = 10\,\mathrm{MHz}$, as high as the value for the optomechanical constant $g_{\mathrm{OM},0} = 10\,\mathrm{MHz}$. The coupling constants both for strain coupling and for optomechanical interaction are summarised by the generalised coupling constant Λ in the following. The Rabi frequency is set to $\Omega = 2\pi \cdot 100\,\mathrm{MHz}$ and the relative detunings Δ_{L}, Δ_{opt}, and Δ_{xy} are used as variable parameters. The cooling efficiency is then evaluated in terms of the cooling rate $\widetilde{\Gamma}_{\mathrm{hybrid}}$ and the asymptotic minimal phonon occupation number $\overline{n}_{\mathrm{m,min}}$.

3.5.1   Effect of the Optical Resonator on the Cooling Performance

In a first step, the influence of the optical resonator on the cooling performance is evaluated. This is done by ignoring all thermal effects, including the thermal population of the mechanical resonator and dephasing of the nitrogen vacancy colour centre excited states ($\gamma^* = 0$, $\overline{n}_{\mathrm{th}} = 0$). In an initial parameter sweep, the optimal detuning between the transition ω_y (from the excited state $|E_y\rangle$ to the ground state $|A\rangle$) and the optical resonator frequency ω_{opt} is determined to $\Delta_{\mathrm{opt}} = 500\,\mathrm{MHz}$. Also the optimal frequency splitting between the two excited state levels $|E_x\rangle$ and $|E_y\rangle$ is identified as $\Delta_{xy} = 2\pi \cdot 1\,\mathrm{GHz}$ corresponding to the frequency of the mechanical resonator mode.
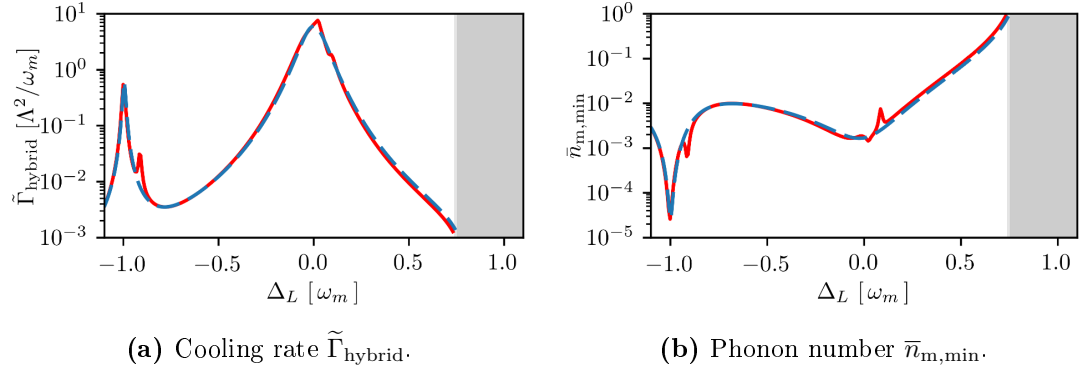
(a) Cooling rate $\widetilde{\Gamma}_{\text{hybrid}}$.

(b) Phonon number $\overline{n}_{\text{m,min}}$.

Figure 3.26: Cooling performance of the hybrid system for different detunings Δ_{L} expressed as cooling rate $\widetilde{\Gamma}_{\text{hybrid}}$ (a) and asymptotic minimal phonon occupation number $\overline{n}_{\text{m,min}}$ (b). The solid red line corresponds to the model including the optical resonator mode whereas the dashed blue line shows the results of the same model omitting the optical cavity. The shaded area indicates the parameter regime where effective heating takes place $\widetilde{\Gamma}_{\text{hybrid}} \leq 0$ or where the asymptotic minimal phonon occupation number exceeds the single particle excitation $\overline{n}_{\text{m,min}} \geq 1$.

Figure 3.26 shows the cooling rate $\widetilde{\Gamma}_{\text{hybrid}}$ as well as the asymptotic phonon occupation number $\overline{n}_{\text{m,min}}$ in presence and in absence of the optical resonator mode. To this end, the detuning Δ_{L} between the frequency of the driving laser ω_{L} and the transition ω_y from the excited state $|E_y\rangle$ to the ground state $|A\rangle$ is varied. It can easily be seen that the optical cavity does not have any effect on the cooling rate $\widetilde{\Gamma}_{\text{hybrid}}$ or the asymptotic minimal phonon occupation number $\overline{n}_{\text{m,min}}$ for most values of the detuning Δ_{L}. There are only two values of the detuning Δ_L where the optical resonator has a significant effect. These can be attributed to the level splitting induced by the coupling between the nitrogen vacancy colour centre and the optical resonator. It can thus be concluded that the optical resonator does not significantly improve the cooling performance for the chosen set of parameters.

3.5.2 Effect of Dephasing on the Cooling Performance

In an earlier work, the cooling of the nitrogen vacancy colour centre based on strain coupling to the excited states $|E_x\rangle$ and $|E_y\rangle$ has been evaluated without considering pure dephasing [311]. The impact of this dissipation effect on the cooling efficiency is evaluated here without considering the minor influence of the optical resonator mode on the cooling performance.

Effect of Dephasing in the Absence of a Thermal Bath

In an initial step, an artificial situation is studied where only dephasing occurs, but where the presence of a thermal bath causing a decoherence of the mechanical resonator mode is omitted. While this does not represent a physical system, the influence of dephasing

on the cooling dynamics can be studied isolated from other thermal effects. Figure 3.27 shows the cooling rate $\widetilde{\Gamma}_{\text{hybrid}}$ and the asymptotic phonon occupation number $\overline{n}_{\text{m,min}}$ for different values of the dephasing γ^* over a wide range of detunings Δ_{L}. The splitting between the excited state levels $|E_x\rangle$ and $|E_y\rangle$ is chosen to be equal to the mechanical resonator frequency $\Delta_{xy} = \omega_{\text{m}}$.
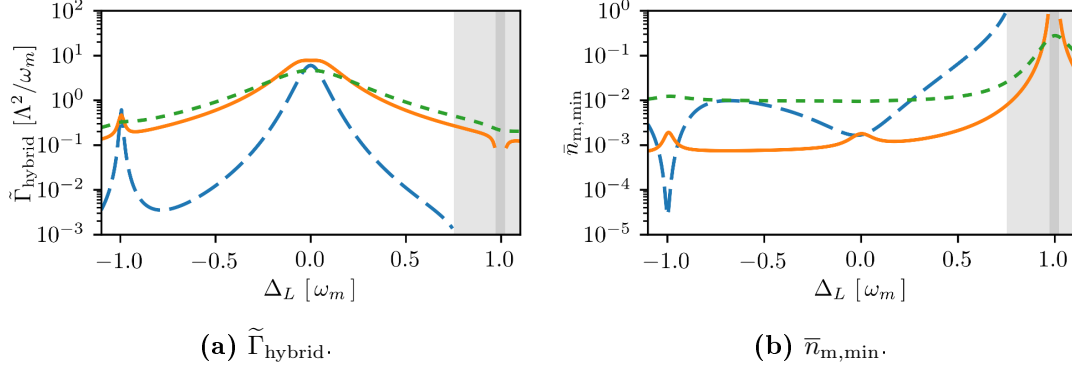

(a) $\widetilde{\Gamma}_{\text{hybrid}}$.   **(b)** $\overline{n}_{\text{m,min}}$.

Figure 3.27: Cooling performance of the hybrid system for different values of the dephasing γ^* and for different detunings Δ_{L} in terms of the cooling rate $\widetilde{\Gamma}_{\text{hybrid}}$ (a) and the asymptotic minimal phonon occupation number $\overline{n}_{\text{m,min}}$ (b). The dotted green line corresponds to a very high dephasing rate $\gamma^* = 10\,\gamma_0$, the solid orange line to a moderate dephasing rate $\gamma^* = \gamma_0$, and the dashed blue line to vanishing dephasing $\gamma^* = 0$. The shaded area indicates the parameter regime where effective heating takes place $\widetilde{\Gamma}_{\text{hybrid}} \leq 0$ or where the asymptotic minimal phonon occupation number exceeds the single particle excitation $\overline{n}_{\text{m,min}} \geq 1$.

The cooling rate increases in presence of dephasing with rate $\gamma^* = \gamma_0$ equal to the decay rate of the excited state levels. Extremely high dephasing rates $\gamma^* = 10\,\gamma_0$, however, do not further improve the cooling. For the asymptotic minimal phonon occupation number, the effect of dephasing is not so clear. For most values of the detuning Δ_{L}, the dephasing decreases the asymptotic minimal phonon occupation number. In the case of dephasing, the dependence of $\overline{n}_{\text{m,min}}$ from the detuning Δ_{L} decreases. The very low asymptotic minimal phonon occupation numbers at the detuning $\Delta_{\text{L}} = -\omega_{\text{m}}$ can, however, not be reached in presence of pure dephasing. For a very high dephasing rate $\gamma^* = 10\,\gamma_0$, the asymptotic minimal phonon occupation number $\overline{n}_{\text{m,min}}$ is generally higher for most values of Δ_{L} but remains below the excitation with a single cavity phonon for all values of the detuning. This analysis shows that dephasing indeed improves the cooling performance and a further study of a more realistic situation should be performed to complement this initial result.

Effect of Dephasing in the Presence of a Thermal Bath

In a next step, the impact of dephasing on the cooling efficiency is evaluated in presence of a thermal bath. This means that a thermal decoherence of the mechanical resonator with the rate Γ_{th} needs to be considered in addition to the damping rate of the mechanical oscillation Γ_{m}. This corresponds to a more realistic situation, as dephasing

originates from a thermal process and cannot be tuned independent from the colour centre's environment. The bath is modelled for temperatures of $T = 4\,\mathrm{K}$ and $T = 0.1\,\mathrm{K}$, corresponding to experimentally relevant conditions in cryogenic measurements.

Figure 3.28 shows the final phonon occupation number $\overline{n}_\mathrm{f}$ for different values of the detuning Δ_L in the absence and in the presence of dephasing. It can be seen that dephasing further decreases the final phonon occupation number $\overline{n}_\mathrm{f}$ compared to the situation without dephasing. It also allows for cooling at values of the detuning Δ_L that do not allow a reduction of the phonon population in the absence of dephasing. This shows that even a dissipation process can improve the performance of a measurement at the single particle level. The dephasing in this case does not add decoherence to the system but provides an additional channel to extract energy from the system.

(a) Bath temperature of $0.1\,\mathrm{K}$.   **(b)** Bath temperature of $4\,\mathrm{K}$.
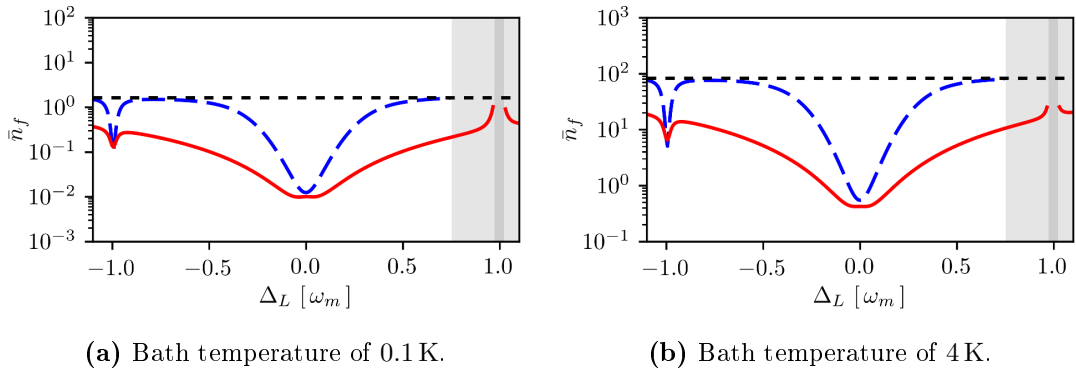
Figure 3.28: Final phonon occupation number $\overline{n}_\mathrm{f}$ of the hybrid system for different values of detunings Δ_L and temperatures of the thermal bath of $0.1\,\mathrm{K}$ (a) and $4\,\mathrm{K}$ (b). The solid red line corresponds to the system in presence of dephasing with a rate $\gamma^* = \gamma_0$, and the dashed blue line shows the same results for vanishing dephasing $\gamma^* = 0$. The horizontal dotted black line indicates the thermal phonon population number $\overline{n}_\mathrm{th}$. The shaded area indicates the parameter regime where effective heating takes place $\widetilde{\Gamma}_\mathrm{hybrid} \leq 0$ or where the asymptotic minimal phonon occupation number exceeds the single particle excitation $\overline{n}_\mathrm{m,min} \geq 1$.

Chapter 4

Experimental Implementation

This chapter shows the fabrication and optical measurement of photonic and phononic crystal structures. First, the fabrication and characterisation of single crystal diamond membranes is shown. The patterning of the photonic and phononic crystal structures is performed with two different methods, focused ion beam milling and reactive ion etching. A post-processing procedure required to recover the crystalline quality of the diamond material and to remove residues from the surface is described. The fabricated samples are optically characterised with fluorescence spectroscopy in a confocal microscope setup. Structures patterned both with focused ion beam milling and with reactive ion etching are investigated and the feasibility of measurements in vacuum, required for the detection of optomechanical interaction and an indirect measurement of the mechanical properties of the structure, is assessed.

4.1 Sample Fabrication

In order to obtain photonic and phononic crystal structures in diamond, a fabrication procedure with a number of individual steps is followed. Membranes of single crystal diamond with good optical properties are fabricated in a size of $150 \, \mu m \times 150 \, \mu m$ and thinned to the desired thickness of a few hundred nanometres. A characterisation step shows the thickness and homogeneity of the thinned diamond membrane. Then, a photonic and phononic crystal structure is patterned into the membranes either by focused ion beam milling or by reactive ion etching. An extensive post-processing procedure assures that the high crystal quality of the diamond is recovered, and that residual graphite or amorphous carbon is removed.

4.1.1 Fabrication of Thin Diamond Membranes

The fabricated structures are based on two different types of diamond samples as base material. As the photonic and phononic crystal structures require a precise thickness of the diamond membrane, both sample types need to undergo a thinning process. A mapping of the diamond thickness and homogeneity acts as quality control for the membrane thinning procedure where a high precision significantly improves the quality of the fabricated samples. The membrane fabrication and characterisation methods used in this work are described in more detail in reference [325].

Base Material for Diamond Membranes

Two types of samples are used as starting material to fabricate photonic and phononic crystal structures in single crystal diamond. One possibility is to use commercially available ultra-pure diamond membranes (Element Six). These can be bonded to silicon substrates containing small windows in order to obtain a free-standing diamond membrane. The bonding is done with the help of a spin-on-glass that is used to glue the two parts together. A subsequent annealing step at temperatures above $550 \, °C$ assures an extraordinarily strong bond between the diamond and the silicon sample that withstands all steps of the fabrication and the post-processing procedure. As alternative,

heteroepitaxially grown diamond can be used as starting material. This sample type comes in a layered structure with silicon as substrate, several intermediate layers and a single crystal diamond layer on the top [326]. By partially removing the substrate layer from the backside, a free-standing diamond membrane can be obtained.

Membrane Thinning

Both sample types undergo an additional reactive ion etching (RIE) step where an oxygen plasma thins the diamond membrane to the required thickness of few hundred nanometres . In the case of heteroepitaxially grown diamond, the etch plasma needs to be applied to the backside of the sample in order to preserve the high-quality top layer and instead sacrifice the nucleation layer of poor crystal quality. Only a very small amount of the diamond material is removed from the topside to assure that residues from polishing do not affect the optical properties of the diamond membrane. Thinning the diamond membrane from the backside leads to a thickness gradient across the membrane as the substrate partially shields the sample. In the case of commercially available diamond membranes bonded to a silicon substrate, the oxygen plasma can be applied to the topside of the sample. Also here, a little amount of material should be etched from both sides in order to remove the thin surface layer potentially affected by the polishing process. Thinning from the top side leads to a much more homogeneously thinned diamond membrane and gives better results than for heteroepitaxially grown diamond.

Membrane Characterisation

In an initial approximative measurement, the overall membrane thickness is estimated by white light transmission spectroscopy. Based on the outcome, further thinning of the membrane is performed until the target thickness of the diamond material is reached. To detect the approximate thickness, the entire diamond membrane is illuminated with a white light source . Maxima and minima can then be identified in the transmission spectrum what allows to determine the average membrane thickness. This method is not very precise and cannot give information about the thickness in a specific region of interest but always gives a mean value over the entire membrane. As the etch rate of the thinning process varies, this method is still helpful as it allows to determine whether further thinning is required.

The resulting thinned membranes undergo a more detailed characterisation in order to identify suitable locations for the fabrication of photonic and phononic crystal structures. This purpose implies that a non-destructive measurement is required in order to preserve the sample quality. To this end, laser scanning microscopy (LSM) is used in combination with white light imaging . The laser scanning microscopy technology is applied to identify neighbouring areas of destructive interference to find a relative scale for the membrane thickness at different locations. With the laser wavelength of $405\,\mathrm{nm}$ and the refractive index of diamond $n_{\mathrm{dia}} = 2.4$, the thickness variation between neighbouring fringes is $84\,\mathrm{nm}$.
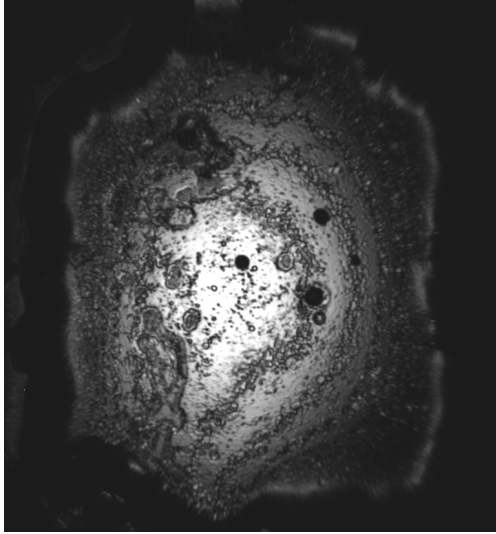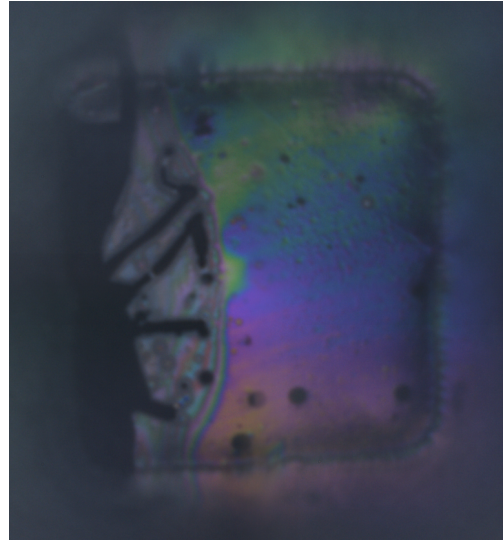
(a) Laser scanning image of a heteroepitaxially grown diamond membrane.
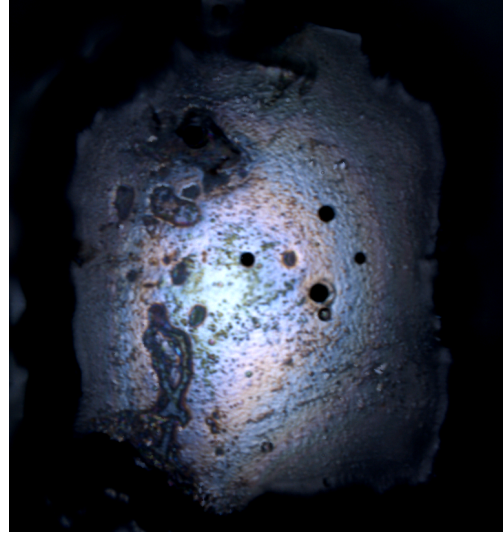
(b) White light image of a heteroepitaxially grown diamond membrane.
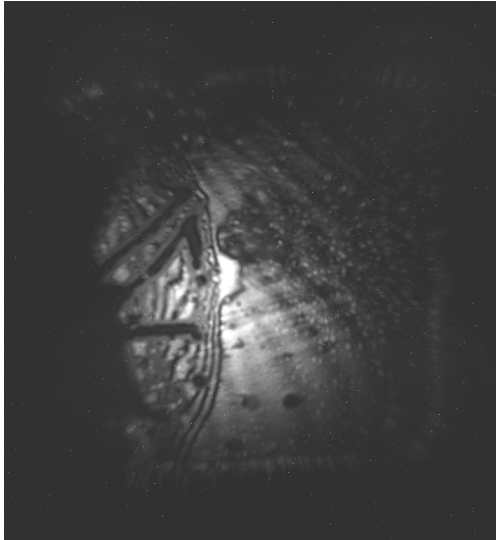
(c) Laser scanning image of a bonded diamond membrane.

(d) White light image of a bonded diamond membrane.

Figure 4.1: Laser scanning microscopy (a,c) and white light images (b,d) of heteroepitaxially grown (a,b) and bonded diamond (c,d) membranes. The interference pattern of the scanning laser reveals the areas of destructive interference as black coloured areas. The white light images allow to establish a finer continuous thickness map of the diamond membrane.

The discrete relative thickness scale obtained by the laser scanning microscopy can further be refined by a complementary white light image. Due to the spectrally broader source, the areas of constructive and destructive interference for different wavelengths appear as differently coloured areas. This gives very precise information on relative

thickness variations and diamond homogeneity throughout the entire membrane. However, an additional absolute calibration of the obtained thickness profile is required. This can be done by cross-sections where the thickness is measured at selected spots of a membrane. Despite the fact that such a measurement renders the test membrane unusable for the fabrication of optical resonators due to a residual platinum pollution dispersed over the entire area, it is very useful as the results can be transferred to all subsequent measurements without further needs for calibration. This allows to fully characterise diamond membranes and test their suitability for the fabrication of photonic and phononic crystal structures.

Figure 4.1 shows both the laser scanning images and the white light transmission spectra obtained from membrane thickness measurements of a heteroepitaxially grown diamond sample and a bonded diamond membrane. The comparison of the different sample types reveals that the diamond membrane thinned from the front is indeed much more homogeneous compared to the heteroepitaxially grown sample. Heteroepitaxially grown samples have to be thinned from the backside and a thickness gradient from the centre toward the edges of the membrane can be seen in figures 4.1(a) and 4.1(b). The absence of dark fringes corresponding to destructive interference in the laser scanning image in figure 4.1(c) indicates that the bonded sample is very homogeneous in thickness. Large areas of homogeneous colour in the white light image in figure 4.1(d) confirm that the thickness variations across the diamond membrane are indeed very small for the bonded sample. Besides the thickness measurement, also defects of the diamond membrane can be visualised with this technique. Especially for less-than-perfect heteroepitaxially grown diamond sample shown in figures 4.1(a) and 4.1(b), craters on the backside of the membrane are revealed that would remain hidden otherwise. This information can then be used to pattern photonic and phononic crystal structures in areas of homogeneous thickness without craters or defects in the diamond.

4.1.2   Patterning of Photonic and Phononic Crystal Structures

For patterning of the photonic and phononic crystal structures, two different techniques are used. A direct writing of the structures with a focused ion beam allows a fast patterning of arbitrary structures in a single processing step. A dry etching procedure allows for the fabrication of the photonic and phononic crystal structures with higher precision and steeper sidewalls. However, it requires a more complex procedure with mask patterning and etching. In the following, both methods are presented and the resulting structures are shown.

Fabrication with Focused Ion Beam Milling

Focused ion beam (FIB) milling is performed with a dual beam system. Here, a scanning electron microscope and an ion beam are integrated in a single device under an angle of 52° allowing for both imaging and patterning. The ion source is a liquid Gallium reservoir where Ga^+ ions are extracted and moved towards the sample by an acceleration voltage of 30 kV. Magnetic lenses allow a precise guidance and focussing of the ion beam onto the sample. A set of apertures allows to adapt the beam diameter and current to

the required resolution. For patterning the holes of the photonic and phononic crystal structure, the grating couplers, and the innermost trenches defining the width of the diamond airbridge, an ion beam current of 9.7 pA is used. This corresponds to an effective beam diameter (FWHM) of 13 nm. To pattern larger trenches that release the structure from the surrounding diamond membrane, only low precision is required and a larger aperture is used in order to reduce the milling time. For patterning grating couplers, focused ion beam milling has the advantage that also the fabrication of designs where the trenches are inclined or do not penetrate the entire diamond membrane is possible. This can improve the performance of the grating coupler structures compared to designs that are compatible with a dry etching technique.

A fabrication of the photonic and phononic crystal structures with focused ion beam milling does in principle not require any preliminary steps. The results can, however, greatly be improved by different means increasing the precision in the lateral direction and diminishing the unwanted effects caused by the profile of the focused ion beam. Clamping the sample on a holder instead of the standard fixation with gluing eliminates sample drift. This allows for a much more precise fabrication of the desired structures as the remaining beam drift is orders of magnitude smaller. The profile of the focused

(a) top view **(b)** inclined view
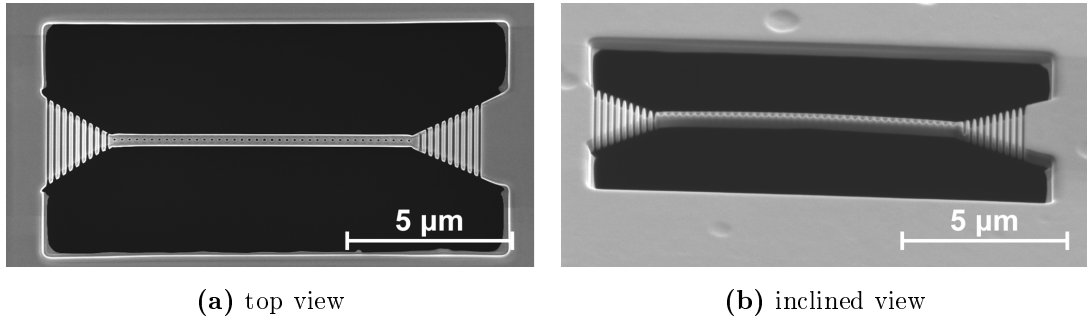
Figure 4.2: Photonic and phononic crystal structure fabricated with focused ion beam milling in top view (a) and inclined view (b).

ion beam leads to an unwanted irradiation of the diamond material surrounding the patterned areas. This does not only lead to inclined sidewalls but also to very round edges at the topside of the structures. A metal layer homogeneously covering the diamond membrane can mitigate some of the issues related to the beam profile. To this end, a chromium mask of 80 nm thickness is sputtered onto the diamond membrane. Besides protecting the diamond from unwanted irradiation that degrades the quality of the material, it also provides the conductive layer required for ion beam operation, and allows to use a so-called over-milling technique. The patterning is then not stopped directly when the photonic and phononic crystal pattern penetrates the entire thickness of the diamond membrane but continued further. The larger sputtering rate under steep angles leads to steeper sidewalls when the over-milling technique is applied. Because of the metal protection layer, the surface of the photonic and phononic crystal structure is not subject to additional beam irradiation. Besides the option to apply the over-milling technique, the metal protection layer also prevents very round edges at the topside of the diamond structures. The beam tails will still remove material around the area that

is intended to be patterned, but most of this additional sputtering is located in the metal layer. The removal of the metal protection layer with chromium etchant after processing leaves a diamond structure without rounded edges.

Figure 4.2 shows a photonic and phononic crystal structure fabricated with focused ion beam milling. The design of the grating couplers is adapted from reference [322]. The hole diameters are much smaller than in the modelled structures as they will grow considerably larger during the post-processing treatment. The inclined view shows that the membrane is not perfectly flat and that the airbridge structure is bending upwards due to residual stress in the diamond material. The hole sidewalls typically have angles between $4°$ and $6°$ for structures fabricated with focused ion beam milling [42,325].

Fabrication with Reactive Ion Etching

In contrast to the fabrication of structures with focused ion beam milling, patterning with a reactive ion etching technique always requires a mask. Here, a material system consisting of two different layers is used for this purpose. A spin-on-glass consisting of hydrogen silsesquioxane (product: Flowable Oxide FOx, Dow Corning) is applied directly on the diamond membrane with a thickness of 50 nm and cured at $400°C$ in vacuum for two hours. On top of this glass layer, a chromium mask of 80 nm thickness is sputtered onto the sample. For etching photonic and phononic crystal structures in diamond membranes, an additional etch step is required between curing of the spin-on-glass and the chromium layer. Through holes and cracks in the diamond membrane, small amounts of hydrogen silsesquioxane arrive at the backside of the sample and residues of the spin-on-glass prevent a full release of the patterned structures as shown in figures 4.3(a) and (b). These residues need to be removed by an additional fluorine etch step to clean the backside of the membrane before applying the chromium layer. If this order is not respected, the chromium layer cracks and parts of the membrane can accidentally be released during the oxygen plasma etch step as shown in figure 4.3(c).
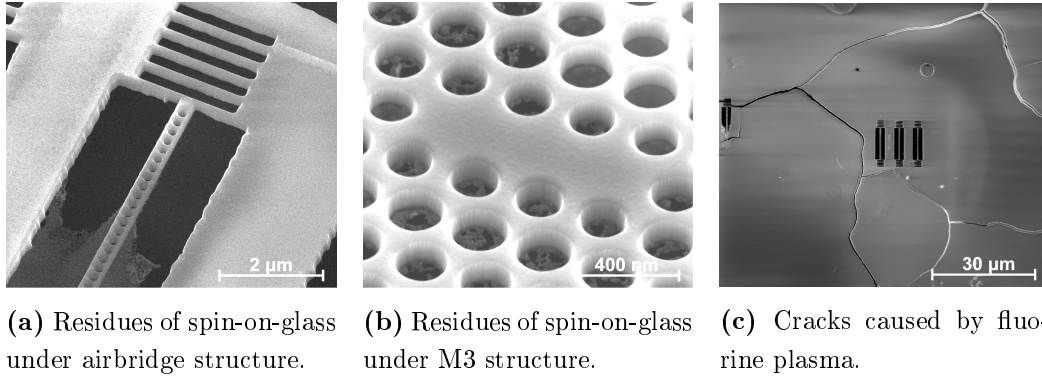

(a) Residues of spin-on-glass under airbridge structure.

(b) Residues of spin-on-glass under M3 structure.

(c) Cracks caused by fluorine plasma.

Figure 4.3: Spin-coating of hydrogen silsesquioxane typically leads to residues of spin-on-glass on the backside of the diamond membrane (a,b). Applying the fluorine plasma to the backside of the sample in order to remove the residues after application of the chromium layer leads to cracks in the metal mask (c).

The chromium mask is patterned using focused ion beam milling. Patterning only the chromium mask is much faster than penetrating the entire thickness of the diamond membrane with a comparably low sputtering rate in case of focused ion beam milling. This reduces the unwanted side effects of beam drift occurring for long structuring times and allows for a much more precise patterning of the photonic and phononic crystal structures. The intermediate glass layer is very important for this mask patterning step as a direct ion beam irradiation of diamond can lead to an unwanted etch resistance of the diamond [327,328]. Therefore, the thickness of the intermediate glass layer and the penetration depth of the focused ion beam upon mask patterning are crucial to obtain structures of high quality. On the one hand, the penetration depth needs to be high enough so that the entire chromium layer is removed in the patterned areas. On the other hand, the diamond should always remain covered with a complete layer of glass in order to avoid accidental masking of the diamond. The profile of the ion beam makes this a challenging task as the dose is much higher in the centre of all patterned areas than on the edges. The intermediate glass layer therefore needs to be thick enough to allow for this beam profile and the patterning depth needs to be calibrated with test structures.
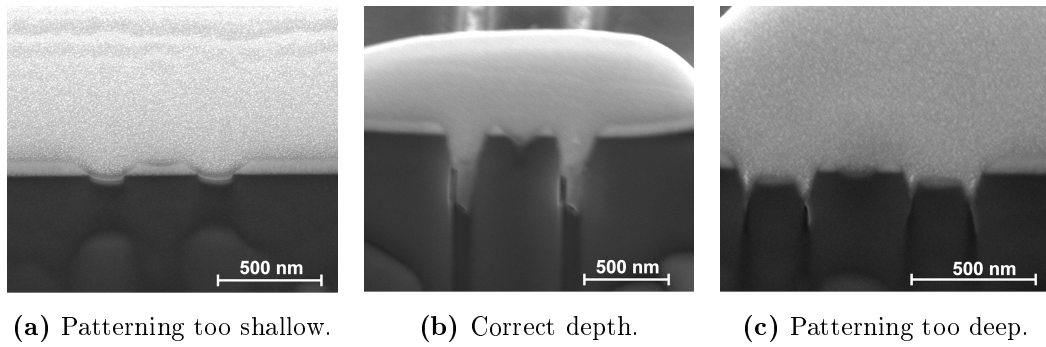

(a) Patterning too shallow.   **(b)** Correct depth.   **(c)** Patterning too deep.

Figure 4.4: Influence of the focused ion beam's penetration depth during mask patterning on the etch result. Only a well-adjusted patterning depth in allows for etching of the diamond (b) without shielding by residual chromium (a) or passivation of the diamond surface through ion beam exposure (c).

Figure 4.4 shows cross-sections of structures with different penetration depths of the focused ion beam. It can be seen that the patterning depth needs to be carefully adjusted as deviations from the optimal penetration depth prevent etching of the photonic and phononic crystal patterns. For a too low patterning depth shown in figure 4.4(a), the chromium layer is not entirely removed in the patterned areas and shields the underlying materials during the etch process. For a too high patterning depth shown in figure 4.4(c), the diamond is passivated through exposure to the ion beam and cannot be etched by the oxygen plasma. A very small stripe at the edges of the patterned area is still etched in this case as the beam tails create a small zone where the diamond is not exposed to focused ion beam irradiation. The milling depth, however, is difficult to adjust in practice as the ion beam current constantly increase during the lifetime of the aperture. The ion beam also sputters material from the aperture so that the effective

beam current increases over time. Therefore, a single calibration is not sufficient to continuously obtain reliable results. Test structures are made and analysed every time a new mask is patterned to assure that the correct depth is reached.

The etch step is performed with an inductively coupled plasma reactive ion etching (ICP-RIE) process . A high density plasma is created by electromagnetic induction and accelerated onto the sample with a bias voltage. This allows at the same time very high etch rates as the plasma density is increased by the electric fields generated through induction, and a highly anisotropic etch process assured by the bias voltage that directs the reactive ions onto the sample in surface normal direction. Etching of the photonic and phononic crystal structures is performed in a two-step process. In the first step, the intermediate glass layer is etched with a fluorine plasma. In a subsequent step, the diamond is etched in an oxygen plasma. For both etch steps, a number of parameters have to be adjusted in order to obtain a good etch result. Especially the flows of the different process gases, the power with which the inductively coupled plasma is generated, and the pressure inside the etch chamber need to be carefully adapted to optimise the process. Table 4.1 shows the optimal set of parameters for both the fluorine

| Parameter	Fluorine Plasma	Oxygen Plasma
Ar flow [sccm]	20	15
CHF_3 flow [sccm]	30	0
O_2 flow [sccm]	0	25
Chamber pressure [mTorr]	30	10
RF bias power [W]	20	100
ICP power [W]	200	750
Table temperature [°C]	20	20
Additional cooling	yes	no
Etch duration [sec]	210	210

Table 4.1: Etch plasma parameters. The intermediate glass layer is etched with the fluorine plasma in a first step, followed by the oxygen plasma to etch the diamond. The additional cooling in the case of the fluorine plasma is combination of a water cooling with 18 °C and a helium flow directed on the backside of the sample.

plasma used to etch the intermediate glass layer and the oxygen plasma used to etch the diamond. This set of parameters is optimised to fabricate photonic and phononic crystal resonators in single crystal diamond membranes.

Figure 4.5 shows different structures fabricated with this set of parameters. Figure 4.5(a) shows a top view of three photonic and phononic crystal resonators with straight grating couplers etched into a bonded diamond membrane. The holes of the three structures are patterned with 70 %, 80 %, and 90 % (from left to right) of the target size to account for the additional increase during etching and post-processing. It can be seen that the diamond bridges between neighbouring holes partly collapse during the etch process. This only appears between the larger innermost holes of the
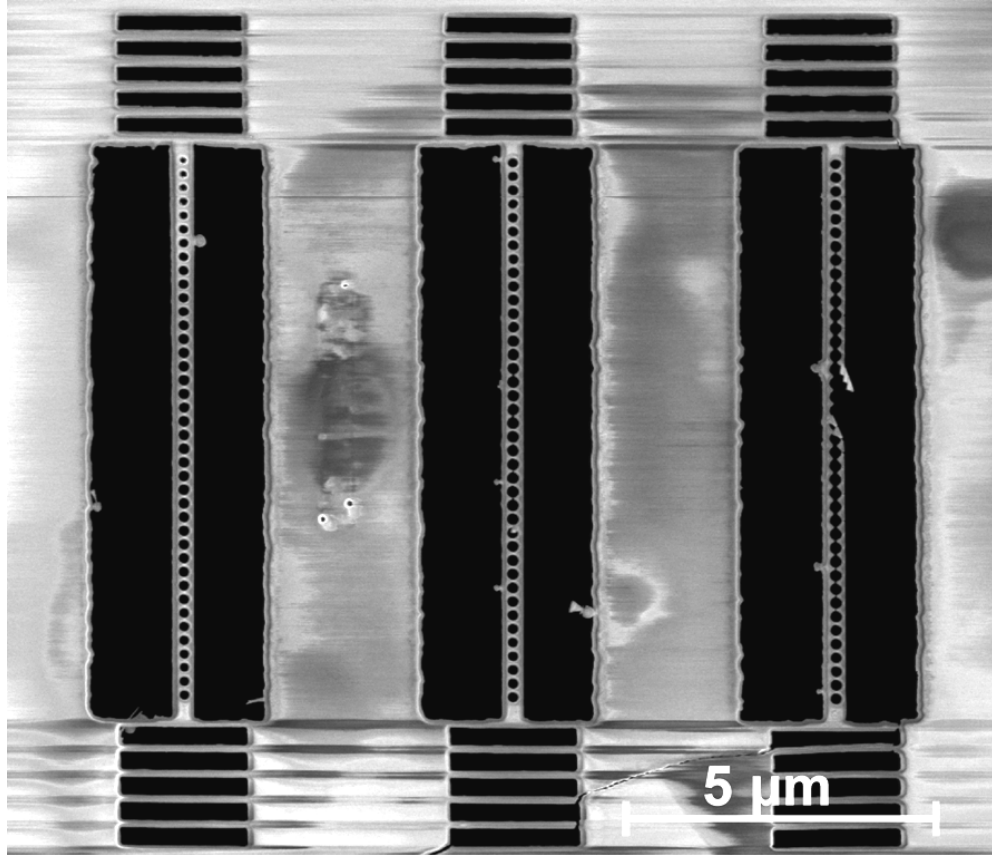
(a) Structures etched in a bonded diamond membrane patterned with 70 %, 80 %, and 90 % of the target size (from left to right).
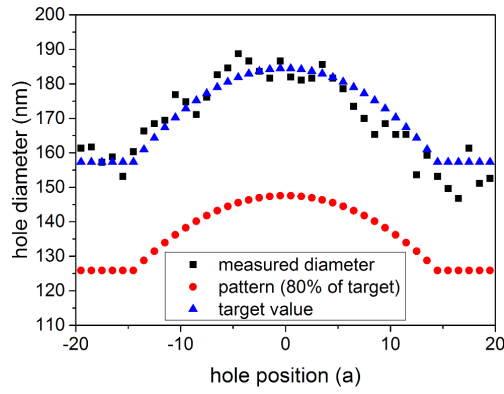
(b) Hole diameters measured from central structure in (a)
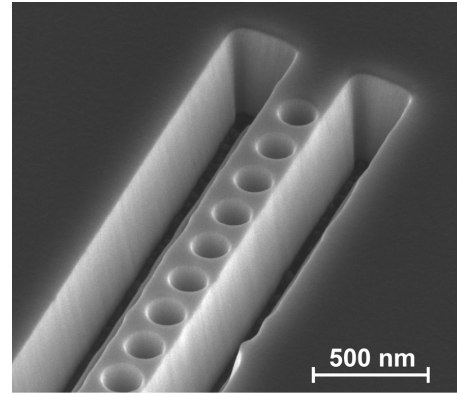
(c) Structure in heteroepitaxially grown diamond.

Figure 4.5: Photonic and phononic crystal structures etched in diamond membranes on different samples. The parameters of the etch processes are specified in table 4.1. The horizontal stripes around the grating couplers in (a) stem from charging of the sample during imaging. The pattern size of (c) is 70 % of the target size.

structures with larger overall hole diameters (centre and right structure). Figure 4.5(b) shows that the hole diameters of the structure patterned with 80 % measured from a high-resolution SEM image match the target values. However, this method is not very accurate and the limited precision of the values needs to be considered. Figure 4.5(c) shows an angled view of a structure etched in heteroepitaxially grown diamond. The sidewalls are smooth and steep and that both holes and trenches are etched.

As the entire etch process was developed in the course of this work, many preliminary steps were required in order to obtain diamond photonic and phononic crystals with steep and smooth sidewall that match the parameters of the modelled structures. In the following, a selection of the results obtained during the development of the etch procedure are shown. Related challenges and solutions are discussed along with the results.

Figure 4.6 shows the etch results for the same parameters as listed in table 4.1 except for a varying power generating the inductively coupled plasma. This parameter directly affects the plasma density and it can be seen that a higher power also leads to a strong mask erosion. The ideal value is thus high enough to allow for high etch rates generating steep and smooth sidewalls but low enough to avoid mask erosion.
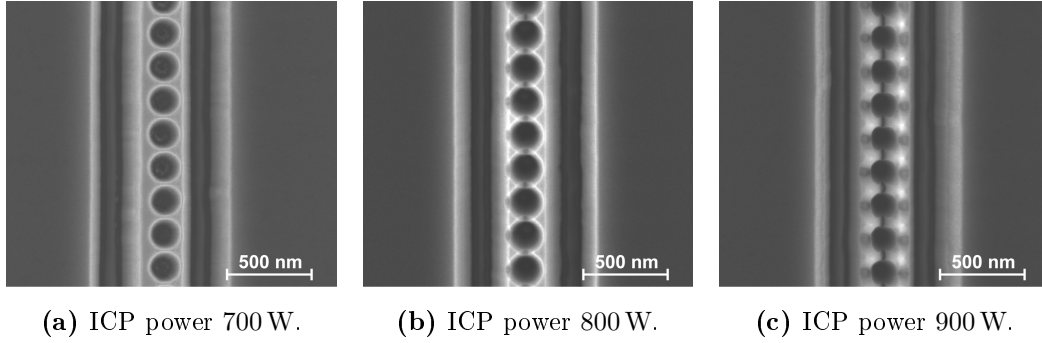

(a) ICP power 700 W.   **(b)** ICP power 800 W.   **(c)** ICP power 900 W.

Figure 4.6: Influence of the ICP power on the etch result for photonic crystal structures fabricated in a bulk diamond sample. Different values of 700 W (a), 800 W (b), and 900 W (c) have been tested. A higher power increases the plasma density and allows for higher etch rates and steeper sidewalls but also causes strong mask erosion.

Figure 4.7 shows other aspects besides the ICP power that have an influence on the etch process. As example for a variation of the gas composition, figure 4.7(a) shows the etch result for a higher oxygen content in the etch plasma. It can be seen that the holes are not properly etched and that the surface quality is not ideal. This leads to grooves in the hole sidewalls and "grass" covering the bottom of the holes. Figure 4.7(b) shows a photonic and phononic crystal structure that was etched at a lower chamber pressure of only 8 mTorr. This results in inclined sidewalls while a higher pressure would cause stronger mask erosion. Figure 4.7(c) shows a structure fabricated with a longer the duration of the oxygen plasma etch step of 240 sec. It can clearly be seen that mask erosion leads to a strong degradation of the structure. Adjusting the duration of each etch step is a crucial factor to obtain photonic and phononic crystal structures of high quality.

During the development of the etch procedure, a number of problems preventing a successful sample fabrication were identified. Figure 4.8 shows a collection of non-perfect etch results that can be attributed to different problems. As there is a limited availability of thin diamond membranes, initial etch tests were also performed in bulk diamond samples. However, the optimal set of parameters found for one sample type cannot directly be transferred to other material systems what can be attributed to deviating thermal and electric conductivity of different samples.

Figure 4.8(a) shows a structure fabricated in a heteroepitaxially grown diamond membrane where the sample was placed on a very thin glass slide during reactive ion etching. This prevents a good conduction of heat and electric currents to the silicon substrate wafer and leads to unevenly etched structures with poor surface quality. This rather drastic example for the influence of conductivity on the etch result illustrates why the optimal set of parameters deviates for structures etched in bulk diamond samples, into the bulk part of diamond grown on or bonded onto a silicon substrate, and thin diamond membranes.
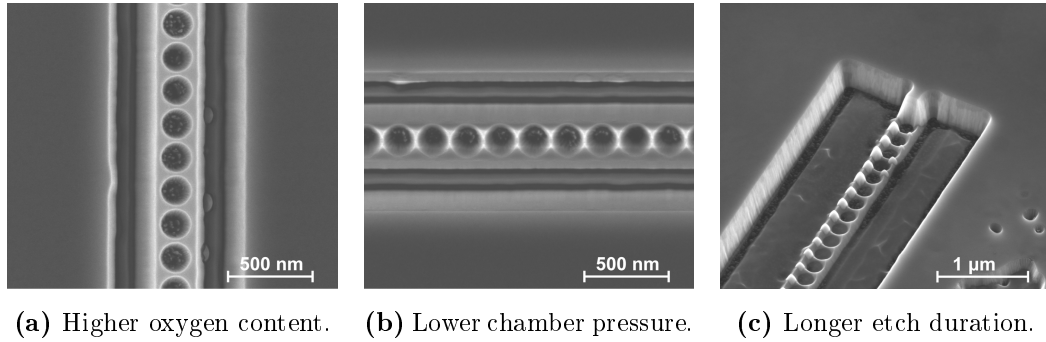

(a) Higher oxygen content. **(b)** Lower chamber pressure. **(c)** Longer etch duration.

Figure 4.7: Photonic and phononic crystal structures etched by oxygen plasma with slightly varying parameters compared to the ones given in table 4.1. (a) Argon flow of 10 sccm and oxygen flow of 30 sccm, bulk diamond sample. (b) Lower chamber pressure of 8 mTorr, bulk diamond sample. (c) Longer etch duration of 240 sec, heteroepitaxially grown membrane.

Figure 4.8(b) shows a structure that was etched in ten short intervals of only 21 sec each. This increases the ignition step's influence on the overall etch result and allows the sample to cool down between the individual etch cycles. This results in a highly uneven etch result with a very low etch rate and almost no material removal in the holes of the photonic and phononic crystal structure.

Figure 4.8(c) is an example for the poor reproducibility of the entire etch process. Both the sample and the fabrication procedure are exactly the same as for the structure shown in figure 4.6(a), but the result is obviously not satisfying. As many steps are required before obtaining diamond photonic and phononic crystal structures, it is not possible to always identify the reasons for the failure of an etch process. There are parameters that are difficult to control in practice, like for example the contamination of the etch chamber, the waiting time between the processing steps, or the ageing of the hydrogen silsesquioxane that is spin-coated onto the sample to create the intermediate glass layer. This also makes it difficult to optimise the process as the result of an individual etch run
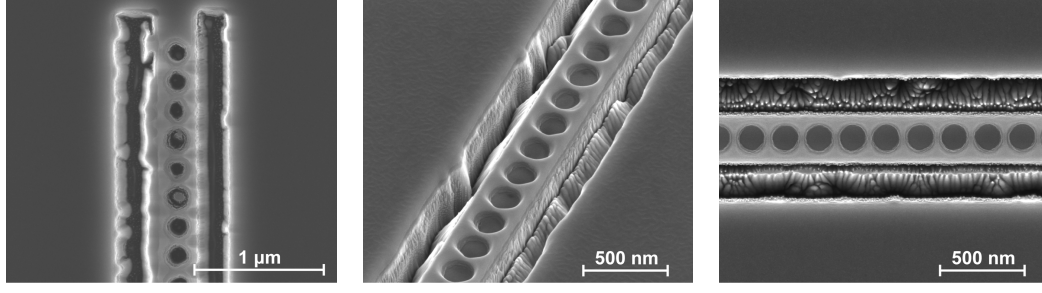
(a) Sample placed on very thin glass slide during etch.

(b) Etch plasma applied in short cycles of 21 sec each.

(c) Example for poor reproducibility of etch process.

Figure 4.8: Non-perfect etch results. (a) Sample placed on very thin glass slide during reactive ion etching. (b) Oxygen plasma applied in ten short cycles of 21 sec each. (c) Parameters as listed in table 4.1, expected to show result as in figure 4.6(a), fabricated on the very same sample.

might either be due to the parameter set chosen for the fabrication, or due to unidentified singular deviations from the regular procedure. The limited number of available samples, but primarily the heavily restricted access to the processing facilities make it impossible to double-check all results. The set of parameters listed in table 4.1, identified to be suitable for the fabrication of diamond nanostructures, might thus be found not to be ideal when an extensive study of the entire parameter range is performed.

4.1.3 Post-Processing Treatment of the Diamond Samples

After the etch procedure, the masks are removed in wet-etching treatments with chromium etchant and hydrofluoric acid. Besides removal of the etch masks, a post-processing procedure is required to recover a diamond material with good optical quality [42]. Especially in the case of structures patterned with focused ion beam milling, the diamond quality is degraded and the damaged layer needs to be recovered or removed. To this end, a high temperature annealing step follows the patterning of the structures. The samples are heated to 1000 °C in vacuum for 120 min. At this high temperature, vacancies and residual Gallium ions become mobile. In the damaged diamond layer, the individual atoms form sp^3 and sp^2 bonds corresponding to diamond or graphite. After high temperature annealing, subsequent oxidation steps remove all graphite and amorphous carbon covering the diamond. Oxidation can be performed thermally by heating the sample to 450 °C in air for 180 min. In addition, a chemical oxidation with so-called piranha solution, a mixture of sulphuric acid and hydrogen peroxide, is performed.

The removal of all diamond areas that have been heavily damaged during patterning, further increases the diameters of the air holes. This increase of hole sizes is different for both patterning techniques and needs to be calibrated in order to match the desired parameters after all processing steps. Photonic and phononic crystal structures fabricated with focused ion beam milling should be patterned with only 30 to 40 % of the desired final hole size, and structures fabricated with reactive ion etching with 70 to 80 %. It

also needs to be considered that especially in the case of structures fabricated with focused ion beam milling, the diameters of larger holes generally increase more during the post-processing procedure than the smaller holes at the ends of the structure. This means, that not only the overall hole sizes but also the distribution of hole sizes needs to be adapted to the fabrication procedure.

In principle, this post-processing treatment is a rather uncritical part of the fabrication procedure and tends not to have a strong impact on the resulting structures. Due to malfunctions of different annealing ovens, however, various photonic and phononic crystal structures fabricated with reactive ion etching in different diamond samples were destroyed. Therefore, the structures shown in figure 4.5 fabricated with reactive ion etching could not further be analysed although they look very promising as the sidewalls are both smooth and steep and the geometric parameters match the target values very well.

4.2 Characterisation of the Fabricated Samples

The optical properties of the fabricated samples are investigated with confocal microscopy [329]. The background fluorescence of diamond is exploited to feed the optical resonator modes. Due to the very high frequencies in the GHz range, mechanical resonator modes can only be detected indirectly via an optical measurement of optomechanical coupling. This requires a measurement in vacuum as friction at the surface leads to a very strong viscous damping. Unexpected issues occurring for measurements in vacuum that prevent a measurement of optomechanical interaction are shown and analysed.

4.2.1 Measurement Setups

Two different setups based on the same measurement principle, but with different individual components are used to characterise the fabricated samples. One of the setups only allows measurements at ambient conditions with the advantage that sample mounting is not required. The other setup allows for measurements in vacuum and at cryogenic temperatures, but the sample needs to be fixed onto an upright holder.

In both setups, the diamond fluorescence is excited by a diode laser at $532\,\mathrm{nm}$ focused onto the photonic crystal structures through a microscope objective with a numerical aperture of $NA = 0.8$. The fluorescence of the sample is collected by the same objective and analysed by a spectrometer based on a nitrogen-cooled camera . The sample chamber of the second setup can be evacuated with the help of a turbo pump that also provides an inbuilt pressure sensor.

4.2.2 Structures Fabricated with Focused Ion Beam Milling

Figure 4.9(a) shows the fluorescence spectrum of the structure depicted in figure 4.2. The photonic and phononic crystal pattern has been fabricated with focused ion beam milling in a heteroepitaxially grown diamond membrane. The broad peak around $740\,\mathrm{nm}$

can be attributed to an ensemble of silicon vacancy colour centres created in the diamond material during growth. With a polariser aligned either along the x-direction or the y-direction, the narrow peak at 720 nm can be identified as resonator mode 4.9(a). The optical resonator modes of the photonic and phononic crystal structures are even modes and can be identified in the spectrum due to their clear polarisation along the y-direction. Figure 4.9(b) shows a Lorentzian fitted to the optical resonator mode. The underlying data set is the difference between the green and red spectra in figure 4.9(a) corresponding to a polariser oriented along the y- or the x-direction, respectively. This method allows to mitigate the influence of the broad background as only the different throughput of the detection path for different polarisations contributes to the difference between these spectra besides the optical resonator modes. With the help of equation 2.6, the quality factor of the resonator mode can be determined to $Q_{\mathrm{opt,FIB}} \approx 1000$. The exact value (here $Q_{\mathrm{opt,FIB}} = 993$ according to the result of the data analysis) should be handled with care as the spectra typically are not noise-free and slightly different starting parameters can alter the result of the fitting algorithm.
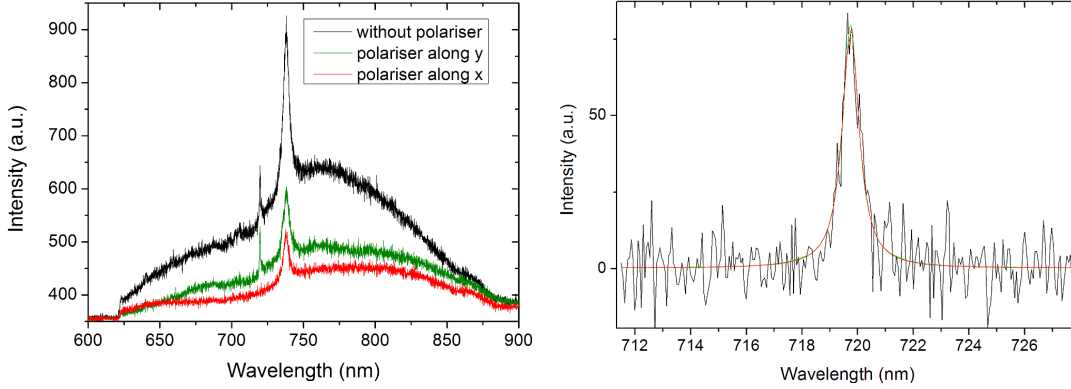
(a) Spectrum of photonic and phononic crystal structure with different polarisation filtering in the detection path.

(b) Determination of the optical quality factor by fitting a Lorentzian peak to the optical resonator mode.

Figure 4.9: Fluorescence spectra measured at ambient conditions of the photonic and phononic crystal structure shown in figure 4.2 fabricated with focused ion beam milling. (a) A clear polarisation along the y-direction characterises the peak at 720 nm as even optical resonator mode. (b) The quality factor can be determined to $Q_{\mathrm{opt}} \approx 1000$ by fitting a Lorentzian peak to the spectrum.

In order to detect optomechanical coupling, a measurement in vacuum needs to be performed. Friction at the surface leads to viscous damping of the mechanical oscillation and is one of the predominant damping mechanisms of the mechanical resonator mode [258]. Optomechanical coupling and the indirect signatures of the mechanical resonator mode can thus only be observed in vacuum. The sample showing the spectrum depicted in figure 4.9(a) is mounted in the setup allowing for measurements in vacuum and at cryogenic temperatures. After evacuation of the sample chamber overnight, no signatures of the optical resonator mode can be detected. The sample is cleaned and

oxidised multiple times, but no resonator modes can be observed in vacuum. However, the resonator mode remains visible when measuring at ambient conditions.

In a next step, the sample chamber was evacuated slowly and fluorescence spectra were taken continuously. To this end, only the pre-pump was used allowing for a very moderate evacuation speed. Figure 4.10 shows a set of spectra taken at different times during the evacuation process. Partly, more than one spectrum is assigned to a single chamber pressure due to the limited resolution of the pressure sensor. In that case, the corresponding spectra were taken with a time delay of 15 min during the continuous evacuation process. The images are shown in the order they were taken, starting at ambient pressure before pumping and ending with venting after the evacuation measurements. The intensities are not calibrated and might deviate slightly due to the required realignments during the evacuation process. The excitation power was much higher for the spectrum shown in 4.10(a), but constant for all other spectra. The heavily varying relative intensity of the optical resonator mode can thus be considered a true result of the measurement.

Figure 4.10(l) shows an evaluation of all spectra taken during the evacuation process and after venting. The wavelengths of all resonator modes are shown for each spectrum depicted in figure 4.10(a) through (k). It can be seen that the resonator mode shifts toward the red wavelength side during the evacuation process. Eventually, additional modes appear that all individually also shift toward longer wavelengths. Also the relative intensity of the individual resonator modes changes over time, resulting in a higher intensity of the peaks at higher wavelengths. All peaks visible in the spectra show a clear polarisation along the y-direction and can thus be identified as even cavity modes. After venting of the sample chamber, the predominant resonator mode almost matching the zero phonon line of the silicon vacancy colour centre ensemble is still visible at the spectral position where it has been observed at the last step of the evacuation procedure.

This result shows that it does not seem as if the pressure directly affects the optical resonator mode. It appears more probable that another mechanism is causing the changes in the spectrum for the measurements in vacuum. To test this hypothesis, another test run is performed with the same photonic and phononic crystal structure. Only the pre-pump is used to evacuate the sample chamber overnight so that no optical resonator modes can be observed in the spectrum as shown in figure 4.11(a). Then, several spectra are recorded directly after venting shown in figure 4.11(b), and for waiting times of two hours shown in figure 4.11(c), and of five hours shown in figure 4.11(d). It can be seen that the spectrum directly after venting does not change significantly compared to the spectrum under vacuum. However, after a waiting time of two hours, optical resonator modes can be observed in the spectrum again. After five hours waiting time, the spectrum again shows a single optical resonator mode, however shifted compared to the original spectrum shown in figure 4.9. This shift can be attributed to multiple oxidation steps that were performed between the individual measurements. The clear polarisation properties of the maxima allow to identify all peaks as even modes of the optical resonator. The absolute intensities of the different spectra cannot directly be compared, but as the excitation power was constant for all spectra, the drastic drop in the overall intensity seems to correlate with the reappearance of the optical resonator modes.
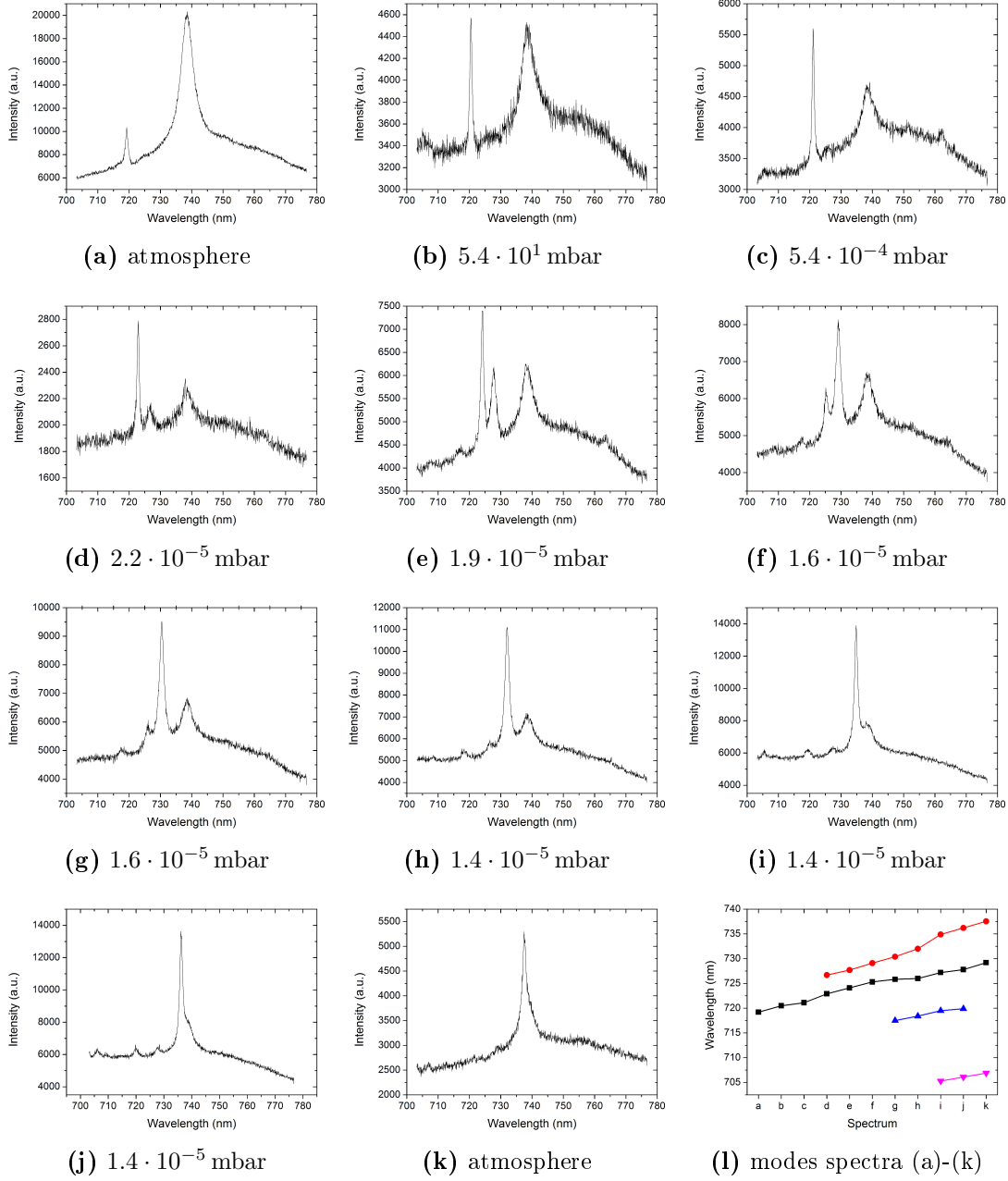
(a) atmosphere

(b) $5.4 \cdot 10^1$ mbar

(c) $5.4 \cdot 10^{-4}$ mbar

(d) $2.2 \cdot 10^{-5}$ mbar

(e) $1.9 \cdot 10^{-5}$ mbar

(f) $1.6 \cdot 10^{-5}$ mbar

(g) $1.6 \cdot 10^{-5}$ mbar

(h) $1.4 \cdot 10^{-5}$ mbar

(i) $1.4 \cdot 10^{-5}$ mbar

(j) $1.4 \cdot 10^{-5}$ mbar

(k) atmosphere

(l) modes spectra (a)-(k)

Figure 4.10: Fluorescence spectra taken during the evacuation process of the photonic and phononic crystal structure shown in figure 4.2 fabricated with focused ion beam milling. The pressure can only be determined with very limited precision giving only a rough estimate, and several spectra corresponding to the same pressure are recorded with a delay of 15 min. The spectra at atmospheric pressure were taken directly before evacuating (a), and directly after venting (k). (l) Wavelengths of the optical resonator modes appearing in spectra (a) - (k).

These results suggest that a mechanism not considered so far is strongly affecting the optical properties of the resonator modes in vacuum. This is slightly surprising as it did not occur in comparable measurements using the same equipment with two-dimensional photonic crystal resonators in diamond [91]. One possible explanation could be the greater susceptibility of one-dimensional structures to small changes of the effective optical structure, when thin layers potentially covering the sample surface desorb during the evacuation process. The time constant observed for the changes in the optical spectrum could very well be explained by adsorption and desorption of a very thin film, possibly water. However, the drastic impact on the optical properties and the shift to the red wavelength side contradict this theory. Based on numerical modelling, the removal of material at the surface should result in a blue-shift of the optical resonator modes by few nanometres. The appearance of additional optical modes after removal of a very thin surface layer covering the entire structure cannot be confirmed with simulation results.
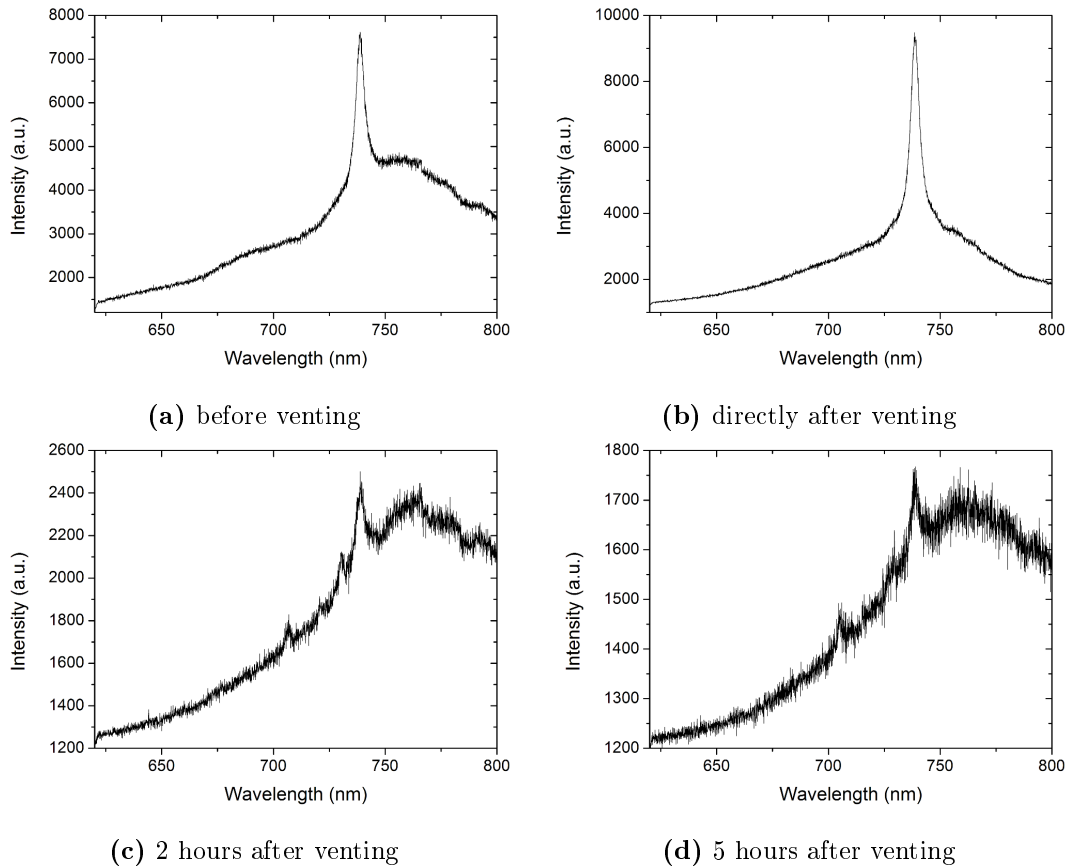

(a) before venting

(b) directly after venting

(c) 2 hours after venting

(d) 5 hours after venting

Figure 4.11: Fluorescence spectra taken during the venting process of the photonic and phononic crystal resonator shown in figure 4.2 fabricated with focused ion beam milling. The different spectra are recorded directly before, directly after and at different waiting times after venting.

Another parameter that could possibly explain the measurement result and not investigated so far is the quality of the diamond starting material. For the measurements in reference [91], commercially available diamond membranes have been used as starting material, whereas the measurements shown here were performed with heteroepitaxially grown diamond. The initial surface termination is not known for both sample types. However, the fabrication procedure including focused ion beam milling and post-processing treatments is the same and should result in similar surface properties and the reasons for the observed shifting and eventual vanishing of the modes upon pumping and venting cannot clearly be identified. This unexpected effect prevents the measurement of optomechanical interaction as an optical resonator mode visible in vacuum is the minimum requirement to find signatures of optomechanical coupling. Therefore, also the mechanical resonator modes cannot be characterised through indirect signatures in the optical properties of the photonic and phononic crystal structures.

4.2.3 Structures Fabricated with Reactive Ion Etching

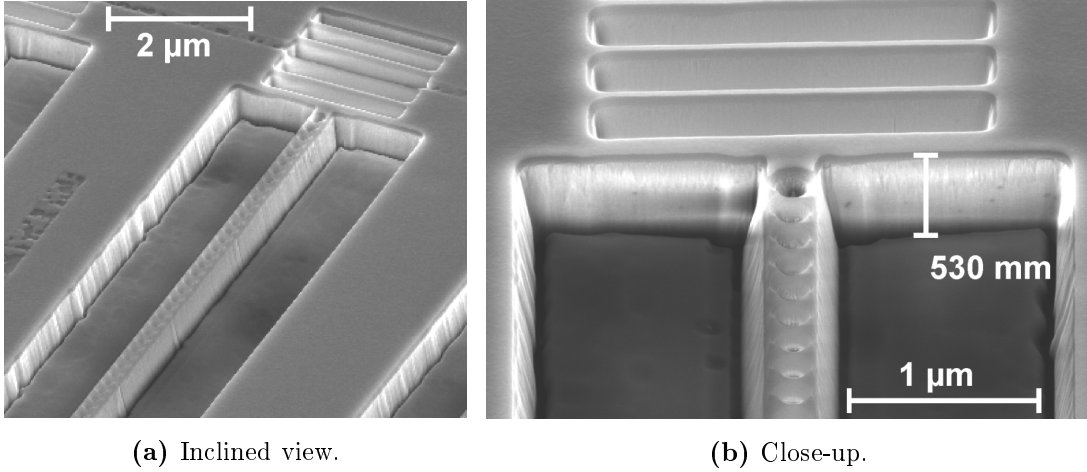(a) Inclined view.   (b) Close-up.

Figure 4.12: Photonic and phononic crystal structure fabricated with reactive ion etching applying the oxygen plasma as described in table 4.1.

The structures depicted in figure 4.5, fabricated in two different sample types with reactive ion etching showed very good results judged from the scanning electron microscopy images. Due to unexpected problems, in particular the malfunction of different annealing ovens, they were unintentionally destroyed during the post-processing treatment and could not be characterised with respect to their optical properties. Therefore, another batch of photonic and phononic crystal structures was fabricated in a heteroepitaxially grown sample with the reactive ion etching process described in section 4.1.2. However, due to the rather poor reproducibility of the etch process, the resulting structures did not turn out nearly as good as the previously fabricated ones. Even a slight variation of the etch plasma parameters did not help with obtaining better results. An optical characterisation was, however, possible and will be shown here to demonstrate

that successful the fabrication of photonic and phononic crystal structures is possible with the reactive ion etching process characterised by the set of parameters given in table 4.1.

The structure shown in figure 4.12 shows a photonic and phononic crystal structure etched with the parameters given in table 4.1 that should in principle deliver the results shown in figure 4.5. The actual structures, however, show rough and inclined sidewalls and the etch depth was not sufficient to release the airbridge from the diamond membrane. In addition, the close-up view reveals that the holes are not patterned properly and "grass" covers their inside. Despite this less-than-perfect fabrication results, this structure still shows optical resonator modes with quality factors of approximately $Q_{\text{opt,RIE}} \approx 1000$. The fluorescence spectrum of the structure shown in figure 4.12 is shown in figure 4.13 a. Several more structures showed optical resonator modes and it is striking that most structures show an unexpected fluorescence spectrum with several modes of unclear polarisation and a very high and atypical background. This indicates that the less-than-perfect appearance of these structures also translates into their optical properties and the results from numerical modelling cannot reliably predict the fluorescence spectrum in this case.
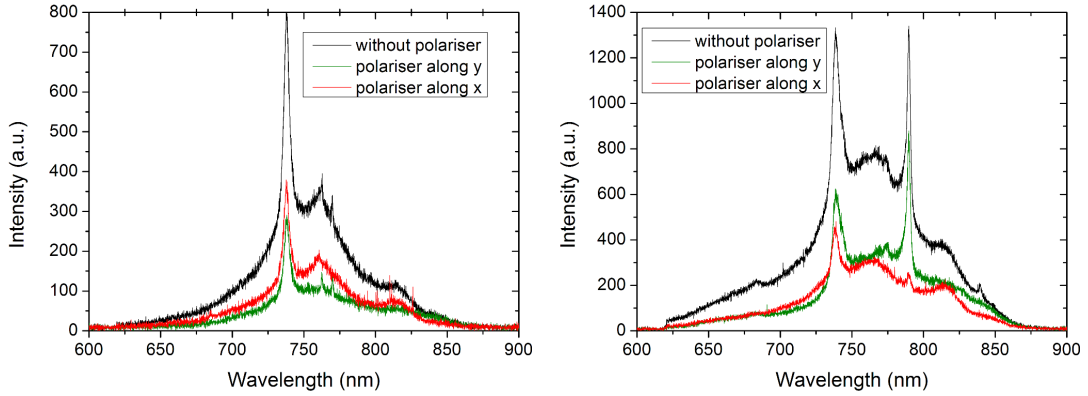
(a) Fluorescence spectrum of the one-dimensional photonic crystal structure shown in figure 4.12.

(b) Fluorescence spectrum of the two-dimensional photonic crystal structure shown in figure 4.14.

Figure 4.13: Fluorescence spectrum of structures fabricated with reactive ion etching measured with different polarisation filters in the detection path. (a) Two modes with quality factors $Q_{\text{opt,RIE}} \approx 1000$ can be detected. (b) The spectrum shows a mode with moderate quality factor $Q_{\text{opt,RIE}} \approx 300$.

In order to obtain etched structures that are fully released from the diamond membrane, another batch of structures is fabricated with the same set of parameters but with a slightly longer duration of the oxygen plasma of 240 sec. Also in this case, many of the fabricated structures show optical resonator modes with quality factors up to $Q_{\text{opt,RIE}} \approx 1000$ although the results of the patterning are rather poor. Also here, the spectra deviate from the ideal case in terms of mode pattern and fluorescence background. To exemplify the optical properties of the characterised structures, figure 4.13

b shows the fluorescence spectrum of a two-dimensional photonic crystal structure with seven missing holes to form a resonator (M7). It can be seen that the optical resonator mode shows a very high intensity indicating that no residues are polluting the surface. Scanning microscope images of the corresponding structure are shown in figure 4.14. A strong sinking of the structures can be observed and the diamond bridges between neighbouring holes at least partly collapsed. Due to the longer duration of the oxygen plasma, the mask eroded what can be seen in the horizontal stripes stemming from charging of the sample where almost no residues of the chromium mask can be found after the reactive ion etching.
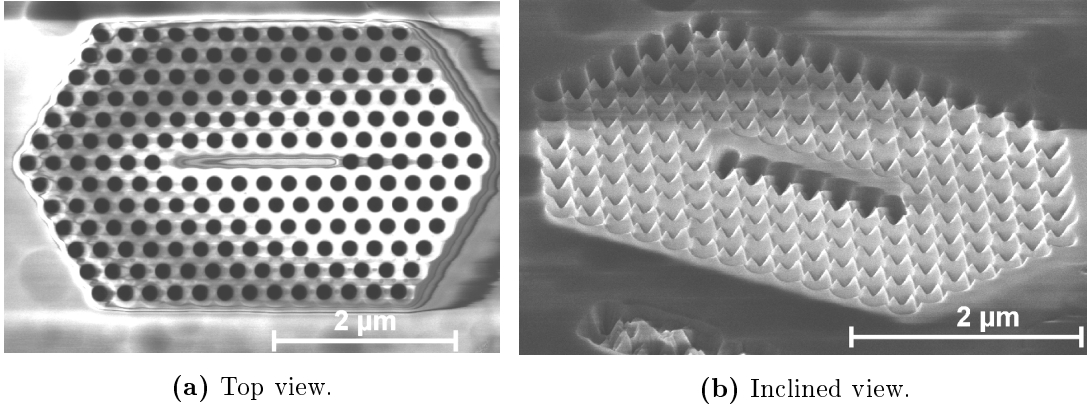

(a) Top view.

(b) Inclined view.

Figure 4.14: Two-dimensional photonic crystal structure fabricated with reactive ion etching applying the oxygen plasma as described in table 4.1 for a slightly longer duration of 240 sec.

It remains to conclude that the issues occurring during the post-processing treatment did not allow to optically characterise the samples that were fabricated with reactive ion etching ans showed good results. Due to the poor reproducibility of the etch process, the only other batch of structures that could be patterned did not show equally good results. However, even with less-than-perfect results, various one- and two-dimensional photonic crystal structures showed optical resonator modes with quality factors $Q_{\mathrm{opt,RIE}} \approx 1000$. Despite its poor reproducibility, the reactive ion etching process still shows promising results. Its reliability is comparable to that of the patterning with focused ion beam milling where only a small fraction of the fabricated structures shows optical resonator modes at all. While a value of $Q_{\mathrm{opt,exp}} \approx 1000$ seems to set a hard boundary in the case of focused ion beam milling, even structures with obvious imperfections show equally high values when fabricated with reactive ion etching.

Chapter 5

Discussion of the Results

This chapter summarises the results of this work and discusses their implications. In particular, several figures of merit for both the optical and mechanical resonator modes are calculated and discussed based on the results from numerical modelling and from measurements of the fabricated samples. Also for optomechanical interaction and strain coupling, the results obtained from numerical modelling are shown and evaluated based on figures of merit characterising the interaction. This analysis is complemented with a critical assessment of realistic experimental possibilities with the fabricated samples. The results for hybrid interaction are discussed considering both the lower quality factors of fabricated structures and the limitations of the model used to describe the dynamics of the integrated system. The fabrication processes described in this work are assessed and possible improvements are identified. Limitations for the experimental characterisation of the fabricated samples in vacuum are analysed. Possible strategies to address these challenges are identified in order to pave the way towards an experimental demonstration of the interactions studied in this work.

5.1   Optical Resonator Mode and Grating Couplers

A localised cavity mode arising from the dielectric band can be confined with the help of an inverse design approach based on the mode gap effect. The even resonator mode shows a very high optical quality factor of $Q_{\mathrm{opt}} = 1.4 \cdot 10^7$ corresponding to a decay rate $\kappa \approx 100\,\mathrm{MHz}$ and a low mode volume of $V_{\mathrm{opt}} = 2\,(\lambda/n)^3$. The optical wavelength can be adapted with the overall scaling by choosing a suitable lattice constant a. For a lattice constant of $a = 233\,\mathrm{nm}$, a resonator mode matching the zero phonon line of the silicon vacancy colour centre at $738\,\mathrm{nm}$ is obtained. A slightly reduced lattice constant of $a = 192\,\mathrm{nm}$ gives an optical cavity in resonance with the zero phonon line of the nitrogen vacancy colour centre at $637\,\mathrm{nm}$. The effective Purcell factor for the interaction between the optical resonator mode and an emitter placed in the centre of the diamond structure is $F = 5.3 \cdot 10^5$. For fabricated photonic crystal structures, the Purcell factor reduces to $F \approx 40$ due to the lower optical quality factor $Q_{\mathrm{opt,exp}} \approx 1000$ corresponding to a decay rate $\kappa_{\mathrm{exp}} \approx 10^{12}\mathrm{Hz}$.

This optical resonator mode can be addressed with grating couplers providing in- and out-coupling at both ends of the airbridge structure. While the concept of grating couplers itself is not new, their design has been adapted to suit the requirements of the particular applications in this work. The grating couplers presented in this work are not only suitable for a fabrication with reactive ion etching, but also optimised to suit the photonic and phononic crystal resonator with respect to the structure dimensions and the resonance frequency. One of the grating coupler designs is based on half-circles whereas the other one consists of a regular pattern of grooves. Both with the round and the straight grating couplers, an in- and out-coupling efficiency of $25\,\%$ can be reached. This results in an external cavity decay rate $\kappa_{\mathrm{ext}} = 0.125\,\kappa$, allowing for an average photon population of $\overline{n}_{\mathrm{opt}} = 100$ when resonantly driving the optical resonator with an input laser power of $P_{\mathrm{L}} = 5\,\mathrm{nW}$. Even when non-perfect fabrication reduces the coupling efficiency to $10\,\%$, an input power of only $P_{\mathrm{L}} = 13\,\mathrm{nW}$ is required to reach a photon population of $\overline{n}_{\mathrm{opt}} = 100$ in the optical resonator mode.

5.2 Mechanical Resonator Mode

Based on the structure investigated with respect to its optical properties, a number of localised mechanical resonator modes can be found. The lowest order fully symmetric mode arising from the Γ-point, G_2, is most suitable for optomechanical interaction and is thus the only mechanical resonator mode analysed in more detail. It shows record mechanical frequencies of $f_{\mathrm{m}} = 12.4\,\mathrm{GHz}$ for dimensions where the optical resonator mode is resonant with the silicon vacancy colour centre, and even $f_{\mathrm{m}} = 14.4\,\mathrm{GHz}$ when adapted to match the zero phonon line of the nitrogen vacancy colour centre. A very high mechanical quality factor of $Q_{\mathrm{m}} = 1.4 \cdot 10^6$ can be reached without modifying the photonic and phononic crystal structure from the parameters optimised with respect to a high quality factor of the optical resonator mode. This corresponds to a decay rate of the mechanical oscillation of $\Gamma_{\mathrm{m}} \approx 10\,\mathrm{kHz}$. Even higher values up to $Q_{\mathrm{m}} = 2.4 \cdot 10^7$ can be reached by introducing a mirror section with holes of constant radius on the edges of the structure. Besides the temporal confinement, the structure also provides an excellent spatial confinement with effective masses below $100\,\mathrm{fg}$ for structures adapted to the nitrogen vacancy colour centre. A population with a single cavity phonon results in an extremely low zero point fluctuation x_{ZPF} corresponding to a maximal elongation of few femtometers.

In contrast to the optical resonator mode, the mechanical resonator mode can be populated thermally. The thermal phonon occupation number of the mechanical cavity can be determined by the approximation given in equation 2.18. For a photonic and phononic crystal structure designed to match the zero phonon line of the nitrogen vacancy colour centre, the thermal phonon population number is $\overline{n}_{\mathrm{th,RT}} \approx 450$ at room temperature, and only $\overline{n}_{\mathrm{th,4K}} \approx 6$ at $4\,\mathrm{K}$. It even drops below a single phonon for temperatures below $0.7\,\mathrm{K}$ and reaches values of $\overline{n}_{\mathrm{th,1mK}} \approx 10^{-3}$ at very low temperatures of $1\,\mathrm{mK}$. This means that the extremely high mechanical frequencies above $10\,\mathrm{GHz}$ allow for cryogenic cooling of the mechanical resonator close to the quantum ground state of motion. This makes mechanical resonator modes localised in diamond photonic and phononic crystal structures a very interesting candidate for studying quantum effects on a nearly macroscopic scale.

Also the decoupling from the thermal environment of $Q_{\mathrm{m}} \times f_{\mathrm{m}} = 10^{17}$ surpasses that of other mechanical resonators [103]. The number of coherent oscillations that can be performed before thermal decoherence appears varies depending on the temperature of the thermal bath between $N_{\mathrm{osc,300K}} \approx 1000$ at $300\,\mathrm{K}$ over $N_{\mathrm{osc,4K}} \approx 10^4$ at $4\,\mathrm{K}$ to over $N_{\mathrm{osc,1mK}} \approx 10^6$ at $1\,\mathrm{mK}$ based on the expression given in equation 2.20.

When considering that the temporal confinement of real fabricated structures is considerably weaker, an experimental mechanical quality factor of $Q_{\mathrm{m,exp}} \approx 1000$ seems realistic based on the analogous degradation of the optical quality factor measured as $Q_{\mathrm{opt,exp}} \approx 1000$. The decay rate of the mechanical resonator mode then increases to $\Gamma_{\mathrm{m,exp}} \approx 100\,\mathrm{MHz}$. Even then the reduced decoupling of $Q_{\mathrm{m}} \times f_{\mathrm{m}} = 10^{13}$ can still very well compete with other mechanical resonators. However, at room temperature not even a single coherent oscillation can take place in this case. A single coherent oscillation can only be performed at cryogenic temperatures around $4\,\mathrm{K}$, while more oscillations $N_{\mathrm{osc,1mK}} \approx 10^4$ are possible at very low temperatures around $1\,\mathrm{mK}$.

5.3   Optomechanical Coupling

The interaction between the optical and the mechanical resonator modes co-localised in the diamond photonic and phononic crystal structure is investigated based on the full cavity fields. Considering both the moving boundaries and the photoelastic effect, the single photon optomechanical coupling constant is in the range $g_{\mathrm{OM},0} \approx 10\,\mathrm{MHz}$ for a mechanical excitation of a single cavity phonon. With the decay rates of the optical and mechanical resonator modes $\kappa \approx 100\,\mathrm{MHz}$ and $\Gamma_{\mathrm{m}} \approx 10\,\mathrm{kHz}$ found in the simulations, a single photon optomechanical cooperativity of $C_{\mathrm{OM},0} \approx 100$ can be reached. This allows for entering the large cooperativity regime where the interaction dominates the dynamics of the coupled system as a coherent population with single photons and phonons is assured during the entire interaction cycle. However, the strong single photon coupling regime giving rise to a shared eigenstate of the optical and the mechanical resonator mode cannot be accessed as the interaction rate does not surpass the decay rate of the optical cavity. However, with a higher photon population, the regime of linearised optomechanical interaction can be exploited and the strong coupling regime can be entered for cavity photon numbers $\overline{n}_{\mathrm{opt}} \geq 100$. For a transmission efficiency of $25\,\%$ provided by the grating couplers shown in this work, a resonant excitation with only $P_{\mathrm{L}} \approx 5\,\mathrm{nW}$ laser power is required to access the strong optomechanical coupling regime.

Besides the interaction strength, also the sideband resolution of an optomechanical device is relevant for practical applications. The high mechanical resonator frequency $f_{\mathrm{m}} \geq 10\,\mathrm{GHz}$ allows for entering the resolved sideband regime. The necessary condition given in equation 2.52 is fulfilled due to the high optical quality factor $Q_{\mathrm{opt}} = 1.4 \cdot 10^{7}$ providing a narrow spectral signature of the optical cavity mode. This means that signatures of optomechanical coupling can directly be detected in the optical spectrum of the device in the form of sidebands to the optical cavity mode, that appear in a spectral distance corresponding to the frequency of the mechanical resonator mode.

Resolved sidebands do not only allow for a direct spectral detection of optomechanical coupling, but also very high optomechanical cooling rates $\widetilde{\Gamma}_{\mathrm{OM,res}}$ are possible in this regime. Based on equation 2.69, the optomechanical cooling rate in the resolved sideband regime can be determined to $\widetilde{\Gamma}_{\mathrm{OM}} \approx 4\,\mathrm{MHz}$ based on the values retrieved from the simulations for optimal excitation on the red-detuned sideband corresponding to $\Delta_{\mathrm{L}} = -\omega_{\mathrm{m}}$. The final temperature that can be reached depends on the initial temperature and is $T_{\mathrm{f}} < 1\,\mathrm{K}$ already for a cooling process that starts at room temperature. In absence of a thermal bath, an asymptotic minimal phonon occupation number of $\overline{n}_{\mathrm{m,min,OM}} \approx 10^{-8}$ can be achieved according to equation 2.73. The more realistic final phonon number $\overline{n}_{\mathrm{f,OM}}$ also taking into account heating from the thermal environment is only slightly above a single quantum of motion for a bath temperature of $300\,\mathrm{K}$ when exploiting the relation given in equation 2.74. The population of the mechanical resonator mode can thus be reduced below a single phonon in combination of optomechanical and moderate cryogenic cooling. For liquid helium temperatures of $4\,\mathrm{K}$, the final phonon occupation number is as low as $\overline{n}_{\mathrm{f,OM}} = 0.014$.

As alternative to cooling, also heating of the mechanical oscillation via optomechanical coupling is possible. A blue-detuned excitation allows for heating rates corresponding to the cooling rates derived for red-detuned excitation. The threshold given

in equation 2.71 marks the border between simple amplification and phonon lasing. This threshold is surpassed for the optomechanical interaction strength provided by the photonic and phononic crystal structure in diamond as the heating rate $\widetilde{\Gamma}_{\mathrm{OM}} \approx 4\,\mathrm{MHz}$ surpasses the decay rate of the mechanical resonator $\Gamma_{\mathrm{m}} \approx 10\,\mathrm{kHz}$. This result shows that a coherent phonon field can indeed be generated based on optomechanical interaction taking place in the photonic and phononic crystal structure studied in this work.

However, when considering the real structures with considerably lower optical quality factors $Q_{\mathrm{opt,exp}} \approx 1000$, sidebands cannot be resolved in the spectrum of the optical resonator. The system is thus in the Doppler regime. Even in the very optimistic scenario when the mechanical quality factor of the fabricated sample is as high as predicted by simulations, the single photon optomechanical cooperativity is low. Taking a much more realistic assumption that the mechanical quality factor of a real structure is comparably low as the measured optical quality factor with $Q_{\mathrm{m,exp}} \approx 1000$, the resulting cooperativity $C_{\mathrm{OM,0,exp}} < 10^{-6}$ shows that the large cooperativity regime is far beyond reach with the structures fabricated by focussed ion beam milling. Even in the case of linearised optomechanical interaction where the coupling is enhanced by a higher population of the optical resonator mode, the large cooperativity regime can only be reached for photon numbers $\overline{n}_{\mathrm{opt}} \geq 10^{6}$. This means that for an in-coupling efficiency of 25 % provided by the grating couplers presented in this work, an excitation with a laser power of $P_{\mathrm{L}} \approx 1\,\mathrm{mW}$ would be required. Besides difficulties to provide such high high pump powers in an experimental setup, they also risk to cause a dynamic instability of the optomechanical system in the Doppler regime. This shows that the measured structures do not provide a coherent population with photons and phonons during the interaction cycle even with optical driving at realistic pump powers as would be the case in the large cooperativity regime. In addition, when considering that also the spatial confinement of both the optical and the mechanical resonator modes could be significantly lower in fabricated structures, the optomechanical interaction could be even weaker in real structures.

Also the optomechanical cooling rate is much lower for fabricated structures compared to the values retrieved from numerical modelling. In the most optimistic case, the spatial confinement of both the optical and the mechanical resonator modes is as high as predicted in the simulations and the values for optomechanical interaction are not reduced compared to the results shown in section 3.3. Even for these quite favourable assumptions and for optimal excitation at detuning $\Delta_{\mathrm{L}} = -\kappa/2$, the optomechanical cooling rate is $\widetilde{\Gamma}_{\mathrm{OM,exp}} \approx 10\,\mathrm{Hz}$ determined according to equation 2.68. The temperature of the photonic and phononic crystal structure can thus hardly be decreased with optomechanical cooling. The minimal asymptotic phonon occupation number in absence of a thermal bath is $\overline{n}_{\mathrm{m,min}} \approx 8$. Considering the more realistic situation including heating from the thermal environment, the final phonon number in the mechanical resonator is basically not affected by optomechanical cooling.

Also with respect to a phonon lasing application, the increased decay rate of the mechanical resonator makes the situation less favourable. Even for a strong driving of the optical resonator mode, the effective amplification rate cannot surpass the decay rate of the mechanical resonator making the generation of a coherent phonon field impossible.

All in all, it would be possible to observe optomechanical coupling in the fabricated

structres with a homodyne measurement. The high optomechanical coupling constants allow to detect a signature of the interaction in the time-resolved intensity modulation of the optical resonator. For an experimental exploitation of optomechanical interaction, like effective cooling of the mechanical resonator mode or phonon lasing, the temporal confinement of the optical resonator mode needs to be greatly improved. Ideally, the regime of resolved optomechanical sidebands should be reached requiring an optical quality factor of $Q_{\mathrm{opt}} \approx 50000$. Very recently reported results suggest that this benchmark is in reach even for structures designed to match the zero phonon line of the nitrogen vacancy colour centre when using a novel dry etching procedure [53].

5.4   Strain Coupling

In the case of strain coupling, the interaction of the mechanical resonator mode with both the ground and the excited state of the nitrogen vacancy colour centre are determined. The strain coupling constants vary over six orders of magnitude between $g_{\mathrm{SC,ground}} \sim \mathrm{Hz}$ and $g_{\mathrm{SC,exc}} \sim \mathrm{MHz}$ for the interaction with the different electronic level. In addition, also the decay rates of the related electronic states of the nitrogen vacancy colour centre vary. The excited state levels with zero spin projection have a decay rate $\gamma_0 = 73\,\mathrm{MHz}$. For the ground state levels, this cannot be determined so clearly as both time constants T_1 and T_2 describing relaxation and dephasing of the spin can vary by orders of magnitude depending on the sample type, the temperature of the thermal bath, and the measurement technique as pointed out in section 2.4.2. Due to these differences regarding both the coupling and the properties of the emitter in these two cases, they are treated separately in the following.

Strain Coupling to the Ground State Levels

Strain coupling to the ground state levels of the nitrogen vacancy colour centre is evaluated based on two different formalisms. One description is based on a pure observation and has been reported from two groups, independently [173, 174]. The other approach is a full group theoretical calculation taking into account the internal symmetry of the colour centre [307]. While both approaches are valid methods that should provide similar values, the results obtained in this work using the two descriptions are different. This can be attributed to a left-handed coordinate system that is used for the group theoretical calculations as internal coordinate of the nitrogen vacancy colour centre. The results obtained from the phenomenological description are thus more reliable. However, some qualitative results obtained from the group theoretical formalism, like for example the orientation-independent radial strain coupling constant in a (111) sample surface, might very well be true. The more detailed consideration of the internal symmetry of the nitrogen vacancy colour centre could in this case deliver more accurate results for arbitrary angles. It remains to conclude that this approach could provide a deeper insight into the mechanisms of strain coupling to the ground state levels, but a more accurate derivation based on a right-handed coordinate system would be necessary in this case.

The single phonon strain coupling constant describing the interaction between the localised mechanical resonator mode and the ground state levels of the nitrogen vacancy colour $g_{\text{SC,ground}}$ centre is up to several hundred Hz, both when evaluated based on the formalism originating from a phenomenological description or the one derived from a group theoretical calculation. Compared to other strain coupling systems, the strongly confined mode allows for this extremely high value outperforming the interaction in diamond cantilevers by over two orders of magnitude when considering that the coupling constants obtained for diamond cantilevers are obtained from experiments with strong mechanical driving far above the single-phonon level [173, 174].

Assessing the internal dynamics for strain coupling to the ground state levels, the large single phonon cooperativity regime can still not be reached with the structure investigated here. However, resolved strain coupling sidebands are formed for moderate dephasing times T_2. With respect to a practical application, this allows exploiting the cooling protocol based on the ground state levels presented in section 2.7.4. The cooling rate that can be achieved depends very much on the spin coherence time of the nitrogen vacancy colour centre. The overall decay rate γ_{ground} can take values between few hundred Hz and up to $1\,\text{GHz}$ determined by the quality of the individual sample and the measurement technique used. For a protocol based on strain coupling to the ground state levels of the nitrogen vacancy colour centre, the resulting cooling rate $\tilde{\Gamma}_{\text{SC,Ground}}$ given by equation 2.119 can take values between $1\,\text{kHz}$ in the case of long spin coherence times and $10^{-4}\,\text{Hz}$ for short coherence times. For the ideal case of long coherence times, the final phonon occupation number $\overline{n}_{\text{f,SC,ground}}$ calculated based on equation 2.120 is in the range of 10^3 for a bath temperature of $300\,\text{K}$, 10^2 for cryogenic temperatures of $4\,\text{K}$ and far below a single quantum of motion for temperatures in the mK range. This means that even in the ideal case, the final phonon occupation number cannot be reduced below the thermal phonon occupation number $\overline{n}_{\text{th}}$ with this cooling protocol considering only the single phonon coupling constant $g_{\text{SC,0}}$. A higher phonon occupation number would increase the strain coupling constant and thus also the cooling rate, allowing for a lower final phonon occupation number. The reduction of the phonon number due to the cooling would bring along a reduction of the effective strain coupling constant over time what inhibits reaching very low final phonon occupation numbers. In addition, high pump powers lead to an additional heating of the diamond structure via thermal effects, what further reduces the cooling efficiency in a strongly driven strain coupled system.

Strain Coupling to the Excited State Levels

The generally much higher strain coupling constants obtained for the interaction with the excited state levels in the range of MHz are much more interesting with regard to cooling applications. The large cooperativity regime can be reached even for an excitation with a single phonon in this case. For a nitrogen vacancy colour centre in a diamond sample with (111) surface orientation or for suitable orientation of the photonic and phononic crystal structure in the (001) sample surface, even the single phonon strong coupling regime can just be reached in the case of interaction with axial strain g_{A_1}. Considering a realistic value for the mechanical quality factor $Q_{\text{m,exp}} \approx$

1000 in fabricated structures, even the large cooperativity regime is very challenging to reach. Also that can only be achieved when the sample type and the orientation of the diamond structure are ideal and allow for strain coupling constants of $g_{\mathrm{SC,exc}} \sim 100\,\mathrm{MHz}$. This restricts the large cooperativity regime to axial strain coupling $g_{\mathrm{A_1}}$ and a suitable orientation of the mechanical oscillation pattern with respect to the symmetry axis [111] of the nitrogen vacancy colour centre. It is thus very questionable whether it can at all be observed if the mechanical quality factor is not substantially higher especially when considering that also the spatial confinement of the resonator mode and thus the strain coupling constant could be lower in a real sample. The regime of resolved sidebands, however, can be reached independent of the temporal mode confinement. It should thus be possible to spectrally detect strain coupling to the excited state levels in the form sidebands in the fluorescence signal of the nitrogen vacancy colour centre.

There are two cooling protocols described in more detail in section 2.7.4 allowing to exploit the strain coupling between the excited states of the nitrogen vacancy colour centre and the mechanical resonator mode. One is a classical sideband cooling while the other protocol exploits the doublet structure of the excited state levels with zero spin projection $|E_x\rangle$ and $|E_y\rangle$ to allow for a more efficient damping. Assuming a Rabi frequency of $\Omega = 10\,\mathrm{MHz}$, the corresponding cooling rates can be calculated based on equations 2.121 and 2.122. For the values retrieved from the numerical model, values up $\widetilde{\Gamma}_{\mathrm{SC,side}} \approx 10\,\mathrm{mHz}$ and $\widetilde{\Gamma}_{\mathrm{SC,doublet}} \approx 100\,\mathrm{kHz}$ can be reached. Optimally adjusting the Rabi frequency for each protocol to $\Omega_{\mathrm{side}} = \omega_{\mathrm{m}}$ for sideband cooling and $\Omega_{\mathrm{doublet}} = \gamma_0$ for doublet cooling, the protocol exploiting the doublet structure created by the excited states $|E_x\rangle$ and $|E_y\rangle$ is more efficient than sideband cooling by a factor of 10^6. When taking into account that the Rabi frequency required to actually reach the optimal cooling rate is different for both protocols, the doublet cooling is even more advantageous. While a Rabi frequency of some tens of MHz, ideal for the doublet cooling, is a very common value, it would need to be some tens of GHZ for the sideband protocol. This implies that the cooling protocol based on the doublet structure is much more relevant for practical application than the one based on the strain coupling sideband. Interestingly, the final phonon occupation number $\overline{n}_{\mathrm{f,SC,exc}}$ given by equation 2.124 is equal for both variants and takes values far below a single quantum of motion even for a thermal bath at room temperature. Even for the much lower mechanical quality factors $Q_{\mathrm{m,exp}} \approx 1000$ expected for fabricated structures, the final occupation of the mechanical resonator mode is much below a single phonon. These considerations show that the quantum ground state of motion could very well be reached based on strain coupling to the excited state levels $|E_x\rangle$ and $|E_y\rangle$ of the nitrogen vacancy colour with a cooling protocol exploiting their doublet structure.

Besides cooling of the mechanical resonator, also phonon lasing has been discussed as possible application of strain coupling. Simple heating can easily be achieved with an excitation of the colour centre's zero phonon line on the blue-detuned sideband. It is, however, possible to create a coherent phonon field when exploiting the doublet structure of the excited states as has been described for the cooling application. To enter the lasing regime, a threshold driving strength $\Omega_{\mathrm{L}} \approx 3\,\mathrm{MHz}$ is required for the values found in the simulation based on the expression given by equation 2.125. Considering the lower mechanical quality factor $Q_{\mathrm{m,exp}} \approx 1000$ expected for fabricated structures,

the phonon lasing threshold increases to $\Omega_{\mathrm{L}} \approx 300\,\mathrm{MHz}$ for real structures. These results show that phonon lasing is indeed a possible application for strain coupling in a photonic and phononic crystal resonator in diamond. Especially when further fabrication improvements allow to reach high experimental quality factors of the mechanical resonator mode, the required driving strength is within reach.

5.5 Hybrid Interaction

To study an integrated quantum system in diamond based on the structure presented in this work, a hybrid interaction between all three degrees of freedom is considered. To this end, the specific application of cooling the mechanical oscillation via strain coupling is evaluated in presence and absence of dephasing and the impact of the optical resonator on the cooling performance is assessed. In general, the values for this evaluation are adapted from numerical modelling in order to obtain a realistic representation of the structure studied in this work. The mechanical resonance frequency, however, is generally set to $f_{\mathrm{m}} = 1\,\mathrm{GHz}$ in the evaluation of the hybrid interaction instead of $f_{\mathrm{m}} = 14.4\,\mathrm{GHz}$ found for a photonic and phononic crystal structure resonant on the zero phonon line of the nitrogen vacancy colour centre. This modification is done for technical reasons to inhibit coupling to higher order excited states in the model.

In a first step, an artificial situation is considered where the nitrogen vacancy colour centre interacts both with the mechanical and the optical resonator mode. To this end, no thermal bath causing a population of the mechanical resonator mode is included to the model, the optical resonator is considered to be only passive, and the optical transition is the only decay channel of the colour centre. The cooling is based on a sideband protocol exploiting strain coupling to the excited state levels that is also described in section 2.7.4. Depending on the detuning between the laser and the zero phonon line of the colour centre, cooling rates $\widetilde{\Gamma}_{\mathrm{hybrid}}$ in the range $100\,\mathrm{Hz}$ to $100\,\mathrm{kHz}$ can be achieved. The maximal cooling rate is obtained for a driving laser in resonance with the optical transition, but very high cooling rates are also possible for the laser resonant on the red-detuned sideband generated by strain coupling. The corresponding asymptotic minimal phonon occupation number $\overline{n}_{\mathrm{m,min,hybrid}}$ takes values of 10^2 for resonant excitation and is even below 10^{-4} for excitation on the red-detuned sideband. However, the optical resonator has almost no influence on the cooling performance. This result does not come as a surprise when considering that a very high mechanical quality factor is the basis for this cooling protocol, allowing for a considerable cooling performance already in the case of pure strain coupling. When using the value $Q_{\mathrm{m,exp}} \approx 1000$ for fabricated structures, it is expected that the optical resonator indeed increases the cooling rate. Also when the optical resonator is actively driven, it is expected to have a much greater impact on the cooling dynamics. In that case, it does not only represent an additional decay channel for the colour centre, but allows for additional cooling due to the optomechanical interaction. This situation is, however, not further investigated in this work.

In a second step, the interaction is studied in presence of dephasing but in the absence of a thermal bath, an artificial situation that does not occur in a real system.

To this end, the effect of the optical resonator is omitted and dephasing rates of $\gamma^* = \gamma_0$ or $\gamma^* = 10\,\gamma_0$ are assumed. The values obtained in the absence of dephasing serve as comparison. The resulting cooling rates $\widetilde{\Gamma}_{\text{hybrid}}$ are comparable for both values of the dephasing and in the range of few kHz to several hundred kHz, generally higher than in the case of vanishing dephasing. Maximal cooling can be achieved for resonant excitation on the zero phonon line of the nitrogen vacancy colour centre. The minimal asymptotic phonon occupation number in absence of a thermal bath is $\overline{n}_{\text{m,min,hybrid}} \approx 10^{-2}$ for most values of the detuning in the case of a very high dephasing rate $\gamma^* = 10\,\gamma_0$, and almost one order of magnitude smaller for a dephasing rate comparable to the radiative decay rate $\gamma^* = \gamma_0$. For both values of the dephasing, the asymptotic minimal phonon occupation number is less dependent on the value of the detuning than in the absence of dephasing. This result indicates that the optimal cooling performance can best be reached for a moderate dephasing rate when the detuning cannot be adjusted accordingly and in absence of dephasing otherwise. However, it should be kept in mind that in a real system, dephasing cannot be adjusted to an arbitrary value. It is closely linked to the temperature of the diamond material and can basically only be increased by choosing a higher bath temperature that will at least partly counteract the cooling efforts.

To allow a more realistic estimate of the influence of dephasing on the cooling performance, the effect of a thermal bath is considered in the last step. Here again, the effect of the optical resonator mode is omitted and the system is studied moderate ($\gamma^* = \gamma_0$) or vanishing dephasing ($\gamma^* = 0$). To take into account for the thermal bath, the more relevant final phonon occupation number is evaluated that also includes a thermal population of the mechanical resonator mode. The corresponding thermal phonon occupation number $\overline{n}_{\text{th}}$ constituting the relevant benchmark is more than one order of magnitude larger than the values given in section 5.2 as a lower mechanical resonance frequency of $f_{\text{m}} = 1\,\text{GHz}$ is used for the investigation of the hybrid interaction. A moderate dephasing rate in the order of the radiative decay rate $\gamma^* = \gamma_0$ is found to be optimal with respect to reaching low final phonon occupation numbers also when considering the influence of the thermal bath. In this case, the hybrid interaction leads to a considerable reduction of the phonon number by roughly two orders of magnitude to a value of $\overline{n}_{\text{f,hybrid}} \approx 1$ found for the most favourable case of resonant excitation on the zero phonon-line at a temperature of $4\,\text{K}$. Considering an even lower temperature of $0.1\,\text{K}$, values down to $\overline{n}_{\text{f,hybrid}} \approx 10^{-2}$ can be reached for resonant excitation of the nitrogen vacancy colour centre zero phonon line.

This evaluation of the hybrid interaction, unique to the photonic and phononic crystal resonator incorporating a single nitrogen vacancy colour centre, is a first step towards investigating more complex diamond-based integrated systems. However, the optical resonator was only considered as passive component opening an additional decay channel in the study shown here. In addition, the very optimistic values for both the optical and the mechanical quality factor issuing from numerical modelling were used for the analysis. Furthermore, several assumptions, like for example a mechanical resonator frequency of $f_{\text{m}} = 1\,\text{GHz}$, needed to be made so that the calculations could be performed at all. This shows that the results obtained for the hybrid interaction cover only a very specific case that can most probably not be put into practice. It is to expect that lower quality factors of fabricated structures will alter the picture. The

effect of the optical resonator is then expected to increase drastically, especially when it is actively driven. Driving of the optical resonator mode could alter the interaction such that optomechanical interaction is the predominant cooling mechanism, or that an interference of strain coupling and optomechanical interaction significantly affects the dynamics of the coupled system. The investigation of hybrid interaction shown here is thus only a first step but could pave the way towards a better understanding of highly integrated diamond platforms.

5.6 Experimental Implementation

5.6.1 Sample Fabrication

The sample fabrication in this work is based on thin diamond membranes. This implies a restriction for possible diamond samples as starting material. Only samples with plane surfaces to both sides can be used as they need be thinned to membranes of the desired thickness in the further processing. True bulk diamond samples cannot be used for photonic and phononic crystal structures fabricated with the methods described in this work. This would be possible with an angled etching technique that can be employed to produce one-dimensional diamond photonic and phononic crystal structures with triangular diameter where a clear selection of only transverse electric modes in not possible [51,52]. Very recently, a novel under-etching technique including a passivation step has been reported [53]. It allows for very high optical quality factors with structures fabricated from bulk diamond and could possibly replace the reactive ion etching method presented in this work.

The method used for thinning the diamond membranes is a well-established process. The comparably low etch rates are not critical in this case as a mask that would be subject to erosion is not required. A detailed characterisation of the fabricated membranes assures that the thickness can be controlled very precisely. This helps with fabricating photonic and phononic crystal structures with a good mode confinement. The height of the airbridge structure is one of the parameters affecting both the resonance frequency and the quality factors of the localised optical and mechanical resonator modes. Membranes of suitable thickness can further be characterised with laser scanning microscopy and white light imaging. This allows to identify homogeneous regions where the diamond thickness precisely matches the target value and that are thus particularly suitable for patterning.

For the fabrication of the photonic and phononic crystal structures, two different techniques were used. While focused ion beam milling allows a reliable fabrication without the need for many processing steps, the optical quality factors that can be reached with this technique are limited. Values around $Q_{\mathrm{opt,FIB}} \approx 1000$ seem to set a hard boundary for this fabrication method. Therefore, a reactive ion etching method has been developed with the aim of improving the quality of the fabricated structures.

A novel mask system consisting of two different materials was developed for this purpose. The layered structure mitigates mask erosion and allows for mask patterning with focused ion beam milling. While mask patterning with focused ion beam milling

technically is not necessary, the corresponding device grants reliable access and provides a continuous high quality of the structures. The two-layered mask system has been engineered such that the diamond is shielded from exposure to ion beam irradiation during mask patterning by the intermediate glass layer. The chromium layer serves as etch mask for this intermediate layer and reduces mask erosion during the reactive ion etching process.

The reactive ion etch process consists of a two-step process. In a fluorine-based etch plasma, the pattern is transferred to the intermediate glass layer. During the subsequent oxygen plasma step, the photonic and phononic crystal pattern is etched in the diamond membrane. A careful adjustment of all fabrication steps including a wide parameter study allows the fabrication of diamond structures with very high aspect ratio. The sidewalls of the resulting structures are very steep and the holes match the target diameters. Scanning electron images of the etched samples indicate that high optical and mechanical quality factors could probably be reached with these etched structures.

After mask removal, the fabricated samples undergo the same post-processing treatment that is also applied to the structures fabricated with focused ion beam milling. This part of the fabrication procedure typically is very uncritical and tends not to have a strong impact on the result. The structures fabricated with reactive ion etching showing a successful patterning, however, were destroyed during the annealing step due to a malfunction of different annealing ovens. An optical characterisation was therefore not possible and the expected higher optical quality factors could not be demonstrated with measurements.

It could, however, be shown that even many structures with less-than-perfect appearance show quality factors $Q_{\mathrm{opt,RIE}} \approx 1000$. This demonstrates that reactive ion etching allows to fabricate structures with at least as good optical properties as focused ion beam milling. The very high intensities of some of the resonator modes indicate that this process also leaves a cleaner sample after all processing steps. An additional advantage of the etching procedure in this work is that the hole radii do not increase nearly as much during the post-processing procedure than when using focused ion beam milling. While this issue can in principle be compensated by adapting the pattern where the holes are milled to the chromium mask with 70 to 80 % of their intended final size in the case of reactive ion etching but only 30 to 40 % with focused ion beam milling, it still imposes design restrictions on the geometries that can be patterned with the corresponding technique.

5.6.2   Measurement

While the optical properties of the fabricated photonic and phononic crystal structure can be characterised with standard confocal microscopy, the mechanical resonator modes can only be detected indirectly as signatures of optomechanical interaction. To this end, a homodyne measurement can be performed where the mechanical resonator mode modulates the optical signal and can directly be visualised in the Fourier transform of the intensity fluctuations. Besides a detector with a high temporal resolution, this method requires a resonant excitation of the optical resonator mode and a transmission

measurement through the diamond structure. The grating couplers are designed such that a transmission measurement is possible. The spatial separation of approximately $10\,\mu\text{m}$ is sufficient to separate reflected fluorescence at the excitation side from the transmitted light in detection path via a pinhole.

However, the measurement of the photonic and phononic crystal structure's mechanical properties is not possible at ambient conditions. Friction at the surface is the predominant damping mechanism and the mechanical oscillation is completely inhibited at atmospheric pressure. This viscous damping can be avoided with measurements in vacuum. However, after evacuating the sample chamber overnight, no optical resonator modes could be detected. A further investigation of this phenomenon showed that this change in the fluorescence spectrum does not directly correlate with the chamber pressure. Instead, the effect occurs with a delay suggesting that the underlying process has a certain time constant. Especially the slow recovery of the spectrum after venting indicates that the disappearance of the optical resonator modes in vacuum is not directly linked to pressure.

It seems more probable that other processes like desorption of a surface layer are involved. Considering the extremely small dimensions of the photonic and phononic crystal structures, a thin water film could influence the optical properties of the device. The time constant especially after venting of the sample chamber would be consistent with an adsorption of water at the sample surface. The red-shifting of the resonator mode during the evacuation, however, contradicts this hypothesis. The desorption of a thin water film should rather lead to a blue-shift of the optical resonator mode. Also the occurrence of several additional resonator modes cannot be explained with a condensed water film that desorbs in vacuum. Interestingly, this issue did not occur with similar measurements of two-dimensional photonic crystal structures in the same setup [91].

It remains therefore an open question whether this modification of the fluorescence spectrum is unique to one-dimensional structures or whether the individual samples have further deviating properties. The sample used in reference [91] was fabricated from a bonded diamond membrane while the photonic and phononic crystal structure investigated in this work is based on a heteroepitaxially grown diamond membrane. Also the surface termination remains unclear in both cases. The oxidation steps performed during the post-processing procedure, especially the wet-etching with piranha solution, create an oxygen-like surface termination. However, this property might still deviate from sample to sample depending on the quality of the diamond material.

Further work is thus required to identify the mechanism causing the disappearance of the optical resonator mode in vacuum. The underlying process inhibiting a characterisation of the mechanical mode properties and the measurement of optomechanical coupling needs to be suppressed so that the interactions occurring in the photonic and phononic crystal structure can be investigated. Alternatively, a quantification of the effect could allow to adapt the pattern design. The problem could then be mitigated directly by adjusting the sample fabrication accordingly. Together with a single nitrogen vacancy colour centre implanted into the diamond structure drawing on the technology shown in reference [91], this would allow to also experimentally demonstrate the interactions investigated based on numerical simulations in this work.

Chapter 6

Conclusion and Outlook

This thesis shows a route towards integrated quantum systems based on a diamond platform. The structure investigated for this purpose is a photonic and phononic crystal structure incorporating a single nitrogen vacancy colour centre. The unique property of the system is an optical cavity mode resonant on the zero phonon line of the emitter, both also interacting with the localised mechanical resonator mode. All mutual interactions occurring in this structure, including a hybrid interaction between all three degrees of freedom, are studied and the route towards an experimental implementation is assessed.

Optomechanical interaction between GHz phonons and optical photons co-localised in the diamond structure is investigated considering contributions from both the moving boundaries and the photoelastic effect. Single photon optomechanical coupling constants on the order 10 MHz were found. While optomechanical interaction between telecom photons and GHz phonons in diamond has been demonstrated in the mean time [52, 61], this is the first investigation of optomechanical interaction with visible light.

For the first time, strain coupling between a colour centre in diamond and a localised mechanical resonator mode in the GHz range has been studied. The single phonon strain coupling constants of several hundred Hz found for coupling to the ground state and in the range of tens of MHz for coupling to the excited state levels cannot be reached in other system investigated for strain coupling interaction to date [163, 173, 174, 176]. The highly confined oscillations occurring in the photonic and phononic crystal structure are thus a very promising platform for a future exploitation of strain coupling.

To study a further integrated system, the hybrid interaction between a single nitrogen vacancy colour centre and both the optical and the mechanical resonator modes confined in the diamond structure is investigated. It could be shown that a cooling of the mechanical resonator mode profits in particular from dephasing occurring for the colour centre's electronic levels while the passive optical resonator mode has only a minor influence on the hybrid interaction. This study involving three degrees of freedom is a novel approach for diamond-based systems and further studies considering the lower quality factors of fabricated structures and a driven optical resonator mode could complement these initial results [312].

With respect to the experimental implementation of the modelled interactions, important milestones have been reached. Photonic and phononic crystal structures with optical quality factors of 1000 can reliably be fabricated with focussed ion beam milling. A reactive ion etching process has been developed to further improve the quality of the fabricated structures. While some structures look very promising judged from scanning electron microscope images, they could not be characterised with respect to their optical properties due to a malfunction of different annealing ovens. Other etched structures could, however, be characterised and still showed quality factors of 1000 although the etch process did not work properly leading to structures with inclined sidewalls, not fully etched holes and a rough surface. The limited number of available diamond samples but even more the very restricted access to some of the processing facilities did not allow to further repeat the process until success.

The practical feasibility of measurements in vacuum, required for detecting optomechanical coupling, is assessed. Unexpected features in the optical mode spectrum are detected and systematically investigated so that a future experimental demonstration of the interactions studied in this thesis is within reach.

Bibliography

[1] V. Giovannetti, S. Lloyd, and L. Maccone, *Advances in Quantum Metrology,* Nature Photon. **5**, 222–229 (2011).

[2] D. P. DiVincenzo, *The Physical Implementation of Quantum Computation,* Fortschr. Phys. **48**, 771–783 (2000).

[3] T. D. Ladd, F. Jelezko, R. Laflamme, Y. Nakamura, C. Monroe, and J. L. O'Brien, *Quantum Computers,* Nature **464**, 45–53 (2010).

[4] N. Gisin and R. Thew, *Quantum Communication,* Nature Photon. **1**, 165–171 (2007).

[5] G. Kurizki, P. Bertet, Y. Kubo, K. Mølmer, D. Petrosyan, P. Rabl, and J. Schmiedmayer, *Quantum Technologies with Hybrid Systems,* Proc. Natl. Acad. Sci. **112**, 3866–3873 (2015).

[6] M. Wallquist, K. Hammerer, P. Rabl, M. Lukin, and P. Zoller, *Hybrid Quantum Devices and Quantum Engineering,* Phys. Scr. **2009**, 014001 (2009).

[7] F. Diedrich and H. Walther, *Nonclassical Radiation of a Single Stored Ion,* Phys. Rev. Lett. **58**, 203–206 (1987).

[8] B. Lounis and M. Orrit, *Single-Photon Sources,* Rep. Prog. Phys. **68**, 1129–1179 (2005).

[9] S. Scheel, *Single-Photon Sources - An Introduction,* J. Mod. Opt. **56**, 141–160 (2009).

[10] I. Aharonovich, D. Englund, and M. Toth, *Solid-State Single-Photon Emitters,* Nature Photon. **10**, 631–641 (2016).

[11] Z. Yuan, B. E. Kardynal, R. M. Stevenson, A. J. Shields, C. J. Lobo, K. Cooper, N. S. Beattie, D. A. Ritchie, and M. Pepper, *Electrically Driven Single-Photon Source,* Science **295**, 102–105 (2002).

[12] N. Sangouard and H. Zbinden, *What are single photons good for?* J. Mod. Opt. **59**, 1458–1464 (2012).

[13] T. E. Northup and R. Blatt, *Quantum Information Transfer using Photons,* Nature Photon. **8**, 356–363 (2014).

[14] Y. L. Lim, S. D. Barrett, A. Beige, P. Kok, and L. C. Kwek, *Repeat-Until-Success Quantum Computing using Stationary and Flying Qubits,* Phys. Rev. A **73**, 012304 (2006).

[15] Y. Greenberg, Y. A. Pashkin, and E. Il'ichev, *Nanomechanical Resonators,* Phys. Usp. **55**, 382–407 (2012).

[16] M. Poot and H. S. J. van der Zant, *Mechanical Systems in the Quantum Regime,* Phys. Rep. **511**, 273 – 335 (2012).

[17] R. L. Badzey, G. Zolfagharkhani, A. Gaidarzhy, and P. Mohanty, *A Controllable Nanomechanical Memory Element,* Appl. Phys. Lett. **85**, 3587–3589 (2004).

[18] N. V. Lavrik and P. G. Datskos, *Femtogram Mass Detection using Photothermally Actuated Nanomechanical Resonators,* Appl. Phys. Lett. **82**, 2697–2699 (2003).

[19] P. S. Waggoner and H. G. Craighead, *Micro- and Nanomechanical Sensors for Environmental, Chemical, and Biological Detection,* Lab Chip **7**, 1238–1255 (2007).

[20] K. Jensen, K. Kim, and A. Zettl, *An Atomic-Resolution Nanomechanical Mass Sensor,* Nature Nanotech. **3**, 533–537 (2008).

[21] J. Chaste, A. Eichler, J. Moser, G. Ceballos, R. Rurali, and A. Bachtold, *A Nanomechanical Mass Sensor with Yoctogram Resolution,* Nature Nanotech. **7**, 301–304 (2012).

[22] M. D. LaHaye, O. Buu, B. Camarota, and K. C. Schwab, *Approaching the Quantum Limit of a Nanomechanical Resonator,* Science **304**, 74–77 (2004).

[23] L. Carrascosa, M. Moreno, M. Álvarez, and L. M. Lechuga, *Nanomechanical Biosensors: A New Sensing Tool,* Trends Anal. Chem. **25**, 196 – 206 (2006).

[24] K. Eom, H. S. Park, D. S. Yoon, and T. Kwon, *Nanomechanical Resonators and their Applications in Biological/Chemical Detection: Nanomechanics Principles,* Phys. Rep. **503**, 115 – 163 (2011).

[25] S. J. M. Habraken, K. Stannigel, M. D. Lukin, P. Zoller, and P. Rabl, *Continuous Mode Cooling and Phonon Routers for Phononic Quantum Networks,* New J. Phys. **14**, 115004 (2012).

[26] R. Ruskov and C. Tahan, *On-chip Cavity Quantum Phonodynamics with an Acceptor Qubit in Silicon,* Phys. Rev. B **88**, 064308 (2013).

[27] S. R. Sklan, *Splash, Pop, Sizzle: Information Processing with Phononic Computing,* AIP Adv. **5**, 053302 (2015).

[28] A. D. Greentree, P. Olivero, M. Draganski, E. Trajkov, J. R. Rabeau, P. Reichart, B. C. Gibson, S. Rubanov, S. T. Huntington, D. N. Jamieson, and S. Prawer, *Critical Components for Diamond-Based Quantum Coherent Devices,* J. Phys.: Condens. Matter **18**, S825–S842 (2006).

[29] D. D. Awschalom, R. Epstein, and R. Hanson, *The Diamond Age of Spintronics,* Sci. Am. **297**, 84 – 91 (2007).

[30] I. Aharonovich, A. D. Greentree, and S. Prawer, *Diamond Photonics,* Nature Photon. **5**, 397–405 (2011).

[31] D. D. Awschalom, L. C. Bassett, A. S. Dzurak, E. L. Hu, and J. R. Petta, *Quantum Spintronics: Engineering and Manipulating Atom-Like Spins in Semiconductors,* Science **339**, 1174–1179 (2013).

[32] K. Nemoto, M. Trupke, S. J. Devitt, A. M. Stephens, B. Scharfenberger, K. Buczak, T. Nöbauer, M. S. Everitt, J. Schmiedmayer, and W. J. Munro, *Photonic Architecture for Scalable Quantum Information Processing in Diamond,* Phys. Rev. X **4**, 031022 (2014).

[33] T. Schröder, S. L. Mouradian, J. Zheng, M. E. Trusheim, M. Walsh, E. H. Chen, L. Li, I. Bayn, and D. Englund, *Quantum Nanophotonics in Diamond,* J. Opt. Soc. Am. B **33**, B65–B83 (2016).

[34] I. Bayn and J. Salzman, *High-Q Photonic Crystal Nanocavities on Diamond for Quantum Electrodynamics,* Eur. Phys. J. AP **37**, 19–24 (2007).

[35] I. Bayn and J. Salzman, *Ultra High-Q Photonic Crystal Nanocavity Design: The Effect of a Low-Epsilon Slab Material,* Opt. Express **16**, 4972–4980 (2008).

[36] S. Tomljenovic-Hanic, A. D. Greentree, C. M. de Sterke, and S. Prawer, *Flexible Design of Ultrahigh-Q Microcavities in Diamond-Based Photonic Crystal Slabs,* Opt. Express **17**, 6465–6475 (2009).

[37] S. Tomljenovic-Hanic, M. J. Steel, C. M. de Sterke, and J. Salzman, *Diamond Based Photonic Crystal Microcavities,* Opt. Express **14**, 3556–3562 (2006).

[38] C. Kreuzer, J. Riedrich-Möller, E. Neu, and C. Becher, *Design of Photonic Crystal Microcavities in Diamond Films,* Opt. Express **16**, 1632–1644 (2008).

[39] J. Riedrich-Möller, E. Neu, and C. Becher, *Design of Microcavities in Diamond-Based Photonic Crystals by Fourier- and Real-Space Analysis of Cavity Fields,* Photon. Nanostruc.: Fundam. Appl. **8**, 150 – 162 (2010).

[40] T. M. Babinec, J. T. Choy, K. J. M. Smith, M. Khan, and M. Lončar, *Design and Focused Ion Beam Fabrication of Single Crystal Diamond Nanobeam Cavities,* J. Vac. Sci. Technol. B **29**, 010601 (2011).

[41] I. Bayn, B. Meyler, J. Salzman, and R. Kalish, *Triangular Nanobeam Photonic Cavities in Single-Crystal Diamond,* New J. Phys. **13**, 025018 (2011).

[42] J. Riedrich-Möller, L. Kipfstuhl, C. Hepp, E. Neu, C. Pauly, F. Mücklich, A. Baur, M. Wandt, S. Wolff, M. Fischer, S. Gsell, M. Schreck, and C. Becher, *One- and Two-Dimensional Photonic Crystal Micro-Cavities in Single Crystal Diamond,* Nature Nanotech. **7**, 69–74 (2012).

[43] C. F. Wang, Y.-S. Choi, J. C. Lee, E. L. Hu, J. Yang, and J. E. Butler, *Observation of Whispering Gallery Modes in Nanocrystalline Diamond Microdisks,* Appl. Phys. Lett. **90**, 081110 (2007).

[44] C. F. Wang, R. Hanson, D. D. Awschalom, E. L. Hu, T. Feygelson, J. Yang, and J. E. Butler, *Fabrication and Characterization of Two-Dimensional Photonic Crystal Microcavities in Nanocrystalline Diamond,* Appl. Phys. Lett. **91**, 201112 (2007).

[45] X. Checoury, D. Néel, P. Boucaud, C. Gesset, H. Girard, S. Saada, and P. Bergonzo, *Nanocrystalline Diamond Photonics Platform with High Quality Factor Photonic Crystal Cavities,* Appl. Phys. Lett. **101**, 171115 (2012).

[46] A. Faraon, P. E. Barclay, C. Santori, K.-M. C. Fu, and R. G. Beausoleil, *Resonant Enhancement of the Zero-Phonon Emission from a Colour Centre in a Diamond Cavity,* Nature Photon. **5**, 301–305 (2011).

[47] B. J. M. Hausmann, B. Shields, Q. Quan, P. Maletinsky, M. McCutcheon, J. T. Choy, T. M. Babinec, A. Kubanek, A. Yacoby, M. D. Lukin, and M. Lončar, *Integrated Diamond Networks for Quantum Nanophotonics,* Nano Lett. **12**, 1578–1582 (2012).

[48] B. J. M. Hausmann, I. B. Bulu, P. B. Deotare, M. McCutcheon, V. Venkataraman, M. L. Markham, D. J. Twitchen, and M. Lončar, *Integrated High-Quality Factor Optical Resonators in Diamond,* Nano Lett. **13**, 1898 – 1902 (2013).

[49] A. Faraon, C. Santori, Z. Huang, V. M. Acosta, and R. G. Beausoleil, *Coupling of Nitrogen-Vacancy Centers to Photonic Crystal Cavities in Monocrystalline Diamond,* Phys. Rev. Lett. **109**, 033604 (2012).

[50] B. J. M. Hausmann, B. J. Shields, Q. Quan, Y. Chu, N. P. de Leon, R. Evans, M. J. Burek, A. S. Zibrov, M. Markham, D. J. Twitchen, H. Park, M. D. Lukin, and M. Lončar, *Coupling of NV Centers to Photonic Crystal Nanobeams in Diamond,* Nano Lett. **13**, 5791–5796 (2013).

[51] M. J. Burek, Y. Chu, M. S. Liddy, P. Patel, J. Rochman, S. Meesala, W. Hong, Q. Quan, M. D. Lukin, and M. Lončar, *High Quality-Factor Optical Nanocavities in Bulk Single-Crystal Diamond,* Nature Commun. **5**, 5718 (2014).

[52] M. J. Burek, J. D. Cohen, S. M. Meenehan, N. El-Sawah, C. Chia, T. Ruelle, S. Meesala, J. Rochman, H. A. Atikian, M. Markham, D. J. Twitchen, M. D. Lukin, O. Painter, and M. Lončar, *Diamond Optomechanical Crystals,* Optica **3**, 1404–1411 (2016).

[53] S. Mouradian, N. H. Wan, T. Schröder, and D. Englund, *Rectangular Photonic Crystal Nanobeam Cavities in Bulk Diamond,* Appl. Phys. Lett. **111**, 021103 (2017).

[54] L. Sekaric, J. M. Parpia, H. G. Craighead, T. Feygelson, B. H. Houston, and J. E. Butler, *Nanomechanical Resonant Structures in Nanocrystalline Diamond,* Appl. Phys. Lett. **81**, 4455–4457 (2002).

[55] A. B. Hutchinson, P. A. Truitt, K. C. Schwab, L. Sekaric, J. M. Parpia, H. G. Craighead, and J. E. Butler, *Dissipation in Nanocrystalline-Diamond Nanomechanical Resonators,* Appl. Phys. Lett. **84**, 972–974 (2004).

[56] J. W. Baldwin, M. K. Zalalutdinov, T. Feygelson, B. B. Pate, J. E. Butler, and B. H. Houston, *Nanocrystalline Diamond Resonator Array for RF Signal Processing,* Diamond Relat. Mater. **15**, 2061 – 2067 (2006).

[57] A. Gaidarzhy, M. Imboden, P. Mohanty, J. Rankin, and B. W. Sheldon, *High Quality Factor Gigahertz Frequencies in Nanomechanical Diamond Resonators,* Appl. Phys. Lett. **91**, 203503 (2007).

[58] M. K. Zalalutdinov, M. P. Ray, D. M. Photiadis, J. T. Robinson, J. W. Baldwin, J. E. Butler, T. I. Feygelson, B. B. Pate, and B. H. Houston, *Ultrathin Single Crystal Diamond Nanomechanical Dome Resonators,* Nano Lett. **11**, 4304–4308 (2011).

[59] P. Ovartchaiyapong, L. M. A. Pascal, B. A. Myers, P. Lauria, and A. C. Bleszynski Jayich, *High Quality Factor Single-Crystal Diamond Mechanical Resonators,* Appl. Phys. Lett. **101**, 163505 (2012).

[60] M. J. Burek, D. Ramos, P. Patel, I. W. Frank, and M. Lončar, *Nanomechanical Resonant Structures in Single-Crystal Diamond,* Appl. Phys. Lett. **103**, 131904 (2013).

[61] B. Khanaliloo, H. Jayakumar, A. C. Hryciw, D. P. Lake, H. Kaviani, and P. E. Barclay, *Single-Crystal Diamond Nanobeam Waveguide Optomechanics,* Phys. Rev. X **5**, 041051 (2015).

[62] Y. Tao, J. M. Boss, B. A. Moores, and C. L. Degen, *Single-Crystal Diamond Nanomechanical Resonators with Quality Factors exceeding One Million,* Nature Commun. **5**, 3638 (2014).

[63] M. Mitchell, B. Khanaliloo, D. P. Lake, T. Masuda, J. P. Hadden, and P. E. Barclay, *Single-Crystal Diamond Low-Dissipation Cavity Optomechanics,* Optica **3**, 963–970 (2016).

[64] S. John, *Strong Localization of Photons in Certain Disordered Dielectric Superlattices,* Phys. Rev. Lett. **58**, 2486–2489 (1987).

[65] E. Yablonovitch, *Inhibited Spontaneous Emission in Solid-State Physics and Electronics,* Phys. Rev. Lett. **58**, 2059–2062 (1987).

[66] J. D. Joannopoulos, P. R. Villeneuve, and S. Fan, *Photonic Crystals: Putting a New Twist on Light,* Nature **386**, 143–149 (1997).

[67] M. Trigo, A. Bruchhausen, A. Fainstein, B. Jusserand, and V. Thierry-Mieg, *Confinement of Acoustical Vibrations in a Semiconductor Planar Phonon Cavity,* Phys. Rev. Lett. **89**, 227402 (2002).

[68] M. Maldovan and E. L. Thomas, *Simultaneous Localization of Photons and Phonons in Two-Dimensional Periodic Structures,* Appl. Phys. Lett. **88**, 251907 (2006).

[69] L. Childress, R. Walsworth, and M. Lukin, *Atom-like Crystal Defects: From Quantum Computers to Biological Sensors,* Phys. Today **67**, 38–43 (2014).

[70] F. Jelezko and J. Wrachtrup, *Single Defect Centres in Diamond: A Review,* Phys. Stat. Sol. A **203**, 3207–3225 (2006).

[71] C. Kurtsiefer, S. Mayer, P. Zarda, and H. Weinfurter, *Stable Solid-State Source of Single Photons,* Phys. Rev. Lett. **85**, 290–293 (2000).

[72] L. Childress, J. M. Taylor, A. S. Sørensen, and M. D. Lukin, *Fault-Tolerant Quantum Communication Based on Solid-State Photon Emitters,* Phys. Rev. Lett. **96**, 070504 (2006).

[73] M. Leifgen, T. Schröder, F. Gädeke, R. Riemann, V. Métillon, E. Neu, C. Hepp, C. Arend, C. Becher, K. Lauritsen, and O. Benson, *Evaluation of Nitrogen- and Silicon-Vacancy Defect Centres as Single Photon Sources in Quantum Key Distribution,* New J. Phys. **16**, 023021 (2014).

[74] G. Waldherr, P. Neumann, S. F. Huelga, F. Jelezko, and J. Wrachtrup, *Violation of a Temporal Bell Inequality for Single Spins in a Diamond Defect Center,* Phys. Rev. Lett. **107**, 090401 (2011).

[75] B. Hensen, H. Bernien, A. E. Dréau, A. Reiserer, N. Kalb, M. S. Blok, J. Ruitenberg, R. F. L. Vermeulen, R. N. Schouten, C. Abellán, W. Amaya, V. Pruneri, M. W. Mitchell, M. Markham, D. J. Twitchen, D. Elkouss, S. Wehner, T. H. Taminiau, and R. Hanson, *Loophole-Free Bell Inequality Violation Using Electron Spins Separated by 1.3 Kilometres,* Nature **526**, 682 – 686 (2015).

[76] E. Togan, Y. Chu, A. S. Trifonov, L. Jiang, J. R. Maze, L. Childress, M. V. G. Dutt, A. S. Sørensen, P. R. Hemmer, A. S. Zibrov, and M. D. Lukin, *Quantum Entanglement between an Optical Photon and a Solid-State Spin Qubit,* Nature **466**, 730–734 (2010).

[77] H. Bernien, B. Hensen, W. Pfaff, G. Koolstra, M. S. Blok, L. Robledo, T. H. Taminiau, M. Markham, D. J. Twitchen, L. Childress, and R. Hanson, *Heralded Entanglement between Solid-State Qubits Separated by Three Metres,* Nature **497**, 86–90 (2013).

[78] G. D. Fuchs, V. V. Dobrovitski, D. M. Toyli, F. J. Heremans, and D. D. Awschalom, *Gigahertz Dynamics of a Strongly Driven Single Quantum Spin,* Science **326**, 1520–1522 (2009).

[79] C. G. Yale, B. B. Buckley, D. J. Christle, G. Burkard, F. J. Heremans, L. C. Bassett, and D. D. Awschalom, *All-Optical Control of a Solid-State Spin using Coherent Dark States,* Proc. Natl. Acad. Sci. **110**, 7595–600 (2013).

[80] L. C. Bassett, F. J. Heremans, D. J. Christle, C. G. Yale, G. Burkard, B. B. Buckley, and D. D. Awschalom, *Ultrafast Optical Control of Orbital and Spin Dynamics in a Solid-State Defect,* Science **345**, 1333–1337 (2014).

[81] K. Beha, H. Fedder, M. Wolfer, M. C. Becker, P. Siyushev, M. Jamali, A. Batalov, C. Hinz, J. Hees, L. Kirste, H. Obloh, E. Gheeraert, B. Naydenov, I. Jakobi, F. Dolde, S. Pezzagna, D. Twittchen, M. Markham, D. Dregely, H. Giessen, J. Meijer, F. Jelezko, C. E. Nebel, R. Bratschitsch, A. Leitenstorfer, and J. Wrachtrup, *Diamond Nanophotonics,* Beilstein J. Nanotechnol. **3**, 895–908 (2012).

[82] J. C. Lee, D. O. Bracher, S. Cui, K. Ohno, C. A. McLellan, X. Zhang, P. Andrich, B. Alemán, K. J. Russell, A. P. Magyar, I. Aharonovich, A. Bleszynski Jayich, D. Awschalom, and E. L. Hu, *Deterministic Coupling of Delta-Doped Nitrogen Vacancy Centers to a Nanobeam Photonic Crystal Cavity,* Appl. Phys. Lett. **105**, 261101 (2014).

[83] S. Pezzagna, D. Wildanger, P. Mazarov, A. D. Wieck, Y. Sarov, I. Rangelow, B. Naydenov, F. Jelezko, S. W. Hell, and J. Meijer, *Nanoscale Engineering and Optical Addressing of Single Spins in Diamond,* Small **6**, 2117–2121 (2010).

[84] I. Bayn, E. H. Chen, M. E. Trusheim, L. Li, T. Schröder, O. Gaathon, M. Lu, A. Stein, M. Liu, K. Kisslinger, H. Clevenson, and D. Englund, *Generation of Ensembles of Individually Resolvable Nitrogen Vacancies using Nanometer-Scale Apertures in Ultrahigh-Aspect Ratio Planar Implantation Masks,* Nano Lett. **15**, 1751–1758 (2015).

[85] M. Lesik, P. Spinicelli, S. Pezzagna, P. Happel, V. Jacques, O. Salord, B. Rasser, A. Delobbe, P. Sudraud, A. Tallaire, J. Meijer, and J.-F. Roch, *Maskless and Targeted Creation of Arrays of Colour Centres in Diamond using Focused Ion Beam Technology,* Phys. Stat. Sol. A **210**, 2055–2059 (2013).

[86] C. A. McLellan, B. A. Myers, S. Kraemer, K. Ohno, D. D. Awschalom, and A. C. Bleszynski Jayich, *Patterned Formation of Highly Coherent Nitrogen-Vacancy Centers using a Focused Electron Irradiation Technique,* Nano Lett. **16**, 2450–2454 (2016).

[87] E. Rittweger, K. Y. Han, S. E. Irvine, C. Eggeling, and S. W. Hell, *STED Microscopy Reveals Crystal Colour Centres with Nanometric Resolution,* Nature Photon. **3**, 144–147 (2009).

[88] A. M. Edmonds, U. F. S. D'Haenens-Johansson, R. J. Cruddace, M. E. Newton, K.-M. C. Fu, C. Santori, R. G. Beausoleil, D. J. Twitchen, and M. L. Markham, *Production of Oriented Nitrogen-Vacancy Color Centers in Synthetic Diamond,* Phys. Rev. B **86**, 035201 (2012).

[89] M. Lesik, J.-P. Tetienne, A. Tallaire, J. Achard, V. Mille, A. Gicquel, J.-F. Roch, and V. Jacques, *Perfect Preferential Orientation of Nitrogen-Vacancy Defects in a Synthetic Diamond Sample,* Appl. Phys. Lett. **104**, 113107 (2014).

[90] J. Michl, T. Teraji, S. Zaiser, I. Jakobi, G. Waldherr, F. Dolde, P. Neumann, M. W. Doherty, N. B. Manson, J. Isoya, and J. Wrachtrup, *Perfect Alignment and Preferential Orientation of Nitrogen-Vacancy Centers During Chemical Vapor Deposition Diamond Growth on (111) Surfaces,* Appl. Phys. Lett. **104**, 102407 (2014).

[91] J. Riedrich-Möller, S. Pezzagna, J. Meijer, C. Pauly, F. Mücklich, M. Markham, A. M. Edmonds, and C. Becher, *Nanoimplantation and Purcell Enhancement of Single Nitrogen-Vacancy Centers in Photonic Crystal Cavities in Diamond,* Appl. Phys. Lett. **106**, 221103 (2015).

[92] P. Lebedew, *Untersuchungen über die Druckkräfte des Lichtes,* Ann. Phys. **311**, 433–458 (1901).

[93] E. F. Nichols and G. F. Hull, *A Preliminary Communication on the Pressure of Heat and Light Radiation,* Phys. Rev **13**, 307 (1901).

[94] A. Ashkin, *Acceleration and Trapping of Particles by Radiation Pressure,* Phys. Rev. Lett. **24**, 156–159 (1970).

[95] T. W. Hänsch and A. L. Schawlow, *Cooling of Gases by Laser Radiation,* Opt. Commun **13**, 68–69 (1975).

[96] D. Wineland and H. Dehmelt, *Proposed 10^{14} $\Delta\nu < \nu$ Laser Fluorescence Spectroscopy on $T1^+$ Mono-Ion Oscillator,* Bull. Am. Phys. Soc. **20**, 637–637 (1975).

[97] V. B. Braginsky and A. B. Manukin, *Ponderomotive Effects of Electromagnetic Radiation,* Sov. Phys. JETP **25**, 653 (1967).

[98] V. B. Braginsky, A. B. Manukin, and M. Y. Tikhonov, *Investigation of Dissipative Ponderomotive Effects of Electromagnetic Radiation,* Sov. Phys. JETP **31**, 829 (1970).

[99] T. J. Kippenberg and K. J. Vahala, *Cavity Optomechanics: Back-Action at the Mesoscale,* Science **321**, 1172–1176 (2008).

[100] I. Favero and K. Karrai, *Optomechanics of Deformable Optical Cavities,* Nature Photon. **3**, 201–205 (2009).

[101] M. Aspelmeyer, P. Meystre, and K. Schwab, *Quantum Optomechanics,* Phys. Today **65**, 29–35 (2012).

[102] P. Meystre, *A Short Walk Through Quantum Optomechanics,* Ann. Phys. **525**, 215–233 (2013).

[103] M. Aspelmeyer, T. J. Kippenberg, and F. Marquardt, *Cavity Optomechanics,* Rev. Mod. Phys. **86**, 1391–1452 (2014).

[104] M. Metcalfe, *Applications of Cavity Optomechanics,* Appl. Phys. Lett. **1**, 031105 (2014).

[105] V. B. Braginsky, Y. I. Vorontsov, and K. S. Thorne, *Quantum Nondemolition Measurements,* Science **209**, 547–557 (1980).

[106] K. Jacobs, P. Tombesi, M. J. Collett, and D. F. Walls, *Quantum-Nondemolition Measurement of Photon Number using Radiation Pressure,* Phys. Rev. A **49**, 1961 (1994).

[107] M. Pinard, C. Fabre, and A. Heidmann, *Quantum-Nondemolition Measurement of Light by a Piezoelectric Crystal,* Phys. Rev. A **51**, 2443 (1995).

[108] C. Fabre, M. Pinard, S. Bourzeix, A. Heidmann, E. Giacobino, and S. Reynaud, *Quantum-Noise Reduction using a Cavity with a Movable Mirror,* Phys. Rev. A **49**, 1337 (1994).

[109] S. Mancini and P. Tombesi, *Quantum Noise Reduction by Radiation Pressure,* Phys. Rev. A **49**, 4055–4065 (1994).

[110] A. A. Clerk, F. Marquardt, and K. Jacobs, *Back-Action Evasion and Squeezing of a Mechanical Resonator using a Cavity Detector,* New J. Phys. **10**, 095010 (2008).

[111] S. Mancini, V. I. Manko, and P. Tombesi, *Ponderomotive Control of Quantum Macroscopic Coherence,* Phys. Rev. A **55**, 3042–3050 (1997).

[112] S. Bose, K. Jacobs, and P. L. Knight, *Preparation of Nonclassical States in Cavities with a Moving Mirror,* Phys. Rev. A **56**, 4175–4186 (1997).

[113] W. Marshall, C. Simon, R. Penrose, and D. Bouwmeester, *Towards Quantum Superpositions of a Mirror,* Phys. Rev. Lett. **91**, 130401 (2003).

[114] M. Paternostro, D. Vitali, S. Gigan, M. S. Kim, C. Brukner, J. Eisert, and M. Aspelmeyer, *Creating and Probing Multipartite Macroscopic Entanglement with Light,* Phys. Rev. Lett. **99**, 250401 (2007).

[115] D. Vitali, S. Gigan, A. Ferreira, H. R. Böhm, P. Tombesi, A. Guerreiro, V. Vedral, A. Zeilinger, and M. Aspelmeyer, *Optomechanical Entanglement between a Movable Mirror and a Cavity Field,* Phys. Rev. Lett. **98**, 030405 (2007).

[116] S. Mancini, D. Vitali, and P. Tombesi, *Optomechanical Cooling of a Macroscopic Oscillator by Homodyne Feedback,* Phys. Rev. Lett. **80**, 688–691 (1998).

[117] P. F. Cohadon, A. Heidmann, and M. Pinard, *Cooling of a Mirror by Radiation Pressure,* Phys. Rev. Lett. **83**, 3174–3177 (1999).

[118] A. Dorsel, J. D. McCullen, P. Meystre, E. Vignes, and H. Walther, *Optical Bistability and Mirror Confinement Induced by Radiation Pressure,* Phys. Rev. Lett. **51**, 1550–1553 (1983).

[119] M. Vogel, C. Mooser, K. Karrai, and R. J. Warburton, *Optically Tunable Mechanics of Microlevers,* Appl. Phys. Lett. **83**, 1337–1339 (2003).

[120] B. S. Sheard, M. B. Gray, C. M. Mow-Lowry, D. E. McClelland, and S. E. Whitcomb, *Observation and Characterization of an Optical Spring,* Phys. Rev. A **69**, 051801 (2004).

[121] S. Gigan, H. R. Böhm, M. Paternostro, F. Blaser, G. Langer, J. B. Hertzberg, K. C. Schwab, D. Bäuerle, M. Aspelmeyer, and A. Zeilinger, *Self-Cooling of a Micromirror by Radiation Pressure,* Nature **444**, 67–70 (2006).

[122] O. Arcizet, P.-F. Cohadon, T. Briant, M. Pinard, and A. Heidmann, *Radiation-Pressure Cooling and Optomechanical Instability of a Micromirror,* Nature **444**, 71–74 (2006).

[123] T. J. Kippenberg, H. Rokhsari, T. Carmon, A. Scherer, and K. J. Vahala, *Analysis of Radiation-Pressure Induced Mechanical Oscillation of an Optical Microcavity,* Phys. Rev. Lett. **95**, 033901 (2005).

[124] H. Rokhsari, T. J. Kippenberg, T. Carmon, and K. J. Vahala, *Radiation-Pressure-Driven Micro-Mechanical Oscillator,* Opt. Express **13**, 5293–5301 (2005).

[125] J. D. Thompson, B. M. Zwickl, A. M. Jayich, F. Marquardt, S. M. Girvin, and J. G. E. Harris, *Strong Dispersive Coupling of a High-Finesse Cavity to a Micromechanical Membrane,* Nature **452**, 72–75 (2008).

[126] G. Anetsberger, O. Arcizet, Q. P. Unterreithmeier, R. Rivière, A. Schliesser, E. M. Weig, J. P. Kotthaus, and T. J. Kippenberg, *Near-Field Cavity Optomechanics with Nanomechanical Oscillators,* Nature Phys. **5**, 909–914 (2009).

[127] C. H. Metzger and K. Karrai, *Cavity Cooling of a Microlever,* Nature **432**, 1002–1005 (2004).

[128] F. Marquardt, J. P. Chen, A. A. Clerk, and S. M. Girvin, *Quantum Theory of Cavity-Assisted Sideband Cooling of Mechanical Motion,* Phys. Rev. Lett. **99**, 093902 (2007).

[129] C. Genes, D. Vitali, P. Tombesi, S. Gigan, and M. Aspelmeyer, *Ground-State Cooling of a Micromechanical Oscillator: Comparing Cold Damping and Cavity-Assisted Cooling Schemes,* Phys. Rev. A **77**, 033804 (2008).

[130] D. Kleckner and D. Bouwmeester, *Sub-Kelvin Optical Cooling of a Micromechanical Resonator,* Nature **444**, 75–78 (2006).

[131] O. Arcizet, P.-F. Cohadon, T. Briant, M. Pinard, A. Heidmann, J.-M. Mackowski, C. Michel, L. Pinard, O. Français, and L. Rousseau, *High-Sensitivity Optical Monitoring of a Micromechanical Resonator with a Quantum-Limited Optomechanical Sensor,* Phys. Rev. Lett. **97**, 133601 (2006).

[132] M. Poggio, C. L. Degen, H. J. Mamin, and D. Rugar, *Feedback Cooling of a Cantilever's Fundamental Mode Below 5 mK,* Phys. Rev. Lett. **99**, 017201 (2007).

[133] A. Naik, O. Buu, M. D. LaHaye, A. D. Armour, A. A. Clerk, M. P. Blencowe, and K. C. Schwab, *Cooling a Nanomechanical Resonator with Quantum Back-Action,* Nature **443**, 193–196 (2006).

[134] A. Schliesser, P. Del'Haye, N. Nooshi, K. J. Vahala, and T. J. Kippenberg, *Radiation Pressure Cooling of a Micromechanical Oscillator using Dynamical Backaction,* Phys. Rev. Lett. **97**, 243905 (2006).

[135] A. Schliesser, R. Rivière, G. Anetsberger, O. Arcizet, and T. J. Kippenberg, *Resolved-Sideband Cooling of a Micromechanical Oscillator,* Nature Phys. **4**, 415–419 (2008).

[136] Y.-S. Park and H. Wang, *Resolved-Sideband and Cryogenic Cooling of an Optomechanical Resonator,* Nature Phys. **5**, 489–493 (2009).

[137] A. Schliesser, O. Arcizet, R. Rivière, G. Anetsberger, and T. J. Kippenberg, *Resolved-Sideband Cooling and Position Measurement of a Micromechanical Oscillator close to the Heisenberg Uncertainty Limit,* Nature Phys. **5**, 509–514 (2009).

[138] T. Rocheleau, T. Ndukum, C. Macklin, J. B. Hertzberg, A. A. Clerk, and K. C. Schwab, *Preparation and Detection of a Mechanical Resonator near the Ground State of Motion,* Nature **463**, 72–75 (2010).

[139] J. Chan, T. P. M. Alegre, A. H. Safavi-Naeini, J. T. Hill, A. Krause, S. Gröblacher, M. Aspelmeyer, and O. Painter, *Laser Cooling of a Nanomechanical Oscillator into its Quantum Ground State,* Nature **478**, 89–92 (2011).

[140] A. H. Safavi-Naeini, J. Chan, J. T. Hill, T. P. M. Alegre, A. Krause, and O. Painter, *Observation of Quantum Motion of a Nanomechanical Resonator,* Phys. Rev. Lett. **108**, 033602 (2012).

[141] S. Gröblacher, K. Hammerer, M. R. Vanner, and M. Aspelmeyer, *Observation of Strong Coupling between a Micromechanical Resonator and an Optical Cavity Field,* Nature **460**, 724–727 (2009).

[142] J. D. Teufel, T. Donner, M. A. Castellanos-Beltran, J. W. Harlow, and K. W. Lehnert, *Nanomechanical Motion Measured with an Imprecision below that at the Standard Quantum Limit,* Nature Nanotech. **4**, 820–823 (2009).

[143] E. Verhagen, S. Deléglise, S. Weis, A. Schliesser, and T. J. Kippenberg, *Quantum-Coherent Coupling of a Mechanical Oscillator to an Optical Cavity Mode,* Nature **482**, 63–67 (2012).

[144] A. H. Safavi-Naeini, T. M. Alegre, J. Chan, M. Eichenfield, M. Winger, Q. Lin, J. T. Hill, D. E. Chang, and O. Painter, *Electromagnetically Induced Transparency and Slow Light with Optomechanics,* Nature **472**, 69–73 (2011).

[145] J. Bochmann, A. Vainsencher, D. D. Awschalom, and A. N. Cleland, *Nanomechanical Coupling between Microwave and Optical Photons,* Nature Phys. **9**, 712–716 (2013).

[146] Y. Liu, M. Davanço, V. Aksyuk, and K. Srinivasan, *Electromagnetically Induced Transparency and Wideband Wavelength Conversion in Silicon Nitride Microdisk Optomechanical Resonators,* Phys. Rev. Lett. **110**, 223603 (2013).

[147] M. W. McCutcheon, D. E. Chang, Y. Zhang, M. D. Lukin, and M. Lončar, *Broadband Frequency Conversion and Shaping of Single Photons Emitted from a Nonlinear Cavity,* Opt. Express **17**, 22689–22703 (2009).

[148] K. Rivoire, S. Buckley, and J. Vučković, *Multiply Resonant Photonic Crystal Nanocavities for Nonlinear Frequency Conversion,* Opt. Express **19**, 22198–22207 (2011).

[149] E. Gavartin, P. Verlot, and T. J. Kippenberg, *A Hybrid On-Chip Optomechanical Transducer for Ultrasensitive Force Measurements,* Nature Nanotech. **7**, 509–515 (2012).

[150] F. Liu, S. Alaie, Z. C. Leseman, and M. Hossein-Zadeh, *Sub-pg Mass Sensing and Measurement with an Optomechanical Oscillator,* Opt. Express **21**, 19555–19567 (2013).

[151] A. A. Clerk, F. Marquardt, and J. G. E. Harris, *Quantum Measurement of Phonon Shot Noise,* Phys. Rev. Lett. **104**, 213603 (2010).

[152] C. Galland, N. Sangouard, N. Piro, N. Gisin, and T. J. Kippenberg, *Heralded Single-Phonon Preparation, Storage, and Readout in Cavity Optomechanics,* Phys. Rev. Lett. **112**, 143602 (2014).

[153] M. R. Vanner, I. Pikovski, G. D. Cole, M. S. Kim, Č. Brukner, K. Hammerer, G. J. Milburn, and M. Aspelmeyer, *Pulsed Quantum Optomechanics,* Proc. Natl. Acad. Sci. **108**, 16182–16187 (2011).

[154] M. Vanner, J. Hofer, G. D. Cole, and M. Aspelmeyer, *Cooling-by-Measurement and Mechanical State Tomography via Pulsed Optomechanics,* Nature Commun. **4**, 1 – 8 (2013).

[155] E. Gavartin, R. Braive, I. Sagnes, O. Arcizet, A. Beveratos, T. J. Kippenberg, and I. Robert-Philip, *Optomechanical Coupling in a Two-Dimensional Photonic Crystal Defect Cavity,* Phys. Rev. Lett. **106**, 203902 (2011).

[156] M. Eichenfield, J. Chan, R. M. Camacho, K. J. Vahala, and O. Painter, *Optomechanical Crystals,* Nature **462**, 78–82 (2009).

[157] P. Rath, S. Khasminskaya, C. Nebel, C. Wild, and W. H. Pernice, *Diamond-Integrated Optomechanical Circuits,* Nature Commun. **4**, 1690 (2013).

[158] S. Ummethala, P. Rath, G. Lewes-Malandrakis, D. Brink, C. Nebel, and W. H. P. Pernice, *High-Q Optomechanical Circuits made from Polished Nanocrystalline Diamond Thin Films,* Diamond Relat. Mater. **44**, 49 – 53 (2014).

[159] I. Wilson-Rae and A. Imamoğlu, *Quantum Dot Cavity-QED in the Presence of Strong Electron-Phonon Interactions,* Phys. Rev. B **65**, 235311 (2002).

[160] T. Ramos, V. Sudhir, K. Stannigel, P. Zoller, and T. J. Kippenberg, *Nonlinear Quantum Optomechanics via Individual Intrinsic Two-Level Defects,* Phys. Rev. Lett. **110**, 193602 (2013).

[161] I. Yeo, P.-L. De Assis, A. Gloppe, E. Dupont-Ferrier, P. Verlot, N. S. Malik, E. Dupuy, J. Claudon, J.-M. Gérard, A. Auffèves, G. Nogues, S. S, J.-P. Poizat, O. Arcizet, and M. Richard, *Strain-Mediated Coupling in a Quantum Dot-Mechanical Oscillator Hybrid System,* Nature Nanotech. **9**, 106–110 (2014).

[162] A. D. O'Connell, M. Hofheinz, M. Ansmann, R. C. Bialczak, M. Lenander, E. Lucero, M. Neeley, D. Sank, H. Wang, M. Weides, J. Wenner, J. M. Martinis, and C. A. N, *Quantum Ground State and Single-Phonon Control of a Mechanical Resonator,* Nature **464**, 697–703 (2010).

[163] D. Lee, K. W. Lee, J. V. Cady, P. Ovartchaiyapong, and A. C. Bleszynski Jayich, *Topical review: spins and mechanics in diamond,* J. Opt. **19**, 033001 (2017).

[164] P. Rabl, P. Cappellaro, M. V. G. Dutt, L. Jiang, J. R. Maze, and M. D. Lukin, *Strong Magnetic Coupling between an Electronic Spin Qubit and a Mechanical Resonator,* Phys. Rev. B **79**, 041302 (2009).

[165] O. Arcizet, V. Jacques, A. Siria, P. Poncharal, P. Vincent, and S. Seidelin, *A Single Nitrogen-Vacancy Defect Coupled to a Nanomechanical Oscillator,* Nature Phys. **7**, 879–883 (2011).

[166] S. Kolkowitz, A. C. Bleszynski Jayich, Q. P. Unterreithmeier, S. D. Bennett, P. Rabl, J. G. E. Harris, and M. D. Lukin, *Coherent Sensing of a Mechanical Resonator with a Single-Spin Qubit,* Science **335**, 1603–1606 (2012).

[167] S. Hong, M. S. Grinolds, P. Maletinsky, R. L. Walsworth, M. D. Lukin, and A. Yacoby, *Coherent, Mechanical Control of a Single Electronic Spin,* Nano Lett. **12**, 3920–3924 (2012).

[168] B. Pigeau, S. Rohr, L. M. De Lépinay, A. Gloppe, V. Jacques, and O. Arcizet, *Observation of a Phononic Mollow Triplet in a Multimode Hybrid Spin-Nanomechanical System,* Nature Commun. **6** (2015).

[169] E. R. MacQuarrie, T. A. Gosavi, N. R. Jungwirth, S. A. Bhave, and G. D. Fuchs, *Mechanical Spin Control of Nitrogen-Vacancy Centers in Diamond,* Phys. Rev. Lett. **111**, 227602 (2013).

[170] E. R. MacQuarrie, T. A. Gosavi, S. A. Bhave, and G. D. Fuchs, *Continuous Dynamical Decoupling of a Single Diamond Nitrogen-Vacancy Center Spin with a Mechanical Resonator,* Phys. Rev. B **92**, 224419 (2015).

[171] E. R. MacQuarrie, T. A. Gosavi, A. M. Moehle, N. R. Jungwirth, S. A. Bhave, and G. D. Fuchs, *Coherent Control of a Nitrogen-Vacancy Center Spin Ensemble with a Diamond Mechanical Resonator,* Optica **2**, 233–238 (2015).

[172] D. A. Golter, T. Oo, M. Amezcua, K. A. Stewart, and H. Wang, *Optomechanical Quantum Control of a Nitrogen-Vacancy Center in Diamond,* Phys. Rev. Lett. **116**, 143602 (2016).

[173] J. Teissier, A. Barfuss, P. Appel, E. Neu, and P. Maletinsky, *Strain Coupling of a Nitrogen-Vacancy Center Spin to a Diamond Mechanical Oscillator,* Phys. Rev. Lett. **113**, 020503 (2014).

[174] P. Ovartchaiyapong, K. W. Lee, B. A. Myers, and A. C. Bleszynski Jayich, *Dynamic Strain-Mediated Coupling of a Single Diamond Spin to a Mechanical Resonator,* Nature Commun. **5**, 4429 (2014).

[175] A. Barfuss, J. Teissier, E. Neu, A. Nunnenkamp, and P. Maletinsky, *Strong Mechanical Driving of a Single Electron Spin,* Nature Phys. (2015).

[176] K. W. Lee, D. Lee, P. Ovartchaiyapong, J. Minguzzi, J. R. Maze, and A. C. Bleszynski Jayich, *Strain Coupling of a Mechanical Resonator to a Single Quantum Emitter in Diamond,* Phys. Rev. Applied **6**, 034005 (2016).

[177] S. Koizumi, C. Nebel, and M. Nesladek, *Physics and Applications of CVD Diamond* (John Wiley & Sons, 2008).

[178] A. Krüger, *Neue Kohlenstoffmaterialien: Eine Einführung* (Springer-Verlag, 2007).

[179] Y. Sato, Y. Tanaka, J. Upham, Y. Takahashi, T. Asano, and S. Noda, *Strong Coupling Between Distant Photonic Nanocavities and its Dynamic Control,* Nature Photon. **6**, 56–61 (2012).

[180] L. S. Hounsome, R. Jones, M. J. Shaw, and P. R. Briddon, *Photoelastic Constants in Diamond and Silicon,* Phys. Stat. Sol. A **203**, 3088–3093 (2006).

[181] A. R. Lang, *The Strain-Optical Constants of Diamond: A Brief History of Measurements,* Diamond Relat. Mater. **18**, 1 – 5 (2009).

[182] R. W. Dixon, *Photoelastic Properties of Selected Materials and Their Relevance for Applications to Acoustic Light Modulators and Scanners,* J. Appl. Phys. **38**, 5149–5153 (1967).

[183] S. Y. Davydov and S. Tikhonov, *Photoelasticity and Quadratic Permittivity of Wide-Gap Semiconductors,* Semiconductors **31**, 698–699 (1997).

[184] V. P. Adiga, A. V. Sumant, S. Suresh, C. Gudeman, O. Auciello, J. A. Carlisle, and R. W. Carpick, *Mechanical Stiffness and Dissipation in Ultrananocrystalline Diamond Microresonators,* Phys. Rev. B **79**, 245403 (2009).

[185] M. Schreck, J. Asmussen, S. Shikata, J.-C. Arnault, and N. Fujimori, *Large-Area High-Quality Single Crystal Diamond,* Mater. Res. Bull. **39**, 504–510 (2014).

[186] A. Tallaire, J. Achard, A. Boussadi, O. Brinza, A. Gicquel, I. N. Kupriyanov, Y. N. Palyanov, G. Sakr, and J. Barjon, *High Quality Thick CVD Diamond Films Homoepitaxially Grown on (111)-Oriented Substrates,* Diamond Relat. Mater. **41**, 34–40 (2014).

[187] K. J. Vahala, *Optical Microcavities,* Nature **424**, 839–846 (2003).

[188] C. J. Hood, T. W. Lynn, A. C. Doherty, A. S. Parkins, and H. J. Kimble, *The Atom-Cavity Microscope: Single Atoms Bound in Orbit by Single Photons,* Science **287**, 1447–1453 (2000).

[189] A. Albrecht, A. Retzker, F. Jelezko, and M. B. Plenio, *Coupling of Nitrogen Vacancy Centres in Nanodiamonds by means of Phonons,* New J. Phys. **15**, 083014 (2013).

[190] R. Albrecht, A. Bommer, C. Pauly, F. Mücklich, A. W. Schell, P. Engel, T. Schröder, O. Benson, J. Reichel, and C. Becher, *Narrow-Band Single Photon Emission at Room Temperature Based on a Single Nitrogen-Vacancy Center Coupled to an All-Fiber-Cavity,* Appl. Phys. Lett. **105**, 073113 (2014).

[191] M. L. Gorodetsky, A. A. Savchenkov, and V. S. Ilchenko, *Ultimate Q of Optical Microsphere Resonators,* Opt. Lett. **21**, 453–455 (1996).

[192] D. K. Armani, T. J. Kippenberg, S. M. Spillane, and K. J. Vahala, *Ultra-High-Q Toroid Microcavity on a Chip,* Nature **421**, 925–928 (2003).

[193] P. Michler, A. Kiraz, C. Becher, W. V. Schoenfeld, P. M. Petroff, L. Zhang, E. Hu, and A. Imamoğlu, *A Quantum Dot Single-Photon Turnstile Device,* Science **290**, 2282–2285 (2000).

[194] J. Niehusmann, A. Vörckel, P. H. Bolivar, T. Wahlbrink, W. Henschel, and H. Kurz, *Ultrahigh-Quality-Factor Silicon-on-Insulator Microring Resonator,* Opt. Lett. **29**, 2861–2863 (2004).

[195] Y. Louyer, D. Meschede, and A. Rauschenbeutel, *Tunable Whispering-Gallery-Mode Resonators for Cavity Quantum Electrodynamics,* Phys. Rev. A **72**, 031801 (2005).

[196] A. Schliesser, G. Anetsberger, R. Rivière, O. Arcizet, and T. J. Kippenberg, *High-Sensitivity Monitoring of Micromechanical Vibration using Optical Whispering Gallery Mode Resonators,* New J. Phys. **10**, 095015 (2008).

[197] T. Asano, B.-S. Song, and S. Noda, *Analysis of the Experimental Q Factors (1 Million) of Photonic Crystal Nanocavities,* Opt. Express **14**, 1996–2002 (2006).

[198] S.-H. Kim, G.-H. Kim, S.-K. Kim, H.-G. Park, Y.-H. Lee, and S.-B. Kim, *Characteristics of a Stick Waveguide Resonator in a Two-Dimensional Photonic Crystal Slab,* J. Appl. Phys. **95**, 411–416 (2004).

[199] Y. Takahashi, H. Hagino, Y. Tanaka, B.-S. Song, T. Asano, and S. Noda, *High-Q Nanocavity with a 2-ns Photon Lifetime,* Opt. Express **15**, 17206–17213 (2007).

[200] J. Vučković, M. Lončar, H. Mabuchi, and A. Scherer, *Design of Photonic Crystal Microcavities for Cavity QED,* Phys. Rev. E **65**, 016608 (2001).

[201] J. Vučković, M. Lončar, H. Mabuchi, and A. Scherer, *Optimization of the Q Factor in Photonic Crystal Microcavities,* IEEE J. Quantum Electron. **38**, 850–856 (2002).

[202] Y. Akahane, T. Asano, B.-S. Song, and S. Noda, *High-Q Photonic Nanocavity in a Two-Dimensional Photonic Crystal,* Nature **425**, 944–947 (2003).

[203] M. Notomi, A. Shinya, S. Mitsugi, E. Kuramochi, and H.-Y. Ryu, *Waveguides, Resonators and their Coupled Elements in Photonic Crystal Slabs,* Opt. Express **12**, 1551–1561 (2004).

[204] Z. Zhang and M. Qiu, *Small-Volume Waveguide-Section High Q Microcavities in 2D Photonic Crystal Slabs,* Opt. Express **12**, 3988–3995 (2004).

[205] Y. Akahane, T. Asano, B.-S. Song, and S. Noda, *Fine-Tuned High-Q Photonic-Crystal Nanocavity,* Opt. Express **13**, 1202–1214 (2005).

[206] J. Hagemeier, C. Bonato, T.-A. Truong, H. Kim, G. J. Beirne, M. Bakker, M. P. van Exter, Y. Luo, P. Petroff, and D. Bouwmeester, *H1 Photonic Crystal Cavities for Hybrid Quantum Information Protocols,* Opt. Express **20**, 24714–24726 (2012).

[207] Y. Song, M. Liu, Y. Zhang, X. Wang, and C. Jin, *High-Q Photonic Crystal Slab Nanocavity with an Asymmetric Nanohole in the Center for QED,* JOSA B **28**, 265–274 (2011).

[208] P. Lalanne, S. Mias, and J. P. Hugonin, *Two Physical Mechanisms for Boosting the Quality Factor to Cavity Volume Ratio of Photonic Crystal Microcavities,* Opt. Express **12**, 458–467 (2004).

[209] C. Sauvan, P. Lalanne, and J. Hugonin, *Slow-Wave Effect and Mode-Profile Matching in Photonic Crystal Microcavities,* Phys. Rev. B **71**, 165118 (2005).

[210] C. Sauvan, G. Lecamp, P. Lalanne, and J. Hugonin, *Modal-Reflectivity Enhancement by Geometry Tuning in Photonic Crystal Microcavities,* Opt. Express **13**, 245–255 (2005).

[211] P. Lalanne, C. Sauvan, and J. P. Hugonin, *Photon Confinement in Photonic Crystal Nanocavities,* Laser& Photon. Rev. **2**, 514–526 (2008).

[212] J. M. Geremia, J. Williams, and H. Mabuchi, *Inverse-Problem Approach to Designing Photonic Crystals for Cavity QED Experiments,* Phys. Rev. E **66**, 066606 (2002).

[213] D. Englund, I. Fushman, and J. Vučković, *General Recipe for Designing Photonic Crystal Cavities,* Opt. Express **13**, 5961–5975 (2005).

[214] B.-S. Song, S. Noda, T. Asano, and Y. Akahane, *Ultra-high-Q Photonic Double-Heterostructure Nanocavity,* Nature Mater. **4**, 207–210 (2005).

[215] B.-S. Song, T. Asano, and S. Noda, *Physical Origin of the Small Modal Volume of Ultra-High-Q Photonic Double-Heterostructure Nanocavities,* New J. Phys. **8**, 209 (2006).

[216] B.-S. Song, T. Asano, and S. Noda, *Heterostructures in Two-Dimensional Photonic-Crystal Slabs and their Application to Nanocavities,* J. Phys. D **40**, 2629–2634 (2007).

[217] B.-S. Song, S.-W. Jeon, and S. Noda, *Symmetrically Glass-Clad Photonic Crystal Nanocavities with Ultrahigh Quality Factors,* Opt. Lett. **36**, 91–93 (2011).

[218] E. Kuramochi, M. Notomi, S. Mitsugi, A. Shinya, T. Tanabe, and T. Watanabe, *Ultrahigh-Q Photonic Crystal Nanocavities Realized by the Local Width Modulation of a Line Defect,* Appl. Phys. Lett. **88**, 041112 (2006).

[219] E. Kuramochi, H. Taniyama, T. Tanabe, A. Shinya, and M. Notomi, *Ultrahigh-Q Two-Dimensional Photonic Crystal Slab Nanocavities in Very Thin Barriers,* Appl. Phys. Lett. **93**, 111112 (2008).

[220] M. Notomi, E. Kuramochi, and H. Taniyama, *Ultrahigh-Q Nanocavity with 1D Photonic Gap,* Opt. Express **16**, 11095–11102 (2008).

[221] C. L. C. Smith, D. K. C. Wu, M. W. Lee, C. Monat, S. Tomljenovic-Hanic, C. Grillet, B. J. Eggleton, D. Freeman, Y. Ruan, S. Madden, B. Luther-Davies, H. Giessen, and Y.-H. Lee, *Microfluidic Photonic Crystal Double Heterostructures,* Appl. Phys. Lett. **91**, 121103 (2007).

[222] S. H. Fan, J. N. Winn, A. Devenyi, J. C. Chen, R. D. Meade, and J. D. Joannopoulos, *Guided and Defect Modes in Periodic Dielectric Wave-Guides,* JOSA B **12**, 1267–1272 (1995).

[223] J. S. Foresi, P. R. Villeneuve, J. Ferrera, E. R. Thoen, G. Steinmeyer, S. Fan, J. D. Joannopoulos, L. C. Kimerling, H. I. Smith, and E. P. Ippen, *Photonic-Bandgap Microcavities in Optical Waveguides,* Nature **390**, 143–145 (1997).

[224] P. Velha, J. C. Rodier, P. Lalanne, J. P. Hugonin, D. Peyrade, E. Picard, T. Charvolin, and E. Hadji, *Ultra-High-Reflectivity Photonic-Bandgap Mirrors in a Ridge SOI Waveguide,* New J. Phys. **8**, 204 (2006).

[225] P. Velha, E. Picard, T. Charvolin, E. Hadji, J. C. Rodier, P. Lalanne, and D. Peyrade, *Ultra-high Q/V Fabry-Pérot Microcavity on SOI Substrate,* Opt. Express **15**, 16090–16096 (2007).

[226] A. R. M. Zain, N. P. Johnson, M. Sorel, and R. M. De la Rue, *Ultra High Quality Factor One Dimensional Photonic Crystal/Photonic Wire Micro-Cavities in Silicon-on-Insulator (SOI),* Opt. Express **16**, 12084–12089 (2008).

[227] P. B. Deotare, M. W. McCutcheon, I. W. Frank, M. Khan, and M. Loncar, *High Quality Factor Photonic Crystal Nanobeam Cavities,* Appl. Phys. Lett. **94**, 121106 (2009).

[228] W. H. P. Pernice, C. Xiong, C. Schuck, and H. X. Tang, *High-Q Aluminum Nitride Photonic Crystal Nanobeam Cavities,* Appl. Phys. Lett. **100**, 091105 (2012).

[229] Y. Zhang, I. Bulu, W.-M. Tam, B. Levitt, J. Shah, T. Botto, and M. Loncar, *High-Q/V Air-Mode Photonic Crystal Cavities at Microwave Frequencies,* Opt. Express **19**, 9371–9377 (2011).

[230] Y. Zhang, M. W. McCutcheon, I. B. Burgess, and M. Loncar, *Ultra-High-Q TE/TM Dual-Polarized Photonic Crystal Nanocavities,* Opt. Lett. **34**, 2694–2696 (2009).

[231] Q. Quan, P. B. Deotare, and M. Loncar, *Photonic Crystal Nanobeam Cavity Strongly Coupled to the Feeding Waveguide,* Appl. Phys. Lett. **96**, 203102 (2010).

[232] E. Kuramochi, H. Taniyama, T. Tanabe, K. Kawasaki, Y.-G. Roh, and M. Notomi, *Ultrahigh-Q One-Dimensional Photonic Crystal Nanocavities with Modulated Mode-Gap Barriers on SiO2 Claddings and on Air Claddings,* Opt. Express **18**, 15859–15869 (2010).

[233] Q. Quan and M. Loncar, *Deterministic Design of Wavelength Scale, Ultra-High Q Photonic Crystal Nanobeam Cavities,* Opt. Express **19**, 18529–18542 (2011).

[234] J. Chan, M. Eichenfield, R. Camacho, and O. Painter, *Optical and Mechanical Design of a "Zipper" Photonic Crystal Optomechanical Cavity,* Opt. Express **17**, 3802–3817 (2009).

[235] Q. Quan, I. B. Burgess, S. K. Y. Tang, D. L. Floyd, and M. Loncar, *High-Q, Low Index-Contrast Polymeric Photonic Crystal Nanobeam Cavities,* Opt. Express **19**, 22191–22197 (2011).

[236] J. Chan, A. H. Safavi-Naeini, J. T. Hill, S. Meenehan, and O. Painter, *Optimized Optomechanical Crystal Cavity with Acoustic Radiation Shield,* Appl. Phys. Lett. **101**, 081115 (2012).

[237] S. B. Legoas, V. R. Coluci, S. F. Braga, P. Z. Coura, S. O. Dantas, and D. S. Galvao, *Gigahertz Nanomechanical Oscillators Based on Carbon Nanotubes,* Nanotechnology **15**, S184 (2004).

[238] M. Notomi, H. Taniyama, S. Mitsugi, and E. Kuramochi, *Optomechanical Wavelength and Energy Conversion in High-Q Double-Layer Cavities of Photonic Crystal Slabs,* Phys. Rev. Lett. **97**, 023903 (2006).

[239] P. H. Kim, C. Doolin, B. D. Hauer, A. J. R. MacDonald, M. R. Freeman, P. E. Barclay, and J. P. Davis, *Nanoscale Torsional Optomechanics,* Appl. Phys. Lett. **102**, 053102 (2013).

[240] S. Gröblacher, J. T. Hill, A. H. Safavi-Naeini, J. Chan, and O. Painter, *Highly Efficient Coupling from an Optical Fiber to a Nanoscale Silicon Optomechanical Cavity,* Appl. Phys. Lett. **103**, 181104 (2013).

[241] R. Ma, A. Schliesser, P. Del'Haye, A. Dabirian, G. Anetsberger, and T. J. Kippenberg, *Radiation-Pressure-Driven Vibrational Modes in Ultrahigh-Q Silica Microspheres,* Opt. Lett. **32**, 2200–2202 (2007).

[242] A. N. Cleland, M. Pophristic, and I. Ferguson, *Single-Crystal Aluminum Nitride Nanomechanical Resonators,* Appl. Phys. Lett. **79**, 2070–2072 (2001).

[243] C. Xiong, X. Sun, K. Y. Fong, and H. X. Tang, *Integrated High Frequency Aluminum Nitride Optomechanical Resonators,* Appl. Phys. Lett. **100**, 171111 (2012).

[244] Y.-G. Roh, T. Tanabe, A. Shinya, H. Taniyama, E. Kuramochi, S. Matsuo, T. Sato, and M. Notomi, *Strong Optomechanical Interaction in a Bilayer Photonic Crystal,* Phys. Rev. B **81**, 121101 (2010).

[245] M. Eichenfield, R. Camacho, J. Chan, K. J. Vahala, and O. Painter, *A Picogram- and Nanometre-Scale Photonic-Crystal Optomechanical Cavity,* Nature **459**, 550–555 (2009).

[246] M. Davanço, S. Ates, Y. Liu, and K. Srinivasan, *Si3N4 Optomechanical Crystals in the Resolved-Sideband Regime,* Appl. Phys. Lett. **104**, 041101 (2014).

[247] M. J. Burek, N. P. de Leon, B. J. Shields, B. J. M. Hausmann, Y. Chu, Q. Quan, A. S. Zibrov, H. Park, M. D. Lukin, and M. Lončar, *Free-Standing Mechanical and Photonic Nanostructures in Single-Crystal Diamond,* Nano Lett. **12**, 6084–6089 (2012).

[248] X. Sun, X. Zhang, and H. X. Tang, *High-Q Silicon Optomechanical Microdisk Resonators at Gigahertz Frequencies,* Appl. Phys. Lett. **100**, 173116 (2012).

[249] M. M. Sigalas and E. N. Economou, *Elastic and Acoustic Wave Band Structure,* J. Sound and Vib. **158**, 377 – 382 (1992).

[250] M. S. Kushwaha, P. Halevi, L. Dobrzynski, and B. Djafari-Rouhani, *Acoustic Band Structure of Periodic Elastic Composites,* Phys. Rev. Lett. **71**, 2022–2025 (1993).

[251] M. Eichenfield, J. Chan, A. H. Safavi-Naeini, K. J. Vahala, and O. Painter, *Modeling Dispersive Coupling and Losses of Localized Optical and Mechanical Modes in Optomechanical Crystals,* Opt. Express **17**, 20078–20098 (2009).

[252] M. Maldovan, *Sound and Heat Revolutions in Phononics,* Nature **503**, 209–217 (2013).

[253] I. E. Psarobas, N. Papanikolaou, N. Stefanou, B. Djafari-Rouhani, B. Bonello, and V. Laude, *Enhanced Acousto-Optic Interactions in a One-Dimensional Phoxonic Cavity,* Phys. Rev. B **82**, 174303 (2010).

[254] S. Mohammadi, A. A. Eftekhar, W. D. Hunt, and A. Adibi, *High-Q Micromechanical Resonators in a Two-Dimensional Phononic Crystal Slab,* Appl. Phys. Lett. **94**, 051906 (2009).

[255] Q. Rolland, M. Oudich, S. El-Jallal, S. Dupont, Y. Pennec, J. Gazalet, J. C. Kastelik, G. Leveque, and B. Djafari-Rouhani, *Acousto-Optic Couplings in Two-Dimensional Phoxonic Crystal Cavities,* Appl. Phys. Lett. **101**, 061109 (2012).

[256] S. El-Jallal, M. Oudich, Y. Pennec, B. Djafari-Rouhani, V. Laude, J.-C. Beugnot, A. Martinez, J. M. Escalante, and A. Makhoute, *Analysis of Optomechanical Coupling in Two-Dimensional Square Lattice Phoxonic Crystal Slab Cavities,* Phys. Rev. B **88**, 205410 (2013).

[257] S. El-Jallal, M. Oudich, Y. Pennec, B. Djafari-Rouhani, A. Makhoute, Q. Rolland, S. Dupont, and J. Gazalet, *Optomechanical Interactions in Two-Dimensional Si and GaAs PhoXonic Cavities,* J. Phys.: Condens. Matter **26**, 015005 (2014).

[258] K. L. Ekinci and M. L. Roukes, *Nanoelectromechanical systems* Rev. Sci. Instrum. **76**, 061101 (2005).

[259] J. Q. You and F. Nori, *Atomic Physics and Quantum Optics using Superconducting Circuits,* Nature **474**, 589–597 (2011).

[260] A. M. Zaitsev, *Optical Properties of Diamond* (Springer Verlag, Berlin, 2001).

[261] M. W. Doherty, N. B. Manson, P. Delaney, F. Jelezko, J. Wrachtrup, and L. C. L. Hollenberg, *The Nitrogen-Vacancy Colour Centre in Diamond,* Phys. Rep. **528**, 1 – 45 (2013).

[262] P. Maletinsky, S. Hong, M. S. Grinolds, B. Hausmann, M. D. Lukin, R. L. Walsworth, M. Loncar, and A. Yacoby, *A Robust Scanning Diamond Sensor for Nanoscale Imaging with Single Nitrogen-Vacancy Centres,* Nature Nanotech. **7**, 320–324 (2012).

[263] P. Appel, M. Ganzhorn, E. Neu, and P. Maletinsky, *Nanoscale Microwave Imaging with a Single Electron Spin in Diamond,* New J. Phys. **17**, 112001 (2015).

[264] I. Aharonovich and E. Neu, *Diamond Nanophotonics,* Adv. Opt. Mater. **2**, 911–928 (2014).

[265] A. E. Hughes and W. A. Runciman, *Uniaxial Stress Splitting of Doubly Degenerate States of Tetragonal and Trigonal Centres in Cubic Crystals,* Proc. Phys. Soc. **90**, 827–838 (1967).

[266] R. Albrecht, *Coupling of a Single Nitrogen-Vacancy Center in Diamond to a Fiber-Based Microcavity,* Doktorarbeit, Universität des Saarlandes (2014).

[267] R. Albrecht, A. Bommer, C. Deutsch, J. Reichel, and C. Becher, *Coupling of a Single Nitrogen-Vacancy Center in Diamond to a Fiber-Based Microcavity,* Phys. Rev. Lett. **110**, 243602 (2013).

[268] G. D. Fuchs, V. V. Dobrovitski, R. Hanson, A. Batra, C. D. Weis, T. Schenkel, and D. D. Awschalom, *Excited-State Spectroscopy using Single Spin Manipulation in Diamond,* Phys. Rev. Lett. **101**, 117601 (2008).

[269] P. Neumann, R. Kolesov, V. Jacques, J. Beck, J. Tisler, A. Batalov, L. Rogers, N. B. Manson, G. Balasubramanian, F. Jelezko, and J. Wrachtrup, *Excited-State Spectroscopy of Single NV Defects in Diamond using Optically Detected Magnetic Resonance,* New J. Phys. **11**, 013017 (2009).

[270] L. J. Rogers, R. L. McMurtrie, M. J. Sellars, and N. B. Manson, *Time-Averaging within the Excited State of the Nitrogen-Vacancy Centre in Diamond,* New J. Phys. **11**, 063007 (2009).

[271] L. Robledo, H. Bernien, T. van der Sar, and R. Hanson, *Spin Dynamics in the Optical Cycle of Single Nitrogen-Vacancy Centres in Diamond,* New J. Phys. **13**, 025013 (2011).

[272] V. M. Acosta, A. Jarmola, E. Bauch, and D. Budker, *Optical Properties of the Nitrogen-Vacancy Singlet Levels in Diamond,* Phys. Rev. B **82**, 201202 (2010).

[273] L. J. Rogers, S. Armstrong, M. J. Sellars, and N. B. Manson, *Infrared Emission of the NV Centre in Diamond: Zeeman and Uniaxial Stress Studies,* New J. Phys. **10**, 103024 (2008).

[274] G. de Lange, Z. H. Wang, D. Ristè, V. V. Dobrovitski, and R. Hanson, *Universal Dynamical Decoupling of a Single Solid-State Spin from a Spin Bath,* Science **330**, 60–63 (2010).

[275] B. Naydenov, F. Dolde, L. T. Hall, C. Shin, H. Fedder, L. C. L. Hollenberg, F. Jelezko, and J. Wrachtrup, *Dynamical Decoupling of a Single-Electron Spin at Room Temperature,* Phys. Rev. B **83**, 081201 (2011).

[276] V. M. Acosta, E. Bauch, M. P. Ledbetter, C. Santori, K.-M. C. Fu, P. E. Barclay, R. G. Beausoleil, H. Linget, J.-F. Roch, F. Treussart, S. Chemerisov, W. Gawlik, and D. Budker, *Diamonds with a High Density of Nitrogen-Vacancy Centers for Magnetometry Applications,* Phys. Rev. B **80**, 115202 (2009).

[277] G. Balasubramanian, P. Neumann, D. Twitchen, M. Markham, R. Kolesov, N. Mizuochi, J. Isoya, J. Achard, J. Beck, J. Tissler, V. Jacques, P. R. Hemmer, F. Jelezko, and J. Wrachtrup, *Ultralong Spin Coherence Time in Isotopically Engineered Diamond,* Nature Mater. **8**, 383–387 (2009).

[278] W. H. Zurek, *Decoherence, Einselection, and the Quantum Origins of the Classical,* Rev. Mod. Phys. **75**, 715–775 (2003).

[279] T. A. Kennedy, J. S. Colton, J. E. Butler, R. C. Linares, and P. J. Doering, *Long Coherence Times at 300 K for Nitrogen-Vacancy Center Spins in Diamond Grown by Chemical Vapor Deposition,* Appl. Phys. Lett. **83**, 4190–4192 (2003).

[280] C. A. Ryan, J. S. Hodges, and D. G. Cory, *Robust Decoupling Techniques to Extend Quantum Coherence in Diamond,* Phys. Rev. Lett. **105**, 200402 (2010).

[281] J. S. Hodges, L. Li, M. Lu, E. H. Chen, M. E. Trusheim, S. Allegri, X. Yao, O. Gaathon, H. Bakhru, and D. Englund, *Long-Lived NV^- Spin Coherence in High-Purity Diamond Membranes,* New J. Phys. **14**, 093004 (2012).

[282] L. M. Pham, N. Bar-Gill, C. Belthangady, D. Le Sage, P. Cappellaro, M. D. Lukin, A. Yacoby, and R. L. Walsworth, *Enhanced Solid-State Multispin Metrology using Dynamical Decoupling,* Phys. Rev. B **86**, 045214 (2012).

[283] X. Xu, Z. Wang, C. Duan, P. Huang, P. Wang, Y. Wang, N. Xu, X. Kong, F. Shi, X. Rong, and J. Du, *Coherence-Protected Quantum Gate by Continuous Dynamical Decoupling in Diamond,* Phys. Rev. Lett. **109**, 070502 (2012).

[284] N. Bar-Gill, L. M. Pham, A. Jarmola, D. Budker, and R. L. Walsworth, *Solid-State Electronic Spin Coherence Time Approaching One Second,* Nature Commun. **4**, 1743 (2013).

[285] H. A. Jahn and E. Teller, *Stability of Polyatomic Molecules in Degenerate Electronic States. I. Orbital Degeneracy,* Proc. R. Soc. Lond., A **161**, 220–235 (1937).

[286] K.-M. C. Fu, C. Santori, P. E. Barclay, L. J. Rogers, N. B. Manson, and R. G. Beausoleil, *Observation of the Dynamic Jahn-Teller Effect in the Excited States of Nitrogen-Vacancy Centers in Diamond,* Phys. Rev. Lett. **103**, 256404 (2009).

[287] T. A. Abtew, Y. Y. Sun, B.-C. Shih, P. Dev, S. B. Zhang, and P. Zhang, *Dynamic Jahn-Teller Effect in the NV^- Center in Diamond,* Phys. Rev. Lett. **107**, 146403 (2011).

[288] P. Siyushev, H. Pinto, M. Vörös, A. Gali, F. Jelezko, and J. Wrachtrup, *Optically Controlled Switching of the Charge State of a Single Nitrogen-Vacancy Center in Diamond at Cryogenic Temperatures,* Phys. Rev. Lett. **110**, 167402 (2013).

[289] B. Naydenov, F. Reinhard, A. Lämmle, V. Richter, R. Kalish, U. F. D'Haenens-Johansson, M. Newton, F. Jelezko, and J. Wrachtrup, *Increasing the Coherence Time of Single Electron Spins in Diamond by High Temperature Annealing,* Appl. Phys. Lett. **97**, 242511 (2010).

[290] K. Ohno, F. Joseph Heremans, L. C. Bassett, B. A. Myers, D. M. Toyli, A. C. Bleszynski Jayich, C. J. Palmstrøm, and D. D. Awschalom, *Engineering Shallow Spins in Diamond with Nitrogen Delta-Doping,* Appl. Phys. Lett. **101**, 082413 (2012).

[291] J. Meijer, B. Burchard, M. Domhan, C. Wittmann, T. Gaebel, I. Popa, F. Jelezko, and J. Wrachtrup, *Generation of Single Color Centers by Focused Nitrogen Implantation,* Appl. Phys. Lett. **87**, 261909 (2005).

[292] J. R. Rabeau, P. Reichart, G. Tamanyan, D. N. Jamieson, S. Prawer, F. Jelezko, T. Gaebel, I. Popa, M. Domhan, and J. Wrachtrup, *Implantation of Labelled Single Nitrogen Vacancy Centers in Diamond using ^{15}N,* Appl. Phys. Lett. **88**, 023113 (2006).

[293] J. Riedrich-Möller, C. Arend, C. Pauly, F. Mücklich, M. Fischer, S. Gsell, M. Schreck, and C. Becher, *Deterministic Coupling of a Single Silicon-Vacancy Color Center to a Photonic Crystal Cavity in Diamond,* Nano Lett. **14**, 5281–5287 (2014).

[294] L. M. Pham, N. Bar-Gill, D. Le Sage, C. Belthangady, A. Stacey, M. Markham, D. J. Twitchen, M. D. Lukin, and R. L. Walsworth, *Enhanced Metrology using Preferential Orientation of Nitrogen-Vacancy Centers in Diamond,* Phys. Rev. B **86**, 121202 (2012).

[295] J. Vučković, C. Santori, D. Fattal, M. Pelton, G. S. Solomon, and Y. Yamamoto, *Cavity-Enhanced Single Photons from a Quantum Dot,* Optical Microcavities. Edited by K. J. Vahala. Published by World Scientific Publishing Co. Pte. Ltd. pp. 133–175 (2004).

[296] H. Mabuchi and A. C. Doherty, *Cavity Quantum Electrodynamics: Coherence in Context,* Science **298**, 1372–1377 (2002).

[297] U. Akram, N. Kiesel, M. Aspelmeyer, and G. J. Milburn, *Single-Photon Opto-Mechanics in the Strong Coupling Regime,* New J. Phys. **12**, 083030 (2010).

[298] L.-D. Haret, T. Tanabe, E. Kuramochi, and M. Notomi, *Extremely Low Power Optical Bistability in Silicon Demonstrated using 1D Photonic Crystal Nanocavity,* Opt. Express **17**, 21108–21117 (2009).

[299] J. D. Teufel, T. Donner, D. Li, J. W. Harlow, M. S. Allman, K. Cicak, A. J. Sirois, J. D. Whittaker, K. W. Lehnert, and R. W. Simmonds, *Sideband Cooling of Micromechanical Motion to the Quantum Ground State,* Nature **475**, 359–363 (2011).

[300] T. Westphal, D. Friedrich, H. Kaufer, K. Yamamoto, S. Goßler, H. Müller-Ebhardt, S. L. Danilishin, F. Y. Khalili, K. Danzmann, and R. Schnabel, *Interferometer Readout Noise below the Standard Quantum Limit of a Membrane,* Phys. Rev. A **85**, 063806 (2012).

[301] V. B. Braginsky and F. Y. Khalili, *Quantum Measurement* (Cambridge University Press, 1995).

[302] V. B. Braginsky and F. Y. Khalili, *Quantum Nondemolition Measurements: the Route from Toys to Tools,* Rev. Mod. Phys. **68**, 1–11 (1996).

[303] D. Leibfried, D. M. Meekhof, B. E. King, C. Monroe, W. M. Itano, and D. J. Wineland, *Experimental Determination of the Motional Quantum State of a Trapped Atom,* Phys. Rev. Lett. **77**, 4281 (1996).

[304] S. G. Johnson, M. Ibanescu, M. A. Skorobogatiy, O. Weisberg, J. D. Joannopoulos, and Y. Fink, *Perturbation Theory for Maxwell's Equations with Shifting Material Boundaries,* Phys. Rev. E **65**, 066611 (2002).

[305] B. E. A. Saleh and M. C. Teich, *Fundamentals of Photonics* (Wiley New York, 1991).

[306] J. R. Maze, A. Gali, E. Togan, Y. Chu, A. Trifonov, E. Kaxiras, and M. D. Lukin, *Properties of Nitrogen-Vacancy Denters in Diamond: the Group Theoretic Approach,* New J. Phys. **13**, 025025 (2011).

[307] M. S. J. Barson, P. Peddibhotla, P. Ovartchaiyapong, K. Ganesan, R. L. Taylor, M. Gebert, Z. Mielens, B. Koslowski, D. A. Simpson, L. P. McGuinness, J. McCallum, S. Prawer, S. Onoda, T. Ohshima, A. C. Bleszynski Jayich, F. Jelezko, N. B. Manson, and M. W. Doherty, *Nanomechanical Sensing using Spins in Diamond,* Nano Lett. **17**, 1496–1503 (2017).

[308] M. W. Doherty, V. V. Struzhkin, D. A. Simpson, L. P. McGuinness, Y. Meng, A. Stacey, T. J. Karle, R. J. Hemley, N. B. Manson, L. C. L. Hollenberg, and S. Prawer, *Electronic Properties and Metrology Applications of the Diamond NV-Center under Pressure,* Phys. Rev. Lett. **112**, 047601 (2014).

[309] G. Davies and M. F. Hamer, *Optical Studies of the 1.945 eV Vibronic Band in Diamond,* Proc. R. Soc. Lond., A **348**, 285–298 (1976).

[310] S. D. Bennett, N. Y. Yao, J. Otterbach, P. Zoller, P. Rabl, and M. D. Lukin, *Phonon-Induced Spin-Spin Interactions in Diamond Nanostructures: Application to Spin Squeezing,* Phys. Rev. Lett. **110**, 156402 (2013).

[311] K. V. Kepesidis, S. D. Bennett, S. Portolan, M. D. Lukin, and P. Rabl, *Phonon Cooling and Lasing with Nitrogen-Vacancy Centers in Diamond,* Phys. Rev. B **88**, 064105 (2013).

[312] L. Giannelli, R. Betzholz, L. Kreiner, M. Bienert, and G. Morigi, *Laser and Cavity Cooling of a Mechanical Resonator with a Nitrogen-Vacancy Center in Diamond,* Phys. Rev. A **94**, 053835 (2016).

[313] A. Taflove and S. C. Hagness, *Computational Electrodynamics: the FDTD Method* (Artech House Boston, London, 2000).

[314] A. F. Oskooi, D. Roundy, M. Ibanescu, P. Bermel, J. D. Joannopoulos, and S. G. Johnson, *MEEP: A Flexible Free-Software Package for Electromagnetic Simulations by the FDTD Method,* Comput. Phys. Commun. **181**, 687–702 (2010).

[315] S. G. Johnson, "Illustration of Yee Lattice," (2005). Retrieved on February 28, 2017 from http://ab-initio.mit.edu/wiki/index.php/Image:Yee-cube.png.

[316] K. Yee, *Numerical Solution of Initial Boundary Value Problems Involving Maxwell's Equations in Isotropic Media,* IEEE Trans. Antennas. Propag. **14**, 302–307 (1966).

[317] A. Farjadpour, D. Roundy, A. Rodriguez, M. Ibanescu, P. Bermel, J. D. Joannopoulos, S. G. Johnson, and G. Burr, *Improving Accuracy by Subpixel Smoothing in FDTD,* Opt. Lett. **31**, 2972–2974 (2006).

[318] A. F. Oskooi, C. Kottke, and S. G. Johnson, *Accurate Finite-Difference Time-Domain Simulation of Anisotropic Media by Subpixel Smoothing,* Opt. Lett. **34**, 2778–2780 (2009).

[319] V. A. Mandelshtam and H. S. Taylor, *Harmonic Inversion of Time Signals and its Applications,* J. Chem. Phys. **107**, 6756–6769 (1997).

[320] V. A. Mandelshtam and H. S. Taylor, *Erratum: Harmonic Inversion of Time Signals and its Applications,* J. Chem. Phys. **109**, 4128–4128 (1998).

[321] L. Kipfstuhl, *Simulation und Herstellung eines Diamantmikroresonators in eindimensionalen photonischen Kristallstrukturen,* Diplomarbeit, Universität des Saarlandes (2011).

[322] C. U. Hille, *Simulation und Untersuchung von Gitterkopplern für photonische Kristalle in Diamant,* Bachelorarbeit, Universität des Saarlandes (2012).

[323] F. Guldner, *Simulation optomechanischer Kristalle in Diamant,* Bachelorarbeit, Universität des Saarlandes (2014).

[324] A. Faraon, I. Fushman, D. Englund, N. Stoltz, P. Petroff, and J. Vučković, *Dipole Induced Transparency in Waveguide Coupled Photonic Crystal Cavities,* Opt. Express **16**, 12154–12162 (2008).

[325] T. Jung, L. Kreiner, C. Pauly, F. Mücklich, A. M. Edmonds, M. Markham, and C. Becher, *Reproducible Fabrication and Characterization of Diamond Membranes for Photonic Crystal Cavities,* Phys. Stat. Sol. A pp. 1–11 (2016).

[326] S. Gsell, T. Bauer, J. Goldfuss, M. Schreck, and B. Stritzker, *A Route to Diamond Wafers by Epitaxial Deposition on Silicon via Iridium/Yttria-Stabilized Zirconia Buffer Layers,* Appl. Phys. Lett. **84**, 4541–4543 (2004).

[327] W. McKenzie, J. Pethica, and G. Cross, *A Direct-Write, Resistless Hard Mask for Rapid Nanoscale Patterning of Diamond,* Diamond Relat. Mater. **20**, 707 – 710 (2011).

[328] S. K. Tripathi, D. Scanlan, N. O'Hara, A. Nadzeyka, S. Bauerdick, L. Peto, and G. L. W. Cross, *Resolution, Masking Capability and Throughput for Direct-Write, Ion Implant Mask Patterning of Diamond Surfaces using Ion Beam Lithography,* J. Micromech. Microeng. **22**, 055005 (2012).

[329] R. H. Webb, *Confocal Optical Microscopy,* Rep. Prog. Phys. **59**, 427 (1996).

Danksagung

An dieser Stelle möchte ich mich bei all jenen bedanken, die mich unterstützt und dadurch diese Arbeit erst ermöglicht haben. Allen voran danke ich meinem Doktorvater Prof. Dr. Christoph Becher für die Möglichkeit zur Promotion auf einem aktuellen und spannenden Thema. Besonders dadurch, dass ich stets neue Ideen einbringen und selbstständig umsetzen durfte, wurden die letzten Jahre zu einer sehr herausfordernden und lehrreichen Zeit. Ein herzliches Dankeschön geht an meine Zweitgutachterin Prof. Dr. Giovanna Morigi, mit der ich immer mal wieder sehr erfolgreich zusammenarbeiten durfte. Ich konnte dabei über die Physik und darüber hinaus lernen und habe den „theoretischen" Blickwinkel stets als Bereicherung empfunden.

Diese Arbeit basiert auf der Zusammenarbeit mit einer ganzen Reihe von Menschen an dieser Uni und außerhalb. Eine ganz besondere Erwähnung verdient dabei Christoph Pauly, der die schönsten FIB-Strukturen der Welt schreibt. Vielen Dank für die unzähligen Stunden an der Helios und die Gewissheit, dass wenigstens ein Schritt des Herstellungsprozesses immer zuverlässig funktioniert. Ein großer Dank geht an die Arbeitsgruppe von Dr. Matthias Schreck in Augsburg für das Wachsen der Diamantfilme. Auch beim Team des Nanostructuring Center Kaiserslautern, Dr. Sandra Wolff, Christian Dautermann und Dr. Bert Lägel, möchte ich mich herzlich bedanken, dass ich stets unkompliziert Zugang zu allen Einrichtungen und Hilfe bei Fragen und Problemen erhalten habe. Vielen Dank auch an Dr. Elmar Kroner, Dr. René Hensel und insbesondere Susanne Selzer vom Leibnitz INM, die mir den Zugang zur Ätzanlage ermöglicht haben, wann immer sie lief. Bedanken möchte ich mich auch bei Jörg Schmauch für die Anfertigung von REM-Bildern, bei Günter Marchand für Hilfe beim Ätzen mit Flusssäure und bei Karin Kretsch für die Unterstützung im Chemielabor. Auf der theoretischen Seite geht ein großer Dank an Luigi Giannelli und Dr. Ralf Betzholz, die unter Anleitung von Dr. Marc Bienert und Prof. Dr. Giovanna Morigi einen großen Beitrag dazu geleistet haben, dass die Simulationsergebnisse dieser Arbeit ihren Weg in ein theoretisches Modell gefunden haben. Ganz besonders möchte ich mich bei Elke Huschens bedanken, die mit großem Engagement und riesiger Hilfsbereitschaft noch jeden Papierkrieg für sich entscheiden konnte. Der Stiftung der Deutschen Wirtschaft bin ich sehr dankbar für die Unterstützung dieser Arbeit mit einem Promotionsstipendium.

Ein großes Dankeschön gilt der Arbeitsgruppe mit all ihren ehemaligen und aktuellen Mitgliedern. Insbesondere bei meinen langjährigen Bürokollegen Janine und Thomas möchte ich mich für die gute Teamarbeit und die schöne Zeit bedanken. Zusammen mit Felix und Cornelia haben sie durch Anregungen, kritische Nachfragen und viel gute Zusammenarbeit zum Gelingen dieser Arbeit beigetragen. In diesem Sinne möchte ich mich auch bei meinen Korrekturlesern Katharina, Thomas und Christoph bedanken.

Selbstverständlich dürfen auch diejenigen nicht unerwähnt bleiben, die mich stets mit Freude von der Arbeit abgelenkt haben. Mein allergrößter Dank gilt meinen Freunden, meinen Eltern und Geschwistern und vor allem Asger, die mich immer unterstützen und einfach für mich da sind.